Deterministic lithographic fabrication of single emitter plasmonic patch nanoantennas, and their characterization

Amit Raj Dhawan

PhD Thesis at the University of Pierre & Marie Curie

Speciality: Particle and condensed matter physics

Realized at

Paris Institute of Nanosciences

by

Amit Raj Dhawan

For obtaining the grade of

Docteur de l'Universite Pierre et Marie Curie

On the subject of

Deterministic lithographic fabrication of single emitter plasmonic patch nanoantennas, and their characterization

Defence scheduled on February 5, 2016

Jury:

M^{me} Elizabeth Boer-Duchemin	Referee
M. Joël Bellessa	Referee
M. Jean Hare	Examiner
M^{me} Laurence Pruvost	Examiner
M^{me} Pascale Senellart	Examiner
M^{me} Agnès Maître	Supervisor

THESE DE DOCTORAT DE L'UNIVERSITÉ PIERRE ET MARIE CURIE

Spécialité : La physique, de la particule à la matière condensée

Réalisée à

Institut des NanoSciences de Paris

Présentée par

Amit Raj Dhawan

Pour obtenir le grade de

DOCTEUR de l'UNIVERSITE PIERRE ET MARIE CURIE

Sujet de la thèse

Fabrication par lithographie déterministe de nanoantennes patch plasmoniques à émetteur unique, et leur caractérisation

Soutenance prévue le 5 Février 2016

devant le jury composé de :

M^{me} Elizabeth Boer-Duchemin	Rapporteur
M. Joël Bellessa	Rapporteur
M. Jean Hare	Examinateur
M^{me} Laurence Pruvost	Examinateur
M^{me} Pascale Senellart	Examinateur
M^{me} Agnès Maître	Directrice de thèse

O Veena-Vaadini
dancing to the tunes you play,
floating on your waters,
I go where you say.

Table of Contents

List of Figures

List of Abbreviations and Symbols

AFM	atomic force microscopy
APD	avalanche photodiode
CCD	charged-coupled device
CGH	computer-generated hologram
CW	continuous wave
e-beam	electron-beam
Eq.	equation
ESPCI	École Supérieure de Physique et de Chimie Industrielles
F_P	Purcell Factor
FWHM	full width half maximum
INSP	Institut des NanoSciences de Paris
LG	Laguerre-Gaussian
LCoS	liquid crystal on silicon
MIBK	methyl isobutyl ketone
MSE	mean squared error
N.A.	numerical aperture
NC	nanocrystals
PBS	polarizing beam splitter
PMMA	polymethyl methacrylate
RMS	root mean squared
rpm	revolutions per minute
SEM	scanning electron microscopy
SLM	spatial light modulator
TEM	transmission electron microscopy
TCSPC	time correlated single photon counting
UHV	ultrahigh vacuum
t_{acq}	acquisition time
Γ	decay rate
Γ_r	radiative decay rate
Γ_{nr}	non-radiative decay rate
$\jmath$	complex imaginary unit $\sqrt{-1}$
λ	wavelength
$\widetilde{\epsilon}$	complex relative permittity
ϵ'	real part of complex relative permittivity or real relative permittivity
ϵ''	imaginary part of complex relative permittivity
τ	lifetime or decay time

This page is intentionally left blank.

Motivation and Outline

The spontaneous emission of an emitter can be controlled by modifying its environment. This effect can be used to enhance the spontaneous emission of single quantum emitters and create efficient single photon sources. The possibility of directing this enhanced emission by using antennas will further improve the efficacy of these structures. Theoretical studies show that plasmonic patch antennas [1], are promising candidates for obtaining accelerated and directed spontaneous emission. Single emitter structures offer unique advantages and the possibility to investigate and understand scientific phenomena which are absent in the averaged response of multi-emitter emission. Using in-situ optical lithography [2], multi-emitter patch antennas have been fabricated [3]. These antennas showed significant acceleration of emission and directivity. But due to the photobleaching and low emission signal of a single emitter (as compared to a cluster of emitters), conventional lithography techniques could not be implemented for fabricating single emitter antennas. Deterministic fabrication and analysis of patch antennas has been the motivation of my PhD work.

To perform deterministic lithography on single emitters, we have found three new techniques. To our knowledge, this thesis is the first report on these techniques and the single emitter plasmonic patch antennas realized by their implementation. Our first method uses in-situ optical lithography with a supercontinuum laser to deterministically position single nanocrystals (which are single photon sources) inside an optical patch antenna. The second procedure uses a combination of in-situ optical lithography and e-beam lithography for the deterministic positioning of single emitters in plasmonic antenna structures. The third method involves generating LG modes and performing deterministic in-situ optical lithography on single emitters. All these techniques offer three-dimensional control in positioning the antenna patch over the emitter. These techniques can be used for realizing a variety of photonic structures, especially those that use single emitters.

The plasmonic patch optical antennas discussed in this thesis use a single CdSe/CdS core/shell nanocrystal as the emitter. These colloidal quantum dots exhibit size-dependent emission-wavelength tunability and stable single photon emission at room temperature [4]. The developments in the field of colloidal quantum dots are improving their emission characteristics. By incorporating them inside patch antennas, we are able to accelerate and direct their emission. Most importantly, the emission from these antennas can be analyzed to gain

insight into the light–matter interactions at a single emitter level. In addition to CdSe/CdS core/shell quantum dots, other emitters like nitrogen vacancy centers in nanodiamonds and other quantum dots can be used as well. The antenna emission wavelength can be tuned by using the appropriate emitters and patch materials.

Chapter 1 introduces the topic of optical patch antennas and describes their characteristics. The later part of the chapter is focused on CdSe/CdS quantum dots, which serve as the antenna emitters. After discussing the chemical synthesis and the luminescence properties of these quantum dots, the last part of the chapter describes single-photon emission and our optical measurement setup for detecting single photons.

In chapter 2, we discuss the fabrication concept of a single emitter nanoantenna. This chapter describes the topics that are common to all our techniques. These include deposition of metal and dielectric films, and their characterization. After discussing the problem of vapor deposition on dielectrics, the topic of spin-coated polymer films is described.

Chapter 3 lays the foundation of our work of deterministic lithography, and describes the protocol of supercontinuum laser lithography. Important aspects of lithography like the choice of resists, the deposition procedure, and the lift-off process are described in detail. As all our techniques perform lithography on a resist bi-layer, many discussions in this chapter are applicable to other chapters as well. The last chapter is about the experimental optical analysis of the realized plasmonic patch antennas.

Our protocol that implements a combination of optical and e-beam lithography is described in chapter 4. After detailing the important aspects of this method, the chapter discusses the optical characteristics of the fabricated patch antennas.

Chapter 5 begins with a description of LG modes and their properties. It then discusses spatial light modulation using liquid crystal displays, which is implemented to generate LG modes. After describing the protocol of in-situ optical lithography with LG laser modes, the emission of the realized patch nanoantennas is analyzed.

The thesis concludes with a summary and gives an outlook on further investigations and improvements.

1 Plasmonic Optical Antenna with a Single Emitter

Antennas have become an important part of our lives as they are crucial for the operation of telecommunication devices like mobile phones, tablets and computers with wireless connectivity, and satellites. Due to their wide range of application, antennas operating at radio and microwave frequencies of the electromagnetic spectrum are widely studied by electrical engineers. An antenna is a structure, usually made from a good conducting material, that has been designed to have a shape and size such that it radiates electromagnetic power in an efficient manner. Generally, an antenna is also a good receiver of electromagnetic power. In order to radiate efficiently, the minimum size of the antenna must be comparable to the wavelength of emitted radiation [5]. The difficulty in fabricating small-size antenna structures (400 – 700 nm) delayed the appearance of optical antennas compared to radio antennas. In recent times, developments in nanofabrication have paved the way for antennas for light [6, 7]. The definition of an antenna can be extended to the optical domain, and following [7], it can be stated that an optical antenna is a device that can convert freely propagating optical radiation into localized energy, and vice versa.

With the inclusion of antennas in the optical regime, many new scientific and technical opportunities have become available and the list is growing. It has been shown that optical antennas can enhance the spontaneous emission of emitters like quantum dots [3, 8, 9], nanorods [10], fluorescent molecules [11], and nitrogen-vacancy defect centers in nanodiamonds [12]. The nanoscopic manipulation of light by optical antennas makes them useful in imaging [13], spectroscopic [14, 15, 16], photovoltaic [17, 18, 19, 20], and lasing [21, 22] applications and studies.

The analogy between optical and radio-frequency antennas has generated scientific interest but due to the difference in the behavior of metals in the two frequency regimes, the well-established concepts of radio-frequency antennas [5, 23] cannot be applied directly to optical antennas [24, 25]. Metals are almost perfect conductors at radio-wave wavelengths and lower, and their skin-depth [26] is truly sub-wavelength—this is no longer true in the visible regime and this results in interesting phenomena that are being investigated and applied. An

example of this is the concept of antenna impedance that has been investigated in references [27], [28], and [29].

Amongst optical antennas, plasmonic optical antennas are the most discussed [24]. These devices benefit from plasmonic phenomena which results in confinement and enhancement of optical fields [25, 30]. There are other semiconductor and high-dielectric constant material-based optical antennas [31, 32] as well.

1.1 Plasmonics terminology

This section will mention briefly the terminology of plasmonics. A **plasmon** is a quantum of collective charge density oscillation in a metal [33]. There are different types of plasmons like volume plasmons, surface plasmons, and localized plasmons. **Volume plasmons** are longitudinal waves, and due to their longitudinal nature, they do not couple with transverse electromagnetic waves [34]. **Surface plasmons** are plasmons confined to the metal-dielectric interface [35]. Surface plasmons can be further characterized as surface plasmon polaritons (**SPP**) and localized surface plasmons (**LSP**) [34]. **Surface plasmon polaritons** are propagating surface wave solutions of Maxwell's equations for certain boundary conditions [25]; they can be treated as transverse waveguide modes [36]. **Localized surface plasmons** (**LSP**) are non-propagating waves of conduction electrons of metallic structures, which exist in bounded geometries of sub-wavelength size, such as metallic particles (nanoparticles, nanorods, nanodisks) [34]. When a time-dependent electromagnetic field is confined to metallic nanoparticles such that the wavelength of the electromagnetic field is much larger than the confining dimensions of the metallic particles, then time-dependent contributions of the electromagnetic field to the solutions of Maxwell's equations can be neglected. This quasi-static approximation leads to an electrostatic solution to field distribution—LSP [36].

1.2 Plasmonic patch nanoantenna

The structure of a plasmonic patch nanoantenna is illustrated in Figure 1.1. It is an optical antenna if it operates in the visible wavelength range. If the emitter of the antenna is a single photon emitter like a quantum dot or a nitrogen vacancy defect center in a nanodiamond, the antenna radiation can be single photon emission. The patch nanoantennas that we have fabricated were theoretically studied by Esteban *et al.* of the Greffet's group at Laboratoire Charles Fabry, Institut d'Optique, Paris [1]. Following this work, Belacel used photolithography in his PhD work [3, 8] in the groups of Maître (INSP, Paris) and Senellart (Laboratoire de Photonique et de Nanostructures, Paris) and fabricated plasmonic patch nanoantennas that used a cluster of quantum dots as an emitter. But as a cluster of quantum dots is not a deterministic single-photon source, antennas using them as emitters do not show deterministic single photon emission nor the possibility to study the phenomena that occur when single emitter emission is coupled to a plasmonic cavity. For these reasons, we chose to place a single CdSe/CdS core/shell nanocrystal as the antenna emitter but conventional lithography techniques could not be used for performing lithography on a deterministically positioned

single emitter. To realize this, we had to formulate new lithography protocols, which has been the main work of my PhD.

Where plasmonic patch nanoantennas can provide more insight into the light–matter interactions involved in these structures, they are of technical importance as well because they can increase and direct the emission of an emitter. When irradiated by light, a quantum dot spontaneously radiates single photons by fluorescence. However, this signal of single photon emission from a quantum dot, such as a colloidal semiconductor nanocrystal, can be low and has very low directional character. To accelerate the emission of single photons and to better control the flow of emitted photons, our nanoantenna draws benefits from the field of plasmonics. This involves the coupling of radiation from the nanocrystal to metal structures placed at optimum distance.

Purcell pointed out that the amount of power emitted by an electromagnetic source depends not only on the nature of the source but also on the environment around the it [37]. By changing the environment around the nanocrystal, its emission properties can be changed. A plasmonic nanoantenna uses this principle with appropriate components to control the flow of light [1, 3].

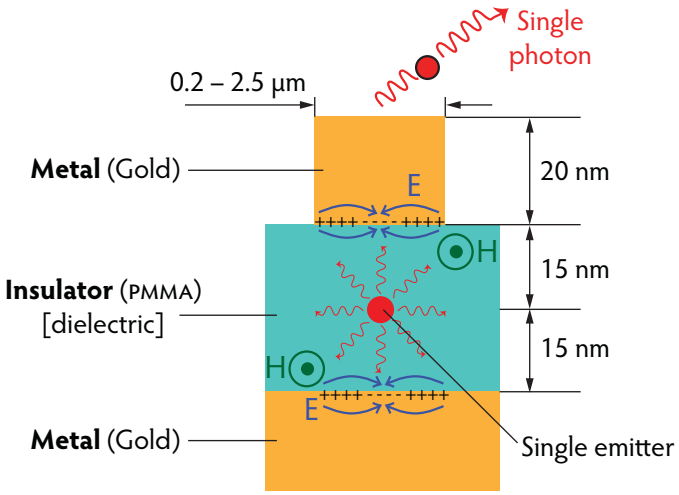

Figure 1.1 *Operation of a single photon emitter plasmonic patch nanoantenna*

Letters E and H denote the electric and magnetic fields, respectively. Note the metal-dielectric-metal structure. We use PMMA as the dielectric and Au as the metal. Other dielectrics and plasmonic metals can be used as well.

Figure 1.1 outlines the operation of a plasmonic nanoantenna. The single photon emitter (in our case, a quantum dot), upon excitation by light, e.g. laser light, emits single photons by fluorescence. Due to the positioning of the appropriate metal structures above and below the emitter at optimum distance, radiation from the emitter is coupled to the metal structures. This leads to the generation of surface plasmons at the metal-dielectric interface. In the gold layers above and below the emitter, these surface plasmons are propagating waves, and as they exist at the metal-dielectric interface and are coupled to photons (fluorescent radiation from the nanocrystal), we can state that they are surface plasmon polaritons (SPP) (see Section 1.1). The SPPs generated at the metal-dielectric interface give rise to confined and strongly enhanced optical near-fields [25], which finally leads to the radiation of photons

from the top of the 20 nm thick patch—this constitutes the antenna radiation. The presence of the metal-insulator-metal structure changes the radiative properties of the single emitter. For example, it can accelerate the radiative emission of the emitter. The plasmonic metal patch functions as an antenna by directing the emitted radiation.

1.2.1 Purcell effect

First described by E. M. Purcell in 1946, the Purcell effect is the phenomenon of change in the emission properties of an electromagnetic source as its environment is changed [37]. An excited nanocrystal placed in vacuum will decay spontaneously by interaction with the vacuum continuum. In this two-level system (Figure 1.8), for a given transition frequency, the decay rate is proportional to the spectral density of modes per volume [38]. When the nanocrystal is positioned between an appropriately placed gold patch and gold film, as in the nanoantenna (Figure 1.1), the situation changes. Radiation from the nanocrystal excites SPPs at the metal-dielectric interfaces above and below it. Moreover, the patch of these antennas appears to be a cavity, inside which the excited SPPs undergo reflection at the edges and interfere constructively showing adequate resonances [1]. These resonances enhance the decay rate of the emitter, thus possibly accelerating the radiative emission.

In general, the Purcell factor is given as the ratio of the decay rate of spontaneous emission within the cavity to the decay rate of spontaneous emission in outside the cavity [39]. This concept can be extended further to describe the emission from patch nanoantennas [8, 40, 1]. The Purcell factor or the acceleration of emission of these patch antennas is stated as [41]:

$$F_P = \frac{\Gamma_{\text{antenna}}}{\Gamma_{\text{vacuum}}} = \frac{\tau_{\text{vacuum}}}{\tau_{\text{antenna}}} \propto \frac{Q}{V} \left(\frac{|\mathbf{d} \cdot \mathbf{E}(\mathbf{r})|^2}{1 + 4Q^2 \left(\frac{\omega}{\omega_0} - 1 \right)^2} \right) \tag{1.1}$$

where Γ_{antenna} and Γ_{vacuum} are the decay rates of the emitter in the antenna environment and vacuum, respectively, and τ_{antenna} and τ_{vacuum} are the lifetimes of the emitter in the antenna environment and vacuum, respectively. Q is the quality factor, V is the mode volume, $\mathbf{d}$ is the dipole moment of the emitter dipole, $\mathbf{E}(\mathbf{r})$ is the electric field in the cavity (patch) as a function of position $\mathbf{r}$, ω_0 is the emission frequency in vacuum, and ω is the emission frequency in the cavity.

Our single photon emitter nanoantennas benefit from the Purcell effect. By controlling the dielectric spacing and the antenna patch size, the Purcell factor of these structures can be further increased.

The nanoantenna emitter—CdSe/CdS quantum dot—can be modeled as a dipole [42] and its orientation strongly influences its coupling to the patch. The simulation results of Belacel *et al.* [3] show that the Purcell factor of a patch nanoantenna is dependent on the patch size, the emitter position between the Au layers, and the orientation of the emitter dipole (Figure 1.2).

Polarization analysis of the emission of an emitter (modeled as a dipole) can be used to find the three-dimensional orientation of the emitter dipole [43, 42]. Using this method, we can select vertically aligned dipoles and fabricate nanoantennas using them, thus benefitting from high emission acceleration. Information about the emitter orientation and the behavior

of the corresponding patch nanoantenna can be used to study the involved optical interactions in these structures. Exploiting this feature will be one of the objectives of our future work on patch nanoantennas.

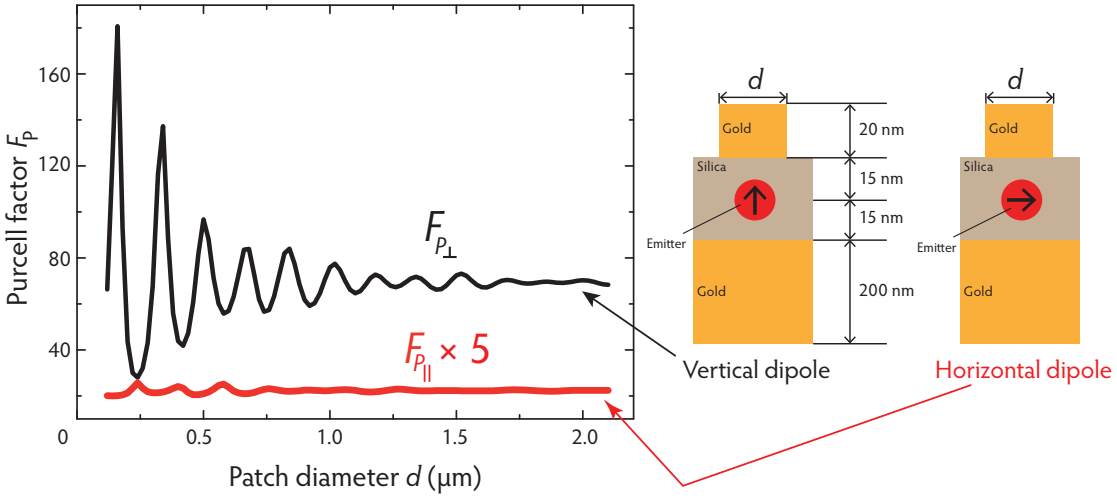

Figure 1.2 *Purcell factor depending on dipole orientation and patch diameter*
The figure shows a simulation result reported in [8]. A point-like emitter, emitting at 620 nm, was placed between the two gold structures that were separated by 30 nm. For two orientations of the emitter dipole—vertical and parallel—the emission acceleration was noted as a function of the patch diameter. To obtain a high Purcell factor, the emitter dipole should be in the vertical orientation.

1.2.2 Directivity

Generally, an antenna does not radiate uniformly in all directions. The variation of radiation intensity with direction is given by directivity $D(\theta, \phi)$ [5]:

$$D(\theta, \phi) = \frac{\text{power radiated per unit solid angle}}{\text{average power radiated per unit solid angle}}$$

$$= \frac{dP_r/d\Omega}{P_r/4\pi} \tag{1.2}$$

where Ω is the solid angle and P_r is the total power radiated by the antenna.

The radiation pattern of an isolated nanocrystal is not of directional character, which means that radiation from the nanocrystal cannot be directed in a particular direction. When the nanocrystal is put as an emitter in a plasmonic antenna then the antenna radiation acquires a very directional character. This property can be used in many ways. For example, a lens of a given numerical aperture will be able to collect more photons from a well placed directional source—in other words, using directive photon emission sources, we can increase the collection efficiency of the lens.

In a plasmonic nanoantenna, the directivity can be controlled by changing the diameter of the gold disk placed on top of the nanocrystal. Figure 1.3 shows the radiation pattern of a plasmonic nanoantenna whose point-like emitter dipole is vertically oriented as shown in Figure 1.2. Patch antenna emission is the most directional when the emitter dipole is vertically oriented [3].

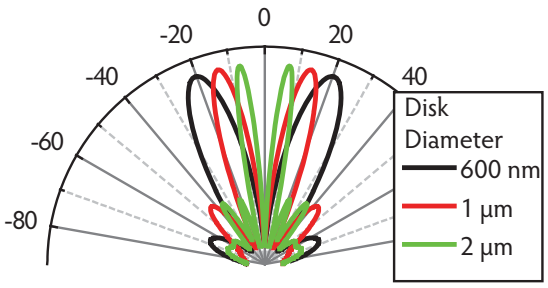

Figure 1.3 *Directivity of plasmonic nanoantennas*

A plasmonic nanoantenna is directional, which means better collection efficiency. From the displayed radiation pattern (plotted for a vertically oriented emitter-dipole), we note that the directivity of a patch nanoantenna can be altered by changing the disk diameter. Image source: [3].

When the emitter dipole of a plasmonic patch antenna is vertically oriented, the antenna shows the best Purcell factor and is the most directive. By estimating the emitter dipole orientation with polarization analysis, we can position different patch sizes on them and attain plasmonic patch antennas with a very high Purcell factor and directivity.

A concise description of optical antenna parameters such as *antenna efficiency, radiation pattern, effective area, gain, reciprocity, aperture, effective wavelength, radiation resistance, lumped circuit elements, inductance*, and *density of states* can be found in reference [25]. Their radio analogs can be found in reference [5] or [23].

1.3 Nanocrystals

A nanocrystal is a crystalline aggregate of atoms, which has a radius between 1–100 nm and typically consists of 10–10^5 atoms [44]. Semiconductor nanocrystals can be synthesized chemically in several forms such as spherical particles, nanorods, spherical core/shell structures, core/shell dot-in-rods, and tetrapods [45, 4].

Semiconductor nanocrystals, whose all three dimensions are in the nanometer range, exhibit three-dimensional quantum confinement; these are also called quantum dots [46]. They define a state between discrete molecules and bulk matter. The possibility of controlling the size, shape, and composition of semiconductor nanocrystals—which directly influences their electronic and optical properties—has made them widely applicable in many areas, such as bio-imaging, colored displays, white light-emitting diodes, photovoltaics, and possibly quantum computing and cryptography.

1.3.1 CdSe/CdS core/shell quantum dot

Our nanoantennas use a spherical core/shell semiconductor nanocrystal as an emitter. These quantum dots consist of a CdSe core ($\phi \approx 3$ nm) which is surrounded by a CdS shell (about 6–8 nm thick). The total diameter of this spherical core/shell quantum dot is about 15–19 nm (Figure 1.4(a)). The shell is constituted of a material with a similar lattice constant as the core, and its presence around the core passivates the surface bonds, thereby making the quantum dot more stable and fluorescent [47]. Moreover, the presence of a thick shell can considerably reduce blinking (fluorescence intermittency) [48]. Due to the high surface to volume ratio in nanoparticles, surface effects are very important.

Due to their chemical composition, which includes II–VI semiconductors, CdSe/CdS quantum dots are known for their stability and quantum yield [49]. Their chemical synthesis is relatively easy and produces high quality quantum dots [4]. Figure 1.4 shows a schematic and a transmission electron microscope image of the quantum dots used in our nanoantennas. These dots show a quasi-spherical shape.

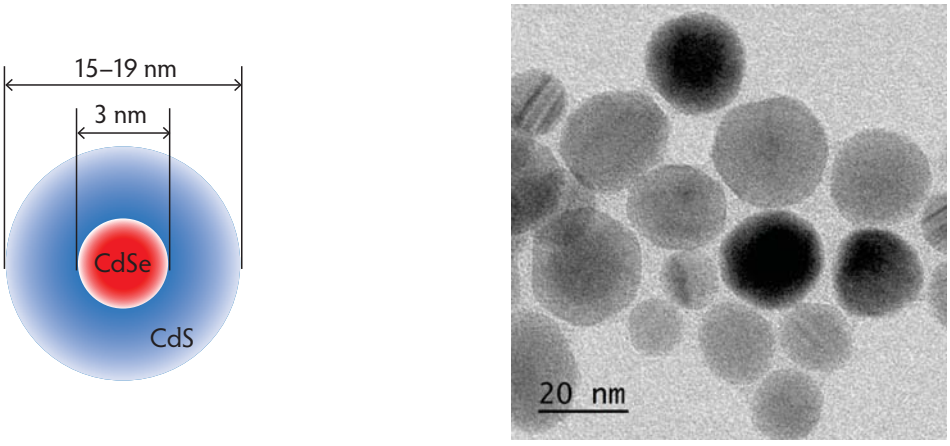

(a) Core/Shell nanocrystal **(b)** TEM image of nanocrystals

Figure 1.4 *CdSe/CdS core/shell quantum dots*

(a) Schematic showing the typical structure of our quantum dots. **(b)** Transmission electron microscope (TEM) image of the quantum dots used in our nanoantennas. Note the size and the size-variation of nanocrystals, both of which can be controlled during the chemical synthesis. Image courtesy of Michel Nasilowski.

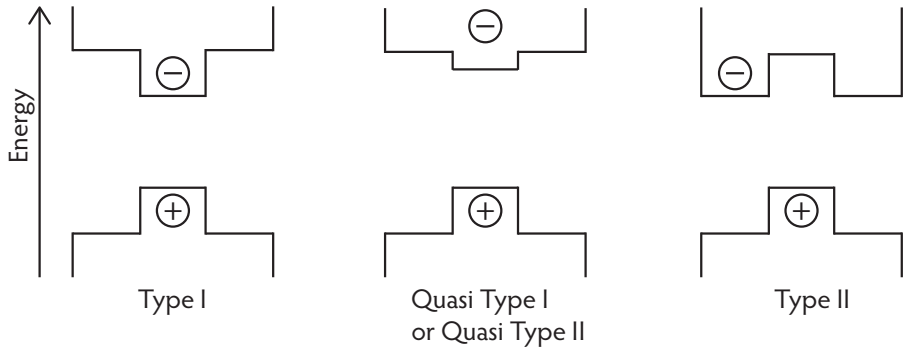

Figure 1.5 *Type I, Type II, and quasi Type I quantum dots*

Energy band alignment diagrams of the valence and the conduction bands of Type I, Type II, and quasi Type I quantum dots.

Depending on the band alignment of the valence and the conduction bands of the core and shell materials of the quantum dot, they can be broadly categorized as Type I, Type II, and quasi Type I (also addressed as quasi Type II). In Type I core/shell quantum dots, such as CdSe/ZnS [50, 51], the shell material has a higher bandgap than the core material and the excited charge carriers—electrons and holes—are confined within the core. Confinement of charge carriers within the core reduces their interaction with surface trap states, thereby suppressing the non-radiative recombination and enhancing fluorescence [25]. In Type II quantum dots, such as CdTe/CdSe and CdSe/ZnTe [52, 51], the shell material has a lower bandgap

than the core, and the excited electrons are mostly localized in the shell. Our relatively thick CdSe/CdS are quasi Type I quantum dots, where the bandgap of the CdS capping is higher than that of the CdSe core [51] but the conduction bands of the two materials are almost aligned, therefore the excited electron can be found both in the core and the shell [53].

1.3.2 Nanocrystal fabrication

The quantum dots used in this work were synthesized in colloidal solutions by Michel Nasilowski working in Benoit Dubertret's group at Laboratoire Photons Et Matière, École Supérieure de Physique et de Chimie Industrielles (ESPCI) in Paris. Firstly, the CdSe cores are synthesized using a protocol based on the work of Peng *et al.* [54, 55] and using the expertise developed in Dubertret's group. The following sections will mention the synthesis and related properties of CdSe/CdS core/shell quantum dots. With the goal of finding the most suitable emitters for our nanoantennas, we tested several batches of CdSe/CdS nanocrystals of varying sizes, which were synthesized using the method explained below. Size and structure variation was achieved by altering some parameters in the chemical process but the general method was the same.

The quality of the synthesized colloidal core/shell nanocrystals is highly dependent on the efficacy of the chemical process. Some experience and understanding of the chemical synthesis of nanocrystals, and their chemistry, allowed me to better tune them to our requirements. An example of this is the regular addition of ligands to the nanocrystal dispersion (section 1.3.5).

1.3.3 CdSe core synthesis

In a 100 ml three-neck flask, 750µl of 0.5 M cadmium oleate [$Cd(C_{18}H_{34}O_2)_2$], 1.5 ml of TOPO [trioctylphosphine oxide, $[CH_3(CH_2)_7]_3PO$], 1.5 ml of octadecene [$C_{18}H_{36}$] are added. The mixture is degassed at 70°C for 3 hours. Then argon gas is let in and the solution is heated from 20°C to 300°C. Very swiftly, 4 ml of trioctylphosphine selenide [TOPSe, $(C_8H_{17})_3P{=}Se$] is added, which is followed by the addition of 3 ml oleamine or oleylamine. The mixture is then annealed for 8 minutes. The flask is let to cool down and this stops the synthesis of the CdSe cores. For room temperature colloidal stability of the dots, 0.1 ml of oleic acid [$C_{18}H_{34}O_2$]is added to the solution. The dots in the solution are precipitated by adding ethanol [C_2H_5OH]. The precipitated CdSe nanocrystals are collected and suspended in hexane (about 5 ml). The final diameter of the dots decides their photoluminescence spectrum.

1.3.4 CdS shell growth

The precipitated CdSe cores from the above step are put in a three-neck flask with 5 ml of octadecane ($C_{18}H_{38}$) and 50 mg of cadmium is added to it. The mixture is degassed at 70°C for 30 minutes and put under argon flow. Then 5 ml of a 8.1 M solution of sulphur in octadecene, 1 ml of 0.5 M cadmium oleate, and 1 ml of oleylamine ($C_{18}H_{35}NH_2$) are added at the injection rate of 2 ml/hour for the first 2 ml and the remaining is injected at 18 ml/hour. The mixture is heated at 300°C for 10 minutes. It is then cooled down to room temperature and the nanocrystals are precipitated with ethanol, centrifuged and dispersed in 5 ml of hexane (C_6H_{14}). Finally, we have a colloidal dispersion of CdSe/CdS core/shell nanocrystals in hexane. Figure 1.6 shows a schematic of a quantum dot with ligands.

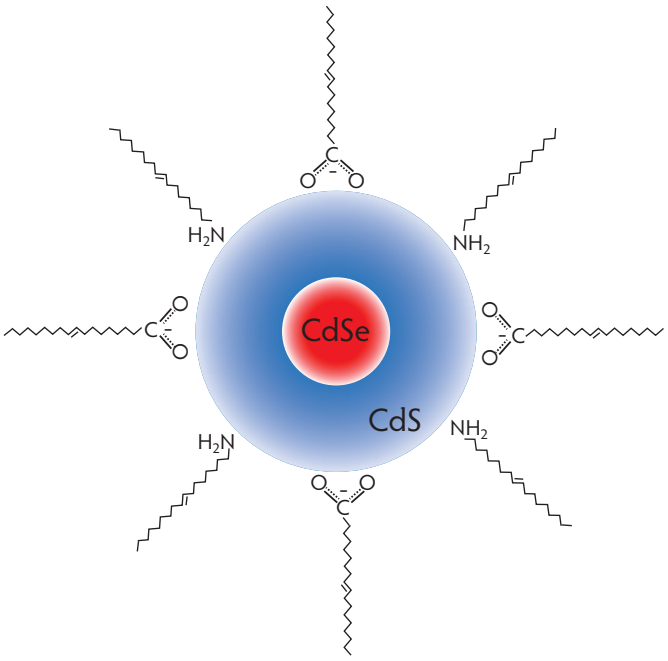

Figure 1.6 *CdSe/CdS quantum dot with ligands*

The ligands synthesized quantum hold the quantum dot in the dispersion. We use hexane as the solvent but any other nonpolar solvent like toluene or chloroform can be used. The ligands attached to the shell consist of an 18-atoms carbon chain, which is terminated by either COO^- or NH_2. The COO^- and NH_2 attach to the quantum dot and the 18-atoms alkyl chain is oleophilic—this ensures the colloidal stability. The double bond between the 9^{th} and 10^{th} carbon atom ensures the stability of the nanocrystals in nonpolar solvents like hexane and chloroform [56].

1.3.5 Nanocrystal preservation

Nanocrystals, like other materials, may degrade with time. Oxidation of nanocrystals can produce defects in nanocrystals that open non-radiative recombination channels [57, 4]. This leads to shutting down of the radiative recombination channels, which are responsible for fluorescence. Nanocrystals, like other fluorophores, are prone to photobleaching. Photobleaching or fading is a photon-induced chemical change that results in permanent loss of fluorescence of a fluorophore [58]. Our nanocrystals are stored as colloidal dispersions. The type and amount of ligands around the nanocrystal and the type and amount of solvent in which they are dispersed can affect their life [56].

Nanocrystal damage becomes even more relevant when we deal with individual emitters, which is our case. Moreover, in our lithography process, we focus high power laser light onto the nanocrystal and this requires the nanocrystal to be robust to bear the input. In our initial work, it was observed that after one year from synthesis, the nanocrystals photobleached much quicker and were not able to bear high laser intensity (especially pulsed laser light) for long. Any significant change in nanocrystal behavior during the initial formulation of the lithographic protocol (which took more than a year) was unacceptable. The protocol involved many parameters—such as wavelength, power, and exposure interval of the laser—that had to be characterized and controlled precisely. As these parameters were affected by the properties of the nanocrystals, it was imperative to fix the parameter of nanocrystal properties and then

decide the other parameters of the protocol. With this in mind we began looking for solutions to the mentioned problem.

One way to preserve the properties of nanocrystals over time is to store them in highly concentrated mother dispersions. It has been observed in several cases that if the concentration of nanocrystals in the dispersion is very low, their properties deteriorate faster. It seems that the interactions responsible for this are nanocrystal–ligand and ligand–solvent. The effect of dilution on nanocrystal properties can be seen from the following experiment. From a nanocrystal mother solution, 10 µl was taken, diluted 100 000×, and kept in an eppendorf. 50 µl from this dilution was spin-coated on a glass slip, which was observed by fluorescence microscopy—homogenously distributed fluorescing emitters were visible. The eppendorf was left undisturbed for 24 hours. The next day, the eppendorf was briskly shaken and 50 µl was spin-coated on a glass slip, which was viewed by the same fluorescence microscope—very few emitters were observed and these seemed to be less bright. To make sure that the precipitation of nanocrystals in the eppendorf was not an issue, the eppendorf was sonicated and the following experiment was repeated but the result was the same as the previous one—very few and dim emitters were visible. We recorded similar results after conducting such experiments a few times on some batches of nanocrystals. The above mentioned made us conclude that for long term stability, concentration of nanocrystals in the solvent should be high. We have assumed, as it should be, that the material of the eppendorf does not alter the nanocrystal properties. As far as producing very high dilutions for spin-coating are concerned, we have always prepared fresh dilutions which were used within 1 hour of preparation.

The role of the ligands is to hold the nanocrystal in the colloidal dispersion but they can also affect the nanocrystal photoluminescence properties [59]. The effect of ligand addition and exchange on the properties of nanocrystals has been a subject of interest [60, 61, 59, 62]. Reports based on in-solution photoluminescence measurements demonstrate the effect of ligand concentration on the photoluminescence of CdSe/CdS core/shell nanocrystals [63]. NH_2 in the ligands can prevent oxidation of the nanocrystal, thereby improving its life and fluorescence. With time, the ligands holding the nanocrystal in the solution may deteriorate [56]. To prevent this, we regularly add ligands to the mother solution of the nanocrystals. At times, we remove the old ligands, precipitate the nanocrystals, and add new ligands. We did not record any significant change in the photoluminescence of the individual quantum dots due to the above mentioned ligand addition, at least not to the extent that it affected our fabrication protocol.

Nanocrystal deterioration may be enhanced by high temperatures and exposure to light. For this reason many manufacturers of colloidal quantum dots recommend storing them in the dark at 4°C [64]. However, it has been observed by our group at INSP that the CdSe/CdS core/shell nanocrystals synthesized by Dubertret's group (ESPCI) can be stored in dark at room temperature without any degradation.

Considering the above mentioned, Dubertret's group (PhD work of Michel Nasilowski) provided us with a highly concentrated batch of colloidal CdSe/CdS core/shell spherical nanocrystals. Figure 1.4(b) shows a TEM micrograph of these nanocrystals. These nanocrystals precipitated or settled down in the solvent in less than 6 hours. As intended [65], the concentrated nature of the dispersion seems to enhance nanocrystal stability. To use these nanocrystals, we shake the bottle of the mother solution and take out 500 µl of the mother solution in a glass vial. The solution in the glass vial now acts as the mother solution—this solution can be

used to prepare about 100–500 samples with spin-coated individual nanocrystals. Every two months, we add 5 µl of oleylamine, 5 µl of oleic acid and 50 µl of hexane (solvent) to the glass vial and sonicate it for 2 minutes. This seems to make the nanocrystals more stable; within 1 year from their synthesis, we did not observe any degradation in their photoluminescence properties, whereas this was not the case with other batches of nanocrystal dispersions stored in the same conditions.

We suppose that the good stability of these nanocrystals is due to one or more of the following reasons: 1) superior quality synthesis, 2) highly concentrated dispersion, and 3) regular addition of ligands to the nanocrystals [65, 56]. Because of their long-term photophysical stability, we could use the same batch of nanocrystals for more than a year throughout the formulation of the lithographic protocol. This was helpful in finalizing the main parameters of the fabrication protocol without being concerned about the parameter of degradation of nanocrystals with time.

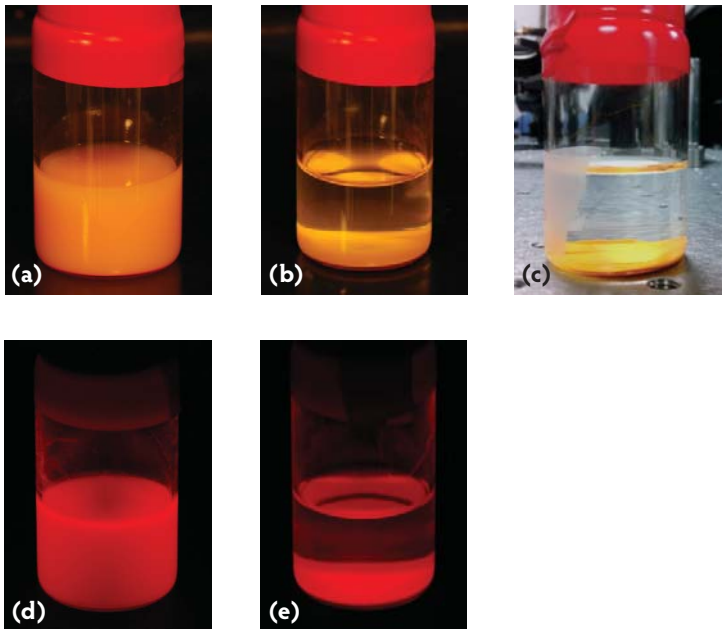

Figure 1.7 *Nanocrystal dispersion—shaken and undisturbed*

Images **(a)**, **(b)** and **(c)** show the colloidal dispersion of nanocrystal in hexane as seen in ambient light. Images **(d)** and **(e)** show them in ultraviolet light. Images **(a)** and **(d)** show how the mixture looks just after being shaken. Photographs **(b)**, **(c)** and **(e)** were taken after leaving the nanocrystals undisturbed for 6 hours; they show the precipitated nanocrystals at the bottom of the glass vial. Image **(c)** highlights the clarity of the solvent after the nanocrystals have settled down.

1.3.6 Nanocrystal luminescence

Non-thermal emission of light is called luminescence [66]. There are several forms of luminescence which include photoluminescence (fluorescence and phosphorescence) and cathodoluminescence. Cathodoluminescence is the phenomenon of emission of light from a material as a result of its interaction with electrons [66]. Well known for their fluorescence properties, CdSe/CdS nanocrystals have been shown to be cathodoluminescent as well [67].

Photoluminescence occurs when a system is excited to a higher energy state by absorbing a photon and then relaxes to a lower energy state by spontaneously emitting a photon. If the higher and lower energy states have the same multiplicity (spin-allowed), the photoluminescence process is called fluorescence , where the typical lifetime is short (0.1–50 ns). If the transitions are between states of different multiplicity (spin-forbidden), the process is known as phosphorescence , which typically has a long lifetime (1 ms–10 s) [66].

Photoluminescent emitters can be described by some form of Jablonski diagram [68]. Photoluminescence of quantum emitters such as luminescent molecules, quantum dots, and color centers nanodiamonds can be described by a three-level system of energy levels using a simplified Jablonski diagram [25]. In a three-level system, the charge relaxation within finer vibration states is neglected. Moreover, because of the absence of intersystem transitions in our quantum dots, their fluorescence can be described by a two-level system as shown in Figure 1.8 [69]. To explain more complex phenomena that occur during quantum dot excitation and emission, more elaborate models than a two-level system are required.

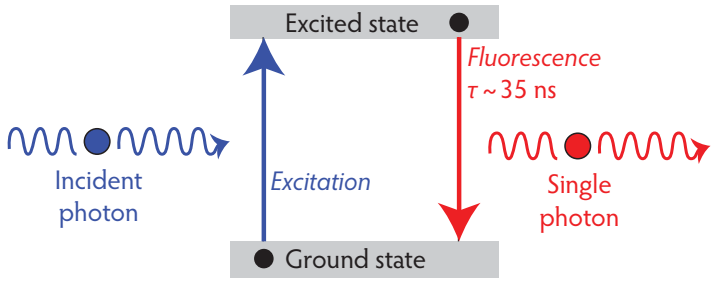

Figure 1.8 *Simplified model to explain nanocrystal fluorescence*

An incident photon, after absorption, excites an electron from the ground state to the excited state creating an electron-hole pair. In bright state transitions, the electron spontaneously recombines with the hole in the ground state resulting in emission of a photon. When placed in homogeneous media, our nanocrystals show a typical lifetime (τ) of about 35 ns.

Two-level emitters are inherently single photon emitters, which usually deliver one photon at a time [70, 71, 72]. A detector capable of detecting photons with 100% accuracy will detect one photon for one incident excitation of a perfect single emitter.

1.3.7 Blinking, photobleaching, and quenching

In 1996, Nirmal *et al.* [73] reported that the fluorescence of a quantum dot can fluctuate between "on" (fluorescent) and "off" (non-fluorescent) states. This phenomenon is called blinking or fluorescence intermittency. Blinking can be observed in almost all fluorophores [74]. The main reason responsible for blinking in quantum dots is reported to be photoionization, where an electron escapes from the excited quantum dot, which means no radiative recombination. At this stage, the quantum dot is positively charged and non-emissive (in "off" state). When the electron returns to the quantum dot, it starts fluorescing again, i.e., it enters the "on" state [4]. It has been shown that blinking dynamics follows Lévy statistics [75]. The 15–19 nm thick CdS shell of our quantum dots (Figure 1.4) makes it difficult for an electron to escape the quantum dot, which makes them almost non-blinking (Figure 1.9).

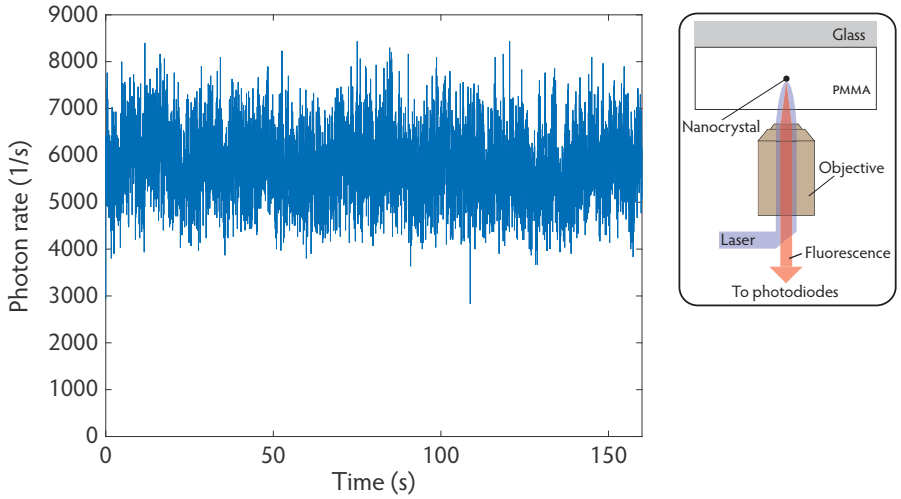

Figure 1.9 *Our CdSe/CdS nanocrystals—almost non-blinking*
Due to their thick shell, our nanocrystals exhibit almost no blinking. The plot shows that the quantum dot, during the 160 s excitation time, maintained a steady emission rate without blinking. The curve was attained by exciting a quantum dot (as illustrated by the schematic on the right side of the figure) by a 405 nm picosecond pulsed laser operating at a repetition rate of 2.5 MHz, with an average power of 11 nW. The laser was focused onto the quantum dot by a 100× microscope air objective (*N.A.* = 0.80). The fluorescence of the quantum dot was captured by an APD and the fluorescence rate was obtained as a function of time.

The fluorescence of an emitter may degrade permanently due to exposure to light, or it can reduce temporarily when the emitter is placed close to a gold surface. The phenomenon of decrease in fluorescence intensity of an emitter is known as fluorescence quenching [68]. As described by reference [58], we regard photobleaching or fading as photon-induced permanent loss of fluorescence due to internal changes in the emitter. In this sense, we categorize reduction in fluorescence as photobleaching or fading (permanent reduction) and quenching (non-permanent reduction). Blinking or fluorescence intermittency is the fluctuation of fluorescence between "on" and "off" states [73]. Demchenko has characterized blinking as a form of quenching [76, 77], where the on/off switching of fluorescence is due to the nature of the fluorophore. In my thesis[1], the term quenching refers to non-permanent reduction in fluorescence intensity of the quantum dot due to external factors, such as the presence of Au near it. Following this description, we do not regard blinking as a form of quenching.

1.3.8 Electron–hole dynamics

As shown in Figure 1.8, an incident photon of sufficient energy can excite a two-level system to a higher energy state creating an exciton. An exciton is a bound electron–hole pair [25, 79]. In addition to excitons, biexcitons and multiexcitons can also be created in a quantum emitter. To explain multiexciton and related phenomena, more complex models than a two-level system are required. In general, photoexcitation of a quantum dot can result in the following electron-hole recombination processes:

[1] In the context of this thesis, the description of the terms photobleaching, quenching, and blinking was required because the terminology may differ from literature to literature. For example, reference [78] describes fading or photobleaching as a reduction in emission intensity, which can be categorized as bleaching and quenching. Bleaching has been reported as a permanent reduction in fluorescence (which is defined as photobleaching or fading by Lakowicz [68] and in this thesis). Quenching has been described as a reduction in fluorescence intensity.

Photoluminescence: The electron and hole of an exciton recombine releasing energy in the form of another photon. This is a radiative process, which may be in the form of fluorescence or phosphorescence as described at the beginning of section 1.3.6.

Auger recombination: Coulomb interactions may result in a non-radiative process, where the energy released from the electron–hole recombination is not emitted as a photon but is used to excite another electron or hole to a higher energy state. The released charge carrier can stay inside the quantum dot or leave it. Exit of a charge carrier makes the quantum dot charged; the effect is called Auger ionization [4, 80]. This electron–hole recombination is called so due to its similarity with the Auger effect observed in the interaction of X-rays with matter [81], which was first reported by P. Auger in 1925–1926 [82].

Thermal dissipation: The electron–hole recombination may lead to non-radiative transitions and collisions which finally result in the generation of heat [25].

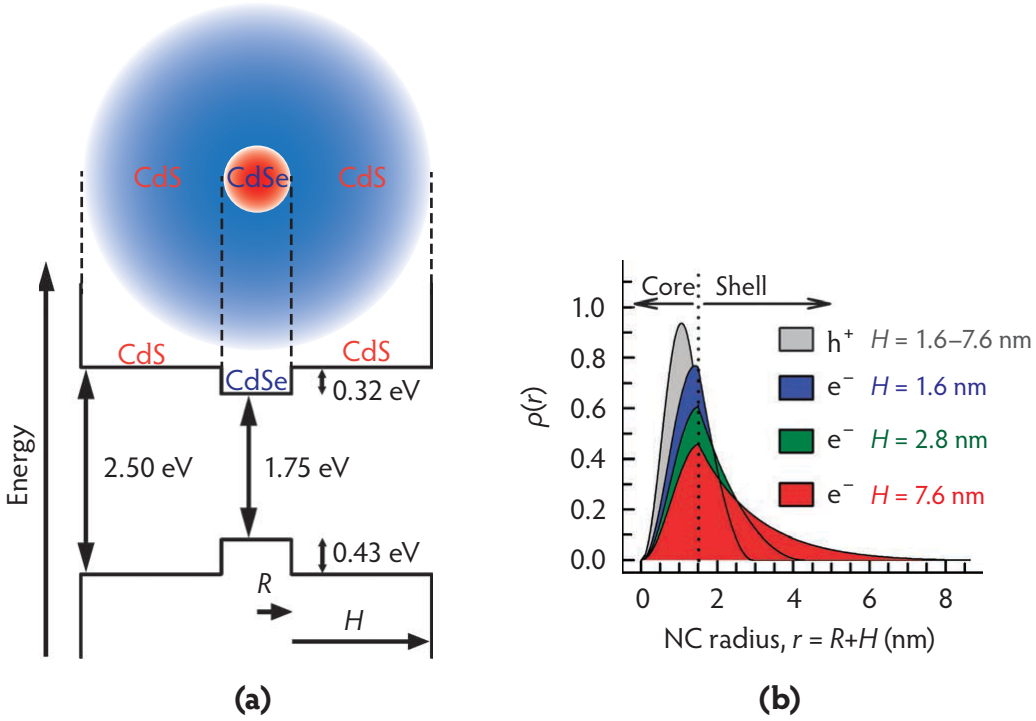

Figure 1.10 *Energy bandgap of CdSe/CdS quantum dots and electron–hole dynamics*

The image has been adapted from [53]. R is the radius of the CdS core ($R = 1.5$ nm). Our cores have the same radius (Figure 1.4). Different batches of nanocrystals had different shell thicknesses H: 1.6 nm, 2.8 nm, and 7.6 nm. With $H = 7.6$ nm, the total diameter of the core/shell was $2(1.5+7.6) = 18.2$ nm. This case is very similar to our nanocrystals, which have a total diameter of 15–19 nm. Figure **(a)** shows the energy band diagram of bulk CdSe and CdS. As the CdSe–CdS band offset well known, the authors of reference [53] had used the limiting values of 0 and 0.32 eV. Figure **(b)** depicts the theoretical spatial probability distribution, $\rho(r)$, of hole (grey region) and electron (colored regions) for $R = 1.5$ nm, $H = 1.6$ nm (blue area), $H = 2.8$ nm (green area), and $H = 7.6$ nm (blue area). $|\Psi_e|$ and $|\Psi_h|$ represent the electron and hole wavefunctions, respectively; $\rho(r) \propto r^2 |\Psi_k|^2$, where k = e or h.

The electron–hole dynamics in quantum dots is not only affected by the nature of the constituting materials but also by other factors such as core size, shell size, temperature, environment in which the dots are placed, ligands, and excitation methods. Brovelli *et al.*

have shown that by manipulating the shell thickness of CdSe/CdS core/shell nanocrystals, the electron–hole dynamics in the quantum dots could be controlled [53]. This led to constant emission rates over a temperature range from 1.5 K to 300 K. The authors reported that with increase in shell thickness, the electron wavefunction leaked from the core, while the hole wavefunction remained within the core (Figure 1.10).

The decay dynamics of a luminophore are characterized mainly by the following quantities [68, 25]:

1) **Lifetime** (τ): It is the time spent by emitter in its excited state. It is also known as the decay time.

2) **Decay rate** (Γ): The decay rate Γ is the rate with which an emitter transits from an excited state to a lower energy state. It is the inverse of lifetime [68]:

$$\Gamma = \frac{1}{\tau}. \tag{1.3}$$

Γ, the total decay rate, takes into account all possible transition rates—radiative and non-radiative:

$$\begin{aligned} \Gamma &= \underbrace{\Gamma_{\text{luminescent}}}_{\Gamma_r} + \underbrace{\Gamma_{\text{Auger}} + \Gamma_{\text{thermal}}}_{\Gamma_{nr}} \\ &= \Gamma_r + \Gamma_{nr} \end{aligned} \tag{1.4}$$

where $\Gamma_{\text{luminescent}}$, Γ_{Auger}, and Γ_{thermal} are the luminescent, Auger, and thermal decay rates, respectively. The radiative and non-radiative decay rates are denoted by Γ_r and Γ_{nr}, respectively. Our quantum dots have a typical lifetime of about 35 ns. Figure 1.11 shows their photoluminescence spectrum (measured in solution) and an emission decay curve of a nanocrystal.

3) **Quantum efficiency**: It is the probability of emission of a photon by an emitter after it has been excited to an emitting state [83]. The terms **quantum efficiency**, **internal quantum efficiency** [84, 25], **fluorescence quantum yield**, **quantum yield** [68], and **radiative yield** [1] are used interchangeably and they signify the ratio of the emitted photons to the absorbed photons. We follow the description of Laverdant *et al.* [83], which distinguishes between quantum efficiency and quantum yield. Quantum efficiency has been described above and the quantum yield of an emitter is the probability of emitting a photon after absorbing an excitation photon. Quantum efficiency just considers the possibility of emission of a photon when an emitter relaxes from the excited emitting state, whereas quantum yield considers other possibilities such as complicated energy levels and decay paths. In this sense, the quantum yield is less than equal to the quantum efficiency. In a two level system, as in the case of our CdSe/CdS core/shell nanocrystals, because there is only one excited state, the quantum efficiency is equal to the quantum yield. The quantum efficiency η is given as:

$$\eta = \frac{\Gamma_r}{\Gamma} = \frac{\Gamma_r}{\Gamma_r + \Gamma_{nr}}. \tag{1.5}$$

If the nanocrystal is pumped off-resonance with a pumping or excitation rate r then in a two-level system in stationary regime, the population of the excited state is [85]:

$$n = \frac{r}{r + \Gamma}. \tag{1.6}$$

In this case, the single photon emission rate R is given as:

$$R = \frac{r\,\Gamma_r}{r + \Gamma}. \tag{1.7}$$

Relation between pumping rate r and the intensity I of exciting radiation at the emitter location is:

$$r = \frac{\sigma I}{hf} \tag{1.8}$$

where h is the Planck's constant, f is the excitation frequency, and σ is the absorption cross-section of the emitter. The term hf gives the energy of the exciting photon.

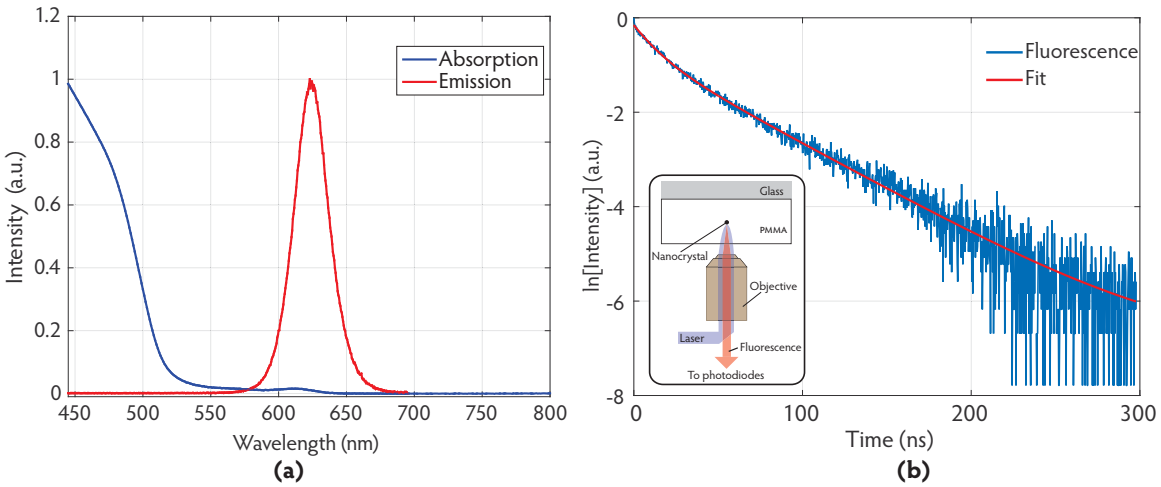

Figure 1.11 *Photoluminescence spectrum and lifetime curve of our nanocrystals*

Figure **(a)** shows the normalized photoluminescence spectrum of the CdSe/CdS quantum dots. The measurement was done in solution and at room temperature. The maximum emission occurs at λ = 624 nm, and the spectral linewidth is 29 nm. The plot in Figure **(b)** displays the decay curve of a quantum dot using a semilog scale along the y-axis. After fitting the curve with an exponential, we obtained a lifetime value of 51 ns. The inset displays the measurement schematic.

1.3.8.1 Decay rate measurement

Analysis of the two-level quantum emitter of Figure 1.8 allows us to quantify the notion of Γ. Suppose a group of quantum emitters are excited by an infinitely sharp or Dirac pulse of light, thereby putting n_0 quantum emitters in the excited state. The excited-state population decays with a rate of Γ as [68]:

$$\begin{aligned} \frac{dn(t)}{dt} &= -\Gamma\, n(t) \\ &= -\left(\Gamma_r + \Gamma_{nr}\right) n(t), \end{aligned} \tag{1.9}$$

where $n(t)$ is the population of the emitters in the excited state at time t, and Γ_r and Γ_{nr} are the radiative and non-radiative decay rates, respectively. The above differential equation has a solution of the form:

$$n(t) = n_0 e^{-\Gamma t}. \tag{1.10}$$

The constant Γ is defined as the decay rate of the quantum emitter and $\Gamma = \Gamma_r + \Gamma_{nr}$. In practice we cannot count the number of emitters in the excited state but we can relate the number of emitters in the excited state to the intensity of emitted fluorescent light, which is measured by a detector, such as a photodiode. In fact, TCSPC counts the emitted photons, which can be related to the light intensity. If I_0 is the fluorescent light intensity recorded by the detector at time $t = 0$, and $I(t)$ is the intensity recorded at time t, then [85]:

$$I(t) = I_0 e^{-\Gamma t}. \tag{1.11}$$

1.3.8.2 Lifetime of our nanocrystals

All the nanoantennas discussed in this thesis were fabricated using single nanocrystals from only one batch of CdSe/CdS core/shell colloidal nanocrystals. Figure 1.4 shows a schematic and TEM image of these nanocrystals. Appropriate spin-coating of these nanocrystals results in an adequately spaced areal distribution of individual nanocrystals. When properly excited, the fluorescence emission of these nanocrystals has always shown photon-antibunching. To estimate the typical lifetime of emission of these individual nanocrystals in a homogeneous medium, some single nanocrystals from this batch were placed in a homogeneous medium and their fluorescence was characterized.

On a glass slip, a PMMA layer of about 100 nm thickness was spin-coated and baked at 150°C for 2 minutes. Above this PMMA layer, individual nanocrystals were spin-coated. Then a PMMA film of about 500 nm thickness was spin-coated and the sample was baked at 150°C for 2 minutes. In this way individual nanocrystals were placed in a homogeneous medium of PMMA. The sample was placed in a microscope and a 405 nm laser was used to excite them. The excitation laser fluence was kept about 3 W/cm^2 and lifetime curves, similar to the one displayed in Figure 1.11, were obtained. By fitting these curves with an exponential, the nanocrystal emission lifetime was obtained.

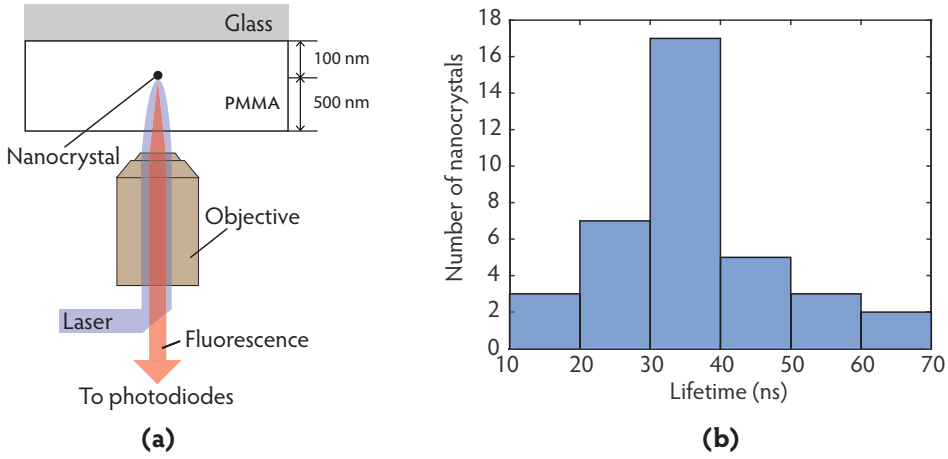

Figure 1.12 *Lifetime of nanocrystal emission in a homogeneous*

Figure **(a)** shows the measurement schematic, and **(b)** is a histogram of the lifetime time of nanocrystals. The mode value of lifetime was 35 ns.

Figure 1.12 is a histogram of the nanocrystal emission lifetime showing the distribution of the lifetime of 37 nanocrystals. For the measured lifetime values, the mean was 36 ns, the mode and median were 35 ns, and the standard deviation was 13 ns. We regards the mode value of 35 ns as the typical lifetime of these nanocrystals, when placed and excited in homogeneous medium. The acceleration of emission or the Purcell factor of our plasmonic patch antennas will be evaluated considering this typical value.

1.3.9 Multiexcitons

If the absorption of light by an emitter generates more than one electron–hole pair, the generated electron–hole pairs are called a multiexciton [86]. A group of two electron–hole pairs generated by one photon is called a biexciton—it is a type of multiexciton. In giant CdSe/CdS core/shell nanocrystals, with a core diameter of about 3 nm and a shell thickness of about 9 nm, multiexciton emission is generally observed and this has been linked to their enhanced fluorescence [87]. Generally, for an emitter, multiexciton lifetime is considerable shorter than exciton lifetime [88, 87, 4].

Figure 1.13 shows the decay curve of one of our CdSe/CdS core/shell nanocrystal that was excited by a 405 nm picosecond pulsed laser with a repetition rate of 2.5 MHz and average power of 11 nW. The laser was focused onto the quantum dot with a 100× ($N.A.$ = 0.80) air objective The dot was surrounded by PMMA, i.e., it was in a homogenous medium. The shorter peak at the beginning of the decay curve is due to multiexciton recombination and the remaining curve shows the exciton lifetime. The curve shows $\tau_{\text{multiexciton}}$ = 1.5 ns and τ_{exciton} = 35 ns. These values were acquired after fitting the emission decay curve with a bi-exponential.

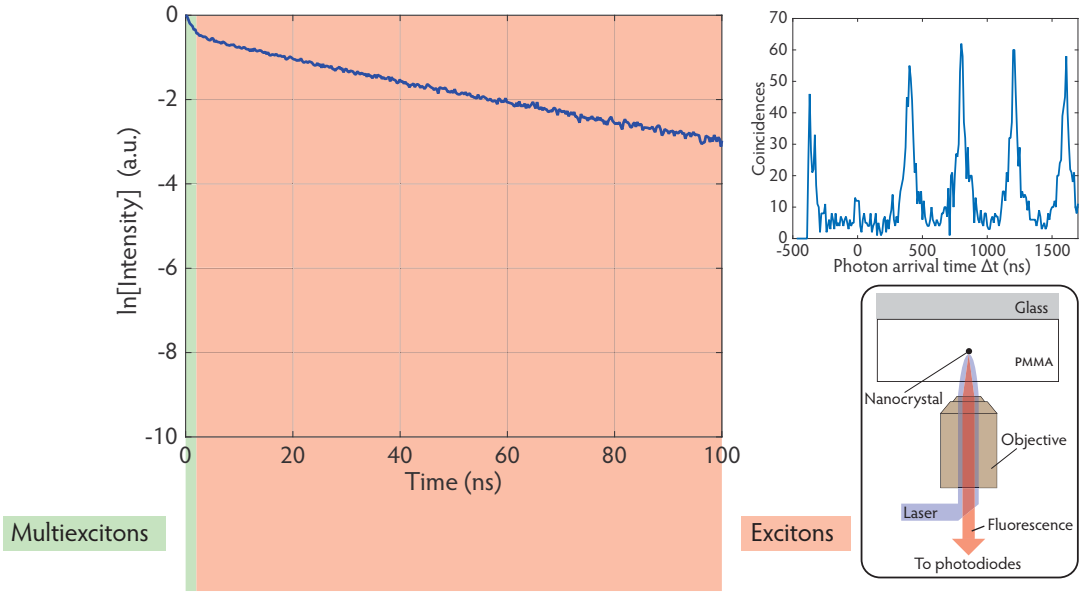

Figure 1.13 *Multiexciton and exciton behavior from decay curve*

The figure shows the decay curve of a CdSe/CdS quantum dot. The curve has a steep slope at the beginning (green background), which is attributed to photons generated by multiexciton recombination. The less steep slope (red background) is due to photons generated by excitons. Fitting the two slopes with respective exponentials and extrapolating the multiexciton fit, we obtain multiexciton and exciton lifetimes as 1.5 ns and 35 ns, respectively. Photon-antibunching measurement is shown by the histogram on the top-right of the image. The measurement schematic is illustrated on the bottom-right of the figure.

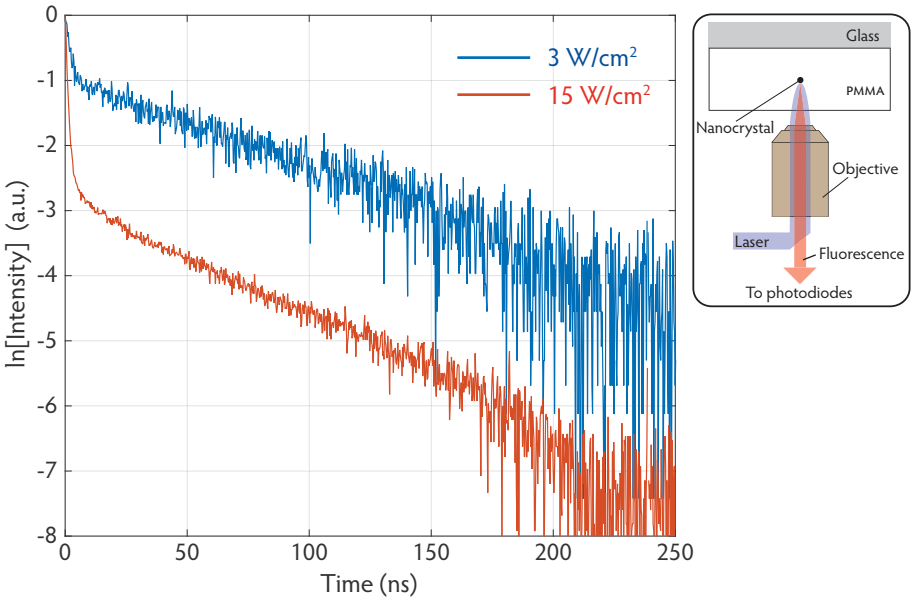

Figure 1.14 *A nanocrystal under different laser intensities*
As shown at the right of the figure, a single CdSe/CdS core-shell nanocrystal was excited by a 405 nm laser at two different intensities. The steep peaks at the beginning of the two curves are due to multiexcitons. Multiexciton emission becomes more prominent as the excitation intensity is increased.

High intensity excitation of a nanocrystal results in multiexciton generation [89]. The multiexciton absorption peak is blue-shifted from the exciton absorption peak [90]. A two-level model is unable to explain the multiexciton behavior. Fisher *et al.* used a four-level system to estimate biexciton and triexciton radiative lifetimes and quantum yields [90]. As reported by them, we also noted that increasing the laser fluence on a nanocrystal resulted in more photon emission from multiexciton recombination. Figure 1.14 displays the result of one such measurement.

Multiexciton radiative emission is usually in competition with Auger recombination, which is non-radiative and is usually more efficient than the former. Therefore, in many cases, the Auger effect results in non-radiative multiexciton recombination, thus preventing photon emission from multiexciton recombination. The emission in these structures is due to exciton recombination, and therefore it is antibunched. However, in thick-shell nanocrystals (as in our case), due to lower multiexciton coupling, the Auger recombination rate—which is inversely proportional to the volume of the quantum dot [91]—is considerably reduced. This may lead to photon emission from multiexciton recombination.

In our nanocrystals, it seems that typically the Auger recombination rate is larger than the multiexciton recombination rate but the two are of the same order. As a consequence, under low excitation, these nanocrystals always exhibit photon-antibunching and usually no photon emission due to multiexciton recombination is noted in the emission decay curve (a typical decay curve is shown in Figure 1.11(b)). Whereas, at high excitation, more multiexcitons are created, and due to the competition between Auger and multiexciton recombination, some multiexcitons recombine radiatively. The decay curve of Figure 1.13 shows an example where the multiexciton and Auger recombination rates are close and this results in radiative multiexciton recombination (fast-slope part of the curve). High intensity excitation of quantum dots can the increase multiexciton radiation.

1.4 Single photon emission

In the previous sections we have discussed that individual CdSe/CdS core/shell nanocrystals are single photon emitters. In fact, they are very promising single photon sources due to their stability, narrow spectral linewidth, short lifetime (more fluorescence), and room temperature operation capability. Developing appropriate lithographic techniques will pave ways for their integration into other structures, thereby enhancing their properties and creating new structures of scientific interest—our patch nanoantennas are an example of this. Quantum dots are more stable than fluorescing organic molecules [71]. Blinking in quantum dots was a drawback for stable single photon emission. The advent of non-blinking quantum dots [48] has provided a solution to this problem. If a quantum dot is excited on resonance by a pulsed laser, then it is highly likely that each laser pulse results in the emission of only one photon from the quantum dot [92]. Modern piezoelectric stages allow the positioning of any small object—such as a quantum dot—at the focus of the laser for a long time. The last two points make quantum dots very suitable on-demand or deterministic single photon sources. References [72],[70], and [93] discuss different types of single photon sources and detectors.

Kimble *et al.* had performed the first demonstration of single photon emission at optical frequencies in 1977 [94] exciting a beam of sodium atoms with a continuous-wave laser and using a Hanbury Brown-Twiss (HBT) measurement setup [95]. Single photon emission from quantum dots was first reported by Michler *et al.* in 2000 [96]. They had excited a CdSe/ZnS core/shell nanocrystal with a 488 nm continuous-wave laser. The use of continuous-wave laser for excitation does not allow the timing of emitted photons—for this purpose, a pulsed laser is required. Later in 2000, Michler *et al.* [97] used a pulsed laser for single photon emission from a self-assembled epitaxial InAs quantum dot.

A single photon source is most often characterized by the second-order temporal correlation function or the normalized intensity temporal correlation $g^{(2)}(\Delta t)$, which is classically written as [71]:

$$g^{(2)}(\Delta t) = \frac{\langle I(t+\Delta t)\, I(t)\rangle}{\langle I(t)\rangle^2}, \tag{1.12}$$

where $\langle\rangle$ denotes a time average, $I(t)$ is the intensity measured at time t, and $I(t+\Delta t)$ is the light intensity measured at time $t+\Delta t$. The function $g^{(2)}(\Delta t)$ tells us how the probability of detecting an intensity at time $t+\Delta t$ depends on the intensity at time t. The normalization is over the average intensity. For a classical light source, it can be shown that $g^{(2)}(0) \geq 1$ and $g^{(2)}(\Delta t) \leq g^{(2)}(0)$. For perfect thermal light: $g^{(2)}(0) = 2$, and for a perfect coherent light (e.g., an ideal laser): $g^{(2)}(0) = 1$ [71].

The quantum mechanical representation of Eq. (1.12), also called the second-order temporal coherence function, is [98]:

$$g^{(2)}(\Delta t) = \frac{\left\langle \hat{E}^-(t)\, \hat{E}^-(t+\Delta t)\, \hat{E}^+(t+\Delta t)\, \hat{E}^+(t)\right\rangle}{\left\langle \hat{E}^-(t)\hat{E}^+(t)\right\rangle^2}, \tag{1.13}$$

where $\hat{E}^+$ and $\hat{E}^-$ are the respective positive and negative frequency parts of the electric field operator. The second order correlation was first introduced by Glauber in 1963 [99]. Using the $g^{(2)}(\Delta t)$ function, light sources can be characterized as [70]:

Bunched : After detecting one photon from bunched light, the conditional probability of detecting another one just after increased. Thermal light sources emit bunched light. For bunched light:

$$g^{(2)}(0) > 1. \tag{1.14}$$

Poisson-like : Light emission from an ideal laser is coherent and follows a Poisson distribution for which:

$$g^{(2)}(0) = 1. \tag{1.15}$$

Antibunched : Light is antibunched if after detecting a photon, the probability to detect a second photon is decreased compared to the former. A quantum dot, such as a CdSe/CdS core/shell nanocrystal, emits antibunched light or sub-Poisson . For an antibunched light source:

$$g^{(2)}(0) < 1. \tag{1.16}$$

For an ideal or perfect single photon source:

$$g^{(2)}(0) = 0, \tag{1.17}$$

which is not true for classical light. Single photon emission is non-classical and it cannot be described in purely classical terms. Figure 1.16 shows single photon emission from one of our quantum dot showing photon-antibunching.

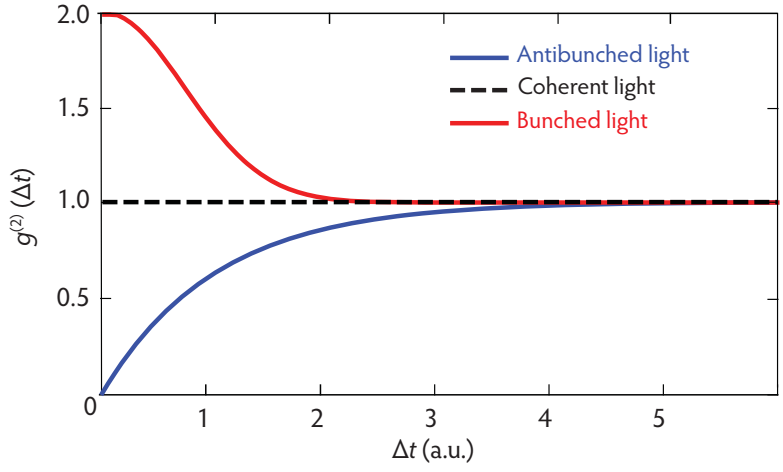

Figure 1.15 *Antibunched, coherent, and thermal light*

Second order correlation functions $g^2(\Delta t)$ for antibunched, coherent, and bunched light.

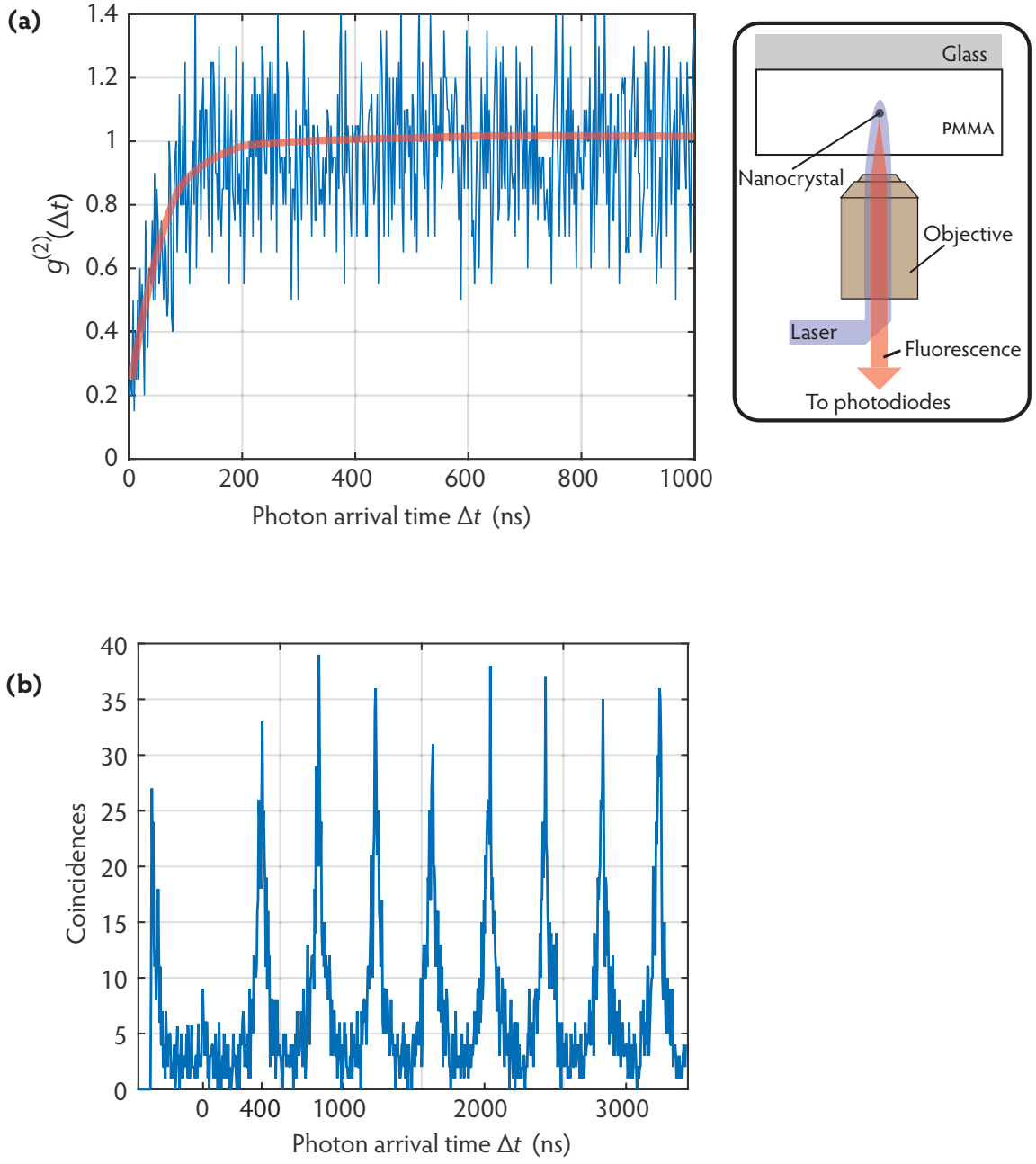

Figure 1.16 *Single photon emission from a quantum dot*

TCSPC measurement was carried out on a CdSe/CdS quantum dot (Figure 1.4) using a 405 nm laser in continuous **(a)** and pulsed mode **(b)**. Figure **(a)** shows the second-order coherence function, $g^{(2)}$, as a function of photon arrival time Δt. The exciting laser was operating in continuous-wave mode. For a perfect single photon emitting system, $g^{(2)}(0)=0$ but in the depicted case: $g^{(2)}(0)\approx 0.2$, which is in agreement with Eq. (1.16). When the laser excites the nanocrystal, photons are emitted by the nanocrystal and also the medium in focus of the laser, which in this case was PMMA (see the schematic on the right side of the image). The medium is not a single photon emitter and the contribution of photons from the medium to the signal leads to $g^{(2)}(0)\neq 0$. A pulsed laser excitation was used to obtain the antibunching curve of Figure **(b)**. On the vertical axis are the number of coincidences or the number of pairs of photons received by the two photodiodes as a function of Δt. The repetition rate of the pulsed laser was 2.5 MHz; this corresponds to the time interval between adjacent peaks in the plot, which is 400 ns. A low peak at $\Delta t=0$ shows the quality of these single photon emitters. The measurement schematic is given in the top-right corner of the figure.

1.5 Our optical microscopy setup

We use an inverted *Olympus IX71* microscope for reflection, fluorescence, and confocal microscopy. Light sources include a mercury lamp (U-LH100HG) and several lasers (405 nm *PicoQuant*, *NKT EXTREME* supercontinuum, 473 nm CW, and 532 nm CW. See A.1). Light beams are appropriately selected, shaped, and guided by means of several optical components such as lenses, mirrors, dichroics, filters, pinholes, beamsplitters, and optical absorbers (numerical densities). Reflection and fluorescence images are captured by a *Photonic Science* CCD camera, and for confocal imaging and single photon counting we use a *Micro Photon Devices* APDs (see A.2). Laser beams can be modulated with a *HOLOEYE LETO* reflective phase-only SLM. The samples are held on a *PI* piezoelectric nanopositioning stage. All these components are placed on a self-leveling active vibration isolation system.

1.5.1 Fluorescence imaging

The schematic in Figure 1.17 depicts our fluorescence imaging optical setup. Violet light from a mercury lamp is filtered by a bandpass filter, reflected by a dichroic filter, and focused by a 100× objective lens on a sample containing fluorescent emitters. The light emitted by the fluorescing emitters is collected by the same objective and is transmitted through the dichroic filter. The following bandpass filter enhances the fluorescence signal by attenuating the unwanted wavelengths. The fluorescence is focused by a tube lens onto the CCD camera and the captured image is displayed on a computer screen.

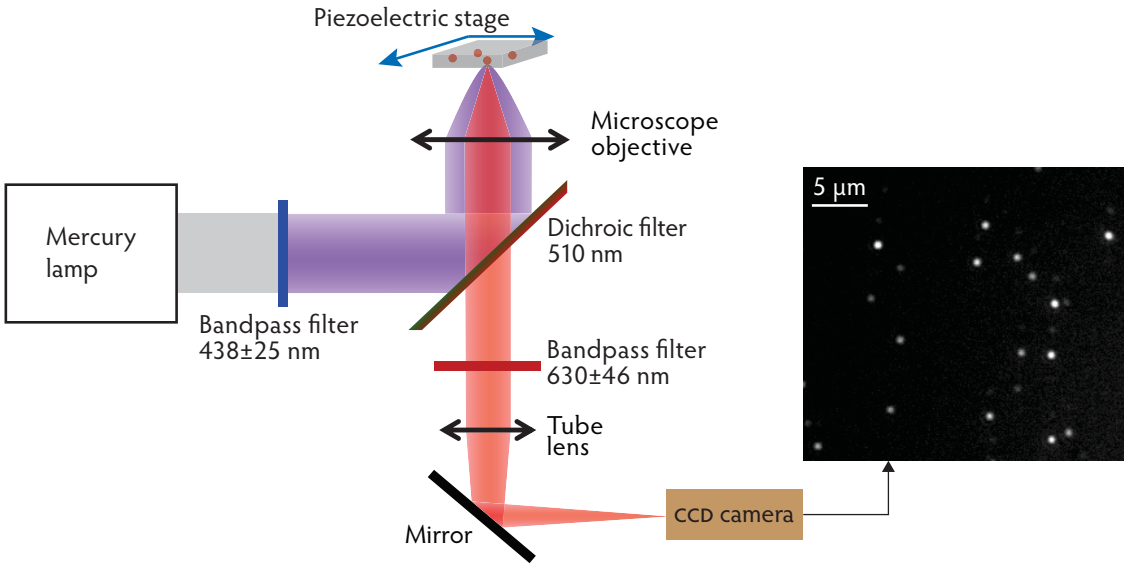

Figure 1.17 *Imaging fluorescence*

The figure illustrates our fluorescence microscopy setup. The inset image shows fluorescing CdSe/CdS quantum dots. With a 0.80 *N.A.* 100× air objective, the size of the image recorded by the CCD camera is 92 µm × 69 µm.

1.5.2 Imaging single emitters and counting photons

The possibility to detect and measure single emitters (individual atoms, molecules, quantum dots, etc.) has been revolutionary. Measurements performed on a single emitter allow accessing nanoscopic parameters that are usually absent in ensemble measurements (due to averaging) [94]. In 1989, Moerner and Kador reported the first optical detection of a single molecule by measuring its absorption [100]. For his contribution to super-resolved microscopy, William E. Moerner shared the 2014 Nobel Prize in Chemistry with Eric Bertzig and Stefan W. Hell. In 1990, Orrit and Bernard demonstrated the first detection of fluorescence from a single molecule [101].

Figure 1.18 illustrates our optical setup for confocally scanning, nanopositioning, and characterizing individual emitters like fluorescent molecules and quantum dots. A single quantum dot confocally scans a laser and its fluorescence signal is sent to a Hanbury-Brown and Twiss (HBT) setup [95] and is treated using time-correlated single photon counting (TCSPC). The reader is referred to [102], [103], and [70] for a description of TCSPC and related issues of single photon counting.

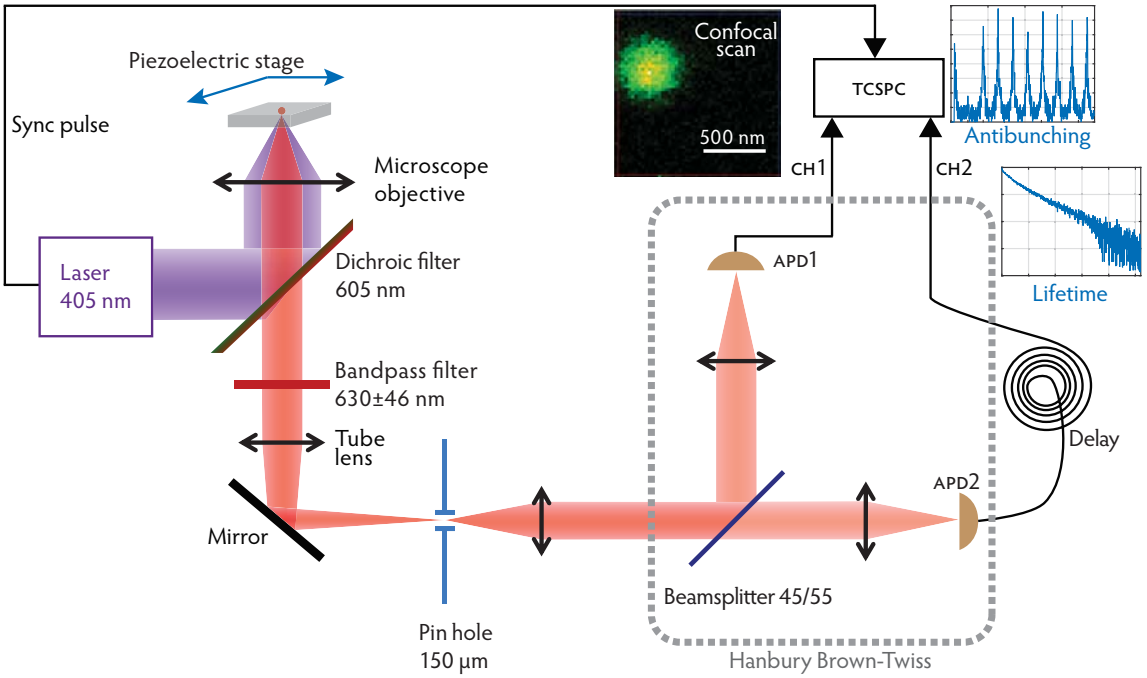

Figure 1.18 *Counting photons emitted by single emitters*

The insets show a typical confocal scan, antibunching curve, and lifetime curve of a typical CdSe/CdS quantum dot used in our antenna.

1.6 Conclusion

The field of optical antennas is important to fundamental science and for technical applications. Benefitting from plasmonic phenomena which causes emission enhancement (Purcell effect), plasmonic optical antennas are amongst the most researched antennas for light. Fabricating single photon emitter antennas would offer field enhancement and directivity to single photon emission. Our plasmonic patch nanoantennas, which operate in the optical regime and can show single photon emission, use individual CdSe/CdS core/shell quantum

dots as emitters. These quantum dots are single photon emitters and exhibit size-dependent emission-wavelength tunability. By including these quantum dots (or other single photon emitters) in nanoantenna structures, we can increase their emission rate and directivity. We characterize our quantum dots and nanoantennas using an HBT optical setup.

This page is intentionally left blank.

2 Fabrication Concept and Deposition Strategy

The development of any new lithographic technique includes finding working solutions to several challenges that are encountered at different stages of development. These include formulating the fabrication concept, and finding appropriate methods and materials to realize it. For any choice of materials and methods, their quality, reproducibility, and effectiveness have be to characterized using specialized tools. We have devised three lithography techniques to fabricate plasmonic patch nanoantennas that use a single quantum dot as an emitter. This chapter will discuss issues that are common to all these techniques. We begin with a description of the fabrication concept followed with sections on selection and deposition of metals and dielectrics.

For characterizing the deposited metal and dielectric films, we have used AFM and ellipsometry. I am grateful to Emanuelle Lacaze of INSP for the AFM apparatus and related discussions, and to Bruno Gallas of INSP for his help with ellipsometry measurements.

2.1 Fabrication concept

In this section, we will discuss the motivation for our fabrication techniques and some involved issues. The general outline, with the required details, will be presented here and the specialized techniques, such as the white laser and Laguerre-Gaussian modes lithography, will be mentioned in the later chapters. The main challenges will be pointed out and in the coming sections of the thesis, we will discuss how these challenges were overcome.

Figure 1.2 shows the schematic of a plasmonic patch nanoantenna which uses the fluorescence from a single quantum dot for emission. These structures can be used to understand light-matter interaction at a single emitter level, and can also be sources of enhanced single photon emission. In their work [1], Esteban *et al.* have analyzed similar structures by means of simulation. These antennas are also called optical patch antennas due to the disk or patch of metal present on top. As plasmonic patch nanoantennas benefit from plasmonic effects, the

metal-dielectric-metal structure, in which the single photon emitter is embedded, should use a metal that is capable of supporting plasmonic modes in the desired wavelength range. The wavelength range of operation is decided by the wavelength of emission of the emitter.

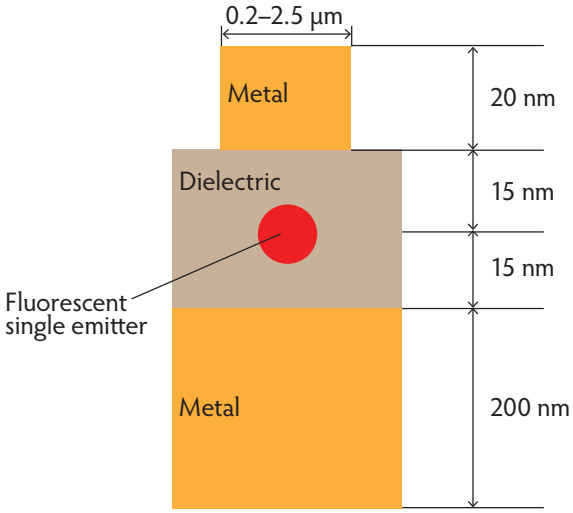

Figure 2.1 *Plasmonic patch nanoantenna structure*

To fabricate a plasmonic patch nanoantenna as shown in the schematic, the following constituents have to be appropriately selected: a metal, a dielectric, and an emitter. Moreover, the fabrication process requires finding methods to assemble the constituents precisely at nanometric separation, as shown above.

The constituents of the nanoantenna are:

1) **Metal**: The choice of the metal is mainly affected by its capacity to support plasmons, ease of manipulation by lithographic procedures, and chemical reactivity. The complex relative permittivity $\widetilde{\epsilon}$ of a material can be written as [104]:

$$\widetilde{\epsilon} = \epsilon' + \jmath\epsilon'' \tag{2.1}$$

where $\jmath$ is the complex imaginary unit, ϵ' is the real relative permittivity and ϵ'' is the imaginary relative permittivity. For a metal to support plasmons at optical frequencies, the following conditions must be satisfied [25]:

$$\left.\begin{array}{l} \epsilon' < 0, \\ |\epsilon'| > |\epsilon''|. \end{array}\right\} \tag{2.2}$$

The conditions imposed by Eq. (2.2) are generally satisfied by noble metals such as Au, Ag, and Cu. Some studies have reported plasmonic propagation in Pt [105], and recently, Al [106, 107, 108] has attracted interest as a plasmonic material. These metals can be deposited by techniques such as thermal evaporation or electron beam evaporation; both of these facilities were available to us. Due to its low losses and resistance to corrosion, we chose to work with Au but we have deposited other metals like Al as well. Figure 2.2 shows ϵ' and ϵ'' of Au as a function of wavelength, which were measured by ellipsometry.

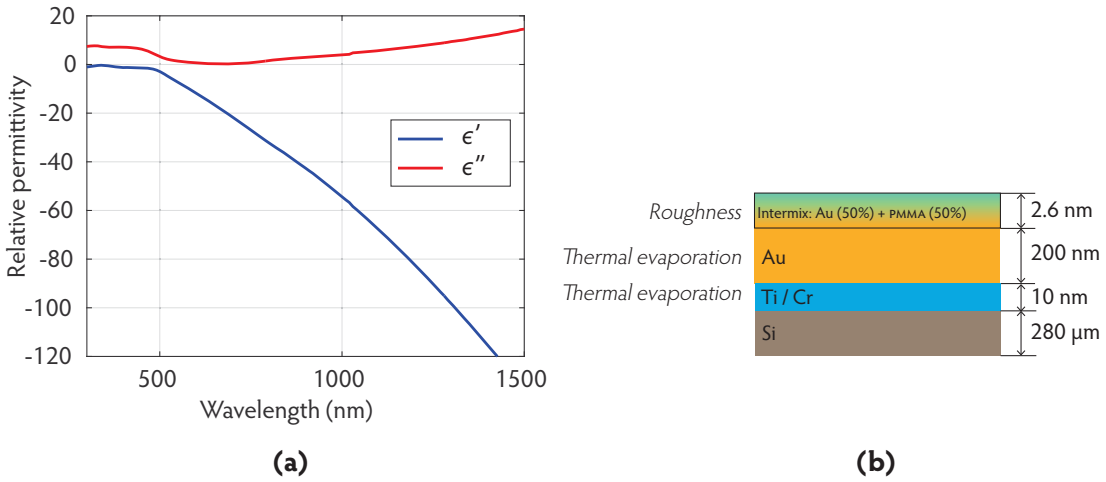

Figure 2.2 *Complex relative permittivity of Au*

(a) The graph of the real (ϵ') and imaginary (ϵ'') parts of the complex relative permittivity of Au. These values were deduced from the ellipsometry measurements done on a 200 nm thick Au film, deposited at INSP. **(b)** The model used to fit ellipsometry data. A roughness of 2.6 nm was included on the Au surface as an intermix layer of Au and air (50% Au + 50% air). The value of roughness was found using AFM.

2) **Dielectric**: Any dielectric material, such as SiO_2, YF_3, or a suitable polymer can be used. As thermal or electron beam deposition of dielectrics was destroying the nanocrystal fluorescence, we had to find other solutions. Finally, we chose to work with PMMA, with which we are able to achieve ultrathin (thickness < 5 nm) and homogeneous (RMS roughness < 1 nm) films by means of spin-coating. The quality of PMMA films was superior to silica films, and spin-coating deposition is much faster and simpler than other techniques like thermal evaporation (section 2.4.3.2).

3) **Emitter**: The nanoantenna can benefit from a single photon emitter like a fluorescent molecule, a nitrogen vacancy center, or a quantum dot. With the motivation of improving wavelength-tunable room-temperature single photon emission by means of a broadband plasmonic patch nanoantenna, we choose to work with CdSe/CdS core/shell quantum dots, which have been discussed in section 1.3.

2.2 Metal deposition

In our fabrication process, metal deposition takes place at two steps: (1) to deposit the optically opaque metal film below the nanocrystal, and (2) to deposit a sufficiently thin metal disk of 200 nm–2.5 µm diameter (Figure 1.2). As mentioned in the previous section, we have mainly used Au as the metal. For an optically opaque lower layer of Au, we deposit a 200 nm thick layer of Au. To create a thin patch above the nanocrystal, we deposit 20 nm of Au.

The deposition of Au can be done by thermal evaporation or by electron beam evaporation. On most of the samples, we have used thermal evaporation (Figure 2.3). Evaporation techniques, such as thermal and electron beam, are a type of physical vapor deposition process. In physical vapor deposition systems, the depositing material is transferred from the source to the substrate in vapor form, and both the source and the substrate are in the same chamber. There are two types of physical vapor deposition methods [44]:

1) **Evaporation**: It includes thermal evaporation and electron beam evaporation. The principle of thermal evaporation is explained in Figure 2.3. In electron beam evaporation deposition, electrons are projected onto the source. The kinetic energy of the projected electrons is used to vaporize the source material. The vapors of the source material settle on the substrate and produce thin films. The energy of the depositing vapor material is typically between 0.05–0.1 eV [109].

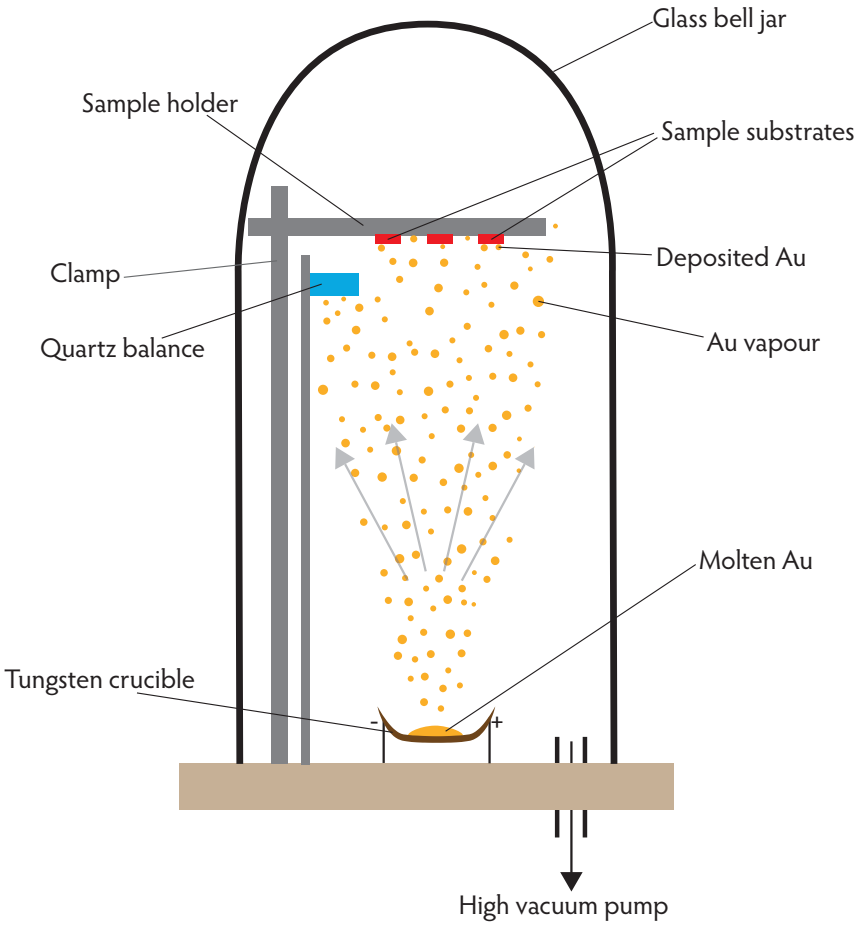

Figure 2.3 *Deposition of gold film by thermal evaporation*

A turbo vacuum pump creates a high vacuum inside the glass bell jar. Electric current flows through the tungsten crucible, heating and melting the Au in it. At a higher temperature, the molten Au starts evaporating in the upward direction as shown by the grey arrows. Evaporated Au condenses on the surfaces inside the glass bell jar, thus leaving a deposited film of Au on the sample substrates and the quartz balance. The rate of evaporation of Au is controlled by regulating the current flowing through the tungsten crucible. The thickness of the deposited film on the substrate is displayed in realtime by the calibrated quartz balance. The evaporation process is stopped by turning off the current or obstructing the evaporation path by means of a mechanical shutter (not shown in the figure).

2) **Sputtering**: In this process, the target source is bombarded with high-energy inert ions (usually argon). The bombarding ions etch atoms or clusters of the source material, which are projected towards the substrate, where they deposit and form a film. Typical energy of the volatile material is in the range of 1–40 eV, but it can be even more than 100 eV [109].

Generally, physical vapor deposition methods do not involve chemical reactions, which makes them highly suitable for depositing several types of metals and dielectrics on different kinds of substrate materials [44, 110]. Moreover, deposition by evaporation—thermal or electron beam—is very useful for producing thin films for optical applications [109]. As compared to evaporation deposition, the energy of the depositing vapor is much higher in sputtering, we utilized the former to avoid any damage to the nanocrystals during the deposition process. We deposited some dielectric films by sputtering as well but found that it was destructive for the substrate material.

2.2.1 Equipment details and parameters

The thermal evaporation deposition of metals was carried out using the Leybold Univex 300 evaporation system available in the cleanroom of INSP. Vacuum was created in the deposition chamber by means of a two-stage rotary vane pump and a turbomolecular pump in 18 hours or more. Some details:

- Vacuum level during deposition: $\sim 5 \times 10^{-6}$ mbar.
- Macroscopic substrate temperature during deposition: Greater than room temperature due to the heat emanating from the crucible. The more the duration of deposition, the higher the temperature of the sample substrate. The exact temperature value is not known due to the unavailability of a temperature sensor.
- Rate of deposition: 0.3 nm/s for the lower 200 nm Au, and 0.01–0.02 nm/s for the top patch.
- Purity of Au: 99.99%
- Sample substrate for 200 nm Au deposition: On a phosphorous doped crystalline silicon wafer (diameter= 5.08 cm, thickness = 280 ± 25 µm), a 10 nm film of chromium or titanium is deposited by thermal evaporation, which acts as an adhering layer for Au. Then a 200 nm thick film of Au is deposited on the titanium or chromium layer, which gives the following structure:

Figure 2.4 *Substrate with gold on top*

On a Si wafer of diameter=5.08 cm, we deposit 10 nm of Ti/Cr and then 200 nm of Au at 0.3 nm/s by thermal evaporation. This is the base structure on which the lithographic protocol was developed.

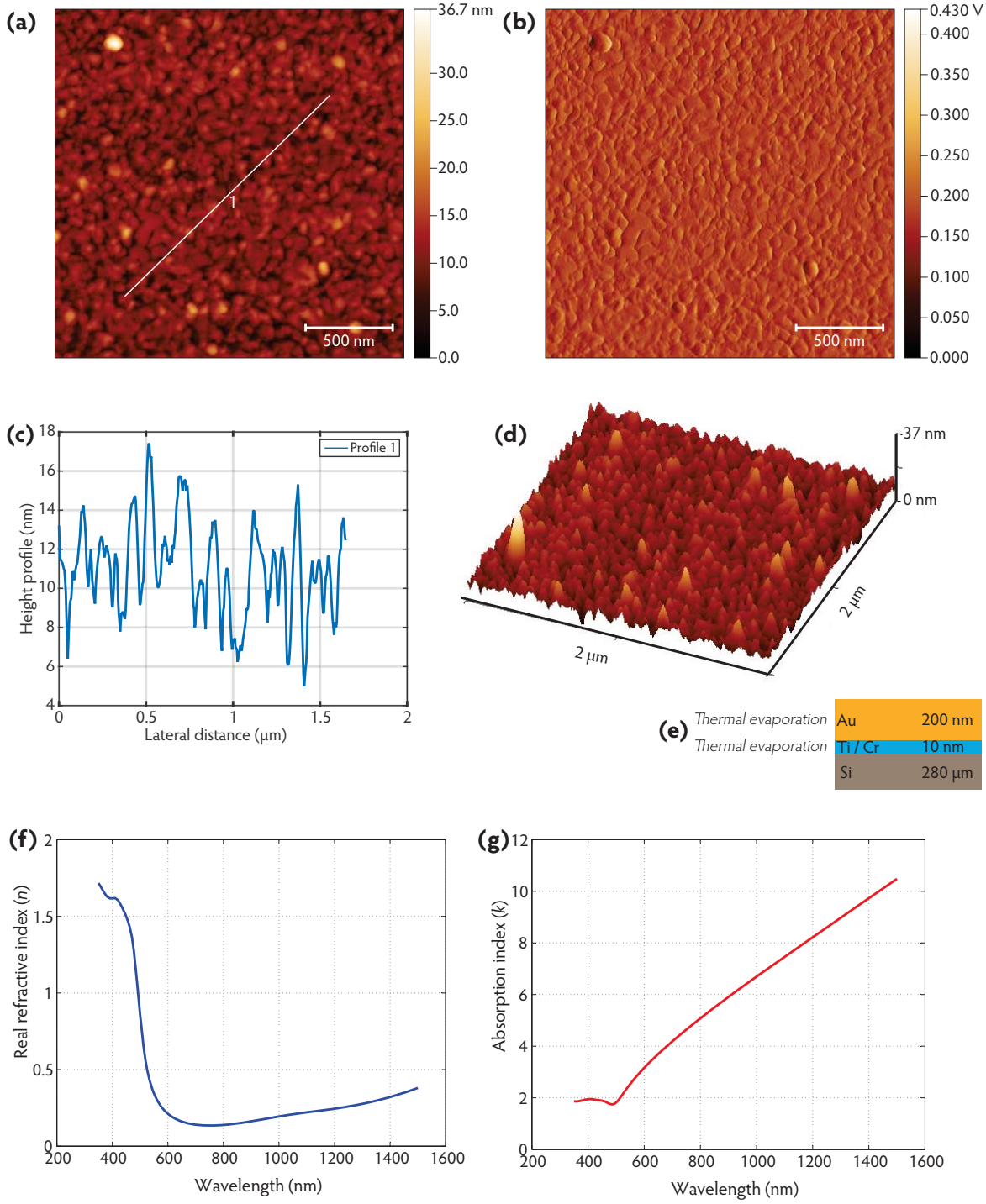

Figure 2.5 *AFM images and complex refractive index of 200 nm thick Au*

(a) shows the AFM topography image based on height data of a 2µm × 2µm surface of the deposited 200 nm thick Au film and image **(b)** shows the corresponding amplitude image. Amplitude images, also known as deflection images, highlight the slope or change in topography of the sample [111]. Figure **(c)** shows the height profile along the white line marked (1) in image **(a)**. For the area shown in the image **(a)**, the RMS roughness was 2.6 nm. Figure **(d)** is a 3-D perspective view of the sample. Figure **(e)** shows the layers in the sample; the top Au layer was deposited by thermal evaporation. Figures **(f)** and **(g)** show the real and the complex refractive index of the deposited Au film as a function of wavelength. The complex refractive index was measured with ellipsometry. Using the measured values of the complex refractive index and Eq. (2.5), the real and the imaginary parts of the complex relative permittivity were found. They are plotted in Figure 2.2.

2.2.2 Gold films produced by thermal evaporation

Thin film properties, like optical constants and surface roughness, depend not only on the properties of the depositing material and the thickness of the film, but also on the characteristics of the deposition method and equipment [112, 113]. The vacuum level inside the chamber affects the film properties. The bulk Au used by us was 99.99% pure. To maintain the Au film properties through all the depositions, for all our samples with nanoantennas, we had carried out the depositions with the same machine (Leybold Univex 300), under the same vacuum level (5×10^{-6} mbar), always using 99.99% pure Au as the source.

To analyze the Au films, we observed them with AFM and characterized them with ellipsometry. For the 200 nm bottom Au film, AFM measurements showed an RMS roughness of about 2.6 nm. For our bottom Au films, given the nominal thickness value of 200 nm and including a roughness of 2.6 nm, we estimated the complex refractive index as a function of wavelength by ellipsometry. All the ellipsometry measurements were carried out using a J. A. Woollam Co. variable-angle spectroscopic VB-400 ellipsometer (section 2.4.3.1). For any material, the complex refractive index $\tilde{n}$ can be expressed as [114]:

$$\tilde{n} = n + \jmath k, \tag{2.3}$$

where n is the real refractive index, and k is the absorption index. For nonmagnetic materials, such as Au, $\tilde{n}$ can be related to the complex relative permittivity (also known as the complex dielectric function) $\tilde{\epsilon}$ as [115]:

$$\tilde{n} = \sqrt{\tilde{\epsilon}} = \sqrt{\epsilon' + \jmath\epsilon''}, \tag{2.4}$$

where ϵ' is the real part and ϵ'' is the imaginary part of the complex relative permittivity. From Eqs. (2.3) and (2.4), we can write:

$$\epsilon' = n^2 - k^2 \quad \text{and} \quad \epsilon'' = 2nk. \tag{2.5}$$

2.2.3 Chamber vacuum and deposition quality

The quality of a film deposited by a physical vapor deposition process is highly dependent on the quality of vacuum in the deposition chamber. To quantify the vacuum level inside a deposition chamber, the value of the pressure inside it is used—low pressure means high vacuum level. The higher the vacuum level, the better the deposition.

When the deposition chamber is opened to introduce the samples, it comes in contact with air. Water molecules in the air adhere to the walls of the chamber due their high dipole moment [116]. Other molecules like O_2, N_2, etc., also enter. The presence of these molecules can contaminate the deposited film. Therefore, by using a vacuum pump, these molecules are extracted. In addition to contamination, the presence of a large number of molecules inside the deposition chamber increases the pressure inside it, and thus influences the deposition mechanism and film formation. The water molecules adsorbed to the walls of the chamber are the most difficult to remove, due to which the lowest obtainable pressure in a chamber is 1.33×10^{-8} mbar [116]. To reduce the pressure further, the chamber has to be heated for about 10 hours to unstick and remove the water molecules with the vacuum pump. For very clean and high quality depositions, ultrahigh vacuum (UHV), where the chamber pressure is lower than 10^{-9} mbar, is recommended. The machine available at our laboratory is able to

reach $\sim 5 \times 10^{-6}$ mbar after about 18 hours of pumping. Based on their optical properties as measured by ellipsometry and their topography as observed by AFM, the Au films deposited under these conditions seem suitable for the lithographic process. However, it will be interesting to explore the effect of UHV deposition (which may generate smoother films) on SPP propagation and antenna behavior.

Our results show that the vacuum level during deposition influences the film formation. By thermal evaporation, 20 nm thick Au films were deposited on PMMA surfaces under different vacuum levels but at similar deposition rates. AFM images showed that the topography of the films was considerably different. It may be possible that it influences their optical behavior as well. Figure 2.6 shows the surface of a 20 nm thick Au film that was deposited on a PMMA surface after pumping the chamber for 3 hours. The exact value of pressure cannot be specified because the pressure gauge was out of order. The deposition was done by the Leybold Univex 300 thermal evaporation machine at INSP. Strange patterns (worms) can be seen in the 25 μm × 25 μm area of Figure 2.6(a). The variation in height was ±5 nm. Figure 2.6(b) shows a 2 μm × 2 μm area on the same film—note the high depressions and elevations in the image.

Figure 2.7 shows the topography of a 20 nm thick Au film that was deposited on a PMMA surface by the Leybold Univex 300 thermal evaporation machine at INSP after creating the vacuum by 18 hours of pumping ($\sim 5 \times 10^{-6}$ mbar). Figure 2.7(a) shows a 25 μm × 25 μm and Figure 2.7(b) shows a 2 μm × 2 μm area. The film seems to have Au clusters (which is normal), but no worms (as seen in Figure 2.6) were observed. The Au depositions of Figures 2.6 and 2.7 were carried out using the same machine, at the same deposition rate, on similar PMMA substrates, but in different vacuum conditions. This suggests that the strange worm-like patterns were formed due to the low vacuum level during deposition.

Figure 2.8 depicts the topography of a 20 nm thick Au film deposited by the Telemark electron-beam deposition system at the cleanroom of Laboratoire Matériaux et Phénomènes Quantiques in Paris. At the beginning of the deposition, the vacuum level was 4.64×10^{-7} mbar, and at the end of the deposition, it was 10^{-6} mbar. Figure 2.8(a) shows a 25 μm × 25 μm and Figure 2.8(b) shows a 2 μm × 2 μm area. The film seems quite uniform, without any worms. The height variation in the films of Figures 2.7 and 2.8 seems similar. The Au cluster size in Figure 2.7(b) is bigger than in Figure 2.8(b). It is difficult to say that if this was due to the better vacuum in the deposition of Figure 2.8 or due to the fact that the deposition was done by electron-beam. If required the dependence of Au cluster size on the deposition method—thermal evaporation or e-beam evaporation—can be investigated.

2.2.3.1 Conclusion

From Figures 2.6 and 2.7 we can conclude that the vacuum level in the deposition chamber influences the film morphology. Higher vacuum level results in better films but generation of UHV or better requires very specialized machines and long pumping duration. For our task, acceptable depositions could be carried out at about 5×10^{-6} mbar. The time taken to achieve this pressure level depends on the efficiency of the pumping system—it took about 18 hours on one machine, and on the other two tested machines, this vacuum level could be attained after 30 minutes of pumping.

Both thermal and electron-beam evaporation methods are machine-specific. From the two, electron-beam evaporation seems to be more promising as it offers precise control over the deposition rate and limited contamination from the source material.

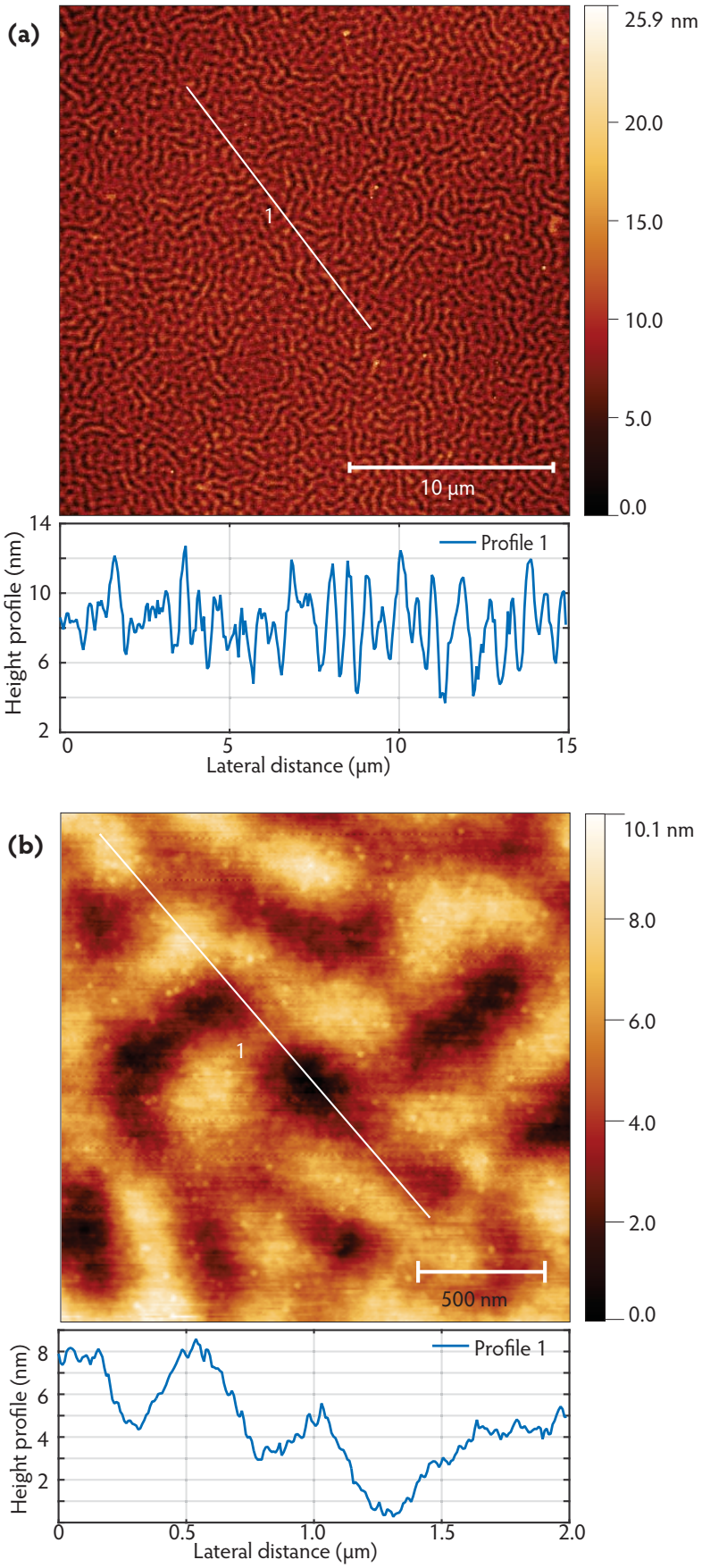

Figure 2.6 *20 nm Au deposition under low vacuum*
AFM images of a 20 nm thick Au film deposited on a PMMA substrate in low vacuum conditions. The RMS roughness was noted as 2 nm in **(a)**, and 1.3 nm in **(b)**.

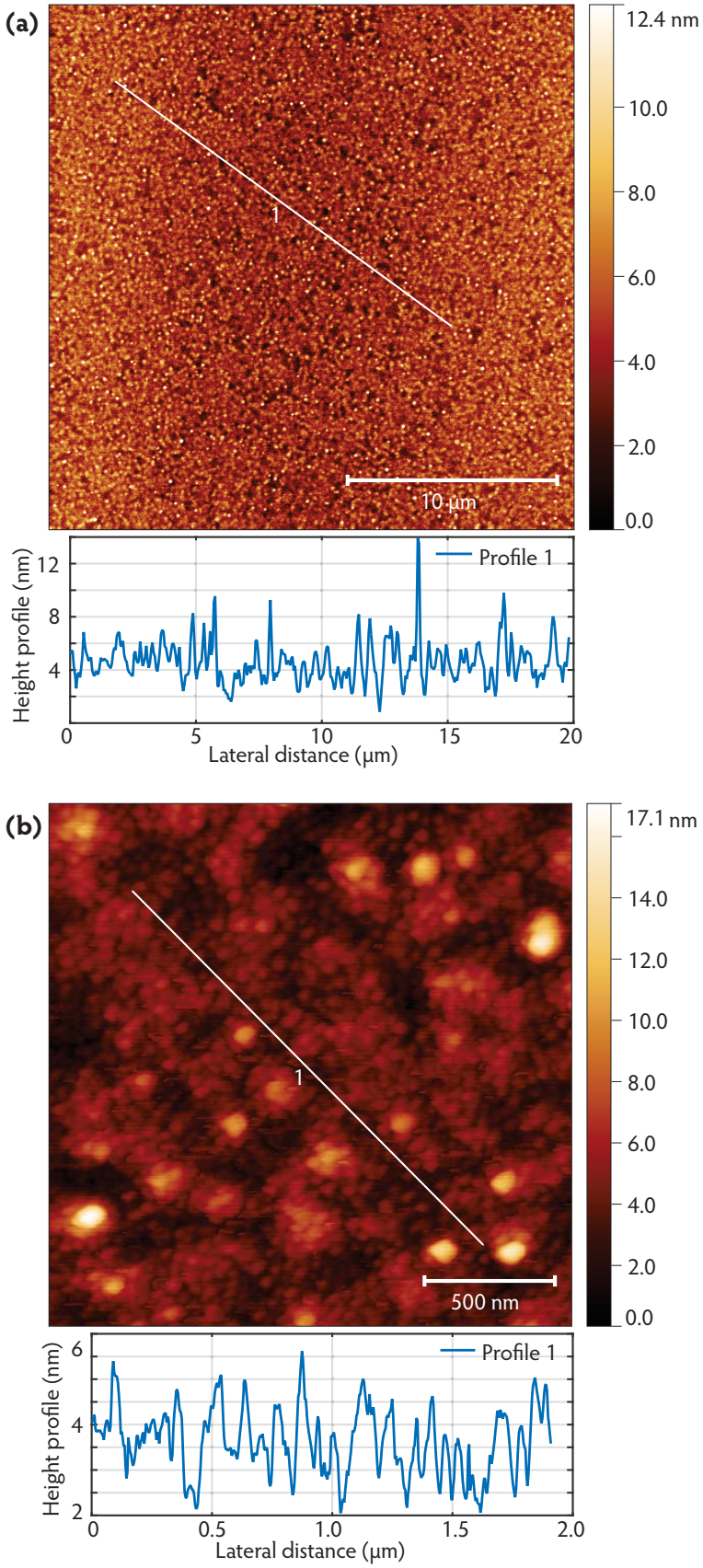

Figure 2.7 *20 nm Au deposition under high vacuum*

AFM images of a 20 nm thick Au film deposited on a PMMA substrate at $\sim 5 \times 10^{-6}$ mbar. The RMS roughness in both cases was 1.1 nm.

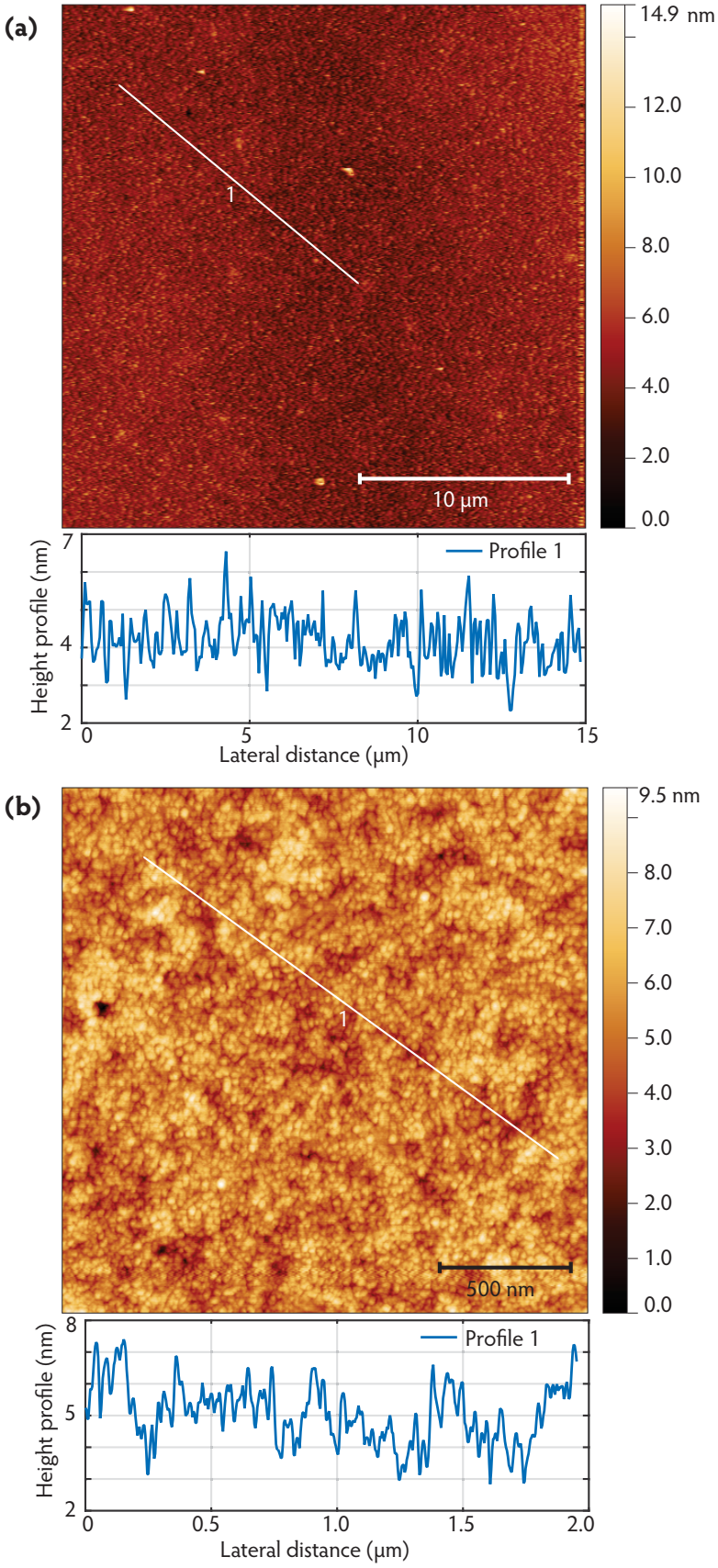

Figure 2.8 *20 nm Au deposition under very high vacuum*

AFM images of a 20 nm thick Au film deposited on a PMMA substrate at 4.64×10^{-7} to 10^{-6} mbar. The RMS rugosity in both cases was 0.8 nm.

2.3 Dielectric deposition on nanocrystals

After depositing a 200 nm thick layer of Au on a Si substrate using 10 nm of Ti/Cr as an adherence layer (Figure 2.4), a layer of dielectric, with the embedded nanocrystal, had to be placed (Figure 1.2). To do this, initially, we proceeded as follows: On the structure of Figure 2.4, 15 nm of SiO_2 was deposited by thermal evaporation. On this layer of SiO_2, CdSe/CdS nanocrystals were spin-coated from an adequately diluted solution. For spin-coating nanocrystals, we have always used these parameters:

Acceleration of spinning:	2000 rpm/s
Maximum speed of spinning:	4000 rpm
Duration of spinning:	40 s

By means of spin-coating we can get uniformly distributed individual nanocrystals on most smooth substrates. After spin-coating nanocrystals on the 15 nm thick SiO_2 layer, we deposited another 15 nm of SiO_2 on the nanocrystals by electron-beam evaporation. In this way we were able to obtain a 15+15 nm thick dielectric (SiO_2) layer with embedded nanocrystals as shown in Figure 1.2. But the electron-beam deposition of SiO_2 had permanently damaged the nanocrystals, such that they stopped fluorescing. The situation is depicted in Figure 2.9. To resolve this problem, we varied the electron-beam evaporation parameters, e.g., modifying the deposition rate, improving the vacuum level to 10^{-9} mbar, and decreasing the thickness of the deposited layer to 5 nm. Several depositions were carried out on three different evaporation machines (two machines used electron-beam evaporation and one utilized thermal evaporation) in Paris, on several batches of nanocrystals, but the results were similar—after the deposition of silica directly on the nanocrystals, they stopped fluorescing.

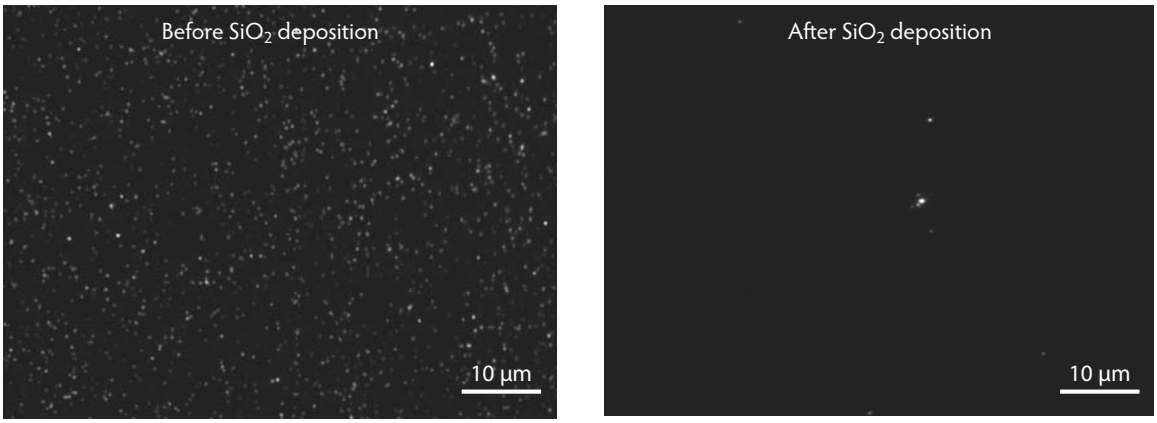

Figure 2.9 *CdSe/CdS quantum dots before and after silica deposition*

Figure **(a)** shows a fluorescence microcopy image of a sample: Si(280 µm) + Ti(10 nm) + Au(200 nm) + SiO_2 (15 nm) + NC. Figure **(b)** shows the same sample after silica deposition by thermal evaporation: Si(280 µm) + Ti(10 nm) + Au(200 nm) + SiO_2(15 nm) + NC + SiO_2(15 nm). In both the images the bright spots are nanocrystals, and most likely individual nanocrystals in **(a)**. It can be seen in figure **(b)** that most of the nanocrystals stopped fluorescing and the luminosity of the very few remaining ones was very low. The two bright spots in **(b)** were clusters of nanocrystals. This indicated that silica deposition was damaging the nanocrystals. The areas shown in **(a)** and **(b)** were on the same sample but not exactly at the same location. However, the conclusion mentioned above is still true because the spatial distribution of nanocrystals on the entire sample was as depicted in **(a)**.

To circumvent the problem of silica deposition, we tried depositing other dielectrics like ZnS, YF_3, and Si_3N_4. But these dielectric depositions damaged the individual nanocrystals in the same way as silica deposition. It should be noted that all the depositions were carried out at about room temperature; therefore, a rise in temperature during deposition cannot be the reason behind nanocrystal damage. Our nanocrystals can sustain 150°C for at least 20 minutes. The failure to obtain successful dielectric depositions using conventional techniques motivated us to look for other solutions, which we found in the form of polymer coatings. This will be discussed in section 2.4.

In an experiment, we deposited 17 nm of SiO_2 by thermal evaporation on clusters of nanocrystals. Based on the fluorescence intensity of the clusters, we assumed that each investigated cluster had at least 10 nanocrystals. After depositing SiO_2 on these clusters, we noted that the fluorescence intensity of each investigated cluster had reduced significantly. On the same sample, we confirmed, as in Figure 2.9, that individual nanocrystals stopped fluorescing after the deposition. From this we concluded that SiO_2 deposition by thermal evaporation certainly damages the nanocrystals. In case of a cluster of nanocrystals, SiO_2 deposition damages some of the outer nanocrystals that come in contact with the depositing material. This reduction in the number of fluorescing nanocrystals in a cluster after deposition lets it fluoresce but at a considerably lower rate.

Conclusion: Our experiments with evaporation deposition (thermal and electron-beam) of dielectrics—SiO_2, ZnS, YF_3, and Si_3N_4—directly on CdSe/CdS core/shell quantum dots show that vapor deposition damages the quantum dots. The damage results in complete bleaching of fluorescence in the case of single quantum dots, and significant reduction in fluorescence when the deposition is carried out on clusters of quantum dots. The deposition of dielectric vapor on a cluster of quantum dots seems to damage some of the outer exposed quantum dots and not the inner ones—thus the cluster fluoresces after the dielectric deposition but with a reduced emission rate.

2.3.1 What damages the nanocrystals during evaporation?

Interaction of charges with nanocrystals can chemically modify the nanocrystals, which can result in shutting down their radiative recombination channels. In other words, nanocrystals stop fluorescing. As far as shutting down of radiative recombination channels is concerned, we may draw some similarity between this process and the photooxidation of nanocrystals, which finally results in photobleaching [117]. Barnes *et al.* have reported the creation of vapors of charged clusters of gold during its thermal evaporation [118]. During the thermal evaporation of copper, there has been evidence of generation of charged clusters [119].

Regarding the bleaching of nanocrystals fluorescence after vapor deposition of dielectrics, my hypothesis is:

1) If thermal evaporation can create charged clusters of a noble metal like gold, then it is very likely that in the process of evaporating materials like SiO_2 and ZnS, charges are created. When these charges (ions, electrons, and charged clusters) interact with the nanocrystals, the latter are damaged.

2) Nucleation of the vapors of the dielectric material directly on the nanocrystal may permanently damage its fluorescence.

The possibility of 1) or 2) results in beaching of nanocrystal fluorescence. Therefore if they are avoided, the nanocrystals can be saved from the damaging effects of vapor deposition.

To test the hypothesis, the following experiment was performed. It should be remarked that when this experiment was performed, we had already solved the problem of dielectric deposition by using spin-coated PMMA films. If the nanocrystals—as claimed by the hypothesis—were being damaged due to charges in the deposition chamber or by the nucleation process, then the presence of a protective coating on the nanocrystals, that prevents their interaction with charges and nucleation effects, should be able to prevent the damage. On a sample, like the one of Figure 2.9(a), was prepared. On this sample, a PMMA film of about 10 nm thickness was spin-coated, and the sample layers were:

Si (280 μm) + Ti (10 nm) + Au (200 nm) + SiO_2 (15 nm) + NC + PMMA (10 nm).

This sample was viewed by fluorescence microscopy and images were recorded. Then it was put in the deposition chamber and 5 nm of SiO_2 was deposited on it by thermal evaporation. After this step, the sample contents were:

Si (280 μm) + Ti (10 nm) + Au (200 nm) + SiO_2 (15 nm) + NC + PMMA (10 nm) + SiO_2 (5 nm).

The sample was observed with fluorescence microscopy (Figure 2.10). All the nanocrystals were fluorescing as before, thus verifying the hypothesis. Successful result of the above mentioned experiment gave us a way of protecting the nanocrystals with a very thin layer of PMMA and then coating dielectric materials. Later this method was used by Fu Feng of our group to fabricate Tamm structures [120].

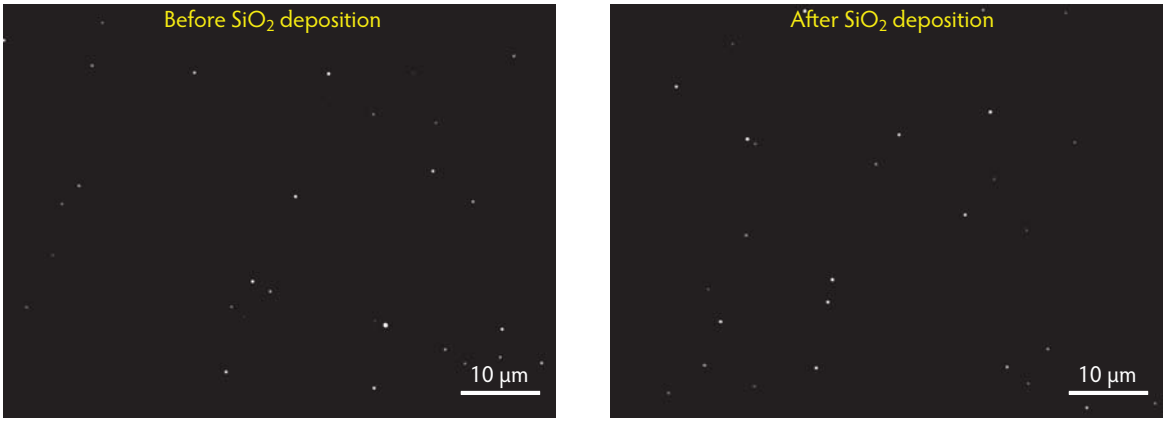

Figure 2.10 *CdSe/CdS quantum dots under PMMA: Before and after silica deposition*
Figure **(a)** shows a fluorescence microcopy image of a sample: Si(280 μm) + Ti(10 nm) + Au(200 nm) + SiO_2 (15 nm) + NC. Figure **(b)** shows the same sample after silica deposition by thermal evaporation: Si(280 μm) + Ti(10 nm) + Au(200 nm) + SiO_2(15 nm) + NC + PMMA(10 nm) + SiO_2(5 nm). The white spots in both the images are fluorescing nanocrystals. The nanocrystals were alive after the silica deposition, indicating that during the deposition, the nanocrystals were protected by the PMMA layer above them. The regions imaged in **(a)** and **(b)** were on the same sample but in different areas, therefore the placing of the nanocrystals is different in the two images. Both the images were recorded with the same parameters. No nanocrystal damage, like reduction or complete suppression of fluorescence, or propensity to photobleaching was observed.

2.4 Polymer coatings

As mentioned in section 2.3, we had tried SiO_2, ZnS, YF_3, and Si_3N_4 depositions with all the available options but in all cases, the depositions resulted in damaging the individual emitters. Our first strategy to deposit a dielectric material on a nanocrystal was evaporation deposition (thermal or electron-beam) because it is widely used to make thin films, especially for optical applications [109, 121]. The failure to deposit dielectric thin films by evaporation on individual nanocrystals without damaging them motivated us to look for other solutions. We had experience in spin-coating PMMA to make 50 nm thick films. The question was: Was it possible to spin-coat polymers and make films that were homogeneous and uniform with thicknesses as low as 5–10 nm? This section will describe our method of attaining and characterizing ultra-thin polymer films, especially PMMA films.

For a spin-coated polymer film, the main factors affecting the film thickness and quality are:

1) **Polymer**: There is a large variety of polymers to choose from and for a given polymer, the choice of its molecular weight also matters. For example, we observed that a higher molecular weight polystyrene generates a thicker spin-coated film than a lower molecular weight polystyrene. The main polymers that we had used are: PMMA, polystyrene, and polyvinyl alcohol (PVA).
2) **Polymer concentration in solution**: Generally, the higher the concentration of the polymer in a solution, the thicker is the spin-coated film. There is a limit to reducing the concentration of the polymer in the solution because films obtained from very low concentrations are not homogeneous.
3) **Spin-coating parameters**: Usually, the higher the spin-coating speed, the lower the thickness of the spin-coated film. Generally, higher acceleration gives more uniform films and ensures that no parts of the substrate are left uncoated [122].
4) **Solvent of the polymer solution**: The viscosity and the density of the spin-coating solution influence the film thickness [123]. These depend on the solute (polymer) and the solvent. For example, a solution of PMMA in toluene deposits films with different thickness and properties than a similarly concentrated solution of PMMA in acetone. The higher the viscosity and the density of the solution, the thicker is the spin-coated film.
5) **Substrate**: The nature of the substrate influences the interaction forces between the substrate and the solution, and therefore, it affects the film thickness. The material and the surface smoothness of the substrate both affect the film thickness.

We have mainly worked with PMMA coatings . We have also worked with polystyrene films, made by spin-coating solutions of polystyrene in toluene; we could obtain films with thicknesses as low as 5 nm. But given the excellent reproducibility of PMMA films, we chose to use it exclusively. The dielectric coating on all the nanoantenna samples discussed in this thesis is a PMMA coating; therefore, the following part of this section will focus on PMMA coatings. We begin with a discussion on the methods of obtaining PMMA thin films, which will be followed by the characterization of the films.

2.4.1 PMMA solution in toluene

To obtain different film thicknesses, different concentrations of PMMA solutions in toluene were used. The concentration of a solution in *percent by mass of solute in solution* [m/m] is written as [124]:

$$\frac{m_{\text{solute}}}{m_{\text{solution}}} \times 100\% = \frac{m_{\text{PMMA}}}{m_{\text{solution}}} \times 100\% = \frac{m_{\text{PMMA}}}{m_{\text{PMMA}} + m_{\text{toluene}}} \times 100\% \tag{2.6}$$

Solutions of 0.5% [m/m], 0.75% [m/m], 1% [m/m], 1.5% [m/m], and 2% [m/m] PMMA in toluene were prepared and tested. To make the solutions, the required amounts of PMMA and toluene were mixed in a tightly closable glass bottle. After mixing, the bottle was closed and put in a water-filled beaker, which was maintained at 50°C by a heating plate. The bottle was left undisturbed in this state for 24 hours—this allowed thorough mixing of PMMA and toluene. Technical specifications of the PMMA powder and toluene are given in the appendix.

2.4.2 Spin-coating PMMA solutions

To spin-coat PMMA on a substrate, we cover it entirely with the PMMA solution and immediately spin it using the following parameters:

Acceleration of spinning:	2000 rpm/s
Maximum speed of spinning:	4000 rpm/s
Duration of spinning:	40 s

Throughout this work, a Karl Suss spin-coating machine was used. We can instruct the spinning plate to turn at a nominal speed, which is generally lower than the actual spinning speed of the substrate (measured by an external sensor). The difference between the measured and instructed speeds depends on the size and weight of the substrate, and the type of sample-holding plate on which it rests. To ensure the correct spinning speed, firstly we spin the substrate without the coating solution and adjust the speed till the desired value (4000 rpm in this case) is attained. Then the substrate is coated with the solution and spun again. Usually, our substrates were small (about 1 cm × 1 cm) and only 15 µl of solution of PMMA in toluene was enough to cover them completely.

We have observed that in order to obtain reproducible homogenous and uniform coatings, it is required that the solution is deposited on the entire sample surface, and spun immediately. If the sample is not fully covered by the solution before spinning, the coated film shows clear demarcations at the edges where there was no solution prior to spinning. After spin-coating, the substrate is baked at 150°C for 2 minutes using a Mettler Toledo heating stage. Baking the spin-coated film helps in removing the remaining solvent and trapped air bubbles, and improves the adhesion of the film to the substrate [125]. Baking the substrate at a temperature higher than the glass transition temperature of the coated resist improves the film properties [126] and its adherence to the substrate [127]. The glass transition temperature of PMMA is about 105°C [128], therefore baking it at 150° C is sufficient. Baking duration also influences the film properties. Because our nanocrystals cannot bear high temperatures (>150°) for long (>10–15 minutes), we chose to heat our substrates for only 2 minutes at 150°C, which was sufficient for baking the PMMA.

2.4.3 Characterization of PMMA thin films

In context of our work, a resist film was characterized by its thickness, homogeneity, and surface smoothness. As shown in Figure 1.2, the thickness of the polymer film decides the separation between the Au layers above and below the nanocrystal, and the distance between the nanocrystal and the Au layers. Therefore, it decides the goodness of the SPP coupling, and thus the nanoantenna operation. The top patch of Au on the nanocrystals is deposited by thermal evaporation on a layer spin-coated PMMA. If the PMMA layer is not smooth, the patch will not be smooth. Given that the Au patch is only 20 nm thick, its uniformity, which depends on the smoothness of the PMMA film, can be crucial to the involved plasmonic processes.

Ellipsometry and AFM were used for characterizing spin-coated polymer films for their thickness, homogeneity, and smoothness. The base substrate on which the PMMA solution was spin-coated was (Figure 2.4):

Si (280 µm) + Ti (10 nm) + Au (200 nm).

A PMMA solution in toluene of a given concentration, e.g., 0.5% [m/m], was dropped on a 200 nm thick layer of Au and spun with the parameters mentioned in section 2.4.2. The layers in the sample after spin-coating were:

Si (280 µm) + Ti (10 nm) + Au (200 nm) + PMMA (?).

In section 2.2.2, we discussed that the optical constants of thermally evaporated thin films (like 200 nm thick Au) are different from bulk materials and are machine dependent. Using ellipsometry, we had measured the optical constants of the 200 nm thick Au layer (Figure 2.2(a) and Figures 2.5(f) & (g)). This was essential because the error in ellipsometric data fitting, and thus the accuracy of the thickness measurement by ellipsometry, depends on the knowledge of the optical constants of the involved layers.

2.4.3.1 Film thickness by ellipsometry

In an ellipsometry measurement setup, a monochromatic or quasi-monochromatic light beam of a known polarization state is sent onto the sample surface, where it is specularly reflected, passed through a polarizer, and then collected by a detector. The change in the p (in the plane of incidence) and s (perpendicular to the plane of incidence) components of polarization is recorded and is used to convey information about the material properties of the sample, such as film thickness and optical constants. The change in polarization ρ is expressed as [129, 130]:

$$\rho = \frac{r_p}{r_s} = \tan(\Psi)\, e^{j\Delta}, \tag{2.7}$$

where r_p and r_s are the complex Fresnel reflection coefficients of the p and s components, respectively. The $\tan(\Psi)$ ($0 \leq \Psi \leq 90°$) is the relative amplitude change and the angle Δ ($0 \leq \Delta \leq 360°$) is the differential phase shift of the p and s linearly polarized components upon reflection. Using the polar form of complex analysis and Eq. (2.7), we can write:

$$\tan \Psi = \frac{|r_p|}{|r_s|} \tag{2.8}$$

and

$$\Delta = \arg(r_p) - \arg(r_s). \tag{2.9}$$

The term 'ellipsometry' is due to the fact that most often, after reflection, polarized light becomes elliptical [131]. It was first used by Rothen [130, 132] in 1945. Ellipsometry can provide realtime information about film growth. Many deposition machines have an in-built ellipsometry measurement setup. An atomic layer deposition machine, which deposits one atomic layer at a time, can benefit from a realtime ellipsometry measurement of film growth, which may be combined with measurements by a quartz microbalance to enhance precision [133]. Ellipsometry is capable of detecting nanometric sub-monolayer changes [134, 135] like the formation of sparsely distributed island-like or sub-monolayer of films of atoms or molecules.

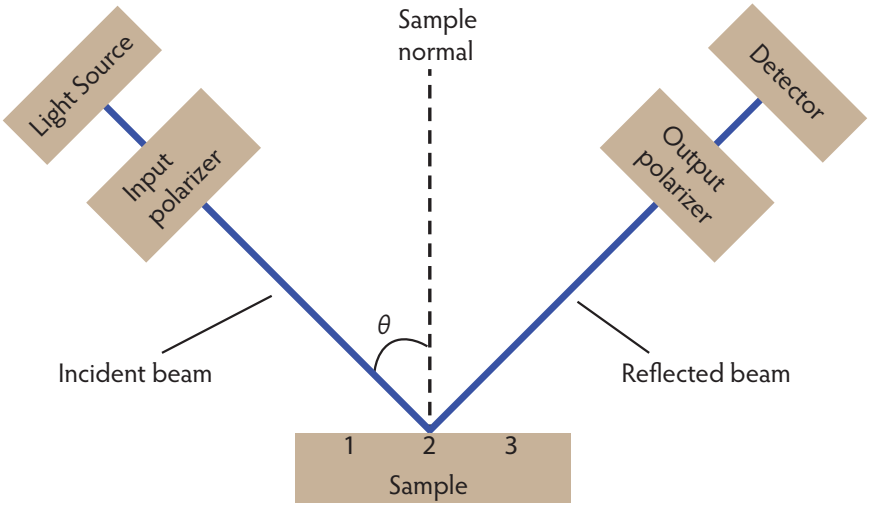

Figure 2.11 *Oblique angle ellipsometry*

A monochromatic or quasi-monochromatic beam of incident light of a known polarization state strikes the sample at an oblique angle θ. The reflected light is analyzed by the detecting assembly. The change in the polarization of light is measured and a model is used to deduce the film thickness or the optical constants of the sample layers. In our measurements, the wavelength of the incident beam was varied from 300–1500 nm and three values of θ were chosen (usually, 50°, 60°, and 70°). These measurements were done on three different points on the sample (marked as 1, 2, and 3)—in this way we could be sure of the homogeneity of the film.

All our measurements were carried out using a J. A. Woollam Co. variable-angle spectroscopic VB-400 ellipsometer. Data was recorded at several wavelengths and at three angles of incidence, which results in more accurate analysis [129, 136, 137]. Usually, the incident angles were chosen as 50°, 60°, and 70°, and the wavelength range was from 300–1500 nm, using an increment of 5 nm. The diameter of the incident beam was 2 mm. The measured data was analyzed using the software WVASE32 Version 3.774. After measuring a sample, a model is constructed to describe the material layers in the sample. Figure 2.12 shows our model to estimate the PMMA film thickness. Using the thickness and optical constants of the concerned materials, Fresnel equations are solved by the software. If these values are not known (in Figure 2.12, the PMMA layer thickness is the unknown), an estimate is used for the first simulation. These calculated values are compared with the measured experimental data to account for the agreement between them. We have used the mean squared error (MSE) as the estimator to compare the calculated and measured values of Ψ and Δ as a function of wavelength, and for the measured incidence angles. Regression algorithms estimate the most accurate film thickness or optical constants by finding the least MSE.

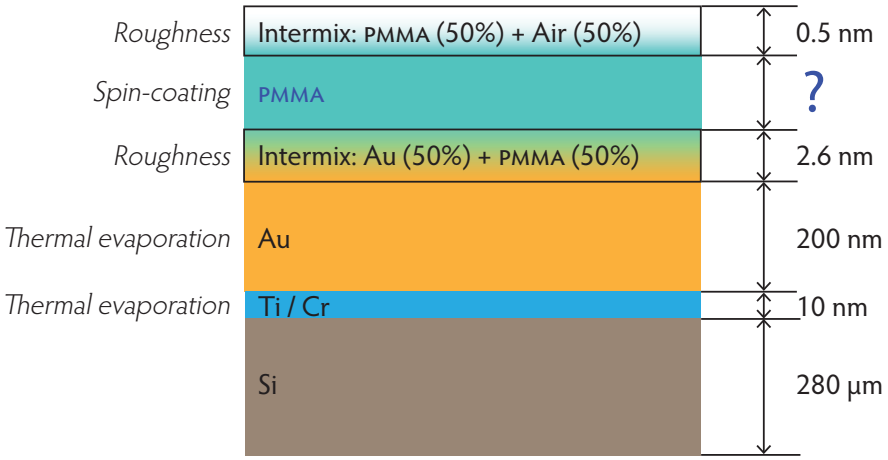

Figure 2.12 *Model to measure PMMA film thickness by ellipsometry*
In the model, the 200 nm Au is optically opaque, and therefore whatever lies beneath it (Ti/Cr and Si) is irrelevant to the estimation of the PMMA thickness. The optical constants of the 200 nm Au were measured as a function of wavelength (Figure 2.2(a) and Figure 2.5(f) & (g)). To account for the roughness of the 200 nm Au film, the RMS roughness of 2.6 nm, as measured by AFM, was used. In the model substrate roughness is incorporated as an intermix layer created by Bruggeman effective medium approximation [138] that uses the optical constants of the substrate and the material/medium above it. The optical constants of PMMA provided by the software were adequate. The roughness of PMMA was also found using AFM. This model was used to estimate the film thickness obtained by spin-coating different concentrations of PMMA solution—it gave a very low MSE (<2), which means that the film thickness was estimated very well.

PMMA concentration [m/m]	Film thickness (nm)
0.50%	10
0.75%	15
1.00%	21
1.50%	35
2.00%	58

Table 2.1 *PMMA film thickness on Au depending on the concentration of the PMMA solution*
The PMMA concentration in the table refers to percent by mass of PMMA in a solution of PMMA & toluene. The solutions were spun at 4000 rpm. The film thicknesses mentioned above could be reproduced within a range of ±5 % on different substrates of similar nature. The precision of three significant figures is not really valid; it is the value presented by ellipsometry estimation, which is due to analytic computation. It should be noted that the mentioned film thicknesses were obtained on a Au surface; generally, on another surface, the corresponding thicknesses will be different.

Using the parameters mentioned in section 2.4.2 and spin-coating PMMA solutions in toluene on a 200 nm thick Au layer (as used in our structures), we obtained the thickness values mentioned in Table 2.1. As shown in Figure 2.11, on each sample the ellipsometry measurements were carried out at three different points on the sample. We confirmed that the layers were homogeneous and the measurements were repeatable within a range of ±5 %, that is, if the ellipsometry measurements were repeated on a sample, the film thickness changed about ±5 %, and when the measurements were made on different areas on the sample, the estimated thickness changed by about ±5 %. Also, when the same PMMA solution was used to spin-coat different substrates of similar nature, the PMMA films were reproducible within a

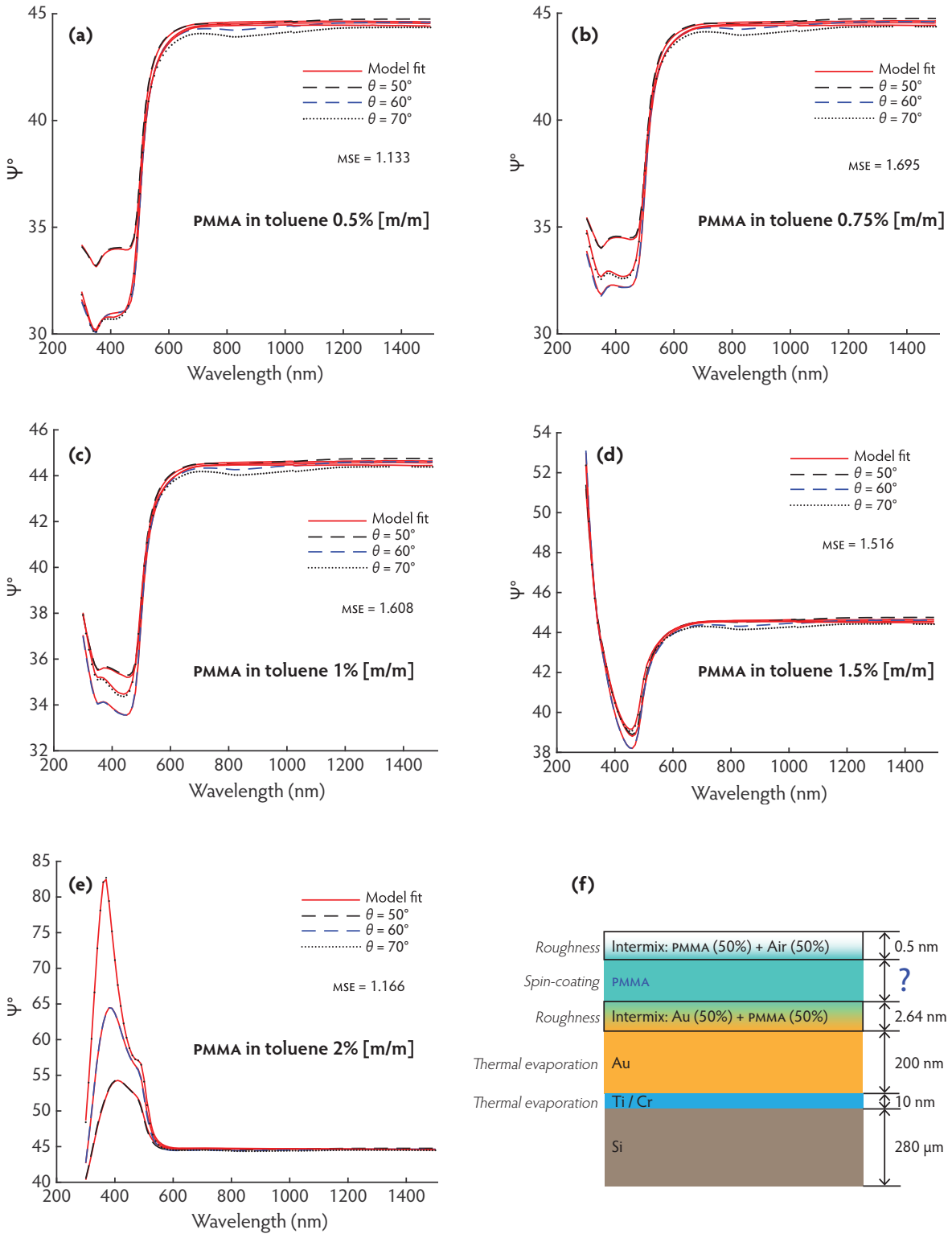

Figure 2.13 *Ellipsometry: estimated data versus experimental data (Ψ plots)*

In figures **(a)**–**(e)**, for the given angles of incidence, the curve in red color represents the model fit and the other curves are plotted from the measured data. For the entire wavelength range, the fitted and the measured curves are almost overlapping (represented as the MSE), which signifies accuracy in the estimated thickness. These figures show the plots of Ψ as a function of λ. Figure **(f)** shows the model used in all the depicted cases. Each plot shows the respective concentration of the PMMA solution in toluene.

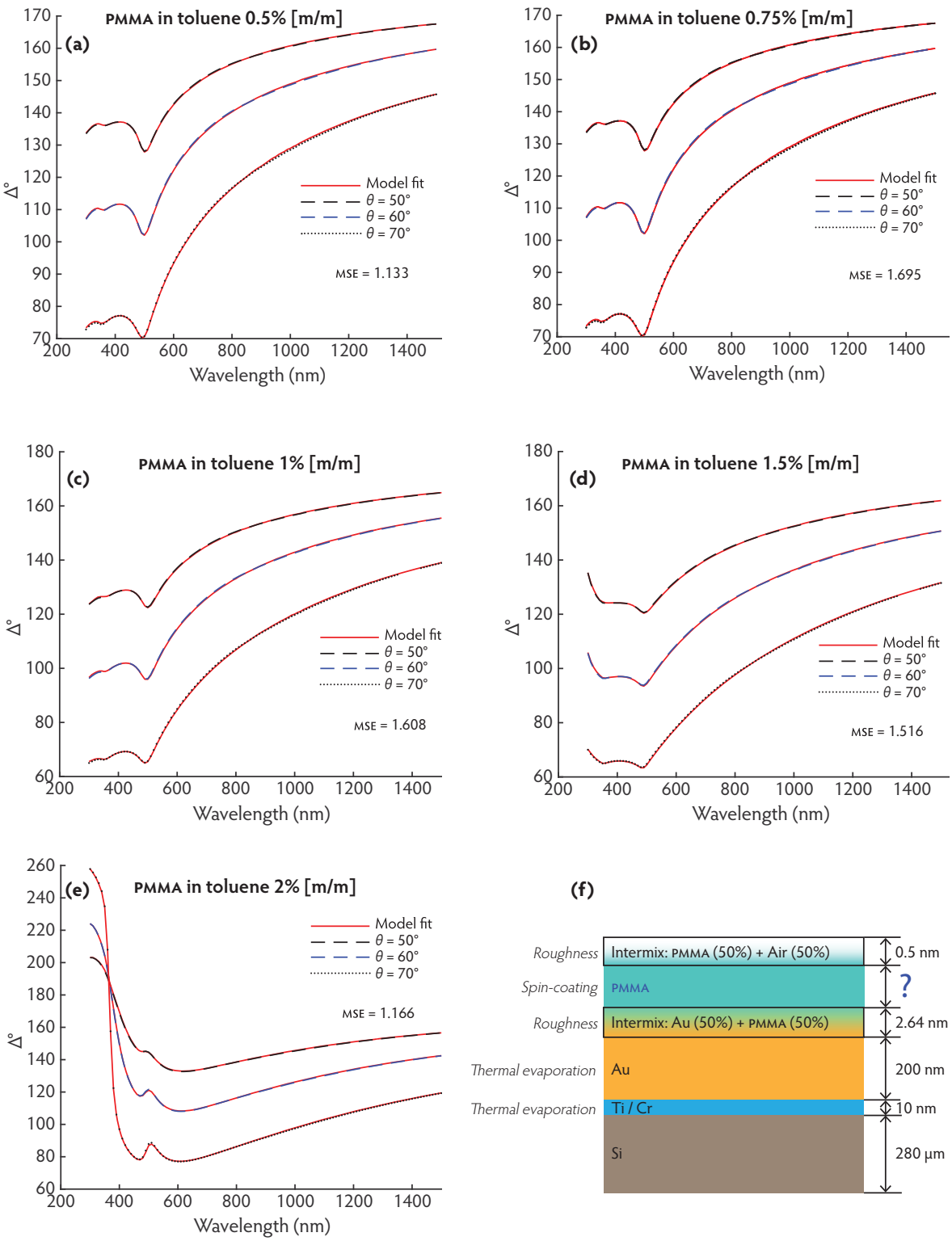

Figure 2.14 *Ellipsometry: estimated data versus experimental data (Δ plots)*

In figures **(a)**–**(e)**, for the given angles of incidence, the curve in red color represents the model fit and the other curves are plotted from the measured data. For the entire wavelength range, the fitted and the measured curves are almost overlapping (represented as the MSE), which signifies accuracy in the estimated thickness. These figures show the plots of Δ as a function of λ. Figure **(f)** shows the model used in all the depicted cases. Each plot shows the respective concentration of the PMMA solution in toluene.

range of ±5 %, i.e., the PMMA film thickness on the coated substrates changed at most by ±5 %. This tells us about the accuracy of the model, and the homogeneity and reproducibility of the film. For these measurements, using the plots of the measured Ψ and Δ values, respectively, and comparing them with the values estimated by the ellipsometry model, Figures 2.13 and 2.14 show the agreement between the model estimation and the experimental measurement.

2.4.3.2 Film analysis by AFM

Atomic force microscopy AFM is a type of scanning probe microscopy, which was first introduced by Binnig *et al.* in 1986 [139]. In all scanning probe microscopy systems, a nanoscale probe, that is driven by a piezoelectric actuator, interacts with the sample. Scanning probe microscopy systems include scanning tunneling microscopy, near field scanning optical microscopy, and AFM [140]. In AFM, the mechanical force between the nanoscale probe (also called the tip) and the sample is used to provide information about the sample surface. AFM is a very useful technique that does not require special operating conditions such as vacuum creation or additional sample preparation, and it can be used on conductive or non-conductive samples, in air or in liquid, and provides a three-dimensional measurement with a lateral resolution of 1 nm and a vertical resolution of 0.1 nm [141, 142].

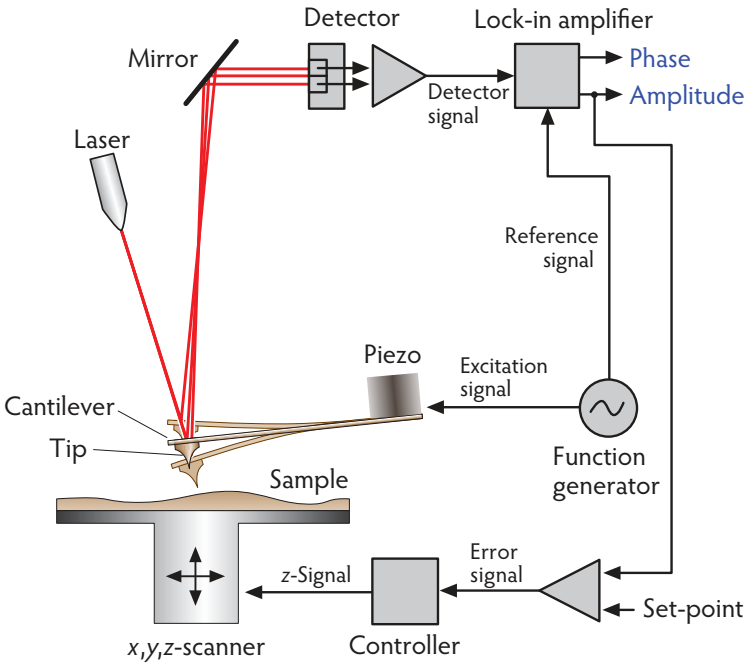

Figure 2.15 *Intermittent contact mode AFM*

The oscillation amplitude and orientation of the cantilever is detected by noting the deflection of the laser beam incident on its backside. The detector signal gives information about the amplitude and phase of the cantilever. The amplitude signal is used as the feedback signal to control the tip–sample distance such that the oscillation amplitude is constant. This is done by selecting an amplitude set-point value, which acts as a reference for the detected signal. As the set-point value controls the force between the tip and the sample, it should be optimally set for good imaging. Image adapted from [44].

There are several modes of operation of AFM, which can be broadly categorized as: 1) topographic modes (e.g., contact and oscillating), and 2) non-topographic modes (e.g., magnetic AFM, force spectroscopy, nanoindentation, phase imaging, electrochemical AFM, and thermal modes) [142]. To image our samples, we use the intermittent contact mode (also called tapping mode), which gives topographic and composition information about the sample surface [143, 144]. In this mode, with the help of a piezoelectric actuator, the cantilever, to which the AFM tip is attached, is made to oscillate just below[2] or at its resonance frequency. Under usual operation conditions, the equilibrium tip–sample separation is less than the oscillation amplitude (typically, 1–100 nm); which leads to the tip touching the sample once per oscillation cycle. The amplitude of this oscillation—signifying the tip–sample interaction—varies according to the topography of the sample surface. For topography imaging, the oscillation amplitude is kept constant by changing the height of the cantilever [141]. The required change in height gives information about the topography of the sample. Phase imaging is a secondary mode of the tapping mode AFM. The phase of oscillation of the cantilever is recorded and compared with the phase of its driving signal. As the change in phase depends on the energy dissipation that occurs during the tip–sample interaction[145, 146], the phase contrast image gives information about material properties such as composition, adhesion, and friction, and it is sensitive to topographical variations (which influences the tip–sample contact area, and thus the energy dissipation) [147]. The principle of operation of a tapping mode AFM is outlined in Figure 2.15. When our Au and PMMA films are imaged with tapping mode AFM, the amplitude images convey information about topography or film smoothness, and the phase images convey information about homogeneity of the film.

All our AFM measurements were done using a Veeco Dimension 3100 AFM in tapping mode. The images were analyzed with Gwyddion version 2.40 software. All the AFM measurements presented in this thesis were done using Bruker RTESPA (Model: MPP-11120-10) tips. The cantilever and tip specifications are mentioned in the appendix.

Figure 2.16 shows AFM images of the surface of a 15 nm thick PMMA coating, that was obtained by spin-coating a solution of 0.75% [m/m] PMMA in toluene on an Au surface. This Au surface had an RMS roughness of 2.6 nm (see Figure 2.5). The overall variation of height of the PMMA coating was about ±1 nm, which seems quite good for a 15 nm thick film. During spin-coating, the PMMA molecules, being in a liquid medium, can cover the irregularities on the Au surface. After spin-coating, the surface roughness or the RMS roughness of the PMMA film was noted as 0.4 nm.

On a similar Au surface, as mentioned in the previous paragraph, we deposited 13 nm of SiO_2 by thermal evaporation. Figure 2.17 shows the AFM topography and phase images of this coating. The RMS roughness of the coating was recorded as 2.2 nm, which is very close to the roughness value of the Au substrate on which the deposition was done. The overall variation of height of the SiO_2 film was about ±5 nm, which seems a lot for a 13 nm thick film. In Figure 2.17(a), clusters of SiO_2 can be seen.

Comparing the AFM topography images in Figure 2.5 with Figures 2.16 and 2.17, we note that the spin-coated PMMA film was smoother than the thermally deposited Au and SiO_2 films. The same was observed in the case of electron-beam evaporated films. A spin-coating proced-

[2] When imaging in the tapping mode or the intermittent contact mode, the device manufacturer recommends setting the drive frequency 5% below the resonance frequency [141].

ure takes about 15 minutes, whereas thermal and electron-beam evaporation on our machine at INSP takes about 1 day. Due to the better quality of spin-coated polymer films as compared to evaporated SiO_2 films, and the ease and rapidity of the spin-coating technique, we chose to use spin-coated polymer films as the dielectric medium in our nanoantenna structures.

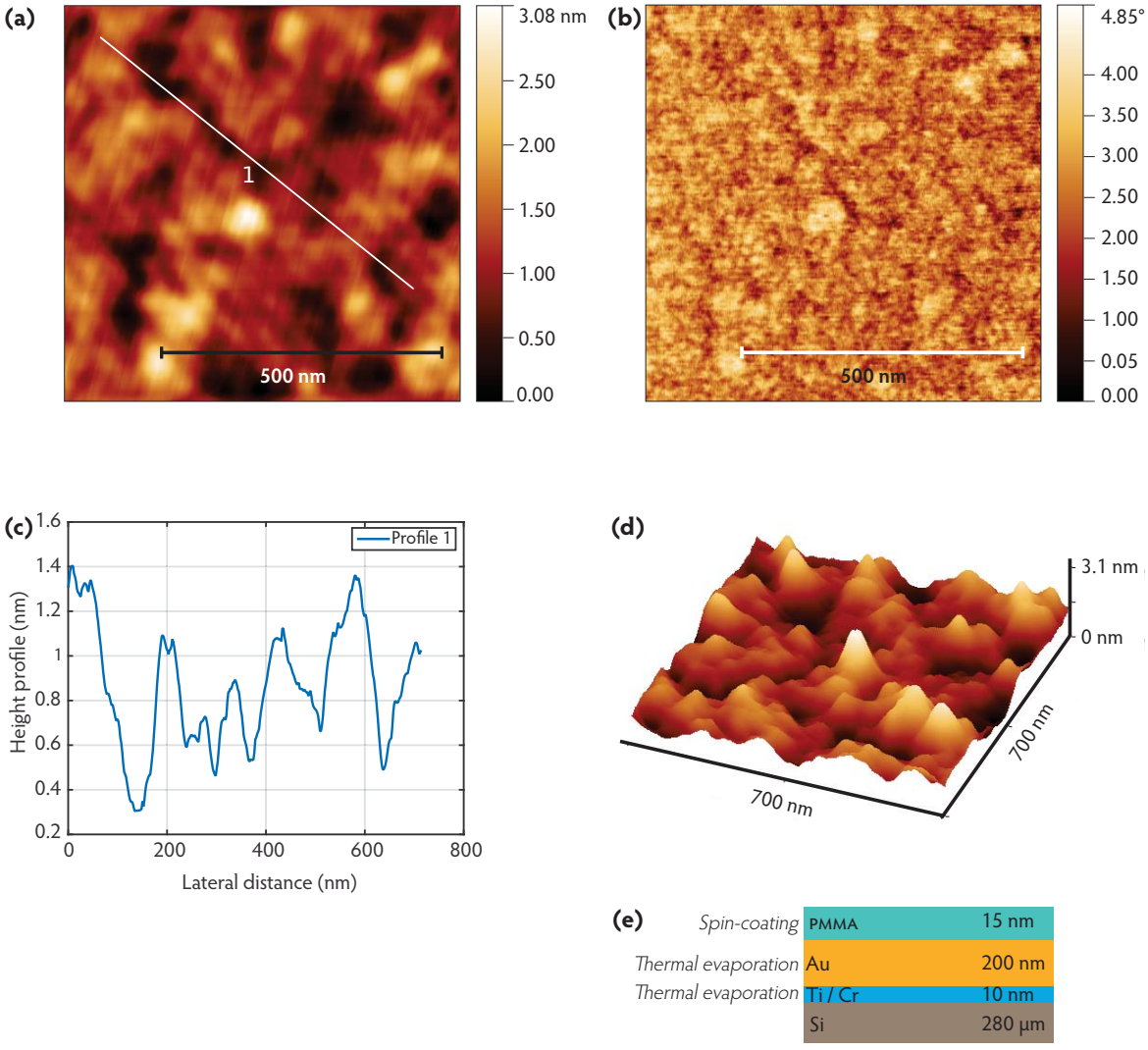

Figure 2.16 *AFM imaging of PMMA coating*

Figure **(a)** shows the AFM topography image of a 700 nm × 700 nm surface of a film made by spin-coating a 0.75% [m/m] solution of PMMA in toluene on an Au substrate. The RMS roughness of the Au surface was 2.6 nm. After the deposition of the ~15 nm thick PMMA film, the RMS roughness of the surface was 0.4 nm. This shows that the polymer deposition made the surface smoother. Figure **(b)** shows the corresponding phase image and **(d)** shows the corresponding 3-D perspective image. In figure **(c)**, the height profile along path 1 (marked in **(a)**), is represented graphically. The maximum variation was less than ±0.5 nm. The total thickness of the PMMA film was 15 nm. Figure **(e)** shows the layers in the sample.

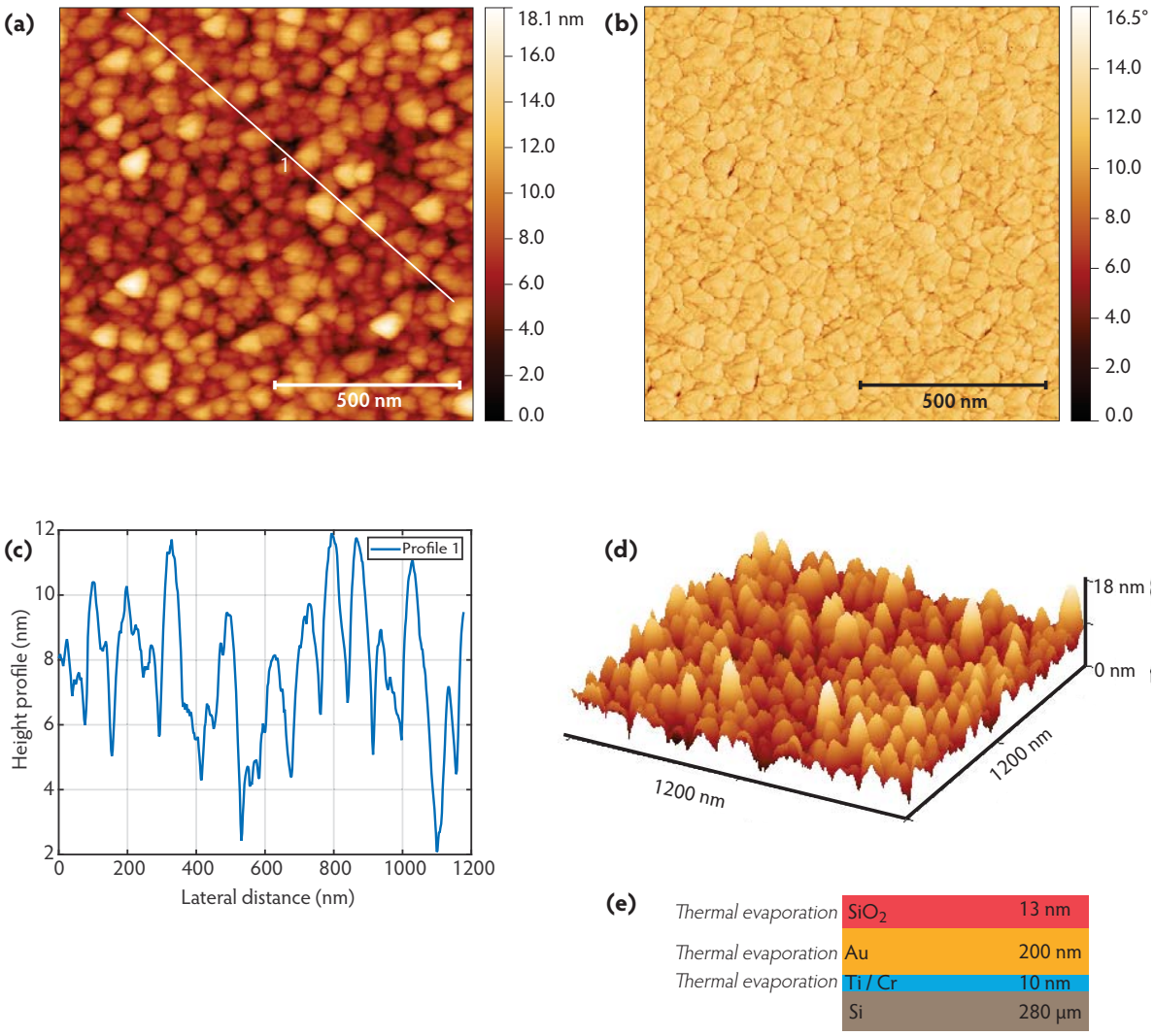

Figure 2.17 *AFM imaging of silica coating*

On a 200 nm thick Au layer, a 13 nm thick film of SiO_2 was deposited by thermal evaporation. The rugosity of the Au surface was 2.6 nm. Figure **(a)** shows the AFM topography image of the surface of the SiO_2 coating. Figures **(b)** and **(d)** are the corresponding phase and 3-D perspective images, respectively. Figure **(c)** shows the height profile along path 1 (marked in **(a)**). The RMS roughness of the SiO_2 was found to be 2.2 nm. Figure **(e)** shows the layers in the sample.

2.5 Conclusion

Lithographic fabrication of nanoscale structures requires addressing many specific issues and overcoming unforeseen challenges. Thin film deposition by evaporation—thermal or electron-beam—can be used for growing metallic layers in our structures. But they cannot be used to deposit materials, such as dielectrics, directly onto individual CdSe/CdS quantum dots as it bleaches them. Dielectric deposition on nanocrystals can be attained by spin-coating ultra-thin polymer films on spatially distributed individual quantum dots. Compatibility with quantum dots, ease of use, smoothness, uniformity, and homogeneity make spin-coated polymer films a better choice than evaporated films.

This page is intentionally left blank.

3 Optical Lithography Protocol and Supercontinuum Laser

We begin this chapter with a description of the plasmonic nanoantenna fabrication protocol. The reason behind choosing this particular protocol, the materials used in it, and the challenges faced in its implementation will be discussed. Most parts of the process are common to the three lithographic techniques that I have developed in my PhD. The process will be described at the beginning of the chapter. The next part of the chapter will expound on one of these techniques—white laser lithography. This was our first successful solution to the problem of deterministically localizing and isolating a quantum dot to serve as an antenna emitter. The next two chapters will elaborate on the other two techniques—electron-beam lithography and LG mode optical lithography—that can serve the same purpose but in a different manner, and increase the application scope of the protocol.

The lithography technique discussed in this chapter is based on in-situ optical lithography, which has been reported by Adrien Dousse of Pascale Senellart's group at Laboratoire de Photonique et de Nanostructures, Marcoussis, France [2]. Cherif Belacel, in his PhD worked (co-advised by Agnès Maître and Pascale Senellart), used in-situ optical lithography to fabricate nanoantennas that used a cluster of nanocrystals as an emitter [3, 8]. The task was achieved by designing a protocol that used in-situ optical lithography on conventional photoresists.

In his fabrication technique [8], Belacel started with a Si substrate on which a 200 nm thick Au film was deposited by physical vapor deposition. Using the same deposition method, a 15 nm thick SiO_2 layer was deposited on the Au film. On the SiO_2 film, clusters of nanocrystals were spin-coated and then another layer of SiO_2 was deposited on them by physical vapor deposition. On this SiO_2 layer, a photoresist layer was spin-coated. Using a low intensity laser and recording the micro-photoluminescence, a cluster of nanocrystals was scanned and selected. The selected region was then exposed to relatively high power laser light to locally develop the photoresist lying above the selected cluster of nanocrystals. Then, using standard lithography techniques, the developed photoresist was etched from the exposed region, and by evaporation, an Au patch was deposited over there. After the lift-off, an operating plas-

monic nanoantenna, that used a cluster of nanocrystals as an emitter, was obtained. The patch size, which affects the emission acceleration and antenna directivity, was varied from 1.4 to 2.1 µm.

But the above mentioned protocol could not be used to fabricate a single photon emitter plasmonic nanoantenna due to the following reason. All photoresists are photoluminescent, which means that when a laser scans a cluster of nanocrystals lying beneath a photoresist, the photoluminescence of the photoresist becomes noise in the real signal of interest (fluorescence of the nanocrystals). However, if the fluorescence signal is more than the photoluminescence of the photoresist and the photoresist is not exposed by the laser fluence, the fluorescing emitter can be scanned successfully. This was the case when the emitter was a cluster of nanocrystals, but when the emitter was a single nanocrystal, the fluorescence signal was comparatively very low. Thereby, a single nanocrystal lying beneath a photoresist could not be scanned. Moreover, in order to increase the fluorescence signal, if the scanning laser intensity was increased, it exposed the photoresist in the entire scanned area, thus making the entire area and the included emitter(s) useless for the lithographic process.

As photoresist lithography, which had worked on a cluster of nanocrystals, could not be used on single nanocrystals, Belacel looked for other solutions. Concerning the choice of lithography resists, a solution was found in the work of Forsén *et al.* [148], who had reported laser lithography on a resist bi-layer in 2004. They had used direct write laser lithography on a resist bi-layer. The resist bi-layer was a stack of two resists: LOR® [149] (a commercial resist) and PMMA, which are not exposed like typical photoresists by visible laser light. Direct write laser lithography techniques allow localized beam-induced surface modification, without using masks. In this sense we can say that in-situ optical lithography is a type of direct laser writing lithography. In our protocol, the choice of resists was inspired by the work of Forsén *et al.*. In the work presented in this thesis, I have used LOR® 3A [150] and LOR® 5A [151] for the lower layer of the resist bi-layer. For the upper layer, we have experimented with several thicknesses of PMMA.

In the visible range, the luminescence of LOR® is less compared to that of a photoresist, and PMMA is almost transparent. Due to this, without exposing or degrading LOR®, individual nanocrystals can be observed beneath a stack of LOR® and PMMA of workable thickness. The nanocrystals can be observed by fluorescence microscopy or by micro-photoluminescence observations that includes laser scanning. When Belacel was improving the method of using a resist bi-layer of LOR® and PMMA, I started my Master's internship with him in 2012, and we characterized the lithographic process in detail by varying parameters and noting their influence by AFM.

Being able to spot individual nanocrystals beneath the resist was a positive development but there were many other challenges that prevented us from making a single photon emitter nanoantenna using laser lithography on the resist bi-layer. The problems were:

1) **Dielectric deposition on individual nanocrystals**: In Belacel's plasmonic nanoantennas, by means of evaporation, a SiO_2 film was deposited on a cluster of nanocrystals. This vapor deposition technique, which worked on a cluster of nanocrystals, could not be used on an individual nanocrystal. It was observed that after physical vapor deposition of SiO_2, the individual CdSe/CdS core/shell nanocrystals stopped fluorescing. The problem has been discussed in detail in section 2.3.

In the first year of my PhD, I solved the problem of dielectric deposition on individual nanocrystals by using ultrathin spin-coated PMMA films. Other polymer coatings, such as polystyrene and polyvinyl alcohol coatings, were also investigated. The polymer coating technique and the characterization of PMMA films has been described in section 2.4. In terms of film thickness and homogeneity, chemical reactivity, baking temperature, and compatibility with LOR®, PMMA showed the best results from all the tested polymers. For this reason, in all our nanoantennas, the dielectric is PMMA.

2) **Survival of nanocrystals under high intensity laser beam**: To burn the resist bi-layer by direct laser writing (specifically, in-situ optical lithography), it was exposed to a high intensity laser beam. This laser exposure that was burning the resist was also photobleaching the nanocrystal just beneath the burned resist. For the burning task, we had used a 405 nm laser in continuous and pulsed wave modes, at different intensities and time durations. The minimum energy required to burn the resist bi-layer was sufficient to photobleach the individual nanocrystals. We had tested nanocrystals from several batches and of different sizes but all of them photobleached before the hole was made on a single nanocrystal. Finding a solution to this problem has been the main work of my PhD. In search of a solution, I have developed three techniques that do the needed. One of them will be described in this chapter and the other two will be described in the subsequent chapters.

3) **Deposition of gold to make the nanoantenna patch**: We found that thermal deposition of a 20 nm thick Au layer on a dielectric material permanently damaged the individual nanocrystals that were lying 15 nm below the deposited Au film. Due to this damage, the nanocrystals did not fluoresce anymore. Complete depletion of fluorescence was not observed when a 20 nm thick Au film was deposited on a cluster of nanocrystals lying 15 nm below a dielectric, but given the reduction in fluorescence after the deposition, it seems that some of the outer nanocrystals of the cluster may have been damaged by the deposition. A solution to this problem was found by studying the survival statistics of individual nanocrystals depending on the separation of the nanocrystals from the deposited Au film, and then choosing an appropriate thickness of PMMA above the nanocrystal. This will be discussed later in section 3.5.

3.1 Optical lithography protocol

Figure 3.1(a) shows the steps involved in the general protocol that is used to realize our plasmonic patch nanoantennas. The thicknesses of the layers in the sample and their deposition methods are depicted in Figure 3.1(b). The deposition and chemical etching steps mentioned here are common to the three lithography methods that we have developed. The steps in the protocol are described below:

1) **First layer of gold**: On a commercial Si crystalline wafer, a 200 nm thick layer of Au is deposited by thermal evaporation. This has been elaborated in section 2.2.

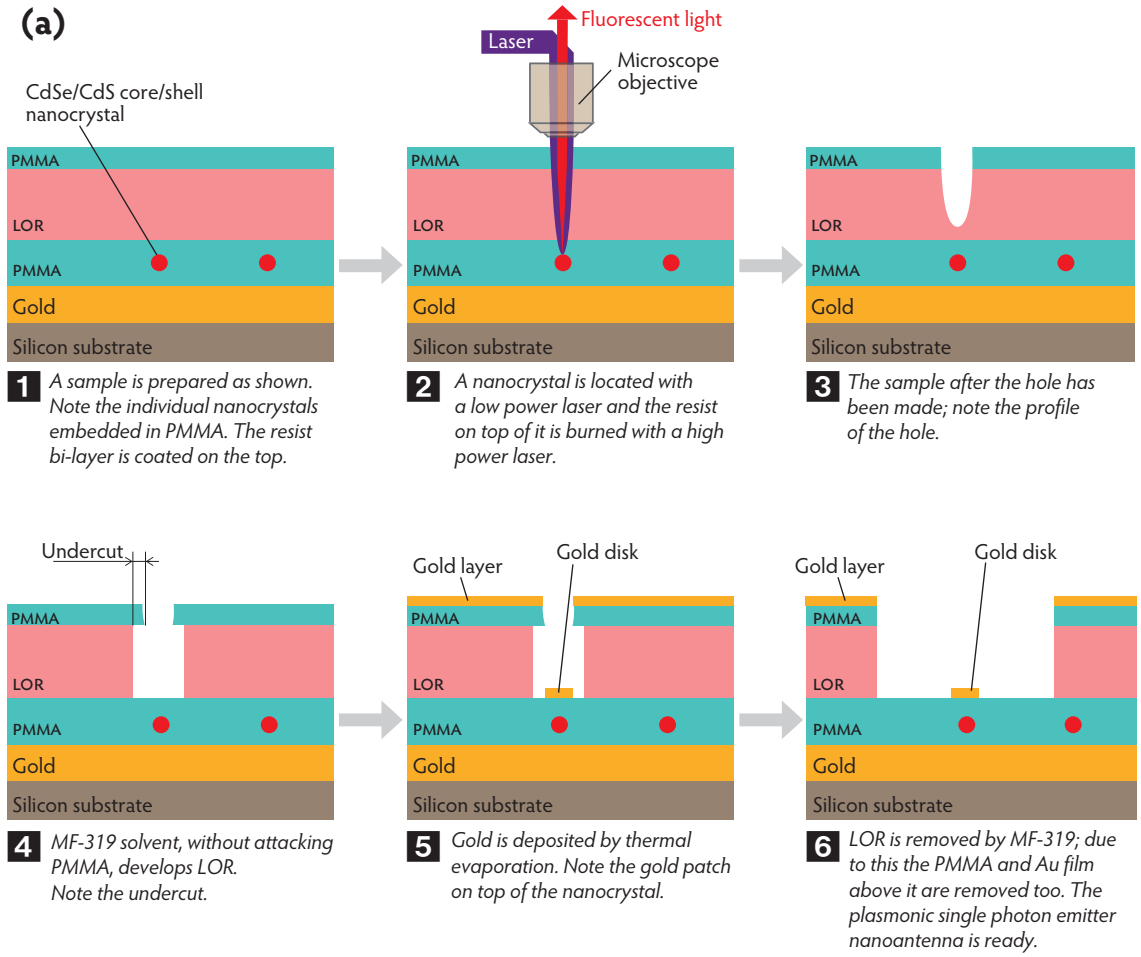

Figure 3.1 *Realization of a single photon emitter plasmonic nanoantenna by in-situ lithography*
Figure **(a)** illustrates the lithographic protocol. Figure **(b)** shows the thickness of the layers and their deposition method. By adjusting the solution concentration, the spin-coated film thickness is varied.

2) **Embedding nanocrystals in a dielectric medium**: On the optically opaque 200 nm thick Au layer, a 10 nm thick film of PMMA is obtained by spin-coating a 0.5% [m/m] solution of PMMA in toluene at 4000 rpm for 40 s. The sample is baked at 170°C for 10 minutes. On this layer of PMMA, CdSe/CdS core/shell nanocrystals are placed by spin-coating a dispersion of nanocrystals in hexane at 4000 rpm for 40 s. This gives us spatially distributed individual nanocrystals, where the distance between neighbouring nanocrystals is at least 5 µm. On top of these nanocrystals, a 15 nm or 35 nm layer of PMMA is spin-coated at

4000 rpm for 40 s. A 15 nm thick film is obtained if a solution of 0.75% [m/m] solution PMMA in toluene is used, and a 30 nm film is formed when a 1.5% [m/m] solution is used. Sections 2.3 and 2.4 discuss these topics in detail.

As PMMA is soluble in toluene, does the solution of PMMA in toluene (used to spin-coat the second PMMA layer) remove (partially or completely) the lower PMMA layer? Using ellipsometry, we have confirmed that when the lower spin-coated film is adequately baked (170°C; 10 minutes) and the PMMA solution in toluene (used to spin-coat a film on it) is spun immediately (in < 2 s) after being placed on the lower film, then the lower PMMA film is not removed by the PMMA solution, and the total thickness of the two PMMA layers is very close to the sum of the two layers deposited separately on two similar substrates under the same conditions.

3) **Deposition of resist bi-layer**: A layer of LOR® [149] is spin-coated on the sample using the following parameters:

Acceleration of spinning:	2000 rpm/s
Maximum speed of spinning:	7000 rpm
Duration of spinning:	50 s

On the samples discussed in this thesis, either LOR® 3A [150] or LOR® 5A [151] was used. For the white laser lithography, we have used LOR® 3A, which gives a thickness of about 300 nm when coated on PMMA. Our other two techniques use LOR® 5A, which gives a thickness of about 500 nm when spin-coated on a layer of PMMA. After depositing the layer of LOR®, the sample is baked[3] at 150°C for 2 minutes.

Then another layer of PMMA is spin-coated on the LOR® surface. For the white laser technique, we spin-coat a 0.5% [m/m] solution of PMMA in toluene at 4000 rpm for 40 s to get a 10 nm thick PMMA film above the surface of LOR® 3A. For the other two techniques, a 2% [m/m] solution of PMMA in toluene is spin-coated to get a 50 nm thick layer of PMMA on the surface of LOR® 5A. After coating PMMA, the sample is baked at 150°C for 2 minutes. At this point, we are at the end of step **1** of Figure 3.1(a).

4) **Scanning nanocrystals and burning the resist above them**: Using micro-photoluminescence, fluorescing nanocrystals on the sample are scanned by a laser. By detecting antibunching on a HBT optical setup, we can confirm if the selected emitter is a single photon emitter (section 1.5.2). To scan a nanocrystal, a low intensity laser is used, e.g., a 405 nm CW laser can scan the emitters with $P \geq 11$ nW. Once the nanocrystal is selected, a high intensity laser beam is used to locally burn the resist on it. This creates a hole in the resist bi-layer. The method will be detailed later. The size and shape of the hole can be varied by changing the burning duration, by defocusing the laser, or by using different

[3] To efficiently remove the solvents and improve adhesion, a lithography resist should be baked at temperatures more than its glass transition temperature. This condition is satisfied when we bake PMMA but not in the case of LOR®. The glass transition temperature of LOR® is about 189°C [152]. LOR® is based on polymethylglutarimide, which has a glass transition temperature between 180-210°C [126]. The manufacturer of LOR® recommends baking it at 200°C for 5 minutes, when using a heating plate (as we do) [153]. Baking the sample at this temperature or higher can damage the nanocrystals. Therefore, we bake the sample at 150°C; this reduces the development time but it gives satisfactory results. The development of LOR® by a developer, and therefore the undercut length, is influenced mainly by the baking temperature and not so much by the baking time [153, 126]. Generally, these resists do not require post-exposure or post-development baking [127].

types of LG modes (e.g., LG_{40}, LG_{20}, etc.). The size and shape of the hole influences the size and shape of the patch. This marks the end of step 2.

5) **Development of LOR®**: Once a hole is created as shown in step 3, such that there is an entrance for a solvent to pass through the top PMMA layer and react with LOR®, the sample is immersed inverted and shaken briskly in a bath of Microposit® MF®-319 for 5–10s. MF®-319 is a commercial developer [154, 155] which, in the mentioned duration, selectively attacks LOR® but not PMMA. Removal of some LOR® by MF®-319 creates an undercut, as shown in step 4. This undercut provides a passage for MF®-319 to react with LOR® even after the Au patch deposition. The length of the undercut is decided by the development time, the processing conditions (baking and spinning parameters), and the type (LOR® 3A or LOR® 5A) of LOR® [126, 152]. For a given development time, the undercut length also depends on the thickness of the LOR® and PMMA layers and the size of the opening in it (through which MF®-319 enters) [152, 153]. Analysis of the developed samples by AFM revealed that a development duration of 5 s was the most appropriate.

6) **Deposition of 20 nm thick gold layer**: By thermal evaporation a 20 nm layer of Au is deposited at a rate of about 0.02 nm/s. The deposition procedure is described in section 2.2. The deposited Au forms a film on the top PMMA layer everywhere on the sample except where there is the hole. Au clusters/atoms go through the hole opening and settle on the lower layer of PMMA, beneath which lies the nanocrystal. This is the end of step 5.

7) **Lift-off**: At step 6, the sample is dipped inverted in a bath of MF®-319 and shaken briskly for 20–90 s. The lift-off time can be varied to some extent. Due to the passage created by the undercut, the solvent enters the developed hole, attacks LOR® and removes it. The removal rate depends on the processing and the type of LOR®. The removal of LOR® removes the PMMA and Au above it as well. In a complete lift-off, all the LOR® is removed from the entire sample. Instead of a complete lift-off, we do a partial lift-off, which removes LOR® from a region that lies within 1–5 μm from the patch. A partial lift-off is equivalent to a complete lift-off if the nanoantenna patch separation from the top Au film is more than 0.3 μm (section 3.6.1) Moreover, because a partial lift-off is carried out in less time than a complete lift-off, MF®-319 has less time to attack the sample. This reduces the chances of removal of the Au patch and the bottom PMMA during the lift-off.

3.2 Burning the resist without photobleaching the nanocrystal

At step 2 of Figure 3.1(a), the nanocrystal is scanned with a low intensity laser, and then the resist bi-layer locally above the nanocrystal is burned using a high intensity laser beam. Burning of the resist results in its evaporation [148] and creates a hole in the resist bi-layer. The depth of this hole should be at least more than the thickness of the upper layer of PMMA, so that there is a passage for MF®-319 to develop LOR® at step 4. The size and shape of the hole in the resist bi-layer (PMMA+LOR®) is mainly controlled by:

- Size of the focused laser spot or defocused laser spot. After focusing a transverse electromagnetic laser mode by a 100× microscope objective with a numerical aperture of 0.8, the laser spot size is about 650 nm. The spot size was found by scanning the focused laser beam with a fluorescing nanocrystal. The focused laser beam spot can be defocused by moving the sample away from the microscope objective. A defocused laser spot is bigger and has a lower energy density, therefore the burnt hole is bigger and takes longer to be formed.
- The laser beam dose, which is decided by its power and exposure duration. We are able to control the light power and the on/off duration of our lasers, which means total control of the laser intensity used to burn the resist bi-layer.

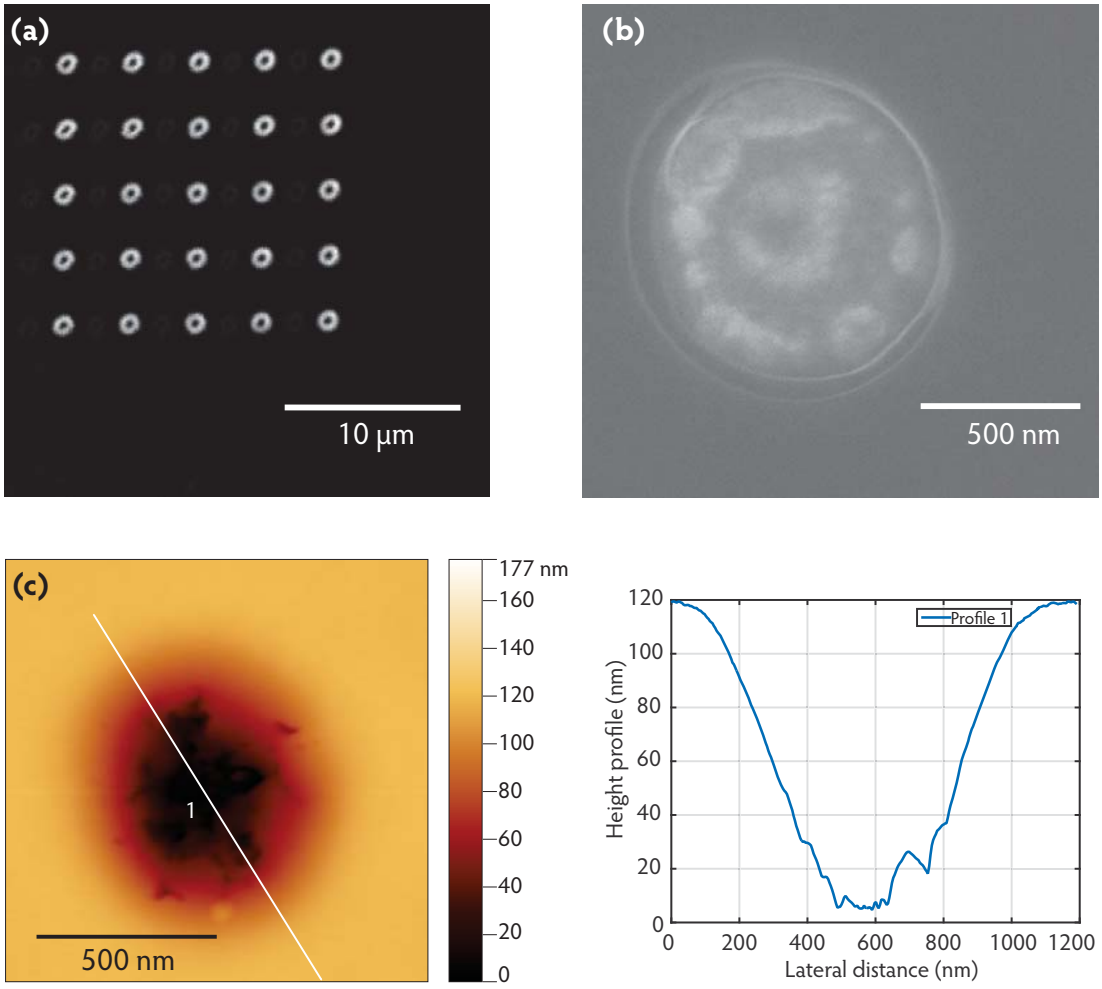

Figure 3.2 *Holes burnt into a resist bi-layer*

Figure **(a)** shows a fluorescence microscopy image of a matrix of holes burnt into a PMMA+LOR® bi-layer using a 405 nm CW laser at 5 mW (exposure time per hole=1.5 s). The sample was held at the focus of the laser by a piezoelectric motion stage, which moved with a typical precision of 1 nm. Figure **(b)** shows a SEM image of a hole burnt into a resist bi-layer by a 405 nm CW laser at 5 mW (exposure time per hole=2 s). Figure **(c)** shows an AFM height image of a hole burnt with a supercontinuum laser into a resist bi-layer of LOR® (diluted) (100 nm) + PMMA (10 nm). The corresponding height profile is displayed on its right, which resembles the Gaussian profile of a laser beam (TEM_{00}). The images in **(a)**, **(b)**, and **(c)** were taken with different samples but the upper resist bi-layer in all these samples consisted of LOR® + PMMA. All the images show the holes before they were developed with MF®-319. Development removes the LOR® resist from the hole, thus giving it a cylindrical profile.

Figure 3.2 shows optical, SEM, and AFM images of holes made by a laser in a resist bi-layer. The images were taken before the development of LOR®, i.e., at step **3** of Figure 3.1(a). When a visible light laser beam is incident on the resist bi-layer, most of the absorption of light is due to LOR® because PMMA is transparent in the visible range. After LOR® is locally heated by the laser beam, it helps in evaporating the PMMA in the region above it. If a layer of PMMA (without any LOR® below) is exposed to the same laser, no hole is made, even if the exposure duration is increased more than a hundred times.

The initial in-situ optical lithography on a resist bi-layer was carried out using a 405 nm PicoQuant diode laser [156]. The power of this laser, just before it enters the microscope, can be regulated between 0–5 mW. This power was measured just before the laser beam entered the microscope, using an Ophir PD300 laser power meter [157]. Using the diode shutter input via a LabVIEW software interface, the laser can be turned on/off for time intervals from 10 ms to more than 100 s. The laser can operate in CW and pulsed modes. To burn the resist bi-layer, it took only 75 ms for this CW laser at $P = 5$ mW. However, by varying all the available options—laser power, burning time, and focusing of the 405 nm laser—we could not succeed in burning a hole without photobleaching the nanocrystal beneath. This inspired us to investigate the problem deeply. We began with the analysis of the absorption spectrum of LOR® and the nanocrystals, with the idea of finding a wavelength at which the nanocrystals absorbed less and LOR® more. By using a laser at this wavelength, a hole could be burned without photobleaching the nanocrystal.

3.2.1 Absorption spectrum of the resist bi-layer

In the resist bi-layer of PMMA+LOR®, the absorption of light is mainly due to LOR®. To measure the spectrum of the resists, a Varian Cary 5000 UV-Vis-NIR spectrophotometer [158] was used. The transmission spectrum was measured, from which the absorption spectrum was estimated.

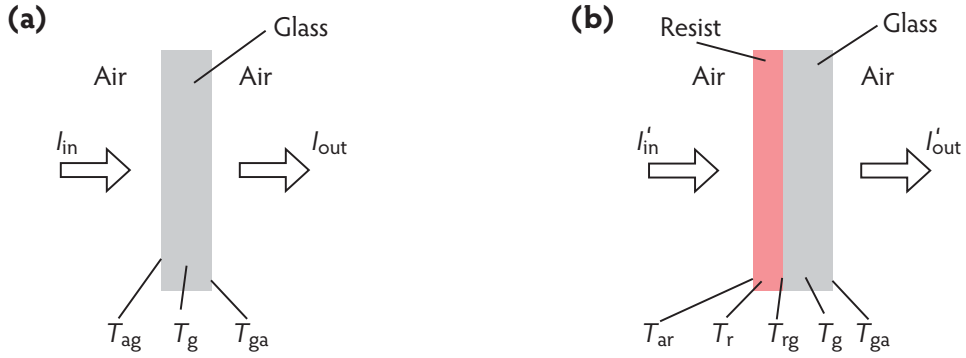

Figure 3.3 *Model to estimate the absorption spectrum*
Illustration **(a)** shows the model used to estimate the product of the displayed transmittances by measuring the incident and transmitted light. After a thick layer of resist is coated on the glass slip, using the information from **(a)**, the absorption of the resist is found using the model in **(b)**.

A thin glass slip was used as a reference and its transmission spectrum was recorded with the spectrometer. The spectrometer sent light at a known intensity I_{in}, and after it passed through the glass slip, it was measured as I_{out}. We chose to work in a wavelength range of about 200–800 nm. Following Figure 3.3(a), we can write:

$$I_{in}\, T_{ag}\, T_g\, T_{ga} = I_{out} \tag{3.1}$$

where T_{ag}, T_g, and T_{ga} are the transmittances of the air–glass interface, glass, and glass–air interface, respectively. We have assumed reasonably that the transmittance of air is 1. At normal incidence, $T_{ag} = T_{ga}$, therefore, from the above equation:

$$T_{ag}^2 \, T_g = \frac{I_{out}}{I_{in}}. \tag{3.2}$$

Then, on the same thin glass slip, a thick film of the resist (either PMMA or LOR®) was coated and it was baked at 150°C for 10 minutes. The transmission spectrum was measured. Following Figure 3.3(b), we can write:

$$I'_{in} \, T_{ar} \, T_r \, T_{rg} \, T_g \, T_{ga} = I'_{out} \tag{3.3}$$

where T_{ar}, T_r, and T_{rg} are the transmittances of the air–resist interface, resist, and resist–glass interface, respectively. We assume that the refractive index of the resist is almost the same as that of glass, which means $T_{rg} = 1$ and $T_{ar} = T_{ag}$. This leads to:

$$T_r = \frac{I'_{out}}{I'_{in}} \frac{1}{T_{ag}^2 \, T_g} \tag{3.4}$$

As a function of wavelength, the values of I'_{in} and I'_{out} were recorded by the spectrometer, and $T_{ag}^2 \, T_g$ can be found from Eq. (3.2). In this way, we estimated T_r. Neglecting the scattering from the resist, we can say:

$$A_r = 1 - T_r \tag{3.5}$$

where A_r is the absorption of the resist. The normalized absorption spectra of PMMA and LOR® are given in Figures 3.4 and 3.5, respectively. For this experiment LOR® 3A was used but the findings are valid even for LOR® 5A because the basic composition all the LOR® A series products is the same [150].

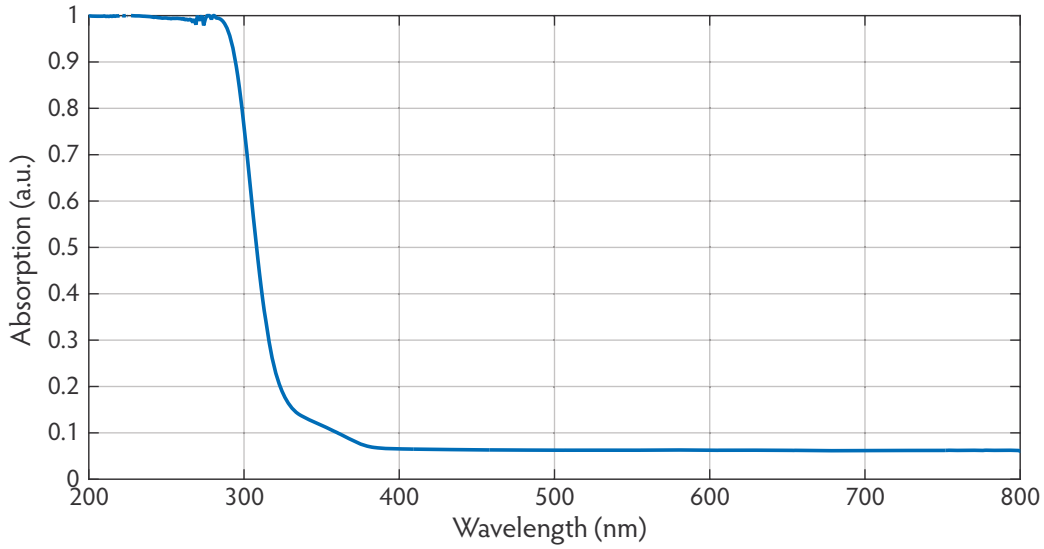

Figure 3.4 *Absorption spectrum of PMMA*

In the visible range (400–700 nm) PMMA shows no significant absorption. It absorbs in the UV but in this region the absorption of nanocrystals is very high too. To prevent nanocrystal damage, we did not pursue burning/exposing the PMMA layer with UV light.

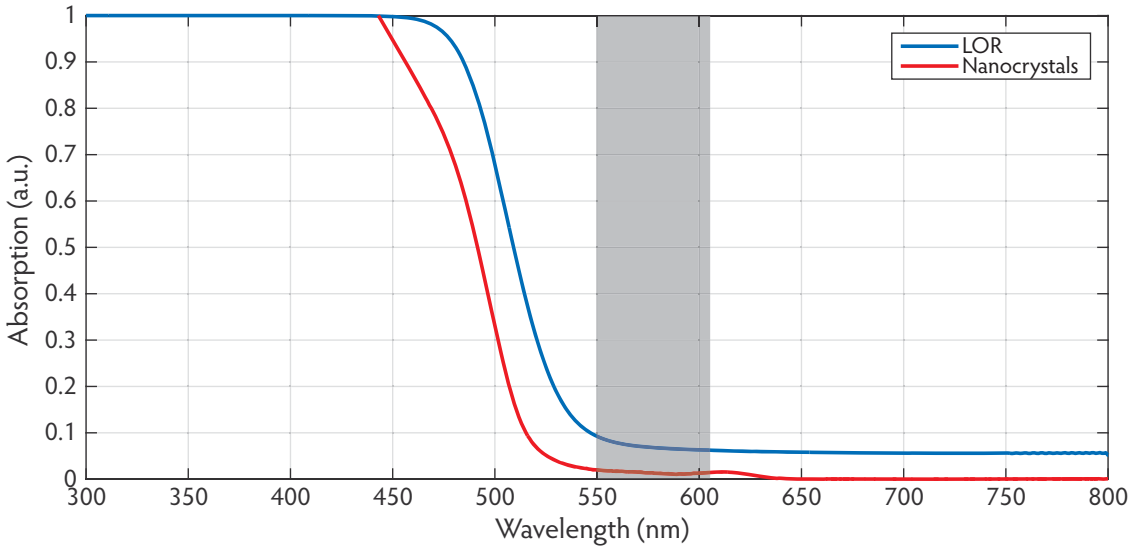

Figure 3.5 *Absorption spectrum of LOR and nanocrystals*

The absorption spectrum of LOR® was obtained as described in this section and the absorption spectrum of the nanocrystals was deduced from the photoluminescence measurements done in solution at ESPCI. Although the two measurements were performed with different apparatus, their comparison gives an idea of the wavelengths where LOR® may absorb relatively more than the nanocrystals, such that the resist may be burnt without photobleaching the nanocrystal beneath. By comparing the absorption spectra of LOR® and the nanocrystals, and selecting laser wavelengths in the range shown in the gray area, we are able to burn the resist without photobleaching the nanocrystal.

From Figure 3.5, it can be said that a 405 nm wavelength laser is very good for exciting the nanocrystals and for burning LOR® as both show high absorption at this wavelength. But due to the high absorption at this wavelength, it was not possible to burn LOR® without photobleaching the nanocrystal. This inspired us to use lasers emitting at other wavelengths.

3.2.2 Supercontinuum laser

In order to tune the laser wavelength for optical lithography, we used a supercontinuum white-light laser. A supercontinuum is generated when high power ultrafast light pulses interact nonlinearly with a transparent material medium and generate light pulses of wavelengths from ultraviolet till near infrared [159, 160]. Usually, a pulsed laser is used to provide ultrafast light pulses and its interaction with a nonlinear medium, such as a photonic crystal fiber, broadens the narrow-band laser radiation into a continuous spectrum, while preserving its spatial coherence [161]. Supercontinuum generation was first reported by Alfano and Shapiro in 1969 [162, 163].

The supercontinuum white-light laser assembly in our laboratory consist of an NKT SuperK EXTREME supercontinuum laser system that gives single mode output in the entire range of 400–2400 nm [164]. Through an optical fiber, laser light from the EXTREME system is fed to a variable bandpass filter (SuperK Varia), which can be controlled by a software interface to choose wavelengths in the range of 400–840 nm [165]. By means of an optical fiber, laser light is passed from the variable bandpass filter to a collimating lens supplied by the manufacturer. After the final collimation, we have recorded emission from 470 to 810 nm. The emitted laser light has a minimum bandwidth (FWHM) < 4 nm and a maximum bandwidth

of 100 nm [165]. With the help of a pulse picker, the repetition rate of the laser can be varied between 2–79 MHz.

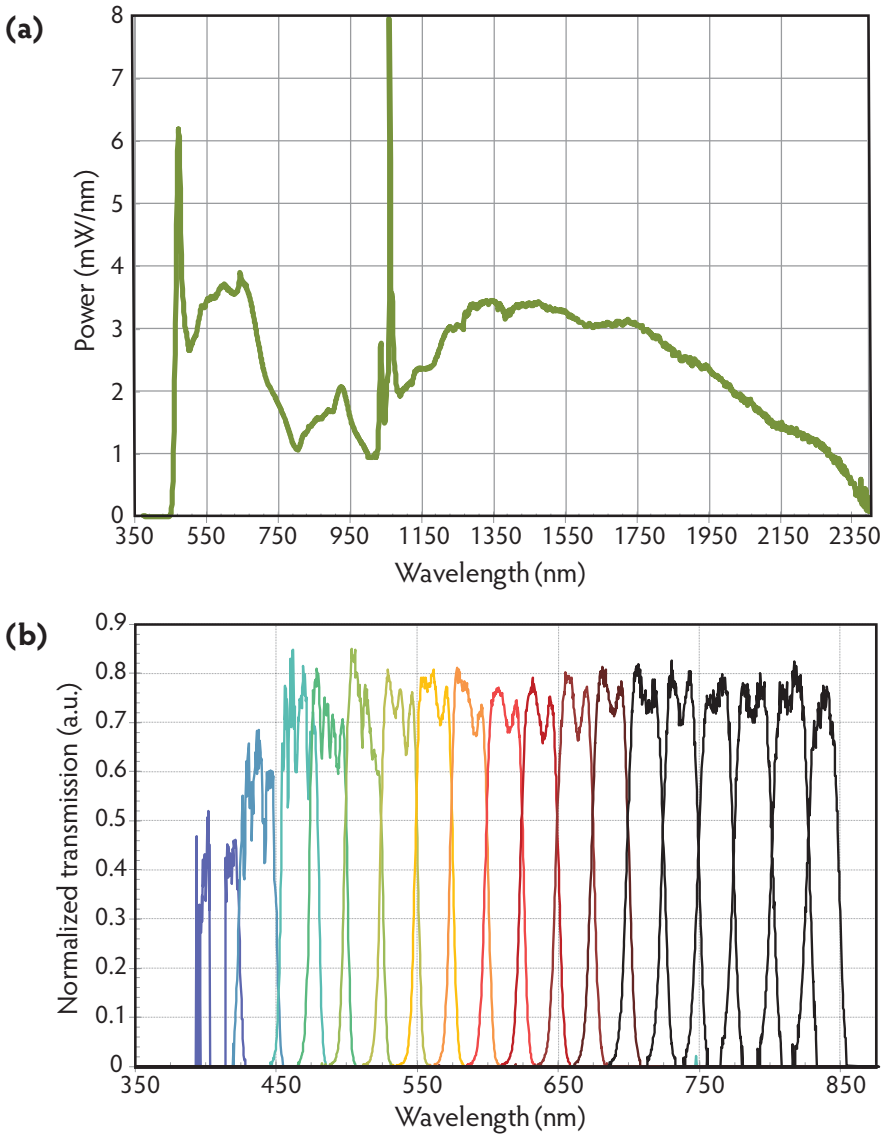

Figure 3.6 *SuperK EXTREME laser system and the Varia filter characteristics*

Figure **(a)** shows the power/nm of the wavelengths emitted at the exit of the SuperK EXTREME system. Note that power levels are not uniform throughout the range. Image adapted from [164]. Figure **(b)** shows a typical transmission spectrum of Varia, which is a variable bandpass filter. Image adapted from [165]. These images do not depict the real output power and wavelengths seen after the final collimator.

Based on the absorption of LOR® and of the nanocrystals, we tested several wavelength ranges to burn the resist bi-layer using the supercontinuum laser. The samples tested for hole-burning were firstly analyzed with optical microscopy (reflection and fluorescence), and if required, the sample was developed with MF®-319 and observed again with fluorescence microscopy. Generally, the holes burned into the resist bi-layer can be seen by reflection and fluorescence microscopy. This is because the holes are usually wider than 600 nm at the top (which is greater than the optical limit of the system), and produce sufficient contrast. But occasionally it may happen that a hole cannot be viewed clearly with the optical microscope.

When such a hole is developed, and if it is a useable hole, then the LOR® beneath the transparent PMMA is removed by the developer. This increases the contrast and makes the hole visible by fluorescence microscopy. For a final confirmation and complete information about a hole (its depth, size, and shape), it is analyzed with AFM. After several tests on numerous samples, the following parameters were found fit for burning the resist bi-layer without photobleaching the nanocrystal beneath:

$$\begin{aligned} \lambda_{min} &= 550\ \text{nm} \\ \lambda_{min} &= 605\ \text{nm} \\ f_r &= 79\ \text{MHz} \\ \%P &= 80\text{–}100\% \\ P &= 18\ \text{mW (measured at 577 nm)} \\ t_{exp} &= 1\text{+}1\ \text{s} \end{aligned}$$

where λ_{min} and λ_{max} are the minimum and maximum limits of the emission wavelength range selected using the supercontinuum laser filter, f_r is the repetition rate of the laser, $\%P$ is the power percentage of the maximum laser power, P is the laser power in the 550–605 nm range measured at 577 nm, and t_{exp} is the time of exposure of the sample to the laser. The choice of the laser wavelength range was obtained by comparing the absorption of LOR® and the nanocrystals (Figure 3.5). The value of λ_{max} was kept as 605 nm because in our optical setup we use a 605 nm dichroic filter to separate nanocrystal fluorescence ($\sim 630 \pm 25$ nm) from the excitation wavelengths.

To burn a hole into the resist bi-layer at a region of interest, it was exposed to the laser beam for two consecutive time intervals, each interval being 1 s long. The value of this exposure is not very precise because the laser exposure onto the sample was managed by a mechanical shutter operated by hand, using a digital chronometer. The laser control software is capable of switching the laser on/off, but after turning on our supercontinuum laser, it takes about 3–5 s to stabilize. To avoid these unmeasured fluctuations in laser light intensity, we turned on the laser for 10–15 s while physically blocking its entrance into the microscope. Then the laser blockage was lifted for about 1 s to let the laser light into the microscope and eventually burn the resist bi-layer. After another 5 s or so, the blockage was lifted again for about 1 s and this finished the resist bi-layer burning process.

As far as photobleaching of the nanocrystal below the resist was concerned, burning the resist in two times was found to be better than burning it continuously in one time. It seems that the nanocrystals are able to better sustain two high power bursts of laser light than one burst which is two times longer, but these are equivalent in heating and evaporating the resist bi-layer.

To make sure that the laser intensity burning the resist bi-layer is the same in every lithography session, we always measure the laser light power just before it enters the microscope. The laser assembly allows controlling the output laser light power. In our lithography protocol, the laser emission is in the range of 550–605 nm. As we did not have the means of measuring the exact total power in the entire wavelength range, we used an Ophir PD300 laser power meter to measure the power at $(550 + 605)/2 = 577$ nm. At this measurement wavelength, the power of the laser in the 550–605 nm range was tuned to 18 mW, and the lithography was carried out. The entire process was performed at 20–21°C.

3.3 Determinstic in-situ optical lithography with supercontinuum laser

This section will describe the protocol of in-situ lithography that uses an NKT SuperK supercontinuum laser. Following the general in-situ optical lithography protocol described in section 3.1 and depicted in Figure 3.1(a), we will summarize all the relevant steps of the protocol when a supercontinuum laser is used for doing the optical lithography.

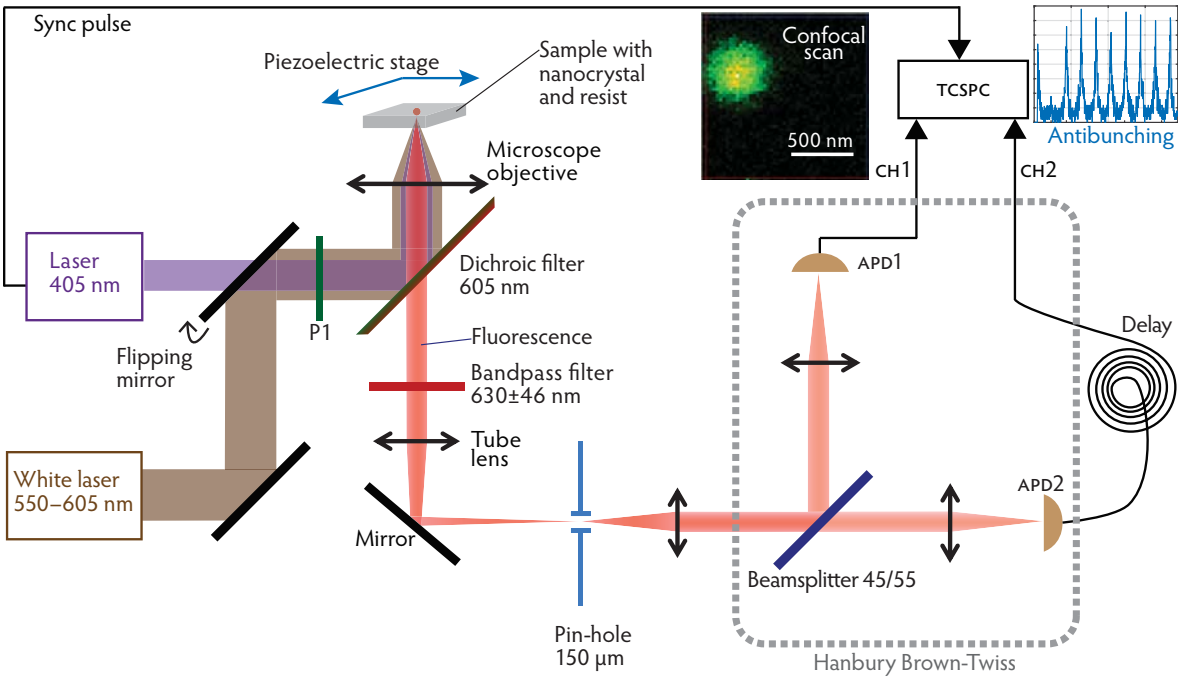

Figure 3.7 *White laser lithography*

A nanocrystal is confocally scanned with a 405 nm laser and then the resist in that area is burnt using a supercontinuum laser emitting between 550–605 nm. The flipping mirror decides which laser beam goes into the microscope. Somewhere near position P1, we place a laser power meter and a removable mechanical shutting system.

1) A sample is prepared as described in section 3.1, after which we are at the end of step **1** of Figure 3.1(a). As far as efficient burning of the resist bi-layer is concerned, we observed that for supercontinuum laser lithography as described in section 3.2.2, LOR® 3A gave better results than LOR® 5A, and for the top PMMA layer, a 0.5% [m/m] solution of PMMA produced more easily burnable films than a 2% [m/m] solution. Therefore, for in-situ supercontinuum laser lithography, the resist bi-layer consists of LOR® 3A and 0.5% [m/m] PMMA solution. A spin-coated film of LOR® 3A is about 300 nm thick, and a 0.5% [m/m] PMMA film is about 10 nm thick,thus giving a total bi-layer thickness of about 310 nm.

2) The sample is scanned with a 405 nm laser. Actually, as shown in Figure 3.7, it is the laser that is scanned by the sample attached to a moving piezoelectric stage. This confocal scan information is provided by the signal from APD1. The left inset image in Figure 3.7 shows a scanned nanocrystal, whose optical size on the confocal scan is the size of the

focused laser spot. We can command the piezoelectric nanoscanner (PI P-713.2SL) to freeze its position at a point, or move with a resolution of 1 nm [166]. In a confocal scan image by our 405 nm laser, the optical size of a fluorescing individual nanocrystal is about 650 nm. In other words, the spot size of the 405 nm laser focused by the 0.8 *N.A.* 100× microscope objective is 650 nm, which is the optically limited size. The physical size of the nanocrystal is about 15–19 nm, which is considerably smaller than its optical size. However, assuming that our nanocrystals are omnidirectional point-like emitters, in the confocal scan of an emitter (or of the laser by an emitter), the emitter should be at the center of the bright spot. With the help of the nanopositioning piezoelectric stage, we can position the sample at the maximum of the focused laser with an accuracy of about ±25 nm. Exciting the selected emitter with the 405 nm laser (usually, in pulsed mode), we can use the signals from APD1 and APD2 to measure photon antibunching, thus verifying if the emitter is a single nanocrystal (inset on the top right of the figure). The emitter lifetime can be retrieved from the antibunching measurement done using a pulsed laser.

We use the 405 nm CW laser for scanning because it generates scans with a higher signal to noise ratio than the supercontinuum laser. If required, even the supercontinuum laser can be used for the same but the scans are usually of lower quality because the lowest wavelength with significant emission is 470 nm, which does not excite the nanocrystals as efficiently as the 405 nm light. Moreover, we have noted significantly more nanocrystal fluorescence damage due to pulsed laser excitation as compared to CW excitation. This is because the peak-power in each pulse if very high.

3) After scanning and selecting a single emitter with the 405 nm laser, the blockage at position P1 (see Figure 3.7) is used to block any laser light from entering the microscope. Then the flipping mirror is placed down to let the supercontinuum laser beam onto the blockage at P1. As mentioned in section 3.2.2, the laser is set to emit at λ_{min} = 550 nm and λ_{max} = 605 nm with a repetition rate of 79 MHz. After the laser has stabilized in 10–15 s, using a laser power meter configured to measure at 577 nm, the power of the laser is set to 18 mW. The microscope objective is moved away from the sample by about 0.3–1 µm. This corresponds to rotating the microscope focus knob by 1/3rd to 1 graduation. The advantage of defocusing is described in section 3.3.2. Then the blockage is removed for 1 s and after another 5 s or so, it is removed for another 1 s. This finalizes the resist bi-layer burning as depicted in step **3** of Figure 3.1.

4) Steps 5–7 of the optical lithography protocol mentioned in section 3.1 are followed, which finally leads to the realization of a single photon emitter plasmonic nanoantenna made by supercontinuum laser lithography.

3.3.1 Aligning the 405 nm and the supercontinuum laser

For positioning the nanocrystal accurately at or near the center of the nanoantenna patch using the protocol mentioned in section 3.3, it is necessary that both the 405 nm laser and the supercontinuum laser are focused as close as possible. On our optical setup, the 405 nm laser beam and the supercontinuum laser beam (emitting at 577 nm) can be aligned such that at the focus of the microscope objective, the centers of the two laser spots are less than 50 nm apart.

Figure 3.8 shows the position of the focused spots of the two lasers. The coordinate origin is the same for both the images. The distance between the centers of the two focused laser spots, d, is about 0.05 µm.

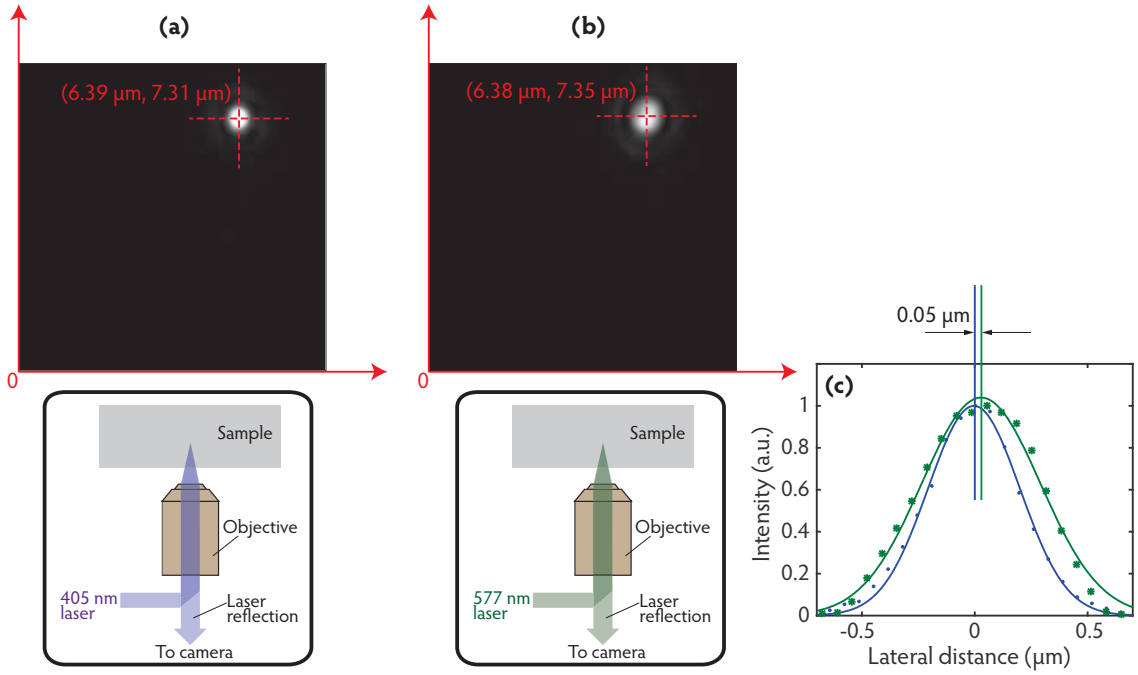

Figure 3.8 *Alignment of 405 nm and 577 nm laser beams*

Figure **(a)** shows the reflection image of a focused 405 nm laser beam spot. With respect to the camera image axis, the position of the center of the laser spot is denoted in red color. The flipping mirror, as shown in Figure 3.7, was flipped to let the supercontinuum laser emitting at 577 nm into the microscope. Figure **(b)** shows the focused laser spot of this laser beam. Comparing **(a)** and **(b)**, we can see that the centers of the two focused laser beams overlap by about ±0.05 µm. The same information is displayed by comparing the Gaussian-fitted light intensity profiles of the two laser spots. The maxima of the 405 nm laser spot (blue curve) and the 577 nm laser spot (green curve) are less than 0.05 µm apart. The schematics below **(a)** and **(b)** show the corresponding measurement configurations.

The supercontinuum laser was set to emit at 577 nm, though it would be better to set the emission from 550–605 nm, which is the real case. For the alignment task, we could not use the light emitted in the entire range of 550–605 nm because even at the lowest possible power settings, the light energy was sufficient to saturate the CCD camera. We did not want to introduce any numerical density or some other kind of attenuator because this could have significantly altered the laser path, especially when a precision of about 50 nm is sought. Therefore we chose to set the alignment with the mean wavelength of the 550–605 nm range, that is 577 nm.

The accuracy of positioning of the blue laser (±25 nm) and the accuracy of aligning the supercontinnum laser with the blue laser (±50 nm). Following the propagation of errors, we can state that the accuracy of positioning the Au patch on the nanocrystal using the supercontinuum laser lithography technique is about 56 nm.

3.3.2 Defocusing the laser for lithography

To bring the nanocrystal at the focus of the microscope objective, the sample is illuminated with blue light (438 ± 12.5 nm) coming from the mercury lamp and filter assembly, and the emitted fluorescence of the nanocrystals is set to the best focus of the eye. Without disturbing the focus, the sample is then excited with a 405 nm laser, and the emitter is scanned. This present focus setting is identical or very close to the focus position of the emitter for the laser. Although our microscope objectives are achromatic or semi-achromatic, generally for different laser wavelengths, the focusing requires some fine tuning. This fine tuning is possible because instead of our eyes or the camera, we use the APD to set the focus, which is very sensitive to the light signal. To do this an emitter is excited with a laser and the emitted fluorescence signal is recorded and reported in realtime by the photodiode. The focusing knob is rotated very carefully till the maximum fluorescence signal is reached. At this point the emitter is at the focus of the microscope objective.

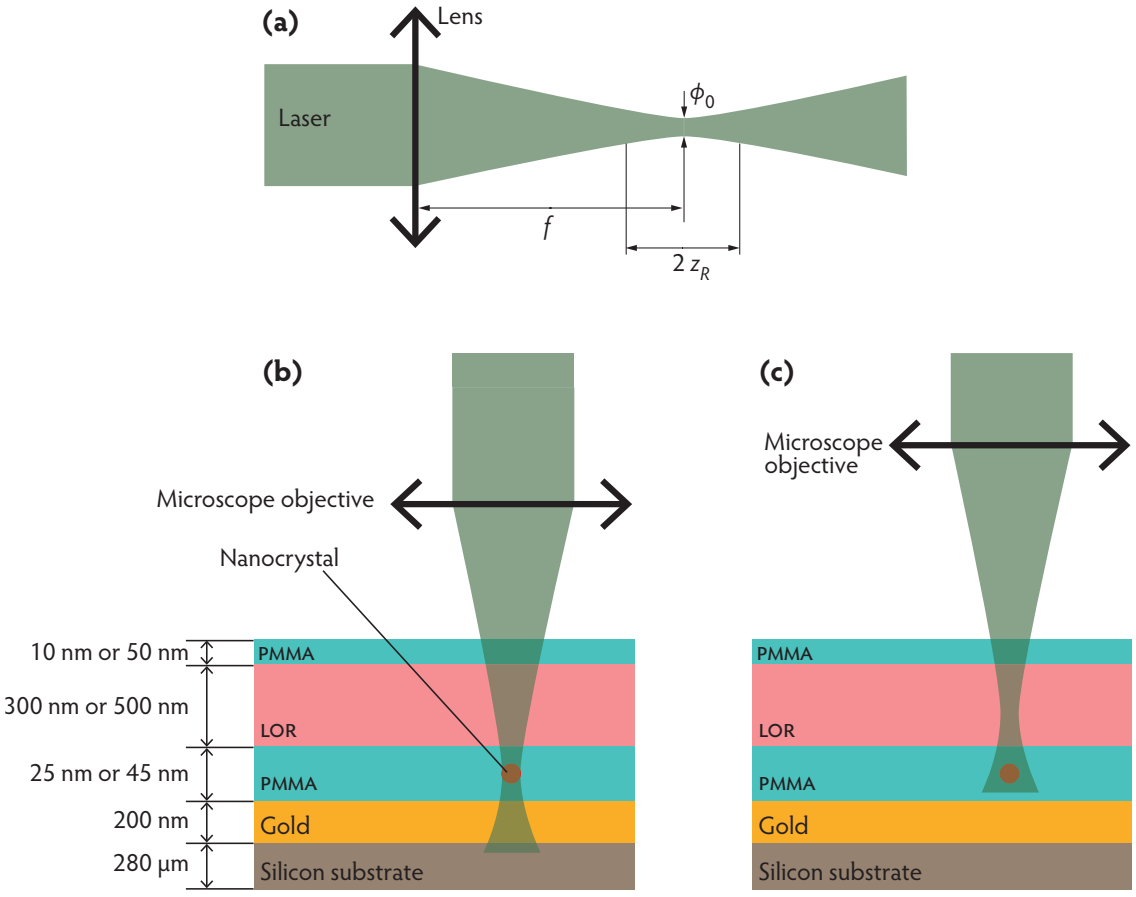

Figure 3.9 *Moving the objective away from the sample when burning the resist*

Figure **(a)** illustrates the focusing of a collimated Gaussian laser beam by a lens. Figure **(b)** shows when the objective is set to focus the nanocrystal emission, and **(c)** shows when it is moved away from the sample to place the focus on the resist to burn it.

As shown in Figure 3.9(a), when a collimated Gaussian laser beam is focused by a lens, the waist diameter of the beam reduces to a minimum size called the spot size ϕ_0. For a strongly

focused Gaussian beam of wavelength λ, where the Rayleigh range z_R is much smaller than the focal length f of the lens, i.e., $z_R << f$, the depth of focus or confocal parameter is [167]:

$$\text{depth of focus} \approx 2z_R \approx \frac{\pi}{2}\frac{\phi_0^2}{\lambda}. \tag{3.6}$$

Figure 3.9(b), illustrates the situation when the emitter is at focus of the laser. At the center of the laser spot is the nanocrystal, which means that the maximum energy of the laser is transferred to the area which has the nanocrystal. This situation is of interest to us when we are looking for the maximum fluorescence signal. For optical lithography, it is better to transfer the maximum laser fluence on the resist rather than the nanocrystal, especially when photobleaching of the nanocrystal is a crucial concern. To reduce the laser fluence on the nanocrystal and to burn the resist better by increasing the laser fluence on it, we move the objective away from the emitter by about 0.3–1 µm, thus focusing on the resist and transferring maximum amount of energy to it. Our choice of this range of motion of the objective is based on practical experience and it may find justification in the notion of the depth of focus and the related variation in laser energy intensity. For a supercontinuum laser emitting at 577 nm, and with a focused spot size of 700 nm, from Eq. (3.6):

$$\text{depth of focus} \approx 1.33\,\mu\text{m}. \tag{3.7}$$

To perform lithography by transferring most energy to the resist bi-layer and not to the nanocrystal, the objective is moved away from the sample (the emitter is defocused). The distance of interest to defocused lithography is (Figure 3.9):

$$\frac{\text{depth of focus}}{2} \approx 0.67\,\mu\text{m}, \tag{3.8}$$

which is within the range of motion of 0.3–1 µm.

By defocusing the laser, we change its focal plane, and therefore control its intensity at particular plane of the resist bi-layer. When a plane is out of focus, the laser intensity at a point on it is lower because the laser spot size is larger. It was found that to burn the resist, the key factor was the laser light energy, i.e., input laser power multiplied by the exposure time (the time for which the area of interest on the sample is exposed to laser light). Following this argument and conducting experiments, we found that by defocusing the laser more and increasing the exposure time, we could make larger holes. In addition to efficient burning of the resist bi-layer, another advantage of the defocusing technique is the ability to control the hole size.

3.3.3 Piezoelectric stage drift

Our optical setup is placed on a self-leveling active vibration isolation system. In our group, we use PI piezoelectric motion (2-D) stages to hold the sample or the microscope objective. With five such stages, it was observed that the piezoelectric stage showed some undesired drift. When the piezoelectric stage was instructed to fix a position, it moved randomly. The rate and direction of this motion vary from day to day. This issue was discussed with the manufacturer and our engineer but it could not be resolved. On my setup, I have used two stages: PI P-714 and PI P-713, and both of them exhibited drifting issues. The movement rate

of the piezoelectric stage has been recorded as high as 60 nm/minute. Figure 3.10 shows a typical example of such motion.

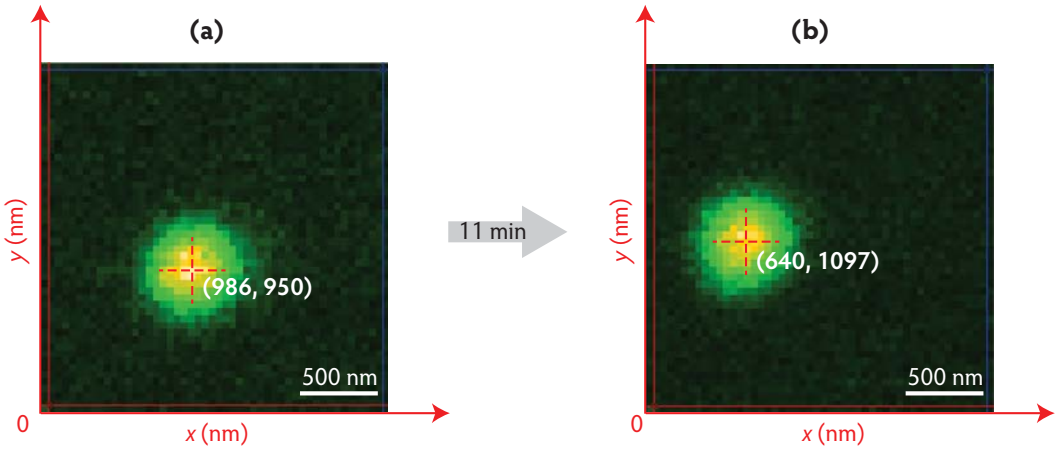

Figure 3.10 *Drifting motion of the piezoelectric stage*

The images are confocal scans of a fluorescing nanocrystal. The fluorescing nanocrystal is shown in artificial colors as a yellow-green diffraction limited spot. The position of the nanocrystal, which is at the center of the spot, is marked by a dashed cross. Image **(a)** shows the confocal scan of a nanocrystal at $t = 0$, and **(b)** shows its confocal scan at $t = 11$ minutes. Ideally, unless commanded, the piezoelectric stage should not move but in this case, the average motion rate was recorded as 34 nm/minute.

In the supercontinuum laser optical lithography protocol, after the confocal scan by 405 nm laser and the selection of a nanocrystal, it takes about 2 minutes to do the lithography with the supercontinuum laser. If the piezoelectric stage drifts by 60–120 nm in this time, the precision with which the nanometric patch (200–2500 nm) can be positioned just above the nanocrystal is affected adversely. This is devastating if we would like to deterministically position the Au patch over the nanocrystal with an accuracy of ~ 50 nm, where it is presumed that the piezoelectric stage does not drift unintentionally.

We tried solving the drift issue by reducing the temperature of the laboratory from 21°C to 17°C and by manipulating the screws attached to the stage, but this did not help. Assuming that the drifting was due to an electronic issue, we let the piezoelectric stage turned on and undisturbed for about 2 hours. Following this when the stage was used for scanning, it was recorded that the drift was about 2 nm/minute, which is insignificant. This solution has always worked so far—before starting the lithographic process, the piezoelectric stage is turned on and left undisturbed for 2 hours or more. It seems that after the piezoelectric stage is turned on and left undisturbed for more than 2 hours, the drift causing signals subside. Consequently, the stage drift almost disappears. It reappears only when the stage is switched on again. The resolution of the drift issue helped us perform more accurate lithography, especially in the cases which required fixing the nanocrystal position for about 2 minutes or more (chapter 5).

3.4 Development of LOR

At step 4 of the lithographic protocol (Figure 3.1(a)), the sample is shaken in a bath of MF®-319 to develop LOR® and create an undercut in the PMMA layer. Figure 3.11 displays three possibilities that may occur after development.

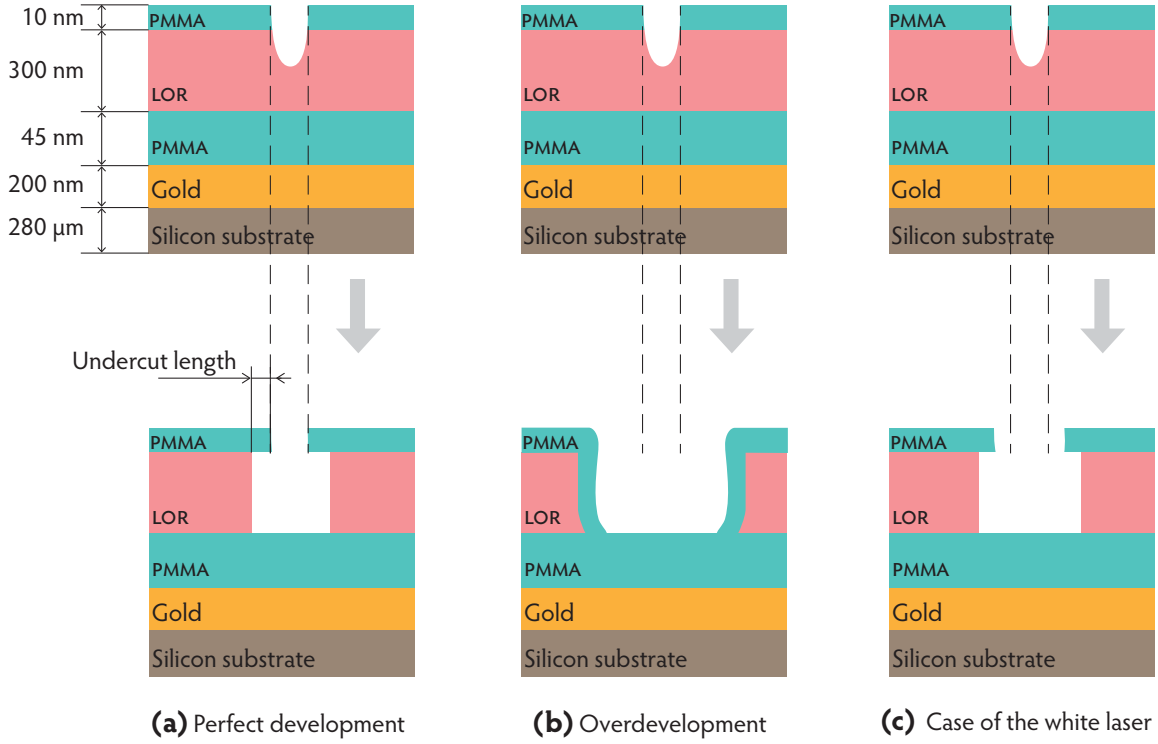

Figure 3.11 *After the development of LOR*

The schematics in the upper row show the situation before the development of LOR®, and the images in the lower row depict three possible situations that may arise after the development. Figure **(a)** displays a case of perfect development. The opening in the PMMA layer, as created by the laser, preserves itself during the development. By the development process, as expected, PMMA is untouched. The size of the Au patch is the same as the size of the PMMA opening made by the laser, as shown in the upper image. Figure **(b)** shows an overdeveloped sample. Long development time or improperly baked resists are the common reasons behind overdevelopment. Here the PMMA layer falls down without creating any undercut. As the passage for the developer to attack LOR® is completely blocked, no lift-off occurs. Figure **(c)** shows a case where the development removes some PMMA from the edges of the opening but leaves an undercut that can allow a lift-off. AFM measurement of the holes before and after the development show that our supercontinuum laser lithography technique results in such structures. The part of the PMMA that does not appear in the undercut length may have fallen down or it may have been removed during the development procedure. The Au patch size is decided by the size of the PMMA opening after development, and therefore in this case, it is bigger than the opening created by the laser (shown in the upper image). In this case both the laser intensity and the development time decide the Au patch size.

In the supercontinuum laser lithography protocol, we use a 10 nm thick PMMA layer on the top. It is easier to burn a thin film than a thick film but a thin film is more likely to fall down or get removed during the development process, thereby rendering the sample useless for the lift-off. As shown in Figure 3.11(c), the development of LOR® following the supercontinuum laser lithography protocol leads to the removal of some PMMA from the opening but still an undercut is made, which makes the lift-off possible. We have many operational plasmonic nanoantennas that substantiate the mentioned. We experimented with a 50 nm thick PMMA film instead of a 10 nm thick film. As expected, more laser intensity was required to burn a 50 nm thick film compared to a 10 nm thick film—this meant more possible damage to the nanocrystals. As in the case of a 10 nm thick PMMA layer (Figure 3.11(c)), the development process removed some PMMA from the sides of the opening even when a 50 nm thick layer

was used. As there was no benefit of using a 50 nm thick PMMA film instead of a 10 nm thick film, and it was easier to burn the latter, we have used a 10 nm thick film in this protocol.

Measurement by AFM and SEM showed that holes burned by the 405 nm CW laser into a resist bi-layer, which had a 10 nm or 50 nm PMMA film on the top, could be developed almost perfectly, as shown in Figure 3.11(a). Figure 3.13 illustrates this through SEM images. White laser lithography leads to the widening of the PMMA opening after the development (Figure 3.12) but as long as it results in a successful lift-off and the opening dimensions can be deterministically controlled by regulating the laser intensity (laser power and exposure duration) and the development time, it is as good as a perfect development. In fact, the possibility of varying the opening size during development is advantageous for obtaining Au patches of deterministically controlled size. Applying this technique, we have developed holes with entrance widths ranging from 200–2500 nm. In other words, we have attained Au patches with diameters from 200 nm to 2500 nm. The rate of flow of the developer through a larger hole is more than the flow rate through a smaller hole. Therefore, to create a significant undercut in a small hole, it requires a longer development time. By systematic study, we were able to find the suitable laser power and exposure duration (that decide the size of the opening in the resist bi-layer) and the corresponding development durations, that allowed us to obtain Au patches of different sizes.

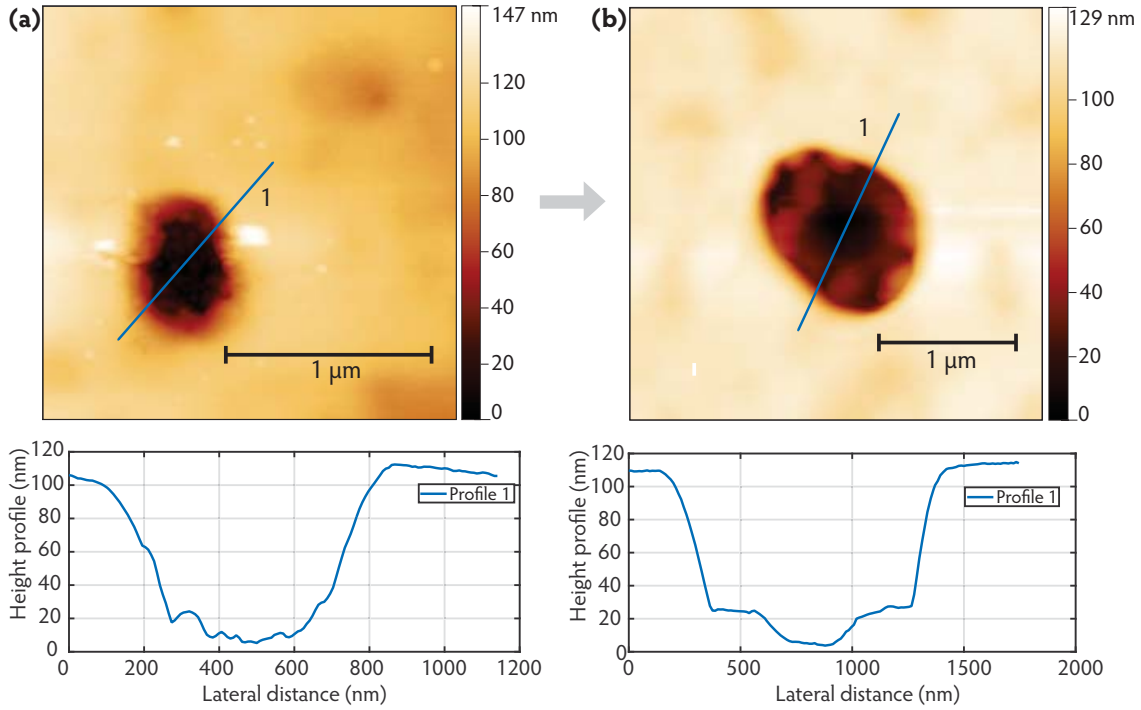

Figure 3.12 *Development of LOR3A (diluted) under 10 nm PMMA*

Figure **(a)** is an AFM image of the hole made by a supercontinuum laser into a resist bi-layer of LOR® 3A (diluted) (100 nm) + PMMA (10 nm). The image below shows the corresponding height profile. Figure **(b)** shows the same hole after being developed with MF®-319 for 10 s. Note the increase in the hole size at the top and the bottom, and the development residue in **(b)** that creates steps on the sides. The fact that we could perform the lift-off around the holes of this sample (Figure 3.21) rules out the possibility of overdevelopment (Figure 3.11(b)). This fact and the increase in hole size suggests that we are in the case of Figure 3.11(c). It seems that during the development, some part of the 10 nm thick PMMA film from the top edge of the hole is removed into the developer solution (thus increasing the entrance size) but an undercut is still created which later allows the lift-off.

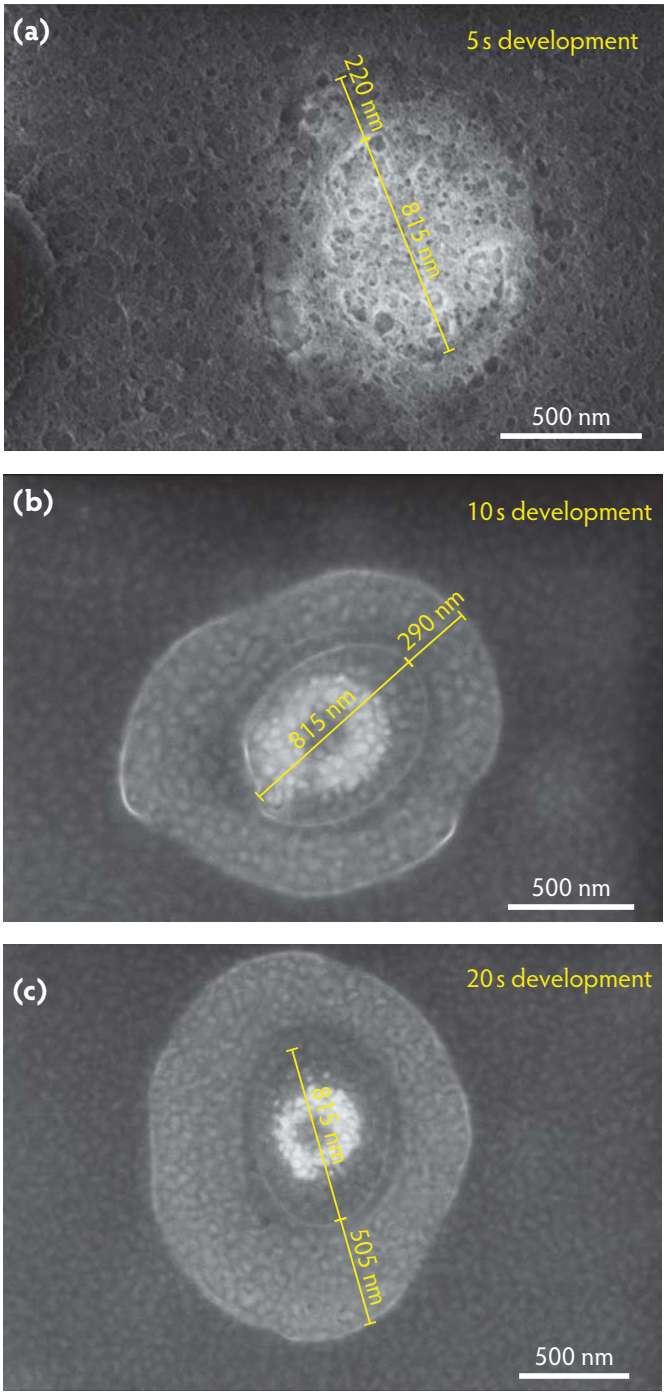

Figure 3.13 *Development of LOR 3A under 10 nm PMMA: 405 nm laser lithography*
On three similar samples that had a resist bi-layer of LOR® 3A+PMMA, holes were burned using a 405 nm laser with the same power and exposure conditions. Figures **(a)**, **(b)**, and **(c)** show SEM images of the holes after the samples were developed with MF®-319 for 5 s, 10 s, and 20 s, respectively. As the resist bi-layer was burned with a 405 nm laser, the opening thus created in the PMMA did not expand after the development—this case is depicted in Figure 3.11(a). The undercut length increased from 220 nm to 505 nm as the development time increased from 5 s to 20 s. Despite increasing the development time, in the presented case, we do not record the PMMA falling down and blocking the development path as shown by Figure 3.11(b). This can be confirmed from the images above and the observation that the sample could be developed further by increasing the time of development.

3.4.1 Fluorescence microscopy view of LOR® development

After a successful development process, as illustrated by step 4 of the lithographic protocol (Figure 3.1(a)), all the LOR® in the concerned area is removed and an undercut is created. The true confirmation of the removal of LOR® after development comes from AFM analysis as depicted in Figure 3.12. The creation of an undercut can be confirmed if a successful lift-off takes place. In case the undercut is not created, in the following step, the depositing Au forms a continuous film, which prevents the solvent from doing a lift-off. It would be possible to image the undercut, observe its shape, and measure its length by imaging a tilted sample with SEM [152, 126].

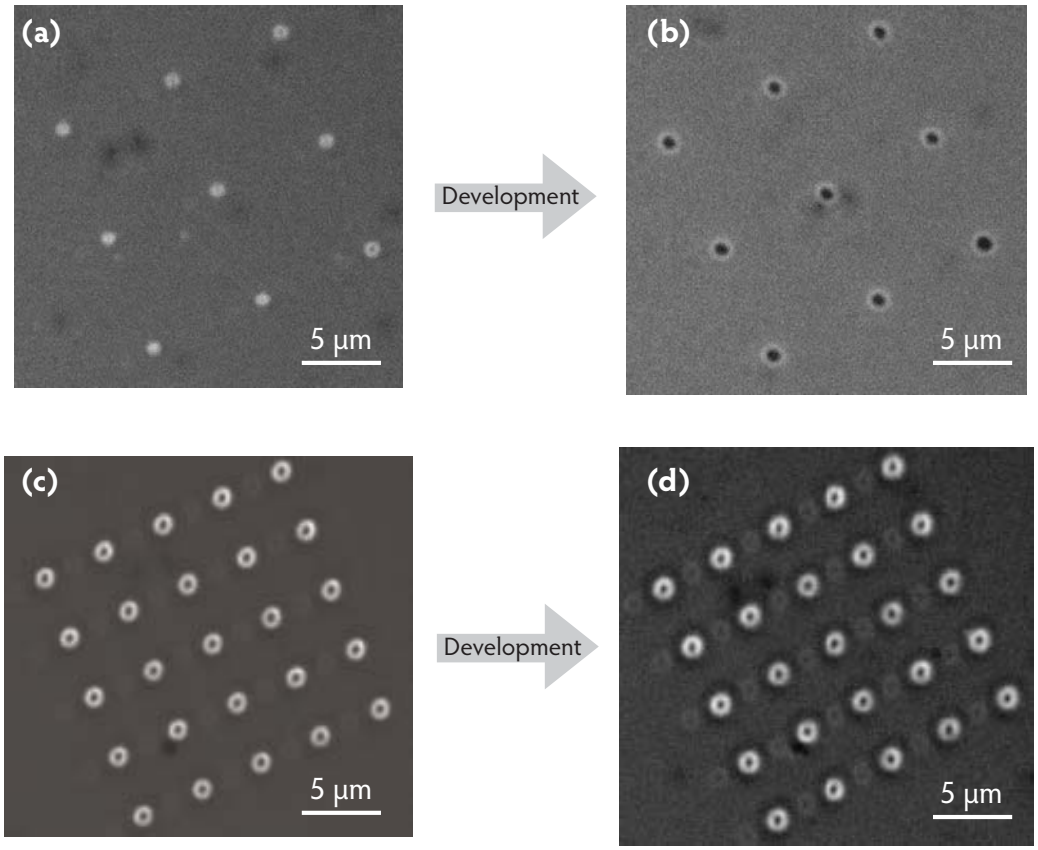

Figure 3.14 *Fluorescence images showing development*

In two different areas of a sample, the resist bi-layer was burned using the supercontinuum laser as shown in **(a)** in one area, and in the other area, as shown by **(c)**, the 405 nm CW laser was used to burn the resist bi-layer. The sample was immersed in a bath of MF-319® for 5 s for development. Figures **(b)** and **(d)** show the areas of figures **(a)** and **(c)**, respectively, after development. As depicted in **(b)** and **(d)**, the development of LOR® changes the contrast at the boundaries—which is a fluorescence microscopy confirmation of development. The change in contrast is more pronounced when the sample is viewed by eye in full colors. Our CCD camera captured only black and white images, therefore full contrast cannot be presented here. We note that after development, the holes burned with the 405 nm laser preserve the entrance diameter, whereas the supercontinuum laser holes widen.

Though AFM and SEM analysis gives accurate information about the development, these imaging techniques are time consuming, and moreover, in the usual experiments, precise information about the development such as the undercut length and shape are not required—it is

sufficient to know whether the development process worked or not. When we started working with the development of LOR®, we noted that using fluorescence microscopy, it was possible to confirm whether the development was successful or not. To validate the mentioned, we took a few samples that showed signs of successful development when viewed with fluorescence microscopy. These samples were then imaged with AFM and the AFM images confirmed that the development had worked. After this result, we have only used fluorescence microscopy to note the development unless there was reasonable doubt that demanded substantiation by AFM analysis. This rapidity and ease of fluorescence imaging to convey information about the development process was timesaving.

Figure 3.14 shows how development can be noted by fluorescence microscopy. The direction of development of LOR® extends outwards from the hole boundary. The development of LOR® results in its removal from the developed area, which changes the luminescence properties of the developed area and this serves as information about the development when the sample is viewed by fluorescence microscopy. Figure 3.14 shows that the development process results are different for the holes burned by the supercontinuum laser and the 405 nm laser. The fluorescence images of Figures 3.14(a) and (b), and the AFM images of Figures 3.12(a) and (b), verify that the development process results in widening the holes in the resist bi-layer when they are burned with the supercontinuum laser. The fluorescence microscopy images of Figures 3.14(c) and (d), and the SEM images of Figures 3.13(a), (b), and (c), suggest the entrance burned by the 405 nm CW laser does not widen after development.

The results discussed above show that the supercontinuum laser (emitting at 550–605 nm) burns the resist bi-layer differently than the 405 nm CW laser. This seems to be because of the following factors: 1) the laser wavelengths are different, and 2) the burning durations are different (very short for 405 nm laser and longer for the supercontinuum laser)—the burning duration depends on the laser wavelength and power.

3.4.2 Is PMMA attacked by the developer?

Our lithographic protocol (Figure 3.1(a)) requires the sample to be immersed in a bath of MF-319® at step **4** for development, and at step **6** for the lift-off. The solvent MF-319® attacks LOR®. Does it attack PMMA? We confirmed that PMMA is not attacked by MF-319® at the development step (5–10 s) or during lift-off (20–60 s). In fact, we have recorded that a 10 nm thick PMMA film is not attacked by MF-319® in 8 minutes, which is much longer than the time required for development or lift-off. As a 10 nm thin PMMA layer is not attacked by MF-319® in 8 minutes, it can be said that during the development and lift-off steps, the PMMA layer in which the nanocrystals are embedded is not damaged and its thickness remains the same. The thickness of this layer affects the SPP coupling and therefore the nanoantenna operation.

To test if PMMA was attacked by MF-319®, a usual sample, as shown in Figure 3.1(b), was prepared. The upper bi-layer on this sample consisted of LOR® 3A (300 nm), and on top of this layer was a 10 nm thick PMMA layer. The nanocrystals on this sample were observed with fluorescence microscopy. Into the upper resist bi-layer on this sample, a 3×3 matrix (similar to the one shown in Figure 3.14(a)) was burned using a 405 nm laser. It should be noted that laser light can burn holes into the resist bi-layer only if LOR® is present. As PMMA does not absorb the 405 nm light, it does not contribute directly to hole burning. After the optical lithography, the sample was put in a bath of MF-319® for 8 minutes and then washed with

water and dried. By observing the sample with a fluorescence microscope, we could observe the fluorescing nanocrystals. This meant that the 8 minute attack of MF-319® on the sample did not attack the lower layer of PMMA (25 nm) in which the nanocrystals were embedded. Near the 3×3 matrix of holes, we observed a lot of development and in the developed areas, we could see the fluorescing nanocrystals. In an undeveloped area, using the laser, we could make holes in the resist—this confirmed the presence of LOR® 3A in the undeveloped areas. After exposing the sample for 8 minutes to MF-319®, LOR® could remain intact only if was protected by the 10 nm thick upper PMMA layer. This concluded that during the time for which the sample was in contact with MF-319®, PMMA on the sample was not attacked.

It should be pointed out that deep cuts or cracks on the sample serve as entrances for MF-319®, and therefore we have avoided such unwanted entrances. When the sample is immersed in the MF-319®, the liquid developer can enter from the uncovered edges of the sample. We ensure that the edges of the sample are sealed during the spin-coating process. During the spin-coating procedure, the entire sample is covered with the PMMA solution, such that the solution overflows the sample edges. In this way we are sure that after the sample is spun, there is a protecting layer of PMMA at the sides of the sample.

3.4.3 Improving the development of LOR®

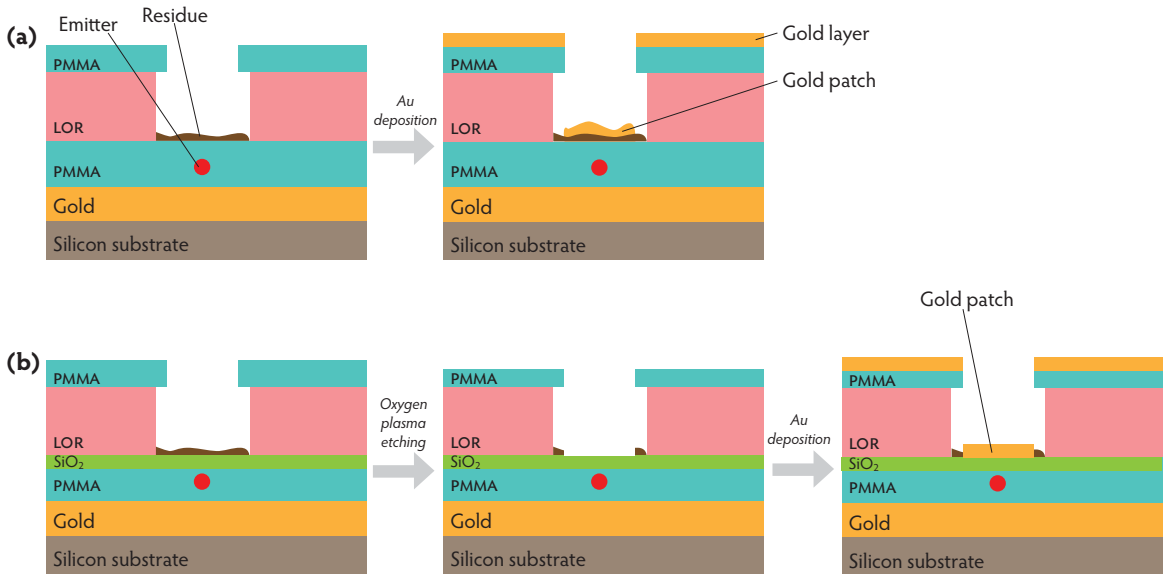

Figure 3.15 *Improving the development process by removing the residue*

Figure **(a)** shows the regular development process that can leave some resist residue, which causes the patch to be unevenly and inappropriately placed above the nanocrystal. Though oxygen plasma etching can remove the resist residue, it can even remove the PMMA covering the nanocrystal. This is avoided by depositing a layer of SiO_2 above the PMMA covering the nanocrystal as depicted in **(b)**. Now oxygen plasma etches the residue without damaging the nanocrystals. In this way, more uniform and appropriately spaced antenna patches can be deposited.

The development of LOR® may leave some residue, which leads to the deposition of a unevenly spaced and nonuniform Au patch. This may affect the antenna performance, and if worse, the extra thickness introduced by the residue can destroy the SPP coupling. The situation is illustrated in Figure 3.15(a). As the residue is a hydrocarbon compound, it can

be removed by oxygen plasma etching [168]. But with this method we risk removing the PMMA (also a hydrocarbon resist) covering the nanocrystal. This has two drawbacks: 1) Plasma etching removes the dielectric covering the nanocrystal, and 2) after the removal of the PMMA on the nanocrystal, the nanocrystal comes in direct contact with the charges in the plasma, which can damage it.

The above mentioned drawbacks can be overcome by depositing a thin film of SiO_2 above the PMMA layer covering the nanocrystals, as described in section 2.3. The thickness of this PMMA layer covering the nanocrystal can be reduced such that the total thickness of the PMMA + SiO_2 layer is as required. In addition to SiO_2, other non-hydrocarbon dielectric materials like ZnS, YF_3, and Si_3N_4 can be used as well. These materials are not attacked by the oxygen plasma and the development residue is etched without damaging the dielectric spacer above the nanocrystal. Though some of the upper PMMA layer (which creates the undercut) is etched by the oxygen plasma, this does not pose a problem if its thickness is about 30 nm or more. To follow this method, we can use an upper PMMA layer of 50 nm thickness. As shown in Figure 3.15(b), the use of oxygen plasma to etch the development residue should result in more flat and uniform patches.

3.5 Deposition of gold on nanocrystals embedded in PMMA

Our plasmonic patch nanoantenna (Figure 1.2) requires the nanocrystal to be embedded in a dielectric, which in our case is PMMA. Above this sandwiched nanocrystal, a gold patch is deposited at step **5** of the lithography protocol (Figure 3.1(a)). As described in section 2.2, the Au deposition is carried out by means of thermal evaporation.

In section 2.3, it has been discussed how physical vapor deposition of a dielectric material, such as SiO_2, ZnS, and YF_3, directly on individual nanocrystals was damaging them permanently. When the same nanocrystals were coated with a PMMA layer of about 10 nm thickness, and then SiO_2 was deposited on them, no nanocrystal damage was recorded.

As expected, after covering or embedding nanocrystals in a layer of PMMA, or PMMA + SiO_2, we have never recorded any quenching. In fact, covering a nanocrystal with PMMA protects it from oxidation, thus increasing its life as a fluorophore. When a fluorophore (such as a quantum dot) is placed very close to a metal (e.g., Au) surface, quenching effects may reduce its fluorescence [169, 68]. If the metal–fluorophore distance is increased, the quenching effects subside, and after a certain distance, they disappear completely. When quantum dots of sizes less than 10–15 nm are placed directly on a Au surface (Figure 2.5), the quenching is very pronounced, such that almost none or very dim fluorescence can be observed [85]. In the case of the quantum dots (ϕ = 15 – 19 nm) that we have used as antenna emitters, the quenching effects are less pronounced because the large size of the shell increases the effective Au–nanocrystal distance. For all the CdSe/CdS core/shell nanocrystals that we have tested, we found that a 10–15 nm thick PMMA film spin-coated on the Au surface was sufficient to prevent any noticeable quenching. The diameter of these spherical nanocrystals from different production batches varied from 5–25 nm.

If the separation distance between the bottom Au surface and the Au patch is increased more than 50–60 nm (Figure 2.1), the SPP coupling is reduced. Given the size of the nanocrys-

tals, we decided to work with a 25 nm separation. To attain this, as described in section 3.1, using a 0.5% [m/m] solution of PMMA in toluene, a 10 nm thick PMMA film was spin-coated on a 200 nm thick Au surface. After baking the sample and spin-coating individual nanocrystals (ϕ = 15–19 nm), another 15 nm thick layer of PMMA was spin-coated using a 0.75% [m/m] solution of PMMA in toluene. Reasoning that if a 0.5% [m/m] PMMA solution coating could protect the nanocrystals from SiO_2 evaporation damage, then a 0.75% [m/m] PMMA solution coating should prevent them from similar damage that could occur when depositing Au by evaporation. But results showed otherwise. Following the Au deposition on nanocrystals embedded in a stack of 10+15 nm PMMA, we attained the structure of Figure 3.16(c). In this structure, none of the nanocrystals could be observed fluorescing. Usually, with a CCD camera acquisition time of 50 ms, we are able to detect significant fluorescence, but in this case, even with acquisition times as high as 8 s, no fluorescence could be observed. A laser is more suited for scanning fluorescent emitters but these emitters could not be scanned even with a 405 nm CW laser. The deposition was carried out at 0.02 nm/s with the Leybold Univex 300 thermal evaporation system at INSP. On similar samples, we carried out the deposition at different rates (0.01–0.3 nm/s), under better vacuum conditions, using thermal and electron beam evaporation, but the result was the same—the nanocrystals didn't fluoresce following the deposition.

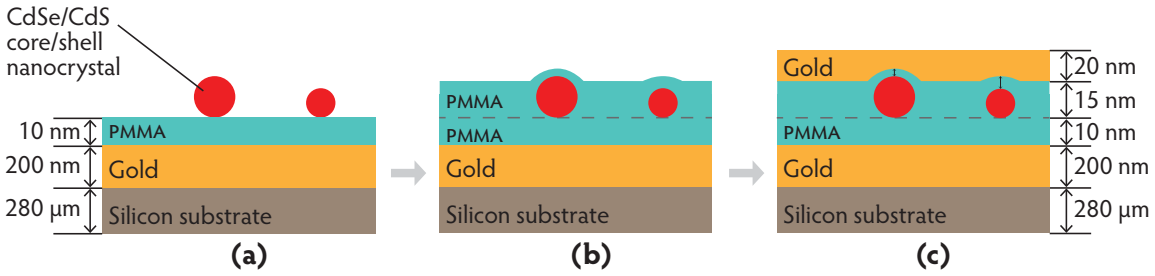

Figure 3.16 *Gold deposition on sandwiched nanocrystals*

Figure **(a)** shows the sample after spin-coating nanocrystals on a PMMA film. Then a drop of 0.75% [m/m] PMMA solution in toluene is placed and after spin-coating it, the sample is shown by illustration **(b)**. The PMMA film thickness on the nanocrystal top surface is very likely different from the film thickness on the lower PMMA substrate. This difference has been pointed out in the figure. By thermal evaporation, a 20 nm thick Au film is placed on the top PMMA film as shown in **(c)**. In figure **(c)**, the distance between the nanocrystal surface and the Au film is shown by the two arrows. It is very difficult to comment on this distance, especially when the shape and size of the spin-coated nanocrystals varies.

If a 10 nm PMMA film could protect these 15–19 nm thick CdSe/CdS core/shell nanocrystals from SiO_2 deposition (section 2.3), then why couldn't a 15 nm PMMA film protect the nanocrystals from Au deposition? In an experiment, we prepared a few samples as shown in 3.16(b). On some of them we deposited Au by evaporation, and on the others we deposited SiO_2 by evaporation. The deposition rate and temperature were kept the same in both the cases. After the deposition of SiO_2, we could observe fluorescing individual nanocrystals on all samples, but on the samples on which Au was deposited, no nanocrystals were found fluorescing. Following this 20 nm thick Au deposition, we were unable to collect the fluorescence signal even with an acquisition time of 10 s. Was this severe reduction in fluorescence due to quenching or some other sort of internal damaging of the nanocrystals during the Au deposition? We will analyze this question in the coming paragraphs.

The quartz balance in the deposition chamber informs us about the average rate of film growth but it does not provide any information about the charge and size of the depositing clusters. Comparing the AFM images of the surface of a 20 nm thick Au film in Figure 2.7 with the surface of a 13 nm thick SiO_2 film, it seems that the grain size is almost the same in the two cases. But this may not imply that the size of the depositing clusters is the same. It has been shown that charged clusters of Au are generated during its thermal evaporation [118]. In the absence of information about charges on clusters, their momentum, and the dynamics at the deposition interface, it is difficult to comment further. However, we are certain that when the nanocrystals are placed near a Au film, their fluorescence quenches, whereas this is not the case when they are placed near SiO_2 films. Moreover, unlike a SiO_2 film, a 20 nm Au film is lossy, which means that a part of the fluorescence of the nanocrystals is absorbed by the film. A 20 nm thick Au film placed on a transparent material like glass gives a bluish tint when looked through.

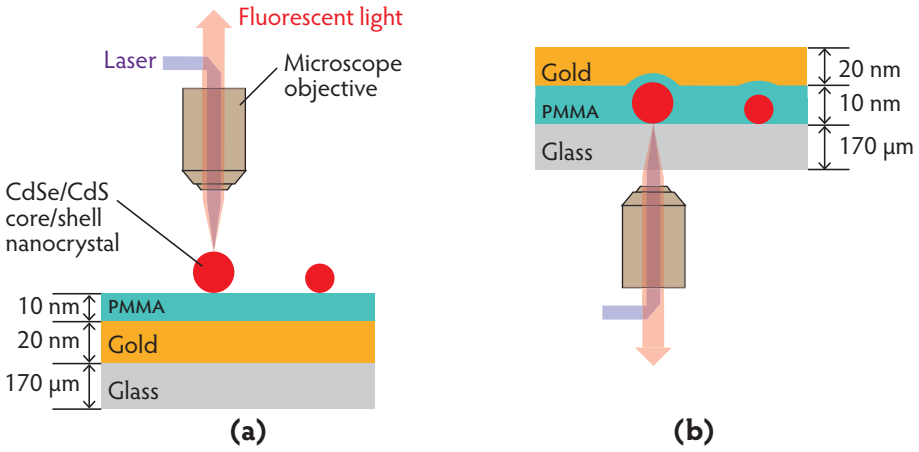

Figure 3.17 *Nanocrystals above and below 20 nm thick gold*

The sample of figure **(a)** was made by spin-coating nanocrystals on a film of PMMA, and the sample of figure **(b)** was made by spin-coating PMMA on nanocrystals, and then evaporating Au on it. Due to a smaller nanocrystal–gold separation and a larger surface area closeness, fluorescence quenching is more pronounced in **(b)**.

We have mentioned that our 15–19 nm thick nanocrystals do not show quenching when placed 10 nm away from a Au surface. As illustrated in Figure 3.16, a PMMA solution that forms a 10 nm thick film when spin-coated on a Au surface, does not give a film with the same thickness on the nanocrystal top. This nanocrystal–Au film distance decides the extent of quenching. Moreover, the former situation (Figure 3.17(a)) is quite different from the latter (Figure 3.17(b)). In an experiment we took a glass slip and deposited a 20 nm thick Au layer on it by thermal evaporation. Then using a 0.5% [m/m] solution of PMMA in toluene, a 10 nm thick PMMA film was spin-coated on it. On top of this layer, nanocrystals were spin-coated and their fluorescence was observed as shown in Figure 3.17(a) . On another glass slip, nanocrystals were spin-coated, and on them a 0.5% [m/m] solution of PMMA in toluene was spin-coated. Then a 20 nm thick Au film was thermally evaporated on it and the sample was observed by fluorescence microscopy as shown in Figure 3.17(b). By positioning the microscope objective below the sample, we avoid losses that the fluorescent light would have incurred if it had to pass through the 20 nm thick Au film. As the separation between

the nanocrystal and the Au surface is less and the surface area proximity is more (the Au film covers the nanocrystal top) in the sample of Figure 3.17(b), the fluorescence quenching is more. If nanocrystals are spin-coated on a Au surface, a particular nanocrystal touches the Au surface at one or a few points. Whereas when Au is deposited by evaporation on a nanocrystal, the depositing clusters cover most of the area of the nanocrystal, thereby creating many contact points. Consequently, quenching in more pronounced in the latter case.

3.5.1 Conclusion

SiO_2 vapor deposition on individual nanocrystals embedded in PMMA did not reduce their fluorescence but they stopped fluorescing when a 20 nm thick Au film was deposited on them under similar conditions. The complete loss of fluorescence after Au vapor deposition could be due to quenching, or by some other mechanisms that occur during deposition and damage the nanocrystals. Both of these issues can be avoided by using a thicker layer of PMMA above the nanocrystals. A thicker layer of PMMA above the nanocrystals can protect the nanocrystals better during the vapor deposition process, and it prevents fluorescence quenching by increasing the effective nanocrystal–Au film distance. The results of the next section suggest that this reduction in nanocrystal fluorescence following Au vapor deposition is due to quenching.

3.5.2 PMMA thickness to keep nanocrystals observable after Au deposition

We have described how Au deposition on nanocrystals (sandwiched in PMMA) reduced their fluorescence. To solve this problem, the effective thickness of the PMMA layer between the nanocrystal and the upper Au film was increased by spin-coating higher concentration PMMA solutions on the nanocrystals. By studying the effect of 20 nm thick Au film deposition on nanocrystals embedded between PMMA films of different thicknesses, we solved the problem of Au vapor deposition.

Four samples were prepared as described in section 3.1 with different thicknesses of the top PMMA layer. The materials stacked in these samples were:

Sample 1: Si + Ti (10 nm) + Au (200 nm) + PMMA (10 nm) + Nanocrystals + PMMA (15 nm)

Sample 2: Si + Ti (10 nm) + Au (200 nm) + PMMA (10 nm) + Nanocrystals + PMMA (21 nm)

Sample 3: Si + Ti (10 nm) + Au (200 nm) + PMMA (10 nm) + Nanocrystals + PMMA (35 nm)

Sample 4: Si + Ti (10 nm) + Au (200 nm) + PMMA (10 nm) + Nanocrystals + PMMA (58 nm)

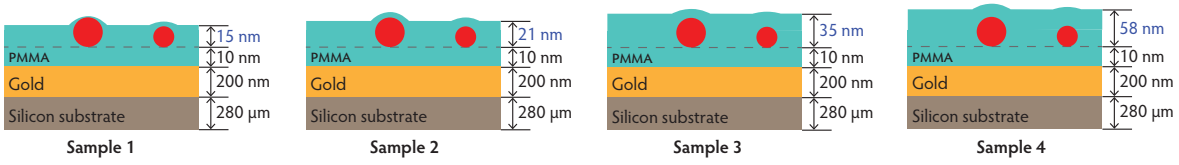

Figure 3.18 *Increasing the spacer above the nanocrystal*

By spin-coating a solution of high concentration, the thickness of the spacer (PMMA) is increased, which enabled us to prevent a reduction in nanocrystal fluorescence after the subsequent Au deposition.

The value of thickness of the top PMMA film is based on measurements of section 2.4.3.1. It is the thickness of the second PMMA layer above the first PMMA layer and probably it is not the real thickness of the PMMA film just above the nanocrystal. However, it can be said that a thicker upper PMMA film usually results in a larger PMMA thickness above the nanocrystal. Figure 3.18 sketches samples *1*, *2*, *3*, and *4*, which have an upper PMMA film that was deposited by spin-coating solutions of PMMA in toluene of concentrations 0.75% [m/m], 1% [m/m], 1.5% [m/m], and 2% [m/m], respectively.

The four samples of Figure 3.18 were placed in the deposition chamber and by thermal evaporation, a 20 nm thick Au film was deposited on them. Figure 3.19 shows the fluorescence microscopy images of three samples before and after the Au deposition. The nanocrystals on *Sample 4* did not show any reduction in fluorescence after the Au deposition (see Table 3.1). The results of *Sample 4* are similar to those of *Sample 3*, therefore its images are not displayed in Figure 3.19.

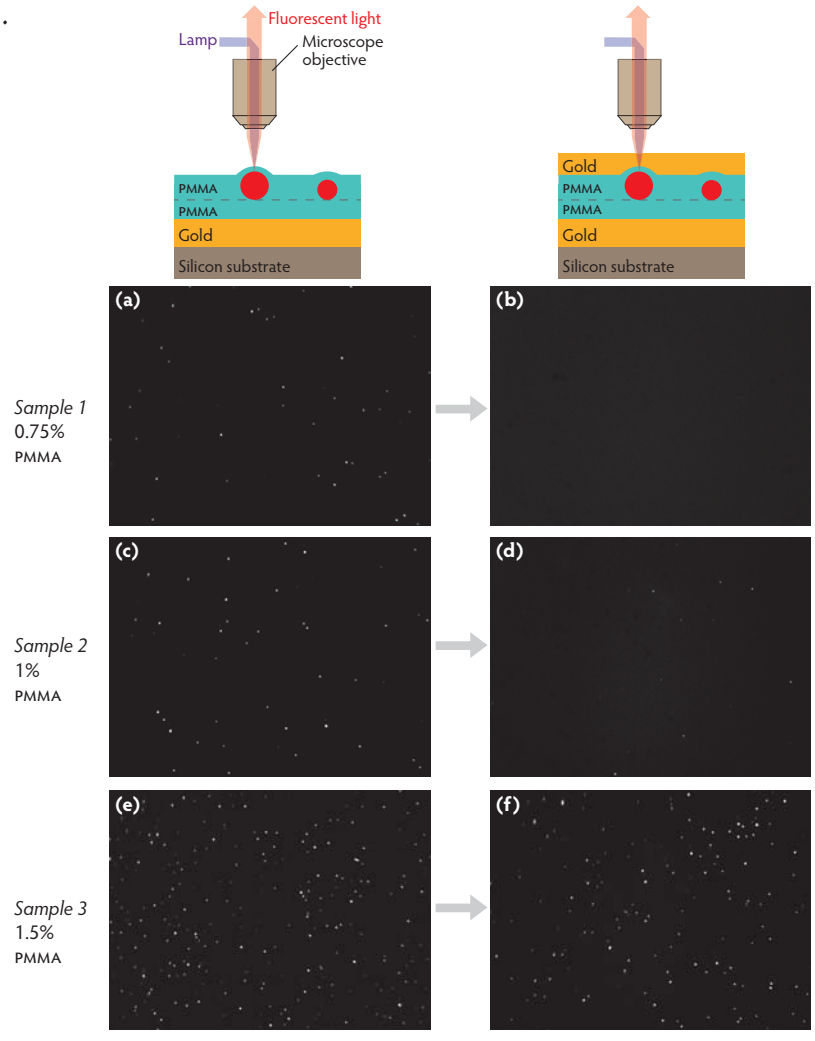

Figure 3.19 *Nanocrystals before and after gold deposition*

These images were recorded with the same CCD camera acquisition time of 200 ms. For the corresponding samples, fluorescence microcopy images **(a)**, **(c)**, and **(e)** show the sample before the 20 nm thick Au deposition, and images **(b)**, **(d)**, and **(e)**, respectively, show it after the Au deposition. After the deposition of Au, no emitters could be observed fluorescing on *Sample 1*, on *Sample 2* a few were visible but they were very dull, and on *Sample 3* almost all of them fluoresced. The before and after deposition areas shown in the figure are not identical but as the spatial distribution of nanocrystals is quite homogeneous, the images give a clear picture of the deposition effect.

Using a Photonic Science CCD camera (appendix A.2), we can usually detect fluorescing nanocrystals with an acquisition time of 50 ms. After depositing Au on the sandwiched nanocrystals, we observed them with acquisition times from 200 ms to 10 s. Table 3.1 summarizes the results about the visibility of nanocrystals on samples 1–4 after the 20 nm thick Au film deposition.

Sample number	PMMA concentration [m/m]	Film thickness (nm)	Visibility			
			Eye	Camera t_{acq} = 200 ms	Camera t_{acq} = 2 s	Camera t_{acq} = 10 s
1	0.75%	15	✗	✗	✗	Very few (16%)
2	1%	21	✗	✗	Few (26%)	Many (58%)
3	1.5%	35	✗	✗	All (100%)	All (100%)
4	2%	58	✓	✓	✓	✓

Table 3.1 *Results of gold deposition on nanocrystals beneath different PMMA thicknesses*
The cross indicates that the nanocrystal fluorescence could not be observed, and the check mark indicates that it could be observed. On each sample, a region was selected and the number of emitters were counted in that region. After the gold deposition, the same region was viewed by fluorescence microscopy. The images were collected with different acquisition times and the number of emitters were counted. On these samples, without the 20 nm thick Au film on top, the nanocrystals could be observed by eye.

The fluorescence reduction in *Sample 1* was very strong. Even with t_{acq} = 10 s, only 16% of the emitters were visible and they were very dim. Confocal scanning by laser is more adequate for scanning emitters but due a to very low fluorescence signal in *Sample 1*, very few emitters could be scanned. Moreover, in order to boost the fluorescence signal, the emitters had to be scanned with high laser power, which was sufficient to photobleach them within 10–20 s. If a nanocrystal cannot be scanned harmlessly by a laser, it cannot be used as a nanoantenna emitter. The least thick PMMA film below which the nanocrystals were visible with 100% success was the film produced by spin-coating 1.5% [m/m] PMMA in toluene (*Sample 3*). *Sample 4* also showed a 100% success rate but it had a thicker film than *Sample 3*. It may be possible to find a film thickness that is less than the film thickness of *Sample 3* and more than the film thickness of *Sample 2*, and that gives a 100% success rate. The results of this experiment were supported by the success rate of antennas that had been made with different thicknesses of PMMA. Antennas that had nanocrystals beneath a film made with 0.75% [m/m] PMMA solution were almost impossible to scan, whereas all the antennas that used a 1.5% [m/m] PMMA film could be scanned. In the case of *Sample 4*, the Au deposition did not reduce nanocrystal fluorescence at all and they could be observed by eye.

3.5.2.1 Conclusion

Because the nanocrystals could be observed by increasing the image acquisition time, the reduction of fluorescence seems to be due to quenching and not because of some other type of permanent nanocrystal damage during the Au deposition. However, we cannot rule out the possibility that the deposition of Au was damaging the nanocrystals by creating some

permanent defects in them. In any case, the results of this experiment show that by using high-concentration PMMA solutions for spin-coating, we can increase the thickness of the PMMA film just above the nanocrystal, and therefore the nanocrystal–Au patch separation. This allows us to avoid any permanent damage to nanocrystal fluorescence due to the vapor deposition of Au.

3.5.3 Enhancing SPP coupling

Two of the most important factors that decide the efficacy of a plasmonic patch nanoantenna are the coupling between the emission and the Au surfaces, and the SPP coupling between the bottom 200 nm thick Au surface and the 20 nm thick Au patch [40]. By using spin-coated films of different thicknesses, we can vary the distance between the bottom Au layer and the Au patch, and we can place a nanocrystal at the intended vertical position between them.

In the nanoantennas discussed in this thesis, the thickness of the PMMA bi-layer stack is 10+35 = 45 nm. If the thickness is less than this, we expect the SPP coupling to be better, which will accelerate the emission of the nanocrystal due to field enhancement. In a working system like this, there is a competition between field enhancement and fluorescence quenching [25, 170], and one has to settle for the best compromise. As 1.5% [m/m] spin-coated PMMA films showed 100% observability, and in the development stage of the lithographic protocol we wanted to use reliable components, we chose to work with the mentioned. Now after the fabrication protocol has been developed, it would be interesting to experiment with thinner PMMA bi-layer films and note the effect on antenna emission.

3.6 Lift-off

At step 6 of the lithographic protocol (Figure 3.1), the lift-off procedure is carried out by immersing a sample inverted inside a bath of MF-319® and shaking it for 20 s or more. The time required for the lift-off depends on the size of the entrance available for the solvent to attack LOR®—the bigger the entrance, the shorter is the lift-off duration. Unlike the development duration, the lift-off duration does not need to be very precise as the only goal of lift-off is to get rid of the material around and above the patch. However, it should be emphasized that the lift-off duration cannot be extended very long because after a certain time, the solvent starts attacking other materials in the sample.

3.6.1 Lift-off requirements

A lift-off operation is intended to *clean* the Au patch by removing the material above and around the patch, especially any material that can degrade the antenna performance. Our main concern is the Au film that is above on the sides of the patch because its presence in the radiation path may alter the radiative behavior of the antenna. The resists (LOR® and PMMA) and their residues (obtained after the lift-off process as a result of the chemical reaction with the developer) are not an impediment to antenna functioning as their refractive index is about 1.5 and they do not degrade the SPP dynamics. Considering the mentioned, we would like to discuss about the requirements of a successful lift-off. This will allow us to perform an appropriate lift-off without investing more effort or time into achieving a thorough lift-off that does not give better plasmonic patch nanoantennas.

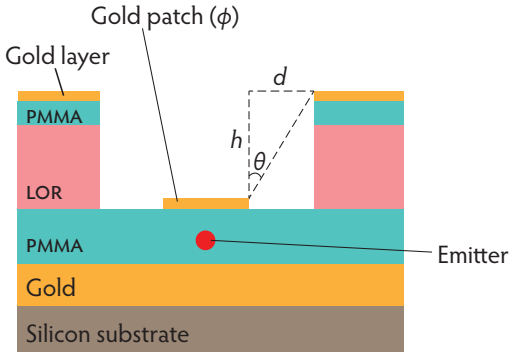

Figure 3.20 *Lift-off requirement*

The figure displays a typical case of a sample after the lift-off process. After the lift-off, the upper Au film is removed such that its edge is at a horizontal distance d from the patch edge. Here h is the vertical distance between the Au patch and the Au film, and θ is the angle made by the edge of the etched upper Au film with the edge of the patch.

Figure 3.20 illustrates a sample after a typical lift-off. The patch antennas discussed in this thesis were obtained by using resist bi-layers of two thicknesses: 1) LOR® 3A (300 nm) + PMMA (10 nm) (used for supercontinuum laser lithography), and 2) LOR® 3A (500 nm) + PMMA (50 nm) (used for e-beam and LG mode lithography, chapters 4 and 5). The simulation results of Figure 1.3 show that the radiation of a patch antenna with a vertically oriented emitter dipole is confined within a cone whose half-angle is less than 30°.

Patch diameter (μm)	Cone half-angle θ (°)	h (nm)	d (μm)
0.6	30	300	0.2
„	„	500	0.3
1	20	300	0.1
„	„	500	0.2
2	10	300	0.05
„	„	500	0.1

Table 3.2 *Optimum patch–film distance after lift-off*

For the given patch diameters and the corresponding cone half-angles, the minimum patch–film distance d, as shown in Figure 3.20, has been listed. We note that $d > 0.3$ μm results in a successful lift-off.

Let us consider a very bad case of low directivity, which increases the demands of lift-off. Consider a patch antenna whose cone half-angle is 70° (not directive), and $h = 500$ nm (worst case). This gives $d = 1.4$ μm. From this we can safely say that $d > 1.5$ μm leads to a successful lift-off, even in worse cases. AFM analysis of our patch antennas demonstrates that all our antennas meet the requirement of $d > 0.3$ μm and many of them even fulfill the more demanding (but most likely not required) condition of $d > 1.5$ μm.

The concept of radiation pattern (Figure 1.3) is applicable for far-field radiation, which is not really the case for the distances mentioned in Table 3.2. However, it can be assumed that the field divergence in the limiting cases of the far-field (like the one discussed above) is less than in the far-field. Therefore, the argument presented above is valid insofar as the radiation path is concerned. Following this and the calculated values listed in Table 3.2, we can say that if the horizontal distance between the patch-edge and the edge of the upper Au film is

more than 0.3 µm, the lift-off is acceptable. It has been observed by AFM measurements that our lift-off strategy satisfies this criterion for all patch sizes, which include patch antennas fabricated using the supercontinuum laser, e-beam, and LG mode lithography.

3.6.2 Supercontinuum laser lithography patch antennas after lift-off

Figure 3.21 is an AFM height image of a gold patch antenna fabricated using supercontinuum laser lithography. The image was recorded after the lift-off. It can be seen that the patch–film distance is about 1 µm, which is more than the requirement of 0.3 µm. There is some lift-off residue above and around the patch but the circular patch of 1 µm diameter is discernable. In one of the areas pointed out in the image, the patch thickness of 20 nm can be observed.

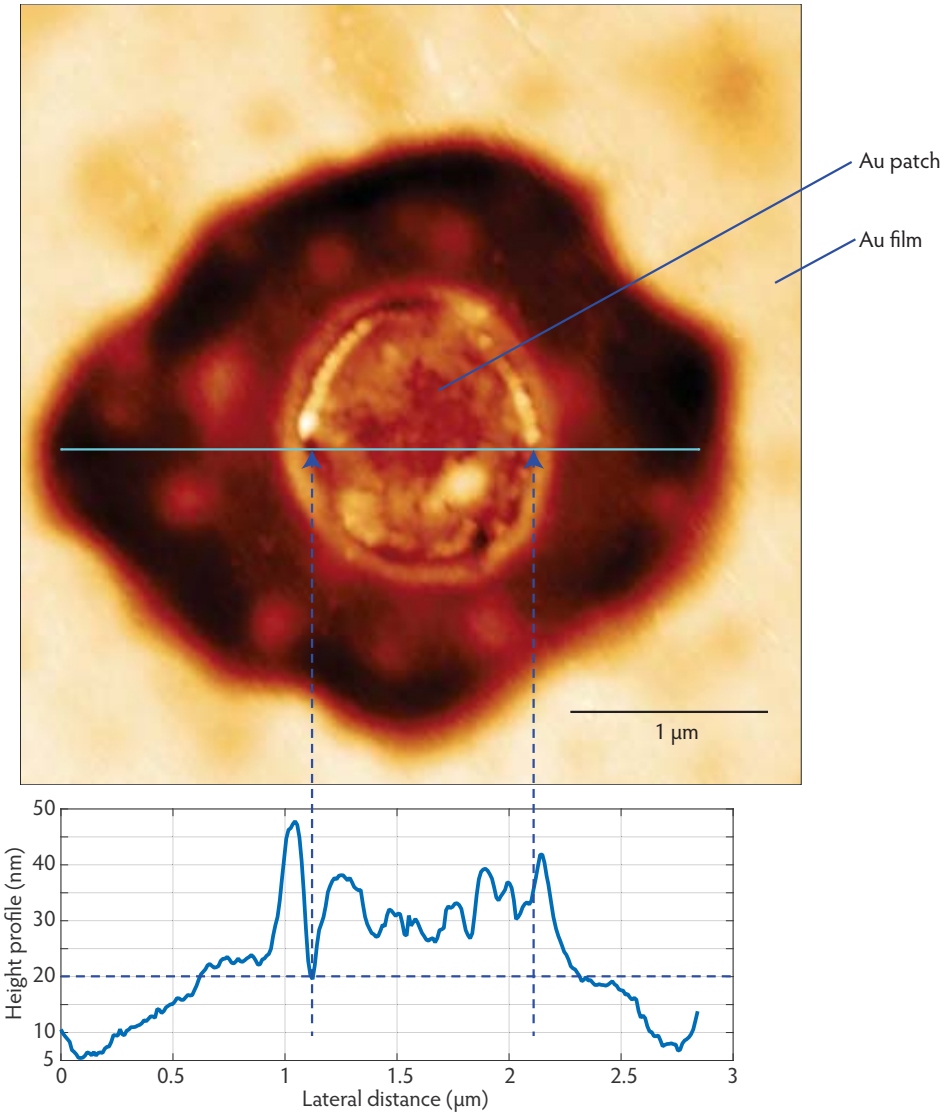

Figure 3.21 *A patch antenna realized by supercontinuum laser lithography*
The AFM height image shows an antenna patch ($\phi \approx 1$ µm) and some leftover lift-off residue. The height profile along the marked straight line is graphed below the AFM image. Though the patch is covered with some lift-off residue, its edge is clearly demarcated. At one point (pointed out by the marked arrow), where there is no lift-off residue, the 20 nm thickness of the patch can be noted. For the plasmonic operation of the nanoantenna, the presence of some lift-off residue is not an issue.

The lift-off process involves the removal of the resist by chemical etching and some residue resulting from this chemical removal may remain on and around the patch after the lift-off. The residue can be reduced by performing the lift-off for a longer duration or by using additional cleaning steps such as oxygen plasma etching. But before performing any further action, we have to analyze if an additional cleaning step is required.

As described in the previous section, we assume that the presence of some resist residue does not depreciate performance of these patch antennas. Moreover, an additional cleaning step may involve undesirable effects. For example, with a longer duration lift-off, we risk removing the patch, and we have found that while reactive-ion etching cleans the residue, it also bleaches the nanocrystal beneath the patch. Our experiments show that mild oxygen plasma etching (e.g., at 30 W for 10 minutes) may be used for cleaning the residue without damaging the nanocrystals.

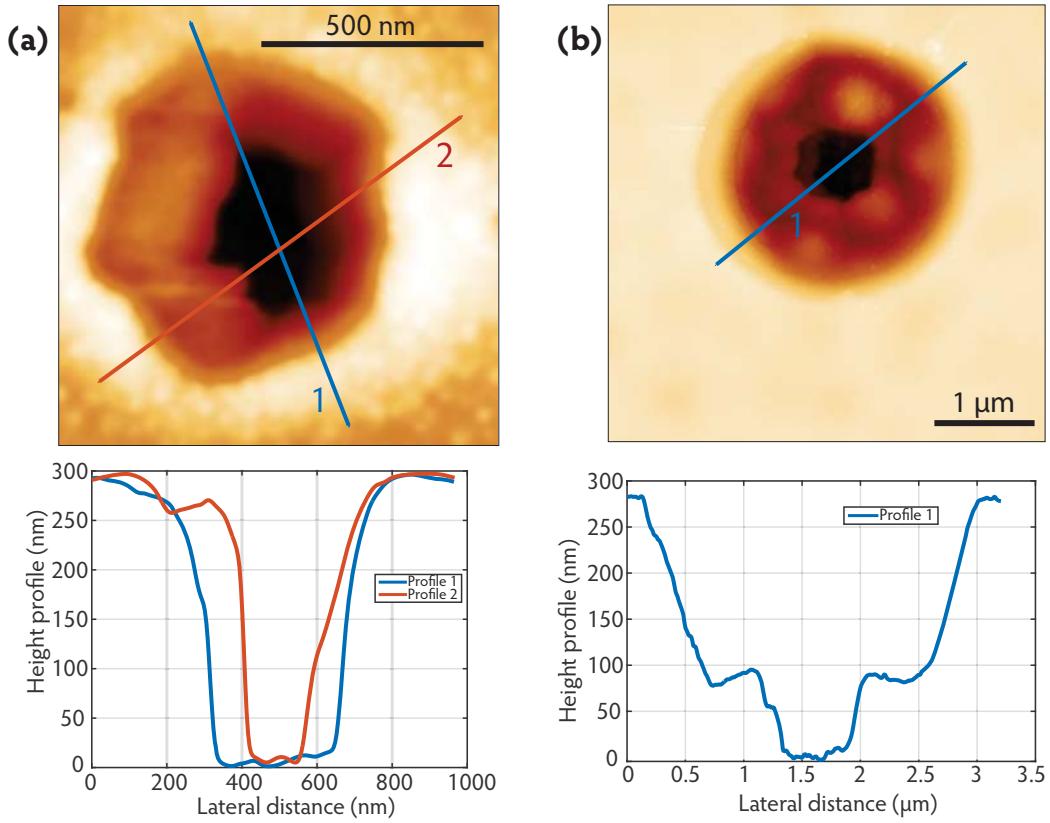

Figure 3.22 *Varying the size and shape of nanoantenna patch*

AFM height images **(a)** and **(b)** show two different nanoantenna patches (black area) fabricated using supercontinuum laser lithography. The corresponding height profiles are given below the AFM images. In the case of **(a)**, the patch shape is roughly elliptical; the major axis is about 250 nm and the minor axis is about 150 nm. This shows that with our technique we are able to achieve patch sizes that are truly sub-wavelength. Laser light in a range of 550–605 nm was used for the lithographic task. The patch in **(b)** is quite circular and its diameter is about 600 nm. In both the cases, some lift-off residue remained around the patch boundary. Its presence is more prominent in the larger patch because when the lift-off was carried out on this sample, more resist was removed from the larger entrance of **(b)** (note the steps on the sides of the patch) than from the smaller entrance of **(a)**. Due to the leftover residue, the boundaries of the patch appear higher than the patch. The emission of the patch antenna of **(a)** is characterized in Figures 3.26(c) and (d). This lithography technique is capable of attaining patches of different sizes and shapes.

3.6.3 Nanoantenna patch size

The acceleration of emission (Figure 1.2) and the directivity (Figure 1.3) of a patch nanoantenna depends on the size of the patch [1, 8]. Sections 3.3.2 and 3.4 elaborate how the supercontinuum laser lithography allows us to vary the patch size by means of controlling the laser power and focusing, exposure time, and the development time. AFM measurements confirm that the supercontinuum laser lithography is able to attain patch diameters in a range of 200 nm to 2.5 µm.

In addition to the size of the patch, its shape can also be of interest. If the laser beam cross-section is circular, it is likely to burn a circular hole in the resist bi-layer, and finally a circular patch is obtained. We can use mirrors to deflect the laser such that it has an elliptical cross-section. A hole burned by such a laser beam is likely to be elliptical and so will be the antenna patch.

The antenna imaged in Figure 3.22(a) was very bright. It showed a very fast decay rate (Figure 3.26(c)) and could be excited with very low laser power at 405 nm. The power was less than 11 nW; the exact value could not be recorded as it was too low to be sensed by the laser power meter. We have never been able to excite a nanocrystal with such low laser intensity. This suggests that, as far as antenna radiative capabilities are concerned, this plasmonic patch antenna was functioning well. Figure 3.23 displays two fluorescence images of this antenna recorded with different acquisition times.

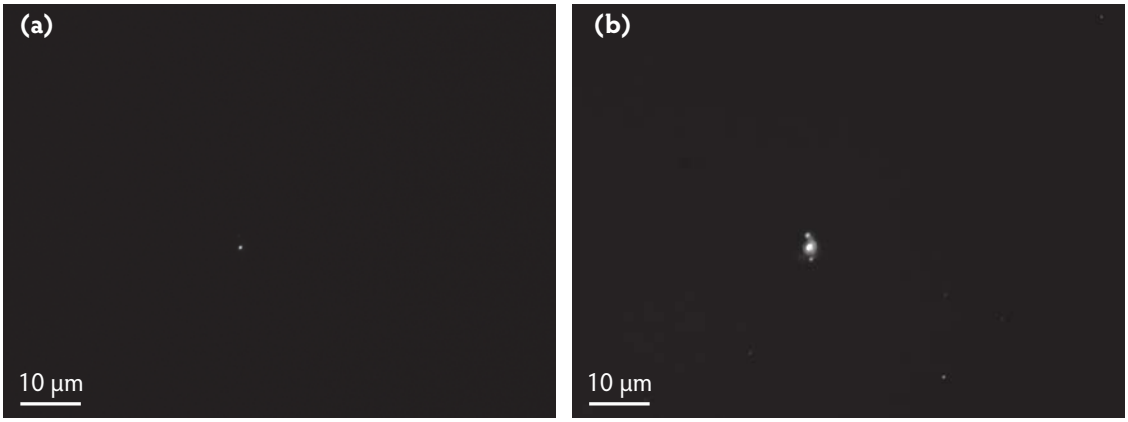

Figure 3.23 *Fluorescence microscopy image of a bright antenna*

The fluorescence microscopy images **(a)** and **(b)** were captured by the CCD camera with the acquisition times of 10 ms and 200 ms, respectively. The bright spot in both the images is the radiating patch nanoantenna of Figure 3.22(a), which is characterized by Figures 3.26(c) and (d). Due to the low acquisition time, we observe no fluorescing nanocrystals in **(a)**. After increasing the acquisition time, they become visible in **(b)** but the bright antenna starts saturating the image. The two light spots above and below the antenna in image **(b)** are due to some parasite optical or electronic effect.

3.7 Nanoantenna characterization

Several nanoantennas were fabricated using the supercontinuum lithography technique. The illustration in Figure 3.24 shows the structure of these antennas. The shape and size of the Au patch can be varied using the methods described in sections 3.3.2 and 3.4. This allows us to control the emission acceleration, antenna directivity, and investigate the physical effects that are affected by the patch size and shape.

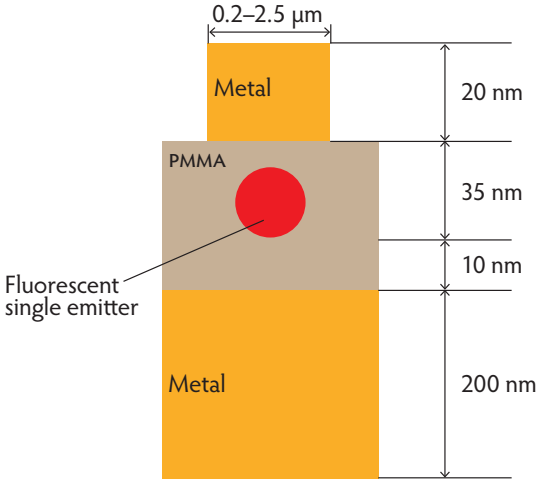

Figure 3.24 *Nanoantenna made by supercontinuum laser in-situ optical lithography*
The emitter in these nanoantennas was a CdSe/CdS core/shell nanocrystal with a total diameter of 15–19 nm. By varying the Au patch size, we can vary the emission acceleration.

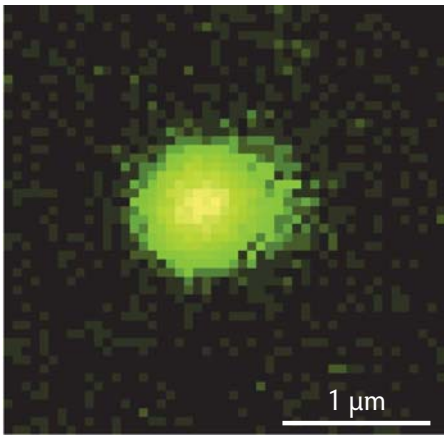

Figure 3.25 *Confocal scan of an antenna*
The colors in the image are artificial. The bright area is the nanoantenna from which the emission was recorded, and the dark area is the background. Note the size of the antenna—it is bigger than the optical size of a nanocrystal (650 nm).

The samples on which the nanoantennas were fabricated were scanned confocally using a 405 nm CW laser. Figure 3.25 shows a confocal scan of an antenna. The fluorescent radiation of the nanocrystal is coupled to the bottom Au layer and the top Au patch, and SPP are generated at the metal–dielectric interfaces. The SPP produce enhanced optical near-fields at the metal surface [25]. As the thickness of the Au patch is only 20 nm, these near-fields result in photon emission from the patch. This emission is directed to a photodiode by means of confocal microscopy, and a confocal scan of the nanoantenna is obtained. The circular shape depicted in Figure 3.25 has a diameter of about 900 nm, which is larger than the optically limited size of a fluorescing nanocrystal (650 nm) on our setup. This is because a fluorescing nanocrystal is a point-like emitter (its physical size is only 15–19 nm), whereas in our nanoantennas, the entire Au patch emits. Therefore, in the case of a nanoantenna, where the SPP coupling exists and whose patch is bigger than 650 nm (the optically limited size when a 405 nm laser is used for scanning with a 0.80 *N.A.* microscope objective), the confocal scan should correspond to the physical size of the nanoantenna patch.

3.7.1 Radiative emission from exciton and multiexciton phenomena

An exciting laser pulse may generate a large number of excitons (electron–hole pair) in a nanocrystal. The higher the intensity of the excitation, the more is the number of excitons. An exciton may recombine radiatively by emitting a photon or non-radiatively. Excitons interacting strongly with each other are called multiexcitons. The Auger effect, which causes multiexcitons to recombine non-radiatively, is in competition with the radiative multiexciton recombination. The multiexciton decay rate Γ_{MX} can be described as:

$$\Gamma_{MX} = \Gamma_{Aug} + \Gamma_{rad}^{MX} \tag{3.9}$$

where Γ_{rad}^{MX} is the radiative multiexciton decay rate, and Γ_{Aug} is the Auger decay rate. When $\Gamma_{Aug} >> \Gamma_{rad}^{MX}$, the non-radiative recombination overcomes the radiative one. For example, in small nanocrystals, which have strong confinement, the Auger effect is very efficient: As the Auger recombination is faster than the radiative recombination, all the interacting excitons (multiexcitons) recombine non-radiatively except the last exciton which may recombine radiatively by emitting a single photon. In large nanocrystals, like the ones used in our antennas, the confinement is weak and the Auger effect is not as efficient. As a consequence, multiexcitons may recombine radiatively. Multiexciton recombination involves a cascading process [4]. For example, in biexciton recombination [171] (which consists of two interacting excitons), the fast recombination (radiative or non-radiative) of one of its exciton is followed by a slower exciton recombination (mostly radiative in our case) that emits a photon. Multiexciton emission from our nanocrystals can be noted in Figure 1.14. The histograms plotted in this figure show that under low intensity laser excitation, the emission decay of has two parts—the fast slope region is due to biexciton recombination and the slower trace is due to exciton recombination. Therefore, the decay curves can be fitted with a bi-exponential equation. Under high excitation, as depicted by the red curve in the figure, the proportion of the photons emitted due to fast recombination increases. This is expected because increasing the laser fluence on a nanocrystal creates more excitons, and therefore more multiexcitons [172].

In most cases, the non-radiative Auger effect is not negligible. Consequently, the number of photons emitted by the radiative biexciton recombination is less then the number of photons due to radiative exciton recombination. Even in the cases where the Auger effect is negligible, the number of photons due to biexciton to exciton radiative recombination can never be more than the number of photons emitted due to radiative exciton recombination.

Excitation of high-confinement structures with high laser fluence creates multiexcitons that can combine radiatively. For example, a tri-exciton can be involved in a three-step cascading recombination: XXX→XX, XX→X, and X→photon. The tri-exciton to biexciton (XXX→XX) and biexciton to exciton (XX→X) transitions can be radiative or non-radiative. Finally, the considered tri-exciton decay emits 1–3 photons. The XXX→XX process is the quickest (and the least efficient in emission), and radiative exciton recombination (X→photon) is the slowest. The decay curve obtained from tri-exciton phenomena requires a tri-exponential fitting. When the Auger effect is negligible, the number of photons emitted by the radiative exciton recombination is less than the photons emitted by XXX→XX and XX→X processes. Our results show that due to the competition between the Auger effect and radiative multiexciton emission, the probability of single photon emission decreases as the probability of radiative multiexciton recombination increases.

Emission from our CdSe/CdS core/shell nanocrystals always shows photon-antibunching ($g^{(2)}(0) \sim 0.25 - 0.4$) when they are excited with a 405 nm laser of intensity as high as 15 W/cm^2 . Figure 1.16 shows a typical antibunching curve obtained when these nanocrystals are excited with a laser intensity of about 3 W/cm^2 . When these nanocrystals were placed in the nanoantenna and excited with less than 3 W/cm^2 of 405 nm laser intensity, we could observe antibunching only in some cases. In their work, Ji *et al.* [173] synthesized 30 nm thick colloidal CdSe/CdS core/shell nanocrystals and chemically coated them with a 35 nm thick SiO_2 shell, and then by chemical synthesis, a 20 nm thick Au shell was grown around the CdSe/CdS + SiO_2 ensemble. Photon-antibunching was not recorded for any of these structures [174] and the typical value of $g^{(2)}(0)$ was 0.9. In such structures and in many of our antennas, due to the Purcell effect, which leads to the acceleration of emission, the Auger processes are overcome by multiexciton radiative recombination, that is:

$$\Gamma_{\text{rad}}^{\text{MX}} >> \Gamma_{\text{Aug}} \tag{3.10}$$

where $\Gamma_{\text{rad}}^{\text{MX}}$ and Γ_{Aug} are the radiative multiexciton and Auger recombination rates, respectively. In these structures, the multiexciton recombination is mainly radiative. This inhibits single photon emission but increases the overall intensity of the radiated light.

3.7.2 Antenna emission lifetime

The emission decay curves of four patch antennas fabricated by supercontinuum laser lithography are plotted in Figure 3.26. In all these patch antennas, significant acceleration of emission can be noted by comparing their decay curves with that of a typical nanocrystal placed in a homogeneous medium (Figure 1.11(b)).

The decay curve of most of these antennas can be fitted with a bi-exponential equation of the form:

$$I(t) = a_1 e^{-t/\tau_1} + a_2 e^{-t/\tau_2} + c \tag{3.11}$$

where τ_1 and τ_2 are the short and long emission lifetimes, a_1 and a_2 are constants, and c is the noise. Fitting the emission decay histogram with equation (3.11) requires finding the parameters a_1, τ_1, a_2, τ_2, and c. We did this using the curve-fitting options of MATLAB®; the corresponding equation has been plotted and mentioned for each decay curve in red color.

To explain the emission characteristics, we attribute $\tau_1 = 1/\Gamma_{\text{MX}}$ to photon emission from multiexciton recombination (probably biexciton), and $\tau_2 = 1/\Gamma_{\text{X}}$ to photon emission from exciton recombination because the former is always faster than the latter [4]. Assuming that in our antennas, the multiexciton phenomena is mainly biexciton phenomena, and therefore treating τ_1 as the biexciton lifetime, we define α as:

$$\alpha = \frac{a_2 \tau_2}{a_1 \tau_1}. \tag{3.12}$$

The parameter α is proportional to the ratio of the number of photons due to exciton recombination (X) to biexciton recombination (XX→X). We have found that generally our patch antennas show antibunching if $\alpha > 5$. It should be noted that the emitter of all our patch nanoantennas is a CdSe/CdS quantum dot from the same production batch (see section 1.3) that is embedded in a 45 nm thick PMMA spacer as shown in Figure 3.24.

Emission from a very few patch antennas could not be described using a bi-exponential equation but it could be fitted with the following tri-exponential equation:

$$I(t) = a_1 e^{-t/\tau_1} + a_2 e^{-t/\tau_2} + a_3 e^{-t/\tau_3} + c \tag{3.13}$$

where τ_1, τ_2, and τ_3 are emission lifetimes in increasing order, and a_1, a_2, a_3, and c are constants. For each emission decay curve, these parameters are found as described above. These emission lifetimes can be attributed to multiexciton recombination (probably tri-exciton and biexciton) and to exciton recombination.

The emission of a nanocrystal is affected by the fluctuations in its environment. Therefore, even if the emission of the nanocrystal is due to exciton recombination, sometimes its decay curve cannot be fitted by a mono-exponential equation. A better fit can be then obtained by using bi-exponential fitting because it offers more fitting flexibility. In such cases, as the bi-exponential fitting is required to account for fine adjustments to a mono-exponential decay, the two lifetimes and the two corresponding coefficients are of the same order of magnitude. The bi-exponential fitting parameters of these decay curves cannot be interpreted as biexciton (XX→X) and exciton (X) emission characteristics. In fact, fitting this curve with a mono-exponential fit reveals more truth about the underlying exciton recombination (which is mono-exponential). The same argument holds for a tri-exponential fit. It should be pointed out that it is very difficult to distinguish if a tri-exponential fit is required to account for fine adjustments or it really depicts a tri-exponential decay due to radiative multiexciton emission (that involves tri-excitons and higher). This is because the lifetimes involved are shorter than or comparable to the temporal resolution of our measurement setup, which is about 300 ps.

The antenna decay curves fitted with a tri-exponential fit contain three lifetime values: 1) τ_1, the shortest lifetime (XXX→XX), which are as short as the temporal resolution of our system, 2) τ_2, which can be attributed to XX→X process, and 3) τ_3, which is the longest and is due to exciton recombination. The values of τ_1 and τ_2 are very close, and therefore, it is difficult to discern if this depicts physical reality (lifetimes of tri-exciton and biexciton processes) or if it just a mathematical adjustment to account for fluctuations. In this latter case, the emission can essentially be fitted by a bi-exponential fit. Therefore, we always plot both the tri-exponential and bi-exponential fitting curves. If the bi-exponential fits are acceptable, we will restrict our discussion to bi-exponential phenomena (biexcitons and excitons). Otherwise, we will consider the tri-exponential fit as as a good physical description of the emission decay.

In conclusion, the emission from most of our antennas can be fitted with a bi-exponential equation, and most of the very few that require a tri-exponential fit can be described with a less good fitting but more reasonable bi-exponential fit. Therefore, we use Eq. (3.11) as the main equation for analyzing the decay curves and for calculating α.

3.7.3 Purcell factor of a patch antenna

As demonstrated in Figure 3.26, the emission of most of our patch antennas can be fit with a bi-exponential. We expand the general definition of the Purcell factor (Eq. (1.1)) and define it for our patch antennas:

$$F_P = \frac{\tau_{\text{homogeneous}}}{\tau_{\text{antenna}}} = \frac{\tau_{\text{typical}}}{\tau_2} = \frac{35}{\tau_2} \tag{3.14}$$

where $\tau_{typical}$ = 35 ns is the typical exciton lifetime of our nanocrystals in a homogeneous medium, and τ_2 is the slow lifetime of the bi-exponential fit of Eq. (3.11), which is associated with the exciton lifetime. Reference [175] has used a similar definition of the Purcell factor.

Our nanocrystals have a very good quantum efficiency and it can be assumed as 1. The plasmonic nanoantenna structure results in strong confinement of electromagnetic field around the nanocrystal embedded inside. This effect leads to a high density of states in the nanocrystal, which accelerates its exciton emission, which is given by the Purcell factor. In other words, when the quantum efficiency of exciton decay $\eta_X \approx 1$, and F_P is the Purcell factor, we have:

$$\begin{aligned}\Gamma_X^{antenna} &= \Gamma_X^{antenna,rad} + \underbrace{\Gamma_{non\text{-}rad}}_{\approx 0 \text{ as } \eta_X \approx 1} \\ &= F_P\,\Gamma_X^{homogeneous,rad}\end{aligned} \tag{3.15}$$

where $\Gamma_X^{antenna}$ is the decay rate of the emitter in the antenna, $\Gamma_X^{antenna,rad}$ is the radiative decay rate of the emitter in the antenna, $\Gamma_{non\text{-}rad}$ is the non-radiative decay rate associated with exciton recombination, and $\Gamma_X^{homogeneous,rad}$ is the radiative decay rate of the emitter in a homogeneous medium. We note that the Purcell factor of the antenna is the same as its acceleration of exciton emission.

The same Purcell factor could be applied to the radiative decay rate of the biexciton as well, but unlike the exciton quantum efficiency ($\sim$ 1), the quantum efficiency of radiative biexciton emission is very small. To some extent we can suppose that the Auger decay rate Γ_{Aug} is not affected by the environment. Therefore, the biexciton decay rate of the antenna can be given as:

$$\begin{aligned}\Gamma_{XX}^{antenna} &= \Gamma_{XX}^{antenna,rad} + \Gamma_{Aug} \\ &= F_P\left(\Gamma_{XX}^{homogeneous,rad}\right) + \Gamma_{Aug}\end{aligned} \tag{3.16}$$

where $\Gamma_{XX}^{antenna}$ is the biexciton decay rate of the emitter in the antenna, $\Gamma_{XX}^{antenna,rad}$ is the radiative biexciton decay rate of the emitter in the antenna, Γ_{Aug} is the Auger decay rate associated with biexciton recombination, and $\Gamma_X^{homogeneous,rad}$ is the radiative biexciton decay rate of the emitter in a homogeneous medium. Influenced by the relative value of Γ_{Aug}, the acceleration of emission from the biexciton recombination is thus always smaller than F_P. It reaches F_P when Γ_{Aug} becomes negligible.

For this reason, the Purcell factor cannot be estimated correctly from biexciton decay rates. Moreover, for estimating the Purcell factor, we have to divide the nanocrystal emission decay rate in the antenna by its decay rate in a homogeneous dielectric medium of the same refractive index. The exciton decay rate of a nanocrystal in a homogeneous medium can be found easily but its biexciton decay rate cannot be estimated easily and rigorously as it is much faster and it is highly dependent on the field confinement and Auger effects. The biexciton decay rate for low excitations can be considerably lower than for high excitations. For example, in Figure 1.14 we note that the biexciton decay rate increases (from 0.5 ns^{-1} to 1.2 ns^{-1}) as the excitation is increased from 3 W/cm^2 to 15 W/cm^2 .

3.7.4 Discussion on the results

The emission decay rates and photon-antibunching curves of some patch antennas fabricated using supercontinuum laser lithography are given in Figure 3.26. A 405 nm pulsed laser (at 2.5 MHz) was focused through an air objective (100×, 0.80 *N.A.*) to excite the antennas. Figure 1.18 shows the optical measurement setup. The F_P and α values of these antennas are given in Table 3.3.

Antenna #	F_P	α	Antibunching
1	12	3.6	×
2	23	0.3	×
3	14	0.3	×
4	4	6.6	✓

Table 3.3 *Characteristics of antennas obtained with supercontinuum laser lithography*

Antenna 1 shows a Purcell factor of about 12, $\alpha \approx 3.6$, and $g^{(2)}(0) \approx 0.8$. It is different from the others because its decay curve, though fitted with a bi-exponential, looks quasi mono-exponential. The fluctuations in the antibunching curve makes it difficult to know if it is completely lost; the calculated value of $g^{(2)}(0) \approx 0.8$ suggests very poor antibunching. Its α parameter shows major exciton emission along with less efficient biexciton emission. Its biexciton lifetime of 1 ns is more than the biexciton lifetime of other antennas. This can be explained by the existence of an efficient Auger effect in the nanocrystal.

Antenna 2 has the fastest decay curve with $F_P \approx 23$ and $\alpha \approx 0.3$. This antenna was exceptionally bright. Its fluorescence image is depicted in Figure 3.23. The brightness of this antenna and its high Purcell factor can be attributed to its small size. An AFM image of this antenna is depicted in Figure 3.22(b). Moreover, it is likely that the nanocrystal dipole had a more vertical orientation, which resulted in a stronger Purcell effect.

Antenna 3 has $F_P \approx 14$, $\alpha \approx 0.3$, and $g^{(2)}(0) \approx 1$.

For *antennas 1* and *2*, the Purcell factor is very high, photon-antibunching is lost, and α is smaller than 1. As discussed in section 3.7.1, this is a sign of radiative multiexciton (at least tri-exciton) emission. The high acceleration of emission leads to an increase in the multiexciton emission rate, which becomes much more than the Auger rate.

Antenna 4 has $F_P \approx 4$, $\alpha \approx 6.6$, and $g^{(2)}(0) \approx 0.6$. Its decay curve has been fitted with a tri-exponential function and with a bi-exponential function as well. Though the fitting is better with a tri-exponential function, the bi-exponential fit makes more sense. The observation of partial photon-antibunching and its $\alpha \approx 6.6$ verifies the condition of $\alpha > 5$. Its value suggests that the majority of the photons are due to exciton recombination. The emission characteristics of this antenna show that the Auger effect is in close competition with the radiative biexciton recombination. It allows some biexciton emission (which tries to increase the $g^{(2)}(0)$ to 1), but intermediate-valued emission acceleration (which increases the exciton emission) and the efficient Auger effect limit the contribution of biexciton emission to the overall emission, thus making antibunching noticeable. In other words, in this case, even though the excitation creates many biexcitons, due to Auger effect, only a few of them recombine to emit photons. And these photons due to biexciton recombination are less than the photons from accelerated exciton emission, which results in photon-antibunching.

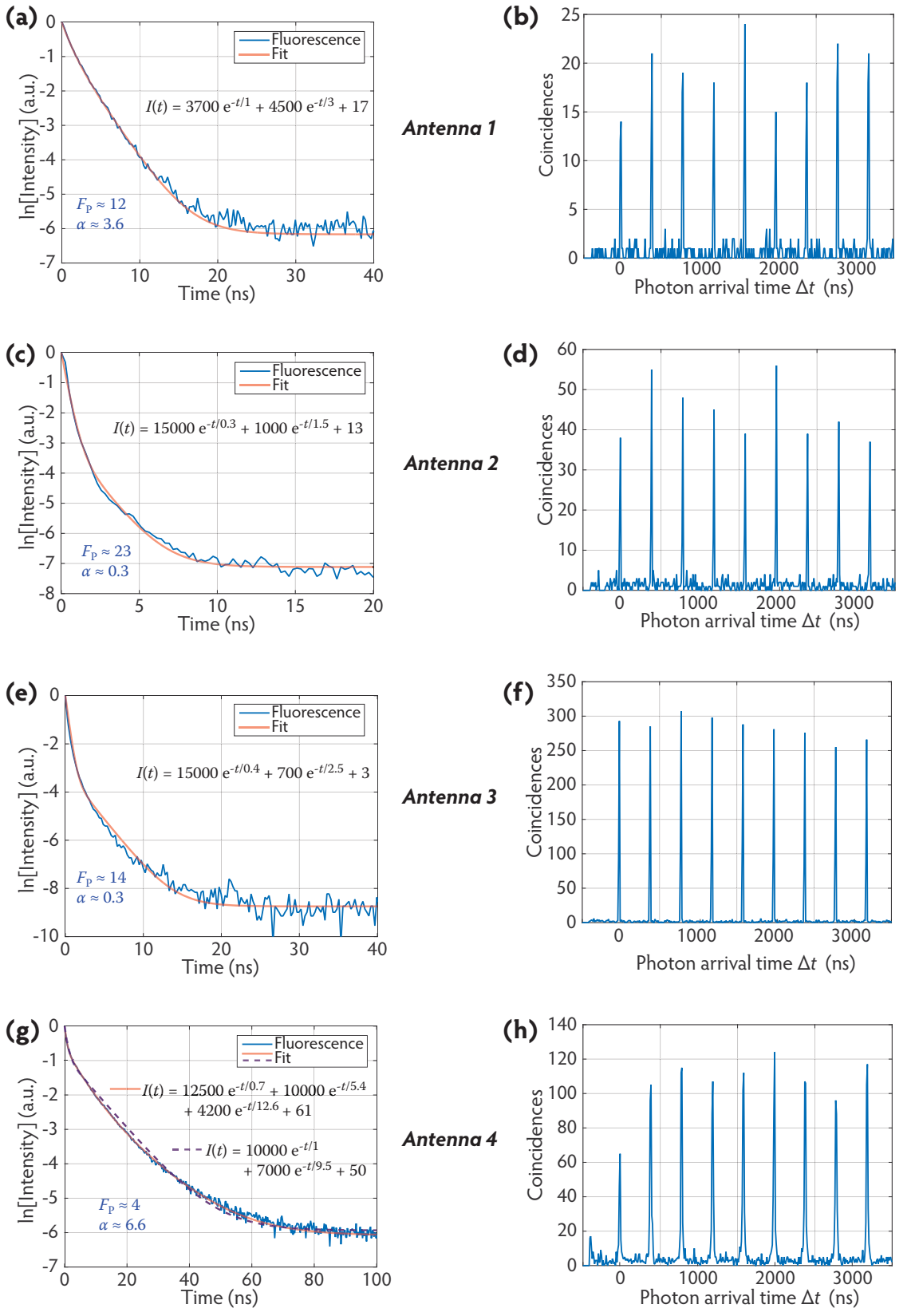

Figure 3.26 *Lifetime and photon antibunching measurements on some nanoantennas*
For four patch antennas (numbered 1–4) that were fabricated by in-situ supercontinuum laser lithography, the histograms in the left and right columns show the lifetime and $g^{(2)}$ (Δt), respectively. Compared to the lifetime of a nanocrystal in a homogeneous (~35 ns) medium, the emitter lifetime in all the nanoantennas is reduced. The reduction in radiative lifetime is very pronounced in antennas 1–3. In antenna 4, the exciton lifetime is relatively longer and we observe partial antibunching as displayed in **(h)**. The temporal resolution of the optical measurement setup was 0.3 ns.

3.7.5 Dynamics of antenna emission

From our first study of these patch antennas, we can recognize some general trends based on the values of α and F_p. In the following chapters, we will note if these trends are followed by patch antennas made by our other lithography techniques.

For $\alpha > 5$, the Purcell factor is usually close to 1 and photon-antibunching can be observed. The larger the value of α, higher is the contribution of single photon emission to the total emission. For many antennas, the Purcell factor is about 4 and α is also about 4. Photon antibunching is not very clear from their $g^{(2)}$ histograms. The last case considers antennas whose $\alpha < 1$. Their emission is due to multiexciton (tri-excitons and higher) recombination and they show no photon antibunching.

3.7.6 Perspectives on improving the patch antennas

The simulation results of Figure 1.2 about the Purcell factor of these patch antennas allow us to comment on the acquired results, but the simulation values cannot be in perfect agreement with the real antennas due to the imperfections of the materials involved, which were not taken into account in the simulation. One parameter that is limiting the Purcell factor of the analyzed antennas is the ~45 nm spacer between the bottom 200 nm thick Au layer and the 20 nm thick Au patch. We can reduce the spacer thickness to 30 nm and this will improve the SPP coupling and the realized antennas will benefit from significantly higher acceleration of emission.

For the fabricated antennas, the orientation of the emitter dipole, which is very crucial for achieving high acceleration of emission, was not estimated. Therefore, it is difficult to relate the emitter orientation with the antenna characteristics. In the future, using polarization analysis, we will estimate the nanocrystal dipole orientation of the single nanocrystals and fabricate patch antennas using well-oriented nanocrystals. For antennas with vertically aligned emitter dipoles, we expect a ten times increase in the Purcell factor. We do not have the radiation pattern measurements of these antennas to comment but this will be accomplished very soon. Finally, the knowledge of emitter orientation (known by polarization analysis) and patch size (0.2–2.5 μm, controlled by lithography and measured by AFM) will result in a significant optimization of these patch antennas.

One motive behind the fabrication of the plasmonic nanoantenna was to achieve accelerated single photon emission. In our antennas, we observe an acceleration of emission, which makes the antenna brighter, but it seems to be at the cost of loss of single photon emission. This effect is very pronounced because already the nanocrystals used in these antennas, due to their large size, have a tendency to show radiative multiphoton recombination. It may be possible to find emitters which show both acceleration of emission and single photon emission when they are positioned appropriately in the antennas. Smaller CdSe/CdS core/shell nanocrystals seem appropriate to begin with. As our technique can work with other type of emitters like nitrogen vacancy centers in nanodiamonds, patch antennas can be made with these emitters as well.

3.8 Conclusion

Performing deterministic optical lithography on single emitters involves several challenges. Developing the technique of deterministic in-situ optical lithography with a defocused superc-

ontinuum laser allowed us to fabricate several single emitter plasmonic patch antennas. More control over the fabrication process will allow effective comparison of these patch antennas with their simulation studies, thus providing better insight into the involved physics. It would be interesting to use emitters like nitrogen vacancy centers in nanodiamonds, rare-earth doped emitters, and other quantum dots. This should reveal some additional information about the concerned emitter. A comparative study of patch antennas using different kinds of emitters can be very informative. The first studies of the fabricated patch antennas have opened ways for optimizing these patch antenna structures to achieve higher Purcell factors, decrease the excitation threshold, and increase the light–emitter interaction. The developed lithography technique can be used for fabricating other photonic structures as well, especially those involving deterministic lithography on single emitters.

4 Electron-beam Lithography

This chapter will describe the second technique that we have developed for fabricating plasmonic nanoantennas. The technique can be used to synthesize a variety of nanophotonic structures, especially single emitter structures such as nanoantennas, Tamm structures, and other photonic cavities with a fluorescent emitter inside. It uses a combination of e-beam and in-situ optical lithography on a resist bi-layer.

To establish the protocol, the initial e-beam test experiments were carried out at the cleanroom of Laboratoire Matériaux et Phénomènes Quantiques (Paris) with the valuable help of Cherif Belacel and Stéphan Suffit. The first successful test of the entire protocol used the e-beam treatment done by Michael Rosticher at the cleanroom of École Normale Supérieure d'Ulm (Paris). To finalize and improve the protocol, most of the e-beam experiments were carried out at the cleanroom of INSP with the generous help of Loïc Becerra. The optical lithography was performed as described in the previous chapter.

Our new lithography procedure has permitted the production of patch nanoantennas with very good control over the patch size and shape. As e-beam lithography offers high resolution and superior control over optical lithography, our method, which uses e-beam writing, can be used to fabricate optical structures of different geometries with high resolution. Moreover, the process in its final form has a success rate of 100%, i.e. we are able to confine all the selected emitters within nanoantenna structures. With the final parameters, no visible nanocrystal damage was recorded throughout the protocol.

We begin this chapter with an introduction to e-beam lithography, our protocol that combines it with in-situ optical lithography and leads to the fabrication of single emitter plasmonic nanoantennas, and related issues. The lithography is done on a resist bi-layer that consists of a stack of LOR® and PMMA but unlike our other protocols, this technique does not burn the resists as such. The incident e-beam exposes the PMMA in a specific region, which is then removed chemically. Given our experience with resist bi-layers and the lack of suitable resists for the task, we decided to work with a resist bi-layer of LOR® and PMMA. The low luminescence of LOR®, its insensitivity to photo-exposure (unlike photoresists), and the ease

of burning it by laser light makes it possible to image fluorescing nanocrystals beneath it and the optical lithography on it.

4.1 Principle of e-beam lithography

As the name suggests, e-beam lithography uses an electron beam to create nanoscale and microscale patterns. The de Broglie wavelength of an electron accelerated to an energy of 25 keV is only 0.0074 nm. As a result of the low wavelength of electrons, the diffraction effects are negligible, which means more precise and controlled lithography [176]. This is the main advantage of e-beam lithography over optical lithography—in the latter, the diffraction effects limit the lithographic resolution. E-beam lithography has been shown to work at resolutions below 5 nm [177].

E-beam lithography is based on the principle of operation of SEM, which was first introduced in its modern form by Zworykin, Hillier, and Snyder in 1942 [178, 179]. E-beam instrumentation was developed in the late 1960s by modifying the SEM apparatus [180]. In our fabrication protocol, the e-beam lithography is done on PMMA, which was first used as an electron resist by Hatzakis in 1969 [181]. This discovery highly increased the application of e-beam lithography in circuit design [182].

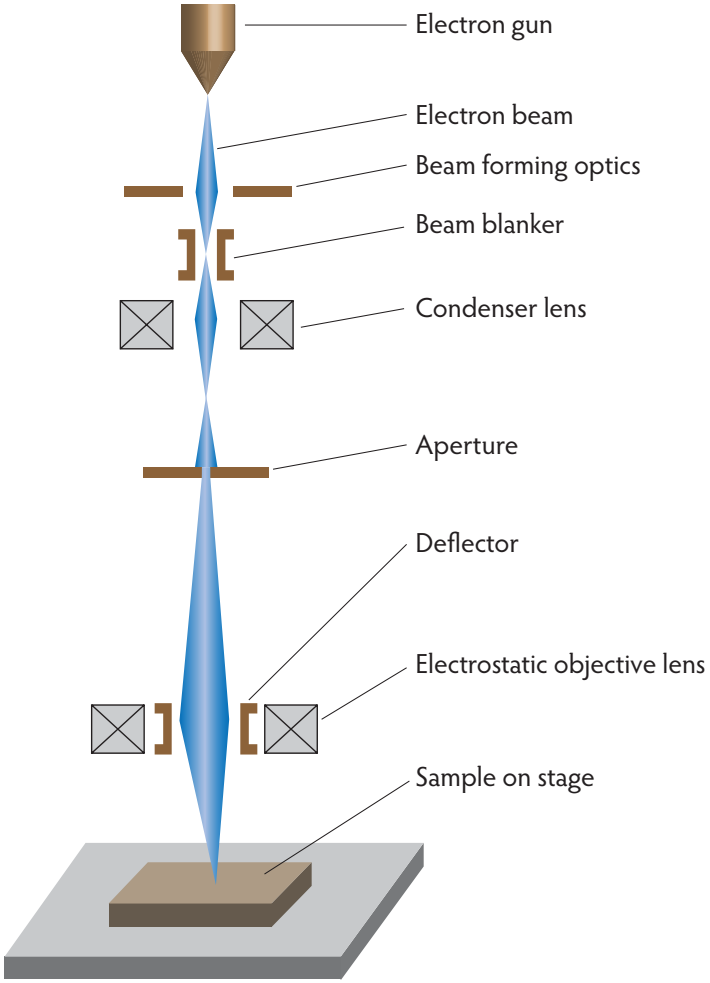

Figure 4.1 *E-beam column*

The schematic demonstrates the principle of e-beam lithography. The image has been adapted from [183].

Figure 4.1 is an illustration of an e-beam column. The electron source or gun emits a beam of electrons, which passes though some beam-forming optics and goes through a beam blanker. The beam blanker can rapidly turn the beam on/off. The condenser lens and the aperture modify the beam shape and diameter. Further, the beam is deflected by the deflector and focused by the electrostatic objective lens to expose selected regions on the sample, which usually rests on a movable stage. The e-beam energy, its shape and size, and the exposure time are chosen according to the resist and the requirements. After the exposure of the resist on the sample, the exposed regions are etched.

The movement of the sample stage can be controlled precisely by laser interferometry [182] or with some basic motion capabilities. Precise motion control enhances the lithography possibilities. In the case of a basic movement stage, the entire lithography area has to be treated by using electron beam deflection, which is limited. We have used such a stage but as our treatment area was less than $100 \times 100\ \mu m^2$, the e-beam deflection was sufficient to cover the entire area precisely.

E-beam machines can be dedicated e-beam lithography machines or converted SEMs that have added components for e-beam lithography [182]. Dedicated e-beam lithography machines offer higher electron acceleration (typically up to 100 kV), superior lithographic performance, and are more expensive. Converted or adapted SEMs allow relatively lower electron acceleration (typically up to 30 kV) but are a very cost effective solution. We have used Zeiss® adapted SEMs for the task. Most of our work, and all the work discussed in this thesis was performed at INSP using a Zeiss SUPRA® 40 converted SEM with a GEMINI® electron optical system [184].

4.2 Protocol for deterministic e-beam lithography on individual nanocrystals

Our technique uses a combination of optical and e-beam lithography to deterministically position metal patches on individual nanocrystals. Firstly, we will discuss the reasons for selecting this fabrication strategy, and then the protocol will be described. Then in the following section (section 4.3), relevant results obtained at different stages of the protocol will be presented.

4.2.1 The fabrication strategy

For e-beam lithography using SEM, the natural choice for deterministic positioning is cathodoluminescence. The group of Reitzenstein has reported deterministic in-situ e-beam lithography on individual InGaAs quantum dots [185, 186, 187]. Our CdSe/CdS quantum dots are cathodoluminescent but performing cathodoluminescent experiments on them can alter their photoluminescence properties. In his work [67], Dijksman discusses how just one cathodoluminescence experiment on CdSe/CdS quantum dots blue-shifted their photoluminescence spectrum by 10–16 nm and reduced their lifetime by a factor of 7–8. It should be noted that doing cathodoluminescence experiments on nanocrystals can damage them and cause very rapid photobleaching. This is due to their interaction with electrons, which is far more devastating than interacting with photons as in the case of fluorescence. Due to the

non-availability of a cathodoluminescent measurement setup in our SEM, and for the mentioned reasons, we did not pursue e-beam lithography based on cathodoluminescent deterministic positioning. However, it would be interesting to explore this option as well.

Our main concern when performing e-beam lithography on nanocrystals was their damage by the electrons of the e-beam. If a polymer, such as PMMA, is used as an electron resist, the penetration of depth of electrons can be of the order of 100 nm and 12 µm when the accelerating voltages are 2 kV and 30 kV, respectively [188]. To avoid this issue, we adapted the resist bi-layer protocol for e-beam lithography. With the help of the LOR® layer in the resist bi-layer stack, the separation between the nanocrystals and the surface could be increased. For this bi-layer, we found the appropriate voltage and charge dose values that could expose the PMMA layer without damaging the nanocrystals. Thanks to the low luminescence of LOR®, we could deposit a sufficiently thick layer of LOR® and observe the fluorescing nanocrystals beneath it.

Using our experience with optical lithography on a resist bi-layer, we adapted the same protocol to work with e-beam lithography. This has two main advantages:

1) For deterministic e-beam lithography on a substrate, alignment marks have to be created on it. The marks are usually created by e-beam exposure and etching of the exposed regions, and this is followed by metal deposition in the etched regions [189]. By adapting our optical lithography protocol, we create the alignment marks by optical lithography, thus avoiding the extra etching and deposition processes. Before the sample is exposed to an e-beam, it has to be imaged by fluorescence microscopy—at this step, we make the alignment marks as well.

2) Our previous knowledge about resist baking, development and lift-off, and Au deposition can be incorporated directly into this protocol, therefore saving the effort of devising new strategies.

4.2.2 The protocol

Described below are the steps of the protocol to fabricate plasmonic patch nanoantennas that use a single nanocrystal as an emitter. We refer the reader to the general fabrication protocol given in section 3.1 for the procedures that are common between the general protocol and this method. After discussing the protocol, we will focus on the crucial aspects of e-beam lithography on our structures in the following section. The protocol is illustrated in Figure 4.2(a).

1) The sample is prepared as described in the general protocol (points 1) to 3) of section 3.1). The resist bi-layer consists of LOR® 5A (500 nm) + PMMA (50 nm). We are at the end of step **1** of Figure 4.2(a).

2) At step **2** of Figure 4.2(a), the sample is imaged by fluorescence microscopy and the single nanocrystals are observed. An area with an appropriate density of nanocrystals is chosen, and at the edges, three 2D lattices of holes are burnt with the laser. One corner hole from each lattice serves as an alignment mark for the e-beam lithography. The number of holes in each lattice is different, which makes them distinguishable—this allows us to designate a position to each fluorescing nanocrystal in the CCD camera image and helps us in orienting the sample throughout the protocol.

On our samples, each hole of the lattice was burned by exposing the sample to a 4.5–5 mW CW 405 nm laser for 3 s. The size of the imaged area depends on the field of view of the CCD camera and the optical setup. The samples were imaged with a 100× objective. Given our optical setup, the 1392 × 1040 pixels on the CCD camera image corresponded to a real size of 92.17 × 68.86 μm^2 . From this we deduce the length of 1 pixel on the CCD camera image as 66.21 nm.

3) From the CCD camera image of the nanocrystals and the alignment marks, an e-beam exposure pattern is created using a compatible software. The image dimensions are calibrated and its center is treated as the origin. The nanocrystals to be exposed are assigned the coordinates accordingly. Around each nanocrystal, the shape to be exposed is drawn. For example, we drew many circles of diameters 600 nm, 1000 nm, and 1500 nm centered on different nanocrystals. On the fluorescence image, markers or flags are placed at the respective centers of the three alignment holes. We had used *Raith ELPHY Quantum* software for the task [190].

4) The sample is scanned rapidly with SEM and the alignment lattices are observed. The scanning should be quick and very optimized because a slow scan or multiple scans on the same area, especially at a high voltage, can expose the scanned PMMA and render the area useless for lithography. After zooming in on the alignment holes, the marker positioning is confirmed, thus making the SEM output correspond with the fluorescence image via the e-beam software. The e-beam is cut temporarily. The writing procedure then commands the e-beam to expose the pattern with the designated exposure charge doses. This process takes about 1 minute. Mentioned below are the e-beam parameters that we had used:
   - Voltage = 10 kV
   - Working distance = 8 mm
   - Aperture = 10 µm
   - Writefield = 100 µm
   - Number of vertices per circle = 128
   - Exposure dose (also called area dose, see Table 4.1)

Circle diameter (nm)	Exposure dose (µC/cm^2)
600	45
1000	40
1500	30

Table 4.1 *Exposure dose for e-beam lithography*

These charge dose values were found after studying the parameters for sufficient PMMA exposure without deteriorating the nanocrystal fluorescence. For example, in the ϕ=1500 nm circles, the dose of 45 µC/cm^2 destroyed the fluorescence of the nanocrystal in many cases, whereas with a dose of 30 µC/cm^2 , all the nanocrystals survived and the e-beam treatment was effective.

5) After the e-beam exposure, the sample is taken out of the machine, and immersed inversely and shaken in a bath of MIBK and isopropanol (mixed in a ratio of 1:3) for 45 s at 20–21°C. Then the sample is cleaned by immersing it in a bath of isopropanol, and is blow-dried. This procedure removes the exposed PMMA, and marks the end of step **3** of Figure 4.2(a).

6) The procedure of points 5) to 7) of the general lithography protocol (section 3.1) is followed, and several patch antennas with three different patch sizes are obtained.[4]

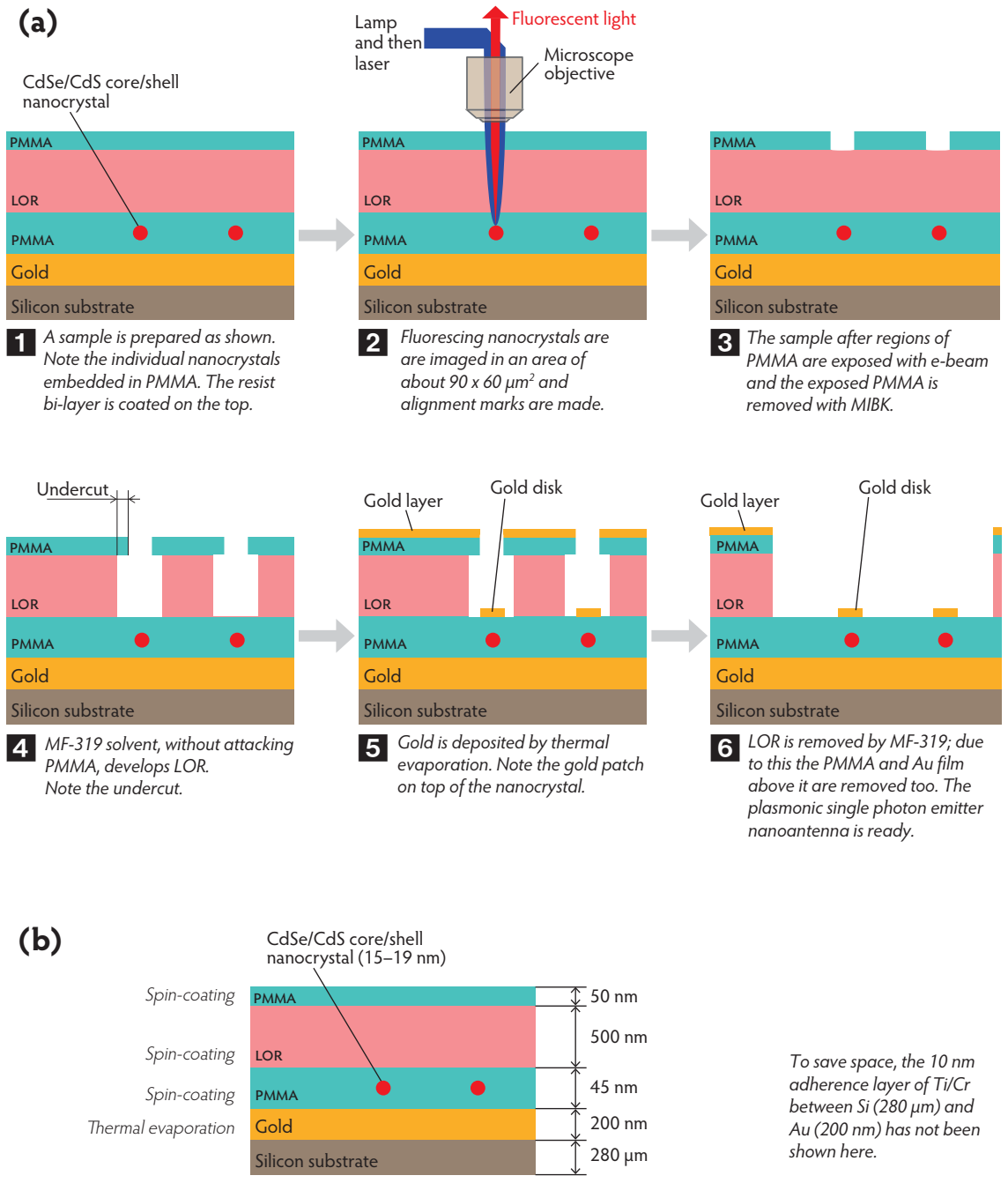

Figure 4.2 *Optical and e-beam lithography protocol*

Figure **(a)** illustrates the lithographic protocol. Figure **(b)** shows the thickness of the layers and their deposition method.

[4] By comparing the sample state at step 3 of the protocols illustrated in Figures 4.2(a) and 3.1(a), it can be said that the minimum development time required by the e-beam lithography protocol is longer than the latter. This is because the development process at step 3 of Figure 4.2(a) has to remove a 500 nm deep layer of LOR®, whereas this is not the case at step 3 of Figure 3.1(a), where the hole burnt by the laser is already deep. Our experimental results show that a development duration between 5 to 10 s is fit for both the cases.

4.3 Aspects of the e-beam lithography method

This section will deliberate on the main issues that were treated during the development of this new technique that combined fluorescence imaging, optical lithography, and e-beam lithography to attain single emitter plasmonic patch nanoantennas. The topics of drawing e-beam writing patterns on fluorescence microscopy images, the accuracy of the technique, e-beam charge dose for the exposure of PMMA, the penetration of e-beam electrons into the resist bi-layer, and the development of LOR® will be discussed.

4.3.1 E-beam pattern on fluorescence images

An area with a good distribution of single nanocrystals is selected on the sample, and the alignment marks are burnt by optical lithography (Figure 4.4). On almost each individual nanocrystal in this image, we would like to place a gold patch of a specific size and shape. To do the mentioned, the 50 nm thick PMMA layer above each nanocrystal (the nanocrystal and the 50 nm thick PMMA layer are separated by a LOR® layer) has to be exposed locally by the e-beam. To carry out the e-beam writing task, the fluorescence image is used as a base on which the e-beam exposure pattern is drawn. Treating the center of this image as origin and using the total real image size, we can assign position coordinates to each nanocrystal and alignment marker. After the sample area is scanned by SEM, we update the position of the three alignment markers on the SEM scan and make the SEM scan image correspond with the fluorescence image. In this way by using the position of a specific nanocrystal on the fluorescence image, we can command the e-beam to go to that nanocrystal on the sample.

The precision with which the Au patch can be placed on the nanocrystal depends on the accuracy of designating coordinates to individual nanocrystals in the fluorescence image, the precision with which the position of the alignment marks can be confirmed in the SEM scan, and finally the precision with which the e-beam can be deflected to a given distance. The following text will treat these topics in detail.

4.3.1.1 Measuring distances on fluorescence images

At step **2** of the protocol (Figure 4.2(a)), after creating the optical marks, the fluorescence image of a sample looks as depicted in Figure 4.4. During the fluorescence imaging and optical lithography procedure, the sample is attached to a piezoelectric stage that has a motion resolution of 1 nm. To create the 4×4 lattice, as shown in Figure 4.4, the sample was brought to focus, and the stage was instructed to move a distance of 10 μm in four steps in the x and y directions. At each point, the stage was brought to rest for 3 s and during this time the 405 nm CW laser at 4.5–5 mW burned the resist bi-layer. After resting for 3 s, the piezoelectric stage takes 10 ms to move to the next position, where it rests for another 3 s. When the stage is in motion (in the 10 ms interval), the laser is automatically turned off. The other two lattices were made in a similar way. As the maximum travel distance of the piezoelectric stage is only 15 μm, additional motion assembly is required to displace the sample by larger distances. The piezoelectric stage is connected to another larger stage, which can be moved mechanically using the attached micrometer motion controller. In this way, we move from one lattice to another. As this is done manually, the lattices are not perfectly aligned but this does not affect the lithography because only one corner hole from each lattice is selected as an alignment marker.

A well-aligned TEM_{00} laser mode isotropically burns very circular holes into the resist bi-layer. Figure 4.6(b) shows the SEM image of such a hole ($\phi \approx 1\,\mu m$) made by our 405 nm laser into the resist bi-layer. The center of these circular holes is clearly distinguishable in AFM, SEM, and optical microscopy images. And we have used this attribute to accurately measure distance with AFM and correspond them with optical microscopy images, thus making it possible to assign accurate distance calibration to optical images.

4.3.1.1.1 Accuracy of piezoelectric stage motion

We use the accuracy of the motion of the piezoelectric stage and the lattice size to determine the number of pixels in one lattice length, and from this we deduce the length of 1 pixel on the CCD camera fluorescent microscopy image. We made several AFM measurements that confirmed the precision and trueness of the piezoelectric stage movement. Figure 4.3 shows an AFM measurement on a sample on which the piezoelectric stage was instructed to make 4×4 matrix or lattice of a length of 15 µm. The AFM measured this distance as 14.99 µm, which is very close to the instructed value of 15 µm.

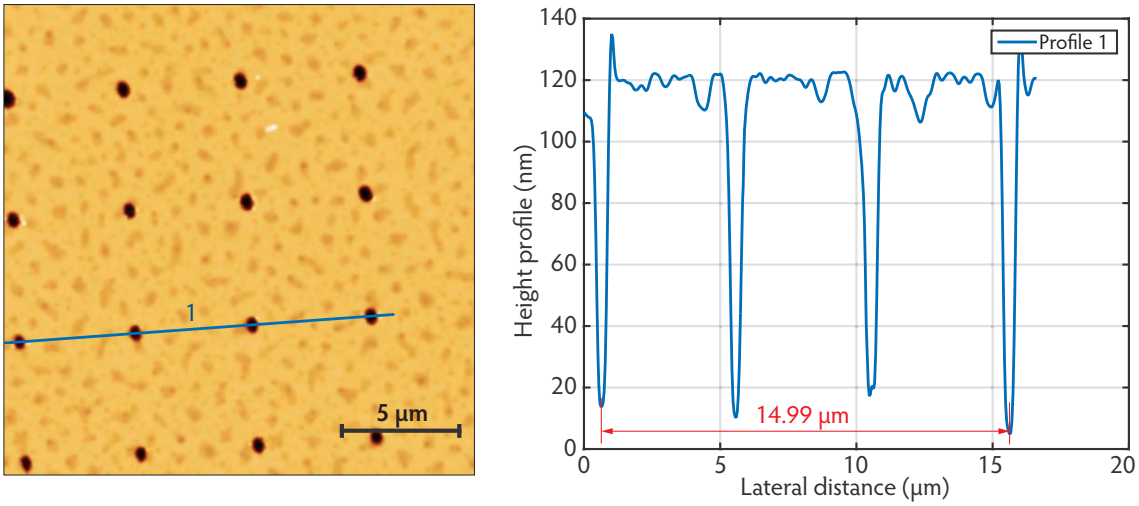

Figure 4.3 *AFM confirmation of the accuracy of piezoelectric stage movement*

Figure **(a)** is an AFM height image of the surface of a resist bi-layer into which holes were burnt by a laser. The piezoelectric stage was commanded to set 15 µm of separation between the two outer holes along profile 1. Figure **(b)** shows the height profile along path 1. The distance between the centers of the two outer holes, as measured by AFM, was 14.99 µm. This value is very close to the nominal value of 15 µm, thus verifying accuracy of movement of the piezoelectric stage.

4.3.1.1.2 Distance calibration on fluorescence images

We use the AFM verified accuracy of the piezoelectric stage movement and appearance of the burned holes in fluorescence images to assign a calibration scale to the fluorescence image and measure distances on it. With our measurements on a sample, we found that:

$$10\,\mu m \text{ of real distance} = 151 \text{ pixels} \tag{4.1}$$

which we have used as the calibration scale for our fluorescence images that were recorded under similar conditions. Using this scale, the total size of the 1392×1040 pixels CCD camera

image is noted as $92.16 \times 68.85\ \mu m^2$ and the length of 1 pixel is deduced as 66.2 nm. These values are entered in the e-beam lithography software along with the fluorescence image. The estimation of these values was extremely important because the accuracy of e-beam writing depends directly on them.

Figure 4.4 shows a sample on which three lattices of 10 µm side length were burned as described in section 4.3.1.1. Using the scale of Eq. (4.1), we noted the displayed distances. By digitally zooming in on an image, we increase the measurement resolution. After digital magnification of the fluorescence image, the center of the circular hole or the fluorescence spot of a nanocrystal can be pointed out clearly and distances can be measured.

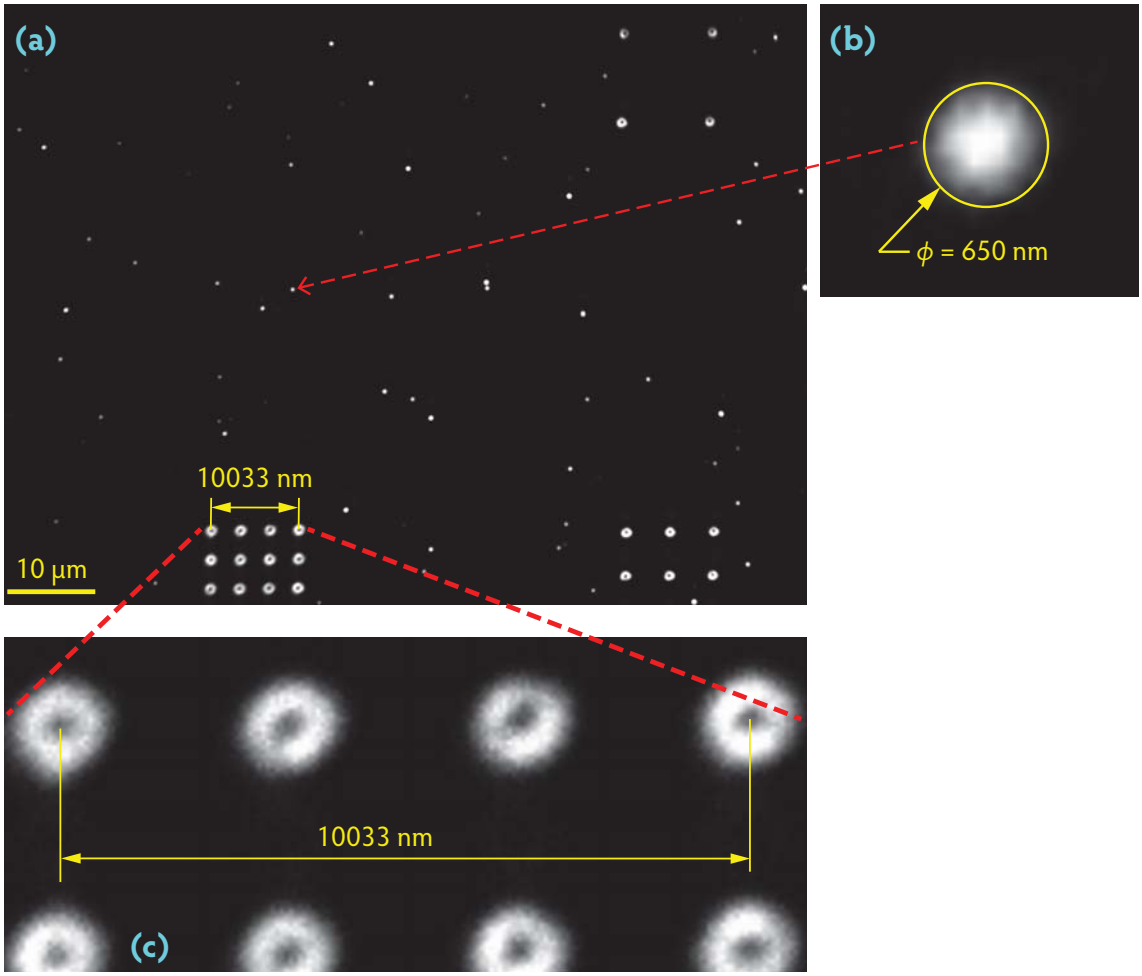

Figure 4.4 *Florescence image with optical alignment marks*

Figure **(a)** is a fluorescence microscopy image recorded using a 100× objective. Note the three lattices with 4×4, 3×3, and 2×2 holes (not all the holes of the lower matrices are visible). One corner hole from each of these lattices serves as an alignment marker. The white dots in the image are fluorescing individual nanocrystals. Figure **(b)** is a digitally magnified image of the nanocrystal pointed in **(a)**. The yellow circle superimposed on the fluorescent spot of a nanocrystal has a diameter of about 650 nm. Note that the 15–19 nm thick nanocrystal is at the center of the circle—this allows us to specify the position of the nanocrystal with accuracy. Image **(c)** is a digitally magnified image of the laser holes of **(a)**. As each of these holes is larger than the optically limited size of the measurement setup, and the edges of the hole fluoresce more than the center, these hollow holes appear like *rings*. Calibrating the length of 151 pixels to 10 µm, the center to center distance between the holes was measured as 10.033 µm, which is very close to the nominal value of 10 µm.

Based on the comparison of distances measured by AFM with the distances measured on the fluorescence images (using the calibration scale described above), we estimate that the error in distance measurement on the CCD camera fluorescence image is less than 0.5%. This accuracy is due to the trueness of the piezoelectric stage motion (which was justified by AFM imaging) and its precision (that was confirmed by measuring multiple movements), and finally on the accuracy of digital zooming.

4.3.1.2 E-beam exposure pattern

The fluorescence microscopy image is opened with an e-beam lithography software. The image size and the nanocrystal and alignment marker coordinates are decided designating the center of the image as the origin and using the real value of the length of a pixel.

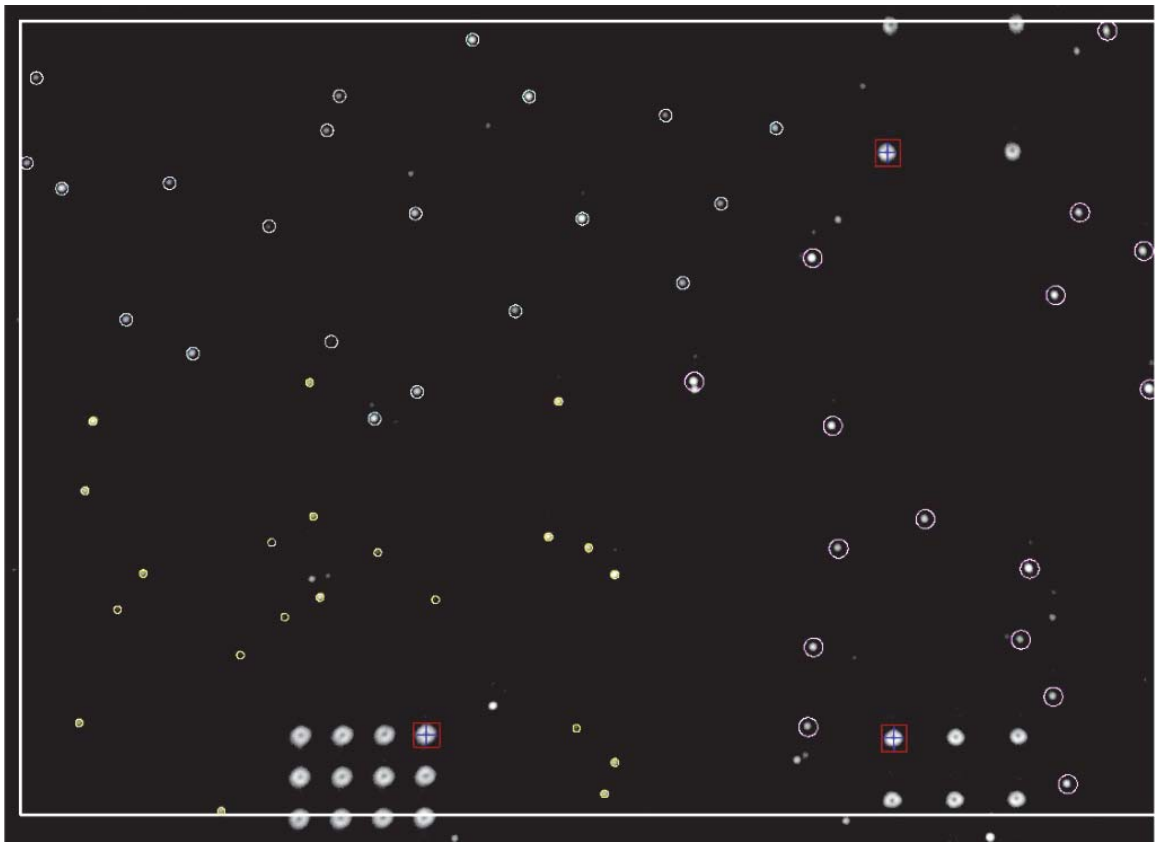

Figure 4.5 *E-beam exposure pattern on a fluorescence image*

The image is a screenshot of the e-beam exposure pattern made using *ELPHY Quantum* software. The yellow (ϕ=600 nm), cyan (ϕ=1000 nm), and pink (ϕ=1500 nm) circles were respectively exposed with a dose of 45, 40, and 30 μC/cm^2 . Each circle was centered on the digitally magnified image of the nanocrystal fluorescent spot as shown in Figure 4.4(b). Due to aliasing and low resolution rendering of the screenshot image above, some circles may not seem exactly centered on the nanocrystals. This is just a visual effect produced in the screenshot image. Actually, the circles were very well centered on the nanocrystals. Note the three flags on the alignment marks—one in each lattice. The white boundary in the image indicates the working area.

To use a nanocrystal as an antenna emitter, the PMMA above the nanocrystal should be exposed locally to the e-beam. To set the exposure area, we digitally zoom in on a nanocrystal in the fluorescence image, and place the exposure region with respect to the center of

its fluorescence spot. We have worked with three exposure regions, which were circles with different diameters. Other shapes such as ellipses, squares, triangles, etc., can also be created and positioned as intended. Using the *elphy Quantum* software, we can assign exposure regions to different writing layers, and the exposure charge dose of each layer can be varied. Once the e-beam writing procedure is run, all the layers are written. Figure 4.5 shows three different exposure regions placed on the nanocrystals. The diameters of the yellow, cyan, and pink circles are 600 nm, 1000 nm, and 1500 nm, respectively.

The blue cross bounded by a red square in Figure 4.5 denotes an alignment mark. There are three such alignment marks that are flagged as 1, 2, and 3, respectively. After these alignment holes are scanned by SEM, the corresponding flags are positioned right at the center of the hole and this ties the movement of the e-beam on the sample to the coordinates on the fluorescence image.

4.3.1.3 Placing markers for e-beam lithography

As the number of holes in different lattices is different, these lattices can be distinguished when the sample is observed with SEM. This helps us visualize the orientation of the sample as placed in SEM, and rotate the sample as required, such that the scanned image of SEM has the same orientation as the fluorescence image. as The distance between the neighboring holes is different in the three lattices. Therefore, when SEM scans are zoomed in on a lattice, we can confirm exactly which lattice it is by noting the difference between the neighboring holes. After discerning the scanned lattice, we zoom in on the alignment hole and place the corresponding numbered alignment marker. We make three alignment marks, which are flagged as 1, 2, and 3—one for a corner hole from each lattice.

With every SEM scan we risk exposing the 50 nm thick PMMA layer. As the lattices are scanned a few times for placing the flags, the scanned areas on the PMMA layer are exposed. Due to this undesired but unavoidable exposure, the regions for e-beam writing (the circles to be exposed) should be positioned at least 10–15 μm away from the alignment marker.

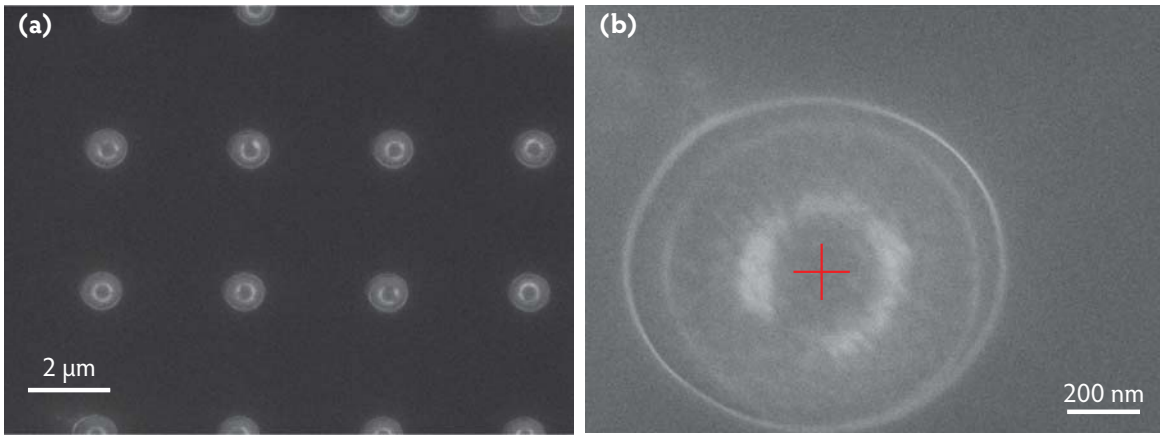

Figure 4.6 *Alignment marker for e-beam lithography*

Figure **(a)** is a SEM scan of a 4×4 lattice, and **(b)** is a magnified scan of the alignment hole from this lattice. The overlaying red cross marks the position of the flag. The accuracy of positioning the flag influences the accuracy of e-beam writing.

How well the alignment markers are placed on the alignment holes scanned by SEM (Figure 4.6(b)) sets the degree of matching between them and the alignment flags on the fluorescence image (Figure 4.5), and therefore affects the accuracy of e-beam writing. Figure 4.6(b) shows that with the help of SEM scans at high magnification and the circular shape of the alignment hole, an alignment marker can be placed accurately at the center of the alignment hole. This results in higher accuracy of the e-beam lithography process.

4.3.2 Accuracy of e-beam deflection

In sections 4.3.1.1 and 4.3.1.3, we discussed two factors—distance measurement on fluorescence images and placement of alignment markers on SEM scans—that influence the accuracy of the e-beam lithography process. Another factor that affects the accuracy of the process is the accuracy of e-beam deflection. To expose different areas on the substrate we rely upon e-beam deflection. At the beginning of the writing process, the e-beam is at the origin (which corresponds to the center of the fluorescence image). Once the writing command is run, the e-beam is deflected to expose the regions of interest.

We perform the e-beam lithography at 10 kV, at a working distance of 8 mm, and with a 10 μm aperture. With these settings, if the e-beam is deflected such that it travels a lateral distance d on the sample then the accuracy of this movement is 0.08% of d [191]. On our samples, the maximum distance covered by the e-beam from the origin is 50 μm, therefore the maximum error due to the e-beam deflection is less than 40 nm. Most exposure regions are less than 30 μm from the origin, therefore the error in positioning the exposure patch is less than 24 nm in most cases.

To reduce the impact of the error due to e-beam deflection, it is preferable to position the small patches of ϕ = 600 nm near the origin, and the large patches of ϕ = 1500 nm far from the origin. In this way we reduce the error in centering the patch over the nanocrystal.

4.3.3 A note on the accuracy of e-beam writing

The error in the accuracy of e-beam writing is mainly due to the calibration of distances on the fluorescence image (section 4.3.1.1) and because of the error in e-beam deflection (section 4.3.2). The total error is decided by taking into account the error due to these two factors. The error due to the positioning of the alignment markers is negligible compared to these two.

Our calculations estimate that the maximum uncertainty in positioning a nanocrystal at the center of a circular region using this protocol is 150 nm. By looking at the fluorescing nanocrystals inside the ϕ = 1000 nm and the ϕ = 1500 nm holes on three samples (where it is possible to distinguish between the nanocrystal fluorescence spot and the edge of the hole), we confirmed that in most cases the positioning error was less than 100 nm. The accuracy of this protocol may be enhanced by using more appropriate imaging optics and piezoelectric stage with a larger travel distance.

4.3.4 Exposure dose

The exposure dose parameter decides the charge per unit area in the exposed or dwelled region. To estimate an appropriate value of the exposure charge dose, a regular sample (as

shown in Figure 4.2(b)) was prepared and several circles with ϕ = 1 µm were dwelled. The dose on these circles was varied from 1 µC/cm^2 to 225 µC/cm^2 . After exposing regions on the 50 nm thick PMMA layer with the e-beam, the exposed areas were chemically etched and observed with reflection microscopy (Figure 4.7). By means of image contrast, we noted signs of etching in circles that were exposed to charge doses of 30 µC/cm^2 and higher.

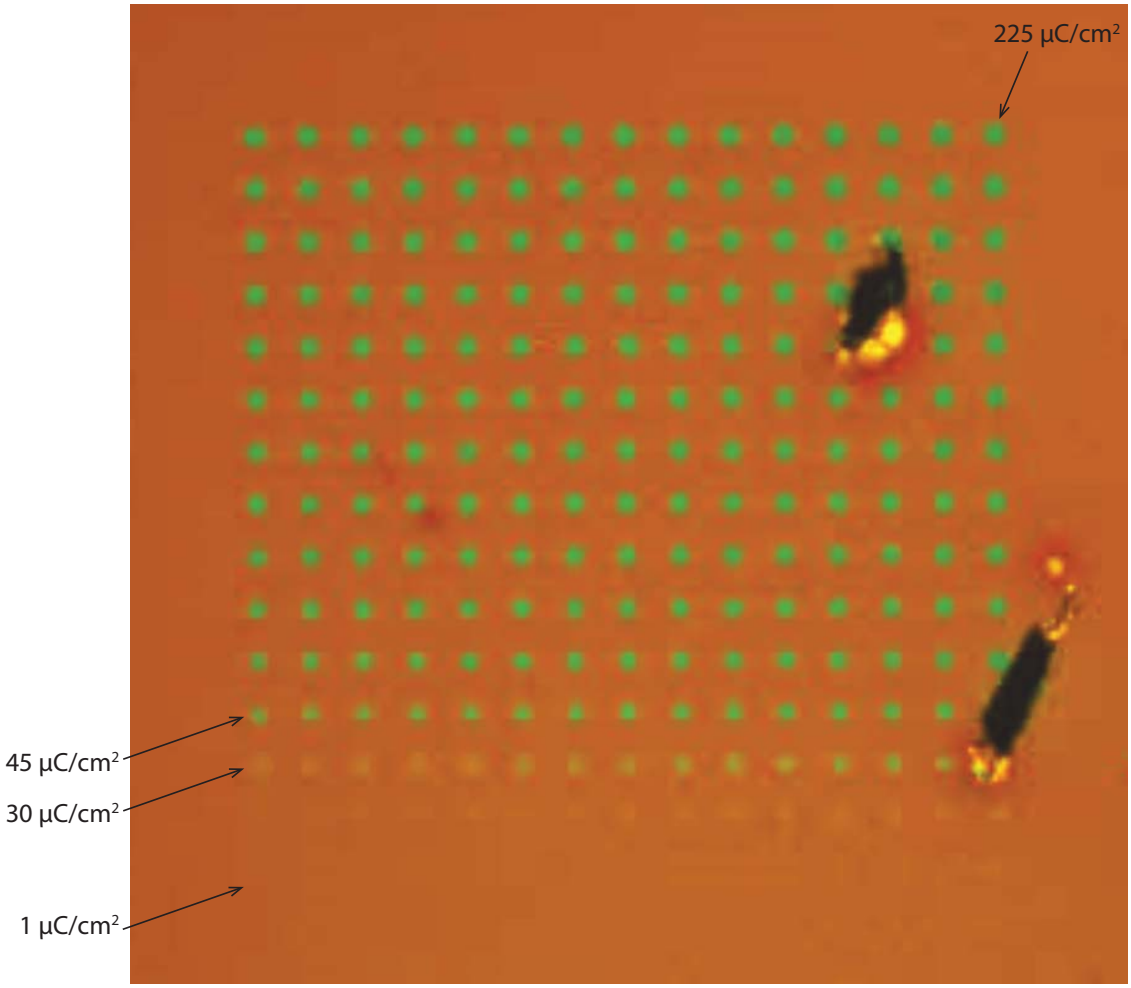

Figure 4.7 *PMMA exposure with different area doses*

The figure depicts a colored reflection microscopy image of the sample on which circles of 1 µm diameter were exposed by e-beam, and the successfully exposed areas were chemically etched. Green spots in the image are successfully etched areas. The 50 nm thick layer of PMMA was exposed to charge doses varying from 1 µC/cm^2 (invisible lower left circle) to 225 µC/cm^2 (top right circle) with an increment of 1 µC/cm^2 . Mild signs of exposure can be seen at 30 µC/cm^2 , and clear exposure can be seen from 45 µC/cm^2 . The two black irregular marks seem to be due to accidental scratches on the sample surface.

As shown by Figure 4.7, the dose of 45 µC/cm^2 seemed appropriate and was selected as the exposure dose. Though reflection microscopy gave information about the signs of PMMA etching, it did not confirm if the PMMA layer in the exposed regions was etched till the bottom, such that the development of LOR® could be carried out. Figure 4.8 illustrates incomplete and complete PMMA etching. To confirm if the PMMA etching was complete, several areas were exposed and etched on another sample with a dose of 45 µC/cm^2. The sample was then put in a bath of MF®-319 for 5 s and then washed with water. By fluorescence microscopy, we

observed that the LOR® in all the holes was developed, thus confirming that the 50 nm thick PMMA layer was etched till the bottom as depicted in Figure 4.8(b).

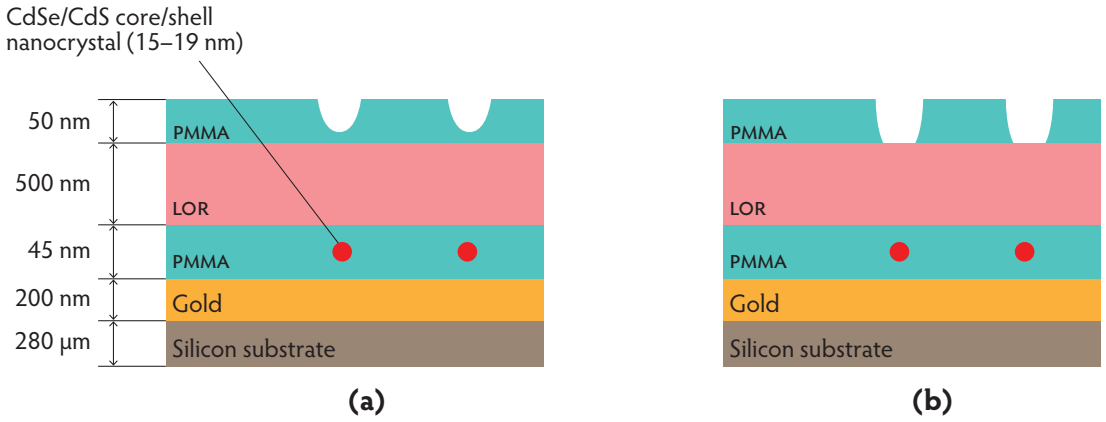

Figure 4.8 *After PMMA etching*

E-beam exposure of certain areas on the 50 nm thick PMMA layer may result in incomplete etching as illustrated in **(a)** or in complete etching as shown in **(b)**. Less than adequate e-beam exposure may result in absolutely no etching at all, which cannot be observed by optical microscopy—this case is not shown here. LOR® below the etched PMMA can be developed only if the PMMA layer is etched till the bottom as demonstrated in **(b)**.

4.3.4.1 Fine adjustment of charge dose

While fabricating the first nanoantennas using an exposure dose of 45 µC/cm^2 on circles of ϕ = 600, 1000, and 1500 nm, after the PMMA etching (step 3 of Figure 4.2(a)), we observed that the nanocrystals in some circles stopped fluorescing. And most of the circles in which the nanocrystals stopped fluorescing were the large circles, mostly with ϕ = 1500 nm and some with ϕ = 1000 nm. Based on the hypothesis that electron charge was damaging the nanocrystals, and the fact that the net charge is more in a larger circle than a smaller circle, we devised of a solution to the problem of damaging of nanocrystal fluorescence after e-beam exposure. In Figure 4.7, it can be noted that the first signs of development begin to show with the dose of 30 µC/cm^2 . Electron scattering should be spatially more widespread when the exposed area has a large diameter. Based on the above stated, we exposed a sample using the doses listed in Table 4.1. These were: 45 µC/cm^2 for ϕ = 600 nm circles, 40 µC/cm^2 for ϕ = 1000 nm circles, and 30 µC/cm^2 for ϕ = 1500 nm circles. After etching the exposed PMMA on this sample, the development of LOR® was successfully carried out in all the circles. By fluorescence microscopy we observed that all the holes had been developed and the nanocrystals in all the holes were fluorescing. On several samples, these charge dose values have given a 100% success rate, i.e., they have exposed the PMMA layer without damaging the nanocrystal beneath.

Our charge dose values (Table 4.1) work for a 50 nm thick PMMA layer, which is produced by spin-coating a 2% [m/m] solution of PMMA in toluene and baking the sample at 150°C for 2 minutes. The weight average molar mass of PMMA was 101 000. The exposure dose is likely to be higher for a thicker PMMA layer. The molecular mass of PMMA also affects the exposure dose.

For e-beam lithography on PMMA resists, Tennant and Bleier recommend a dose of 900 µC/cm^2 at 100 kV [183], and MicroChem® recommends a dose of 50–500 µC/cm^2 in the

energy range of 20–50 kV [192]. To avoid nanocrystal damage due to electron penetration, we expose the PMMA layer at only 10 kV with a dose as low as 30 μC/cm^2. We are able to perform e-beam lithography with low charge doses at low energy because we use a relatively thin PMMA layer, which is only 50 nm thick. For nanoantenna fabrication this solution works very well and offers decent lithography resolution.

4.3.5 Chemical etching of exposed PMMA

After the e-beam exposure of the selected regions on the 50 nm thick PMMA layer, the exposed PMMA is chemically etched by MIBK. The etching takes place at step **3** of the protocol (Figure 4.2(a)). The sample is inserted inverted in a solution of MIBK and isopropanol (ratio 1:3) for 45 s, and then washed with isopropanol and blow dried. Figure 4.9 shows the sample of Figures 4.4 and 4.5 after the exposure and etching of the selected areas on the PMMA layer.

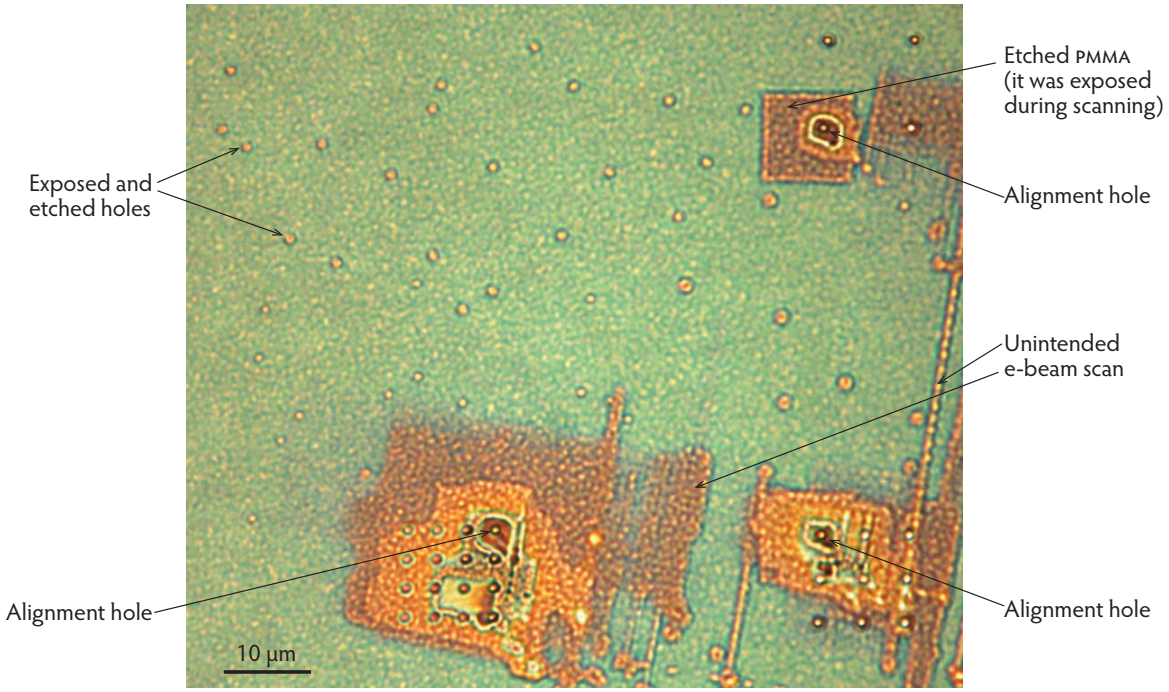

Figure 4.9 *The sample after chemical etching of exposed PMMA*

This is a reflection microscopy colored image of the sample after the e-beam lithography. The circles in the image are regions that were exposed and etched. The diameters of the exposed circles were 600 nm, 1000 nm, and 1500 nm, respectively. Note the 4×4, 3×3, and 2×2 lattices, and the corresponding alignment holes. Note the regions around the lattices which were exposed while scanning. The scanning in the 2×2 lattice was very precise—just the alignment hole was scanned.

Figure 4.10 shows AFM height images of two regions from which the exposed PMMA was removed by chemical etching. We note that the exposed PMMA was well removed. The e-beam used for writing had a Gaussian intensity profile along its cross-section. In the absence of scattering of electrons from the material, the energy distribution into the resist should be a Gaussian like the incident e-beam (or at least show a strong radial dependence) [183]. But due to scattering, it is not the case. However, if the resist layer to be exposed is not very

thick, like in the case of our 50 nm thick PMMA layer, a clean cleavage can be obtained as shown in Figure 4.10(a) and (c). For lithography with higher resolution, higher e-beam energy is recommended [192] but a high energy e-beam can damage the nanocrystals. Therefore, we did not use a high energy e-beam, and moreover, the lithography resolution obtained with our low energy parameters is acceptable. Wenchuang *et al.* have reported improvement in lithography resolution by using cold chemical etching at 4–10°C [193]. It would be interesting to test cold etching on our structures.

The width of the bottom of the PMMA hole decides the size of the nanoantenna Au patch. For a given set of e-beam parameters, the size of the patch can be related accurately to the diameter of the exposure circle. In this way, the patch size can be varied with an accuracy of tens of nanometers.

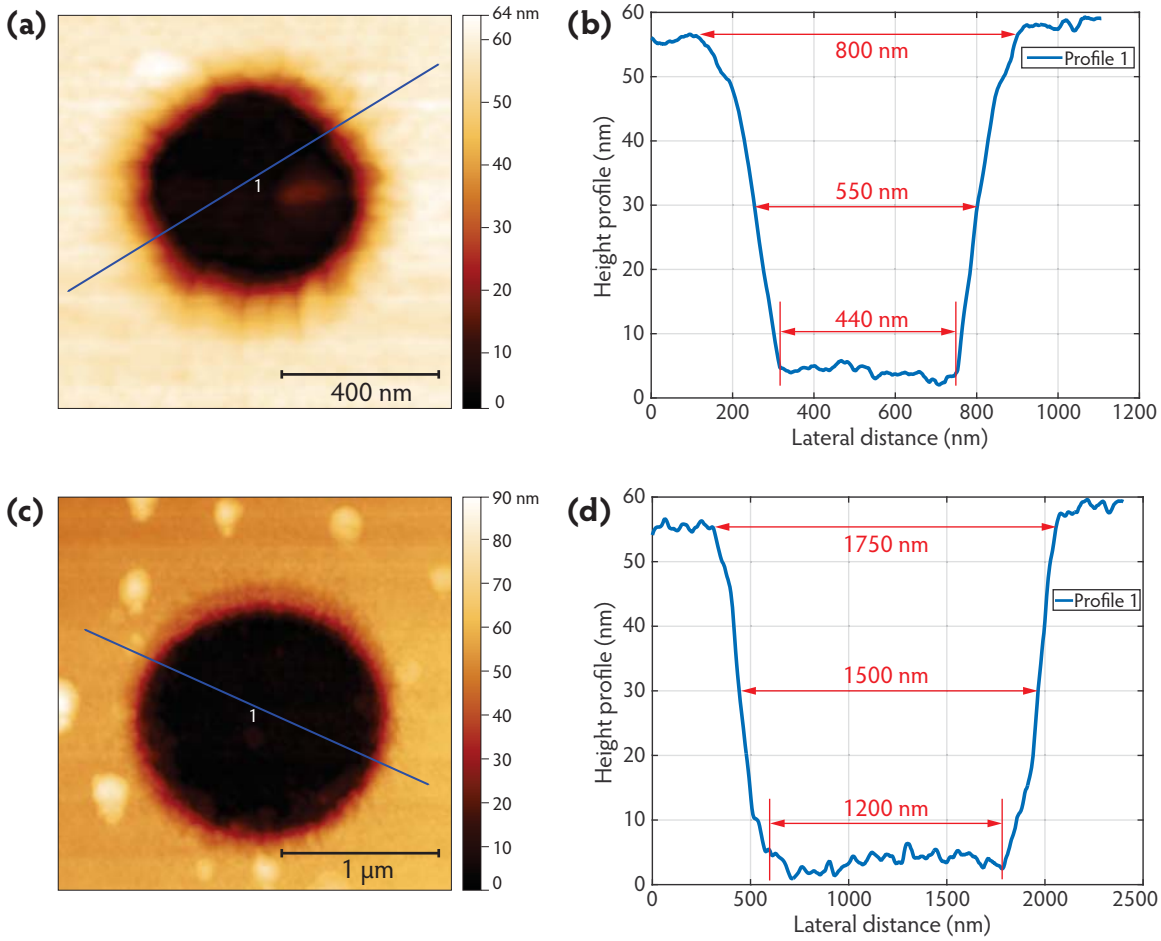

Figure 4.10 *Holes in PMMA made by e-beam lithography*

On a sample, by e-beam lithography, holes were made in a 50 nm thick upper layer of PMMA of the resist bi-layer LOR® (500 nm) + PMMA (50 nm). The instructed exposure areas were circles of ϕ=600 nm and ϕ=1500 nm. Figure **(a)** is an AFM topography image of a ϕ=600 nm exposed area. After etching the exposed PMMA, the hole looks very circular but it is not perfectly cylindrical. Figure **(b)** shows the height profile along path 1 in **(a)**. The removal of the exposed PMMA was thorough. The lower part of the hole is 440 nm broad and its FWHM is 550 nm. Figure **(c)** is an AFM topography image of a ϕ=1500 nm exposed region. The height profile along path 1 is shown in **(d)**. The hole is 1200 nm wide at the bottom, and its FWHM is 1500 nm. The geometry of the bottom of the PMMA hole decides the Au patch geometry.

4.3.6 The development of LOR®

After removing the exposed PMMA, at step 4 of the protocol of Figure 4.2(a), the sample is treated with MF®-319. This results in the development of LOR® from the etched regions. Figure 4.11 shows the sample of Figures 4.4 and 4.5 after the development of LOR®. The removal of LOR® from the developed holes makes the nanocrystals beneath them more visible because the luminescence of LOR® does not contribute to the fluorescence signal.

In Figure 4.11, the 1000 nm and 1500 nm diameter circles are clearly visible as they have even larger darker boundaries after the removal of LOR®. Comparing this image to Figure 4.5, we can even point out the nanocrystals in the 600 nm diameter circles. Their small size provides a small entrance for MF®-319, as a result of which the boundary created after the development of LOR® is also small. The nanocrystal spot is about 650 nm, which is not much smaller than the developed LOR® region boundary. This makes it more challenging to identify ϕ = 600 nm circles in fluorescence images. But upon close examination they become evident, especially when viewed in full colors by directly looking through the microscope eyepiece. Lifetime measurements on the nanocrystals inside all the developed holes confirmed the absence of LOR® in the holes.[5]

Figure 4.11 *A sample after the development of LOR*

This is a fluorescence image of the sample after the development of LOR®, which is a luminescent material. Therefore, its removal from some regions makes them appear darker in the image. This image shows 34 emitters inside developed holes.

[5] If lifetime measurements are made on a nanocrystal lying beneath a layer of LOR®, then the lifetime curve contains contribution of the lifetime of the luminescence of LOR®. As the luminescence lifetime of LOR® is much shorter than the fluorescence lifetime of the nanocrystals, the former can be distinguished from the latter.

We end this section with a note that very fine control over the development of LOR® may require different development times for entrances of different sizes. The development of LOR® creates an undercut in the PMMA layer, whose length depends on the size of the entrance for the developer and the thickness of the PMMA layer [152]. Developing LOR® under a large and a small PMMA entrance for the same time can result in an underdeveloped small entrance or an overdeveloped large entrance (Figure 4.11(b)). As the development time affects the entire sample, it would be good to use one sample per entrance size. That is, for a more controlled development, circles with the diameters of 600 nm, 1000 nm, and 1500 nm may require three different samples.

4.3.7 The thickness of LOR and the deposition of gold

Section 3.5 elaborated on the problem of deposition of a 20 nm thick Au layer on individual nanocrystals sandwiched in PMMA. We concluded that placing the nanocrystals above a 10 nm thick PMMA layer and below a 35 nm thick PMMA layer (as in *sample 3* of Figure 3.18) resulted in successful Au deposition (Table 3.1). Incorporating this result about Au deposition to the supercontinuum laser lithography protocol, many nanoantennas were fabricated. Throughout this protocol, LOR® 3A was used to spin-coat the lower layer of the resist bi-layer. The thickness of this layer was about 300 nm.

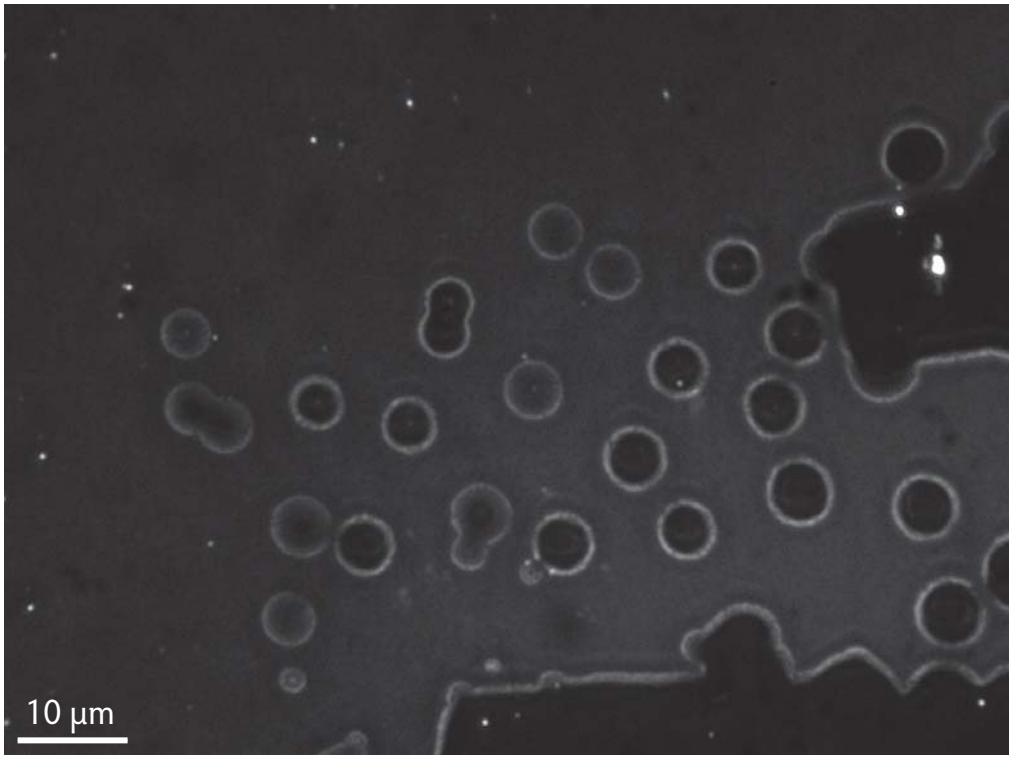

Figure 4.12 *An e-beam lithography sample with LOR3A after lift-off*

The image is a fluorescence microscopy image taken after the lift-off. Each circle in the image has a nanoantenna at its center, and the nanocrystals in these regions were fluorescent until the deposition of Au. After the deposition of Au (20 nm) by thermal evaporation, the nanocrystals in the nanoantennas stopped fluorescing. The nanocrystals outside the holes (on the left side of the image) were fluorescing. The image was captured with an acquisition time of 3 s—an acquisition time of 2 s is sufficient to observe the nanoantennas.

The first experiments with e-beam lithography used a resist bi-layer of LOR® 3A (300 nm) + PMMA (50 nm). The e-beam lithography was carried out with 100% success till step **4** of Figure 4.2(a). After the e-beam exposure and the etching of the selected areas on the 50 nm thick PMMA film, the LOR® 3A beneath them was developed, and all the nanocrystals in the developed holes could be observed with fluorescence microscopy. But after the thermal evaporation deposition of a 20 nm thick Au film, almost no nanocrystal in any of the holes could be observed fluorescing. Figure 4.12 shows such a sample after the lift-off. We note that none of the nanocrystals in the holes were fluorescent. However, the nanocrystals outside the holes showed fluorescence.

4.3.7.1 Hypothesis about Au deposition and e-beam lithography

The key observations that helped us in hypothesizing about the problem of Au deposition and finding a solution are:

1) In the supercontinuum laser protocol, the Au deposition can be carried out successfully on samples with the following initial structure:

   Si + Ti (10 nm) + Au (200 nm) + PMMA (10 nm) + Nanocrystals + PMMA (35 nm) + LOR® 3A (300 nm) + PMMA (10 or 50 nm).

   In the antenna structures, the Au patch is deposited on the 35 nm thick PMMA layer, which holds the nanocrystal just below. But when e-beam lithography is done on these structures, the nanocrystals stop fluorescing after the Au deposition.

2) On these samples, the nanocrystals in the holes survive the e-beam lithography and are visible after the development of LOR® 3A (Figure 4.11), but they stop fluorescing after the deposition of Au (Figure 4.12). On the same sample, nanocrystals that had not been subjected to e-beam exposure fluoresce even after the Au deposition.

3) We have observed that thermal evaporation of materials on nanocrystals can damage the nanocrystals.

From the above mentioned points and the fact that e-beam exposure involves penetration of electrons, we hypothesized that during the e-beam exposure of selected regions on the 50 nm thick PMMA layer, some electrons penetrated into the LOR® 3A layer beneath it, and into the PMMA layer below it, and possibly even the surface of the nanocrystal. From the fluorescence and photobleaching measurements, we did not record any nanocrystal damage just after the e-beam lithography. The thermal evaporation of Au seems to have activated the damaging of the nanocrystals which were sandwiched in PMMA just below the Au patch—these nanocrystals were placed below the regions that were exposed to the e-beam earlier. The nanocrystals that were not under the e-beam exposed regions fluoresce even after the Au deposition, during which they lie beneath a resist bi-layer of LOR® 3A + PMMA.

4.3.7.2 Solution to the problem

To solve the problem of nanocrystal fluorescence damage after the Au deposition, we increased the thickness of the LOR® layer, reasoning that a thicker layer will be more efficient in stopping the penetrating electrons of the e-beam. By using LOR® 5A instead of LOR® 3A, we obtained a

500 nm thick layer. The solution worked—the Au deposition was carried out successfully and operating plasmonic patch nanoantennas were obtained with 100% success.

Our method of e-beam lithography on a resist bi-layer benefits firstly from the usual selective etching of the layers, and secondly from the attribute that if the top layer is the electron resist then the lower layer—due to its thickness—can function as a electron-protecting layer for the materials beneath it. In this way, as witnessed in our case, it would be possible to perform e-beam lithography on materials that would been damaged if they were covered directly with an electron resist.

4.4 The fabricated nanoantennas

We have fabricated several patch nanoantennas using the protocol described in this chapter. The Au patches were of three different sizes, with an approximate diameter of either 600, 1000, or 1500 nm. The Au patch size and shape can be varied because of high resolution writing capabilities of e-beam lithography. The material of the patch can be varied too. Instead of Au, other plasmonic metals such as Ag and Al can be used as well. Figure 4.13 illustrates the structure of these patch nanoantennas.

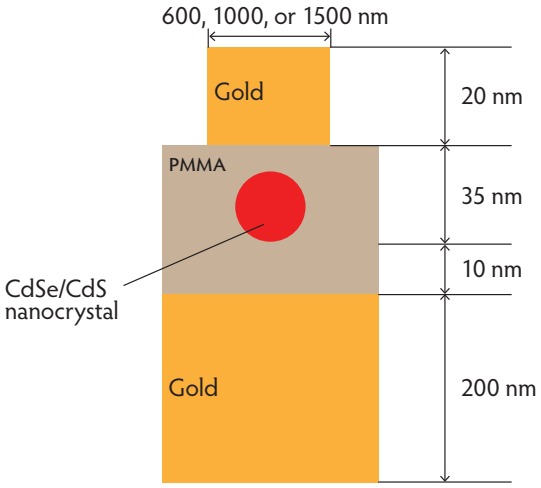

Figure 4.13 *Nanoantenna made by optical and e-beam lithography*

The antenna emitter was a CdSe/CdS quantum dot about 15–19 nm thick.

Figure 4.14 presents AFM analysis of two patch antennas (ϕ = 600 nm and ϕ = 1000 nm) after the lift-off process. The accuracy of e-beam writing results in very circular antenna patches. The residue of lift-off can be observed but this does not limit the functioning of the nanoantenna. If required, the lift-off duration can be extended for a more thorough lift-off. Mild cleaning processes like oxygen plasma etching at lower power and for short duration can be used as well.

Figure 4.15 shows the confocal scans of two patch nanoantennas with different patch diameters (ϕ = 600 nm and ϕ = 1500 nm). The antennas were scanned using a 405 nm CW laser. The optical size of the nanoantennas was larger than the optical size of a nanocrystal (it is a point-like emitter and its optical size is restricted by the optical limits of the imaging

system). The same was observed in the case of the nanoantennas made by supercontinuum laser in-situ optical lithography (section 3.7). In plasmonic patch nanoantennas which meet the coupling requirements, the SPPs generated in the patch cause the whole patch to radiate (antenna effect), and therefore the confocal scan is larger than the optical limit of the system when the patch dimensions are more than the optical limit.

The patches that were obtained with the e-beam method were very circular. The high resolution of e-beam writing allows the fabrication of several shapes (circles, ellipses, rectangles, triangles ...) of different sizes with high precision. This can be used to fabricate a variety of single emitter photonic devices and study the involved phenomena.

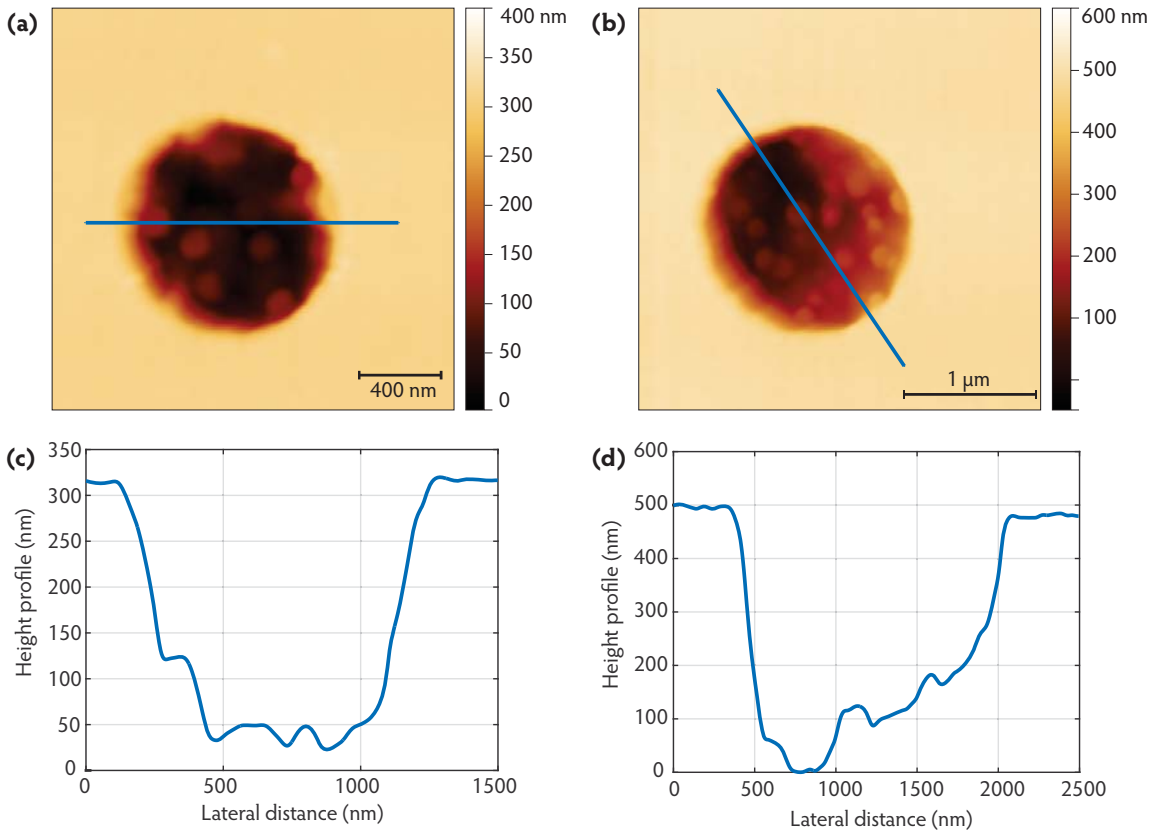

Figure 4.14 *Patch antennas fabricated with e-beam lithography*

On a sample, patch antennas were fabricated using the e-beam lithography protocol described in this chapter. Figures **(a)** and **(b)** are AFM height images that respectively show a $\phi = 600$ nm and $\phi = 1\,\mu$m patch antenna after the lift-off. Corresponding to **(a)** and **(b)**, the height profiles are plotted in **(c)** and **(d)**, respectively. The lift-off residue can be noted in both the images because of which the antenna patch cannot be discerned. The resist bi-layer of LOR®+ PMMA was about 550 nm thick. Because the smaller $\phi = 600$ nm provides a narrower entrance for MF®-319, the efficiency of the lift-off procedure in this case is less than for the larger $\phi = 1\,\mu$m hole. The thickness of the lift-off residue in the $\phi = 600$ nm hole of **(a)** is about 200 nm. There is a 500 nm deep area in **(b)**, and on its opposite side, we observe a slope created by the residue. The emission of the antenna of **(a)** has been characterized in Figures 4.17(g) and (h). The emission decay and photon-antibunching curve of the antenna of **(b)** are given in Figures 4.18(c) and (d), respectively.

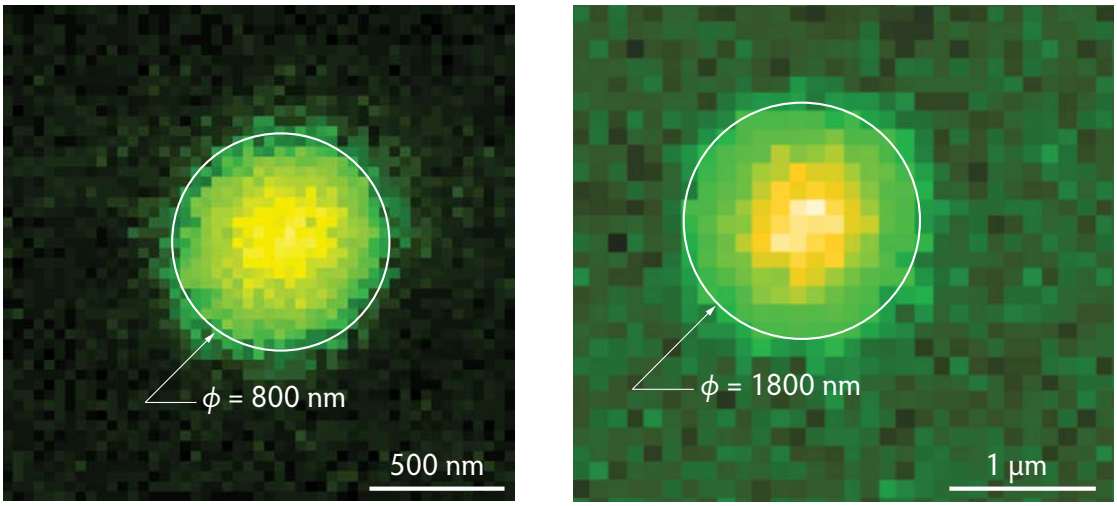

Figure 4.15 *Confocal scans of two nanoantennas*

The images display the confocal scans of two nanoantennas in artificial colors. The e-beam exposure areas to fabricate the patch antennas of figures **(a)** and **(b)** were circles of 600 and 1500 nm diameters, respectively. The confocal scan size of a nanocrystal (a point-like emitter) is about 650 nm, which is the optical limit of our imaging system. Due to the SPP coupling, the entire nanoantenna patch emits. Therefore, the confocal scans of patch antennas are larger as they correspond to the physical size of the patch, which is more than the optically limited size. The overlaying white circles in the two images correspond to the physical size of the patch—for such structures, due to imaging limitations, the observed optical size is usually slightly larger than the physical size.

4.4.1 Patch antenna brightness and excitation efficiency

One major advantage of these antennas is that they can be excited with very low laser intensities. This is very interesting because when these antennas are imaged with fluorescence microscopy (Figure 1.17) that uses excitation light at 438 ± 25 nm (filtered from a mercury lamp), usually we cannot observe them with eye or with 200 ms of CCD camera acquisition time.[6] This is in agreement with theory, according to which patch antennas are generally not bright. If the antenna emitters (nanocrystals) are placed on a glass slip, using the same imaging conditions, they can be observed by eye or with 50 ms of CCD camera acquisition time.

When viewed with fluorescence microscopy, generally the antenna emission is significantly low (CCD camera acquisition time of at least 500 ms is required to observe them) as compared to the nanocrystals around. Figure 4.16 is a fluorescence image of four patch antennas and some nanocrystals. As the lift-off removes the resist only from the vicinity of the antenna, the nanocrystals in other areas were beneath the following layers: LOR® 5A (500 nm) + PMMA (50 nm) + Au (20 nm). Despite the absorption of fluorescence light by the 20 nm Au layer above the nanocrystals which were not inside an antenna, these nanocrystals were much brighter than the patch antennas.

[6] We have recorded two exceptionally bright antennas. One of them has been discussed in Figure 3.23. These antennas could be excited with very low laser intensity. We have never been able to excite individuals nanocrystals (placed on a glass surface) with such low laser intensities.

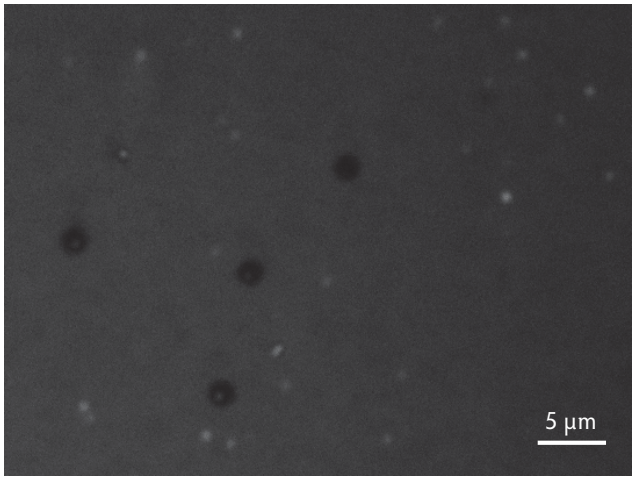

Figure 4.16 *Antenna fluorescence vs nanocrystal fluorescence*
The figure shows a fluorescence microscopy CCD camera image of a sample taken after performing the lift-off. The image was recorded with an acquisition time of 400 ms, and the excitation light was filtered from a mercury lamp through a 438±25 nm optical filter. The four patch antennas (dark spots) are very dull compared to the nanocrystals (white spots) elsewhere, which were fluorescing from beneath the following stack: LOR® (500 nm) + PMMA (50 nm) + Au (20 nm). This shows that patch antennas are not bright.

We observed that under blue light (438±25 nm) excitation from a mercury lamp source, our nanocrystals placed inside the patch antennas fluoresced considerably lower than similar individual nanocrystals placed on a glass surface. However, these antennas could be confocally scanned with very low laser excitation at 405 nm. The laser intensity required to scan the patch antennas was generally less or similar to the one required to scan individual nanocrystals placed on a glass slip. And this intensity was less than that was required to scan other individual nanocrystals outside the patch (like the ones imaged in Figure 4.16). This is intriguing because it is expected that weak emitters, such as patch antennas, need to be excited with higher intensity but our observations show otherwise.

Disregarding the role of wavelengths in this phenomenon, we suppose that the interaction of focused excitation laser light with the antenna patch results in more efficient excitation of the nanocrystal that is placed at a distance of a few nanometers behind the patch. The same patch, however, is not able to efficiently excite the nanocrystal when excitation source is a blue light emitting lamp. It seems that the patch causes efficient excitation only when the excitation light has a high intensity like focused laser light. Our analysis states that insofar as laser light excitation is concerned, the plasmonic metal patches—by means of the involved light–matter interactions—increase the efficiency of excitation.

4.4.2 Lifetime and antibunching measurements

To treat the emission decay curves of the patch antennas fabricated by e-beam lithography, we use bi-exponential fitting of these curves, which has been described in section 3.7.2. The Purcell factor is calculated using Eq. (3.14) and α is found using Eq. (3.12).

The antenna emission was recorded after exciting them with a 405 nm pulsed laser (repetition rate: 2.5 MHz) using an air objective (0.80 $N.A.$, 100×). See Figure 1.18 for an illustration of the optical measurement setup. Figures 4.17, 4.18, and 4.19 show the emission characteristics of several ϕ = 600 nm, ϕ = 1000 nm, and ϕ = 1500 nm patch antennas, respectively. The results of these figures have been summarized in Table 4.2.

	Antenna #	F_P	α	Antibunching
ϕ = 600 nm	1	1	14.4	✓
Figure 4.17	2	8	0.5	×
	3	4	4	×
	4	4	4.4	×
ϕ = 1000 nm	1	4	0.3	×
Figure 4.18	2	5	4	×
	3	2	12.2	✓
	4	2	5.1	✓
ϕ = 1500 nm		2	0.5	×
Figure 4.19				
Other antennas	1	3	1.4	×
Figure 4.20	2	1	10	✓
	3	1	10.3	✓

Table 4.2 *Purcell factor and α of patch antennas obtained with e-beam lithography*

600 nm diameter patch antennas (Figure 4.17)

Antenna 1 has $F_P \approx 1$ and $\alpha \approx 14.4$, and it shows antibunching ($g^{(2)}(0) \approx 0.6$) at low excitation. The Purcell effect is negligible, and the decay curve almost looks like that of a nanocrystal, though the antibunching is not as good.

Antenna 2 is a fast antenna and its shows significant multiexciton emission. Using the bi-exponential fitting equation, we find $F_P \approx 8$ and $\alpha \approx 0.5$. No antibunching is witnessed due multiexciton emission.

Antenna 3 has $F_P \approx 4$ and $\alpha \approx 4$. The contribution of biexciton emission is comparable to exciton emission.

Antenna 4 is quite similar to *antenna 3*. With $F_P \approx 4$ and $\alpha \approx 4.4$ it shows intermediate acceleration and almost no antibunching.

1000 nm diameter patch antennas (Figure 4.18)

Antenna 1 requires a tri-exponential fit. It shows intermediate acceleration with $F_P \approx 4$ but with high multiexciton emission with $\alpha \approx 0.3$.

Antenna 2 is similar to 600 nm diameter *antennas 3* and *4*. Its $F_P \approx 5$ and $\alpha \approx 4$.

Antenna 3 has $F_P \approx 2$ and $\alpha \approx 12.2$. It shows good antibunching.

Antenna 4 shows a quasi mono-exponential decay curve. As described in section 3.7.2, a mono-exponential fit is more suited in this case. A bi-exponential fit is required to accommodate fluctuations; the short lifetime of 4.2 ns does not depict biexciton lifetime. A Purcell factor of about 2.5 can be estimated from $1/e$ change in the decay curve. As expected, the antenna shows good antibunching.

1500 nm diameter patch antenna (Figure 4.19) show multiexciton emission with $\alpha \approx 0.5$ and $F_P \approx 2$, and shows no antibunching.

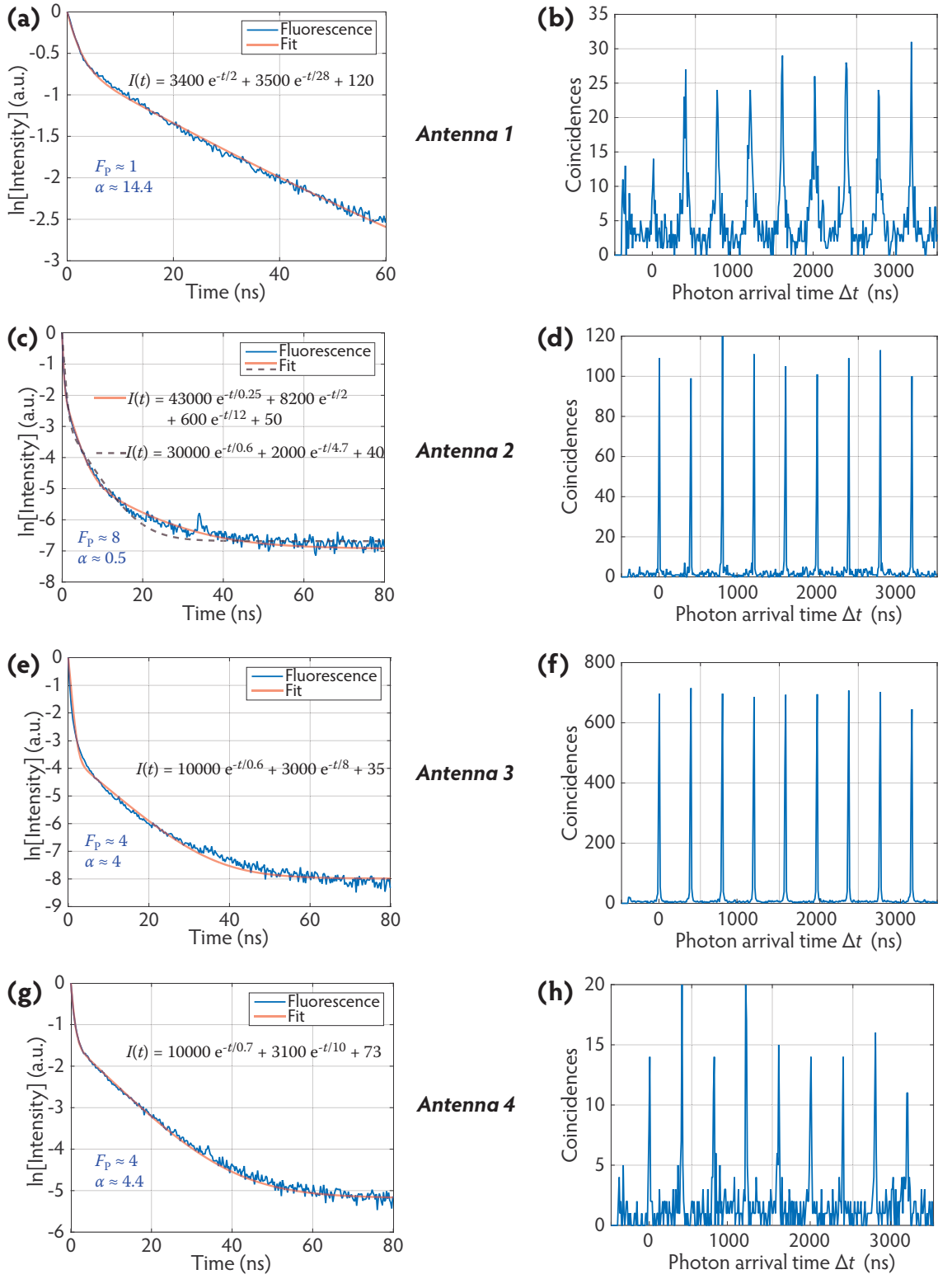

Figure 4.17 *Lifetime and photon antibunching measurements of 600nm patch nanoantennas*
The figure shows the response of four 600 nm diameter patch antennas (numbered 1–4) that were fabricated by the protocol described in this chapter. The histograms in the left and right columns show the lifetime and $g^{(2)}(\Delta t)$, respectively. The equation of the bi-exponential fit equation is mentioned for each decay curve. The small and big values of τ correspond to the biexciton and exciton lifetimes, respectively. Compared to the typical lifetime of a nanocrystal in a homogeneous medium (~35 ns), the emission lifetime of most nanoantennas is reduced. Where the contribution of the fast decay component is more (*Antennas 1* and *2*), no photon-antibunching is recorded. In *antenna 1*, the slow decay rate component contributes significantly to the lifetime curve in **(a)**, and in **(b)** we can observe partial photon-antibunching.

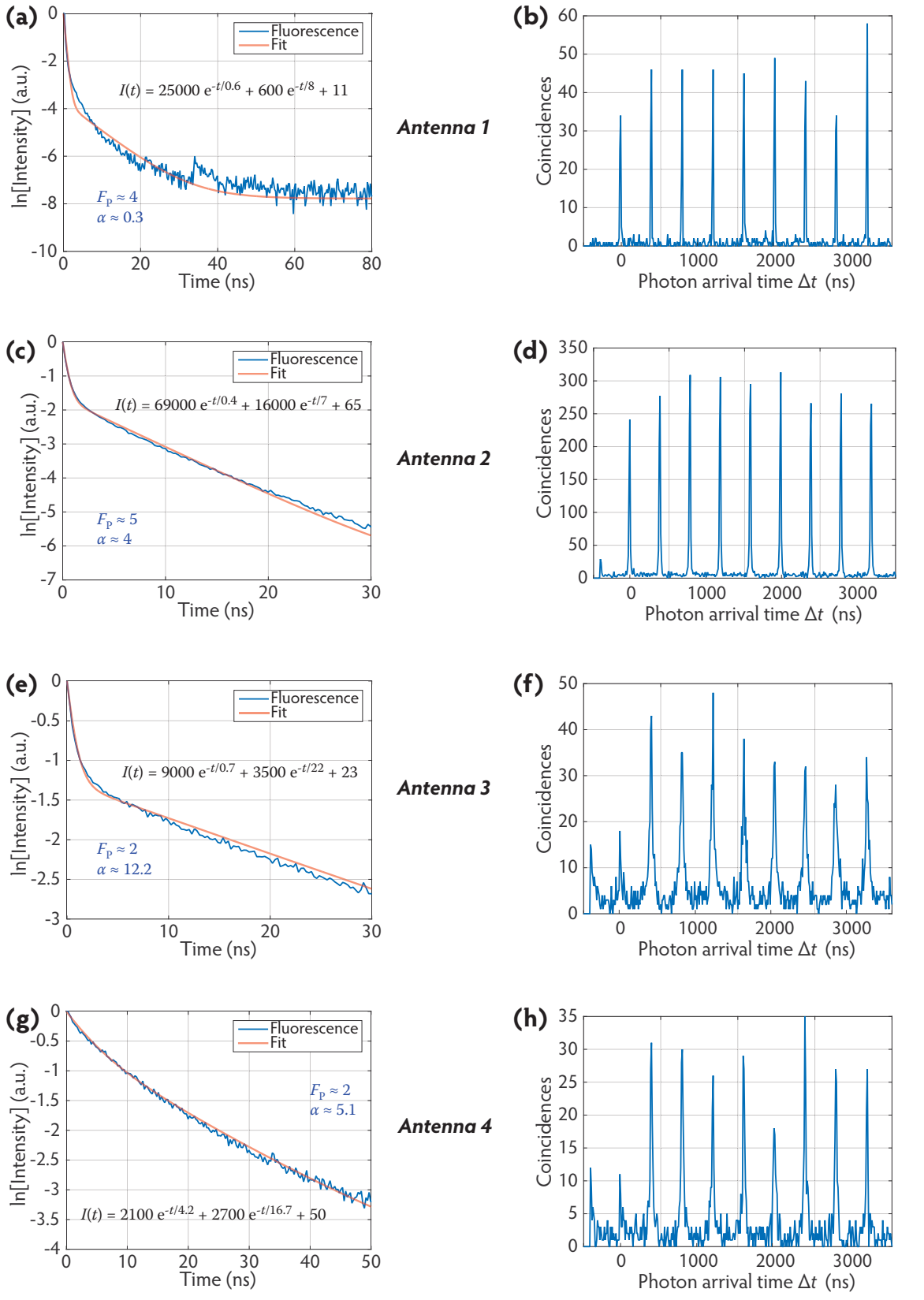

Figure 4.18 *Lifetime and photon antibunching measurements of 1000nm patch nanoantennas*
The figure shows lifetime and photon antibunching histograms of four patch nanoantennas made by the e-beam exposure of 1000 nm diameter circles. As noted before, photon antibunching is observed in the cases where the contribution of the slow decay component is more (*antennas 3* and *4*).

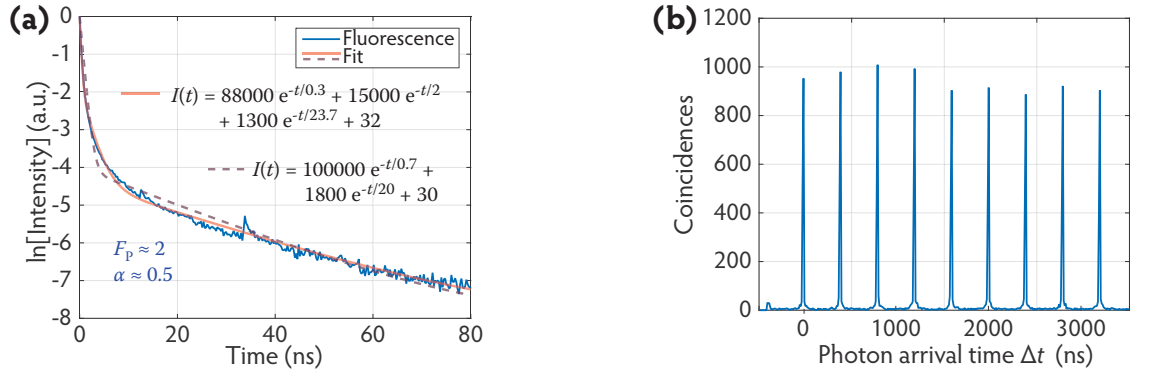

Figure 4.19 *Lifetime and photon antibunching measurements of 1500nm patch nanoantenna*

The figure shows the lifetime and photon antibunching histograms of a 1500 nm diameter patch nanoantenna made with the technique demonstrated in this chapter.

From the Purcell factor shown by different antennas (Figures 4.17, 4.18, and 4.19) with different patch sizes (ϕ = 600, 1000, and 1500 nm), it does not seem that the smaller antennas show a higher Purcell factor. This is probably due to the orientation of the nanocrystal dipole in the antenna and moreover, for patch diameter greater than 1.2 µm, the Purcell factor variation remains almost constant (Figure 1.2). To note the effect of patch size on the Purcell factor, more antennas with varying diameters (e.g., ϕ = 300 – 1500 nm) with known emitter orientation should be analyzed. This will be treated by our future work on patch antennas.

4.4.3 The effect of lithography on nanocrystal fluorescence

From the fabrication perspective it is valid to question how the process of fabrication affects the constituent materials. The same applies to our fabrication of plasmonic patch nanoantennas. Our fabrication process involves the deposition of metal, polymers, and nanocrystals, and the baking of the sample at various stages of the process. Our experiments suggest that the most sensitive of these—in fact the deciding factor—is the effect of any fabrication process on nanocrystal fluorescence. Throughout the thesis this problem has been discussed at various points. We have mentioned about the destruction of nanocrystal fluorescence due to direct dielectric (SiO_2, ZnS, etc.) deposition, plasma vapor deposition of Au, photobleaching by high intensity laser light, and the electrons of the e-beam. In sections 4.3.4 and 4.3.7 we discussed how inappropriate e-beam charge doses and excessive electron penetration were destroying the fluorescence of nanocrystals. After solving these problems, we fabricated patch nanoantennas with a 100% success, that is all the selected nanocrystals could be placed within the nanoantenna structure and all of these nanoantennas fluoresced. The measurements on the nanoantennas (some of them presented in Figures 4.17, 4.18, and 4.19) were carried out within a week after their fabrication. It is true that all the nanoantennas fluoresced just after their fabrication, but are they still active after a few months? This issue is more pertinent when we use e-beam lithography because the electrons involved may interact with the nanocrystal, thus creating defects in them which eventually result in destroying their fluorescence.

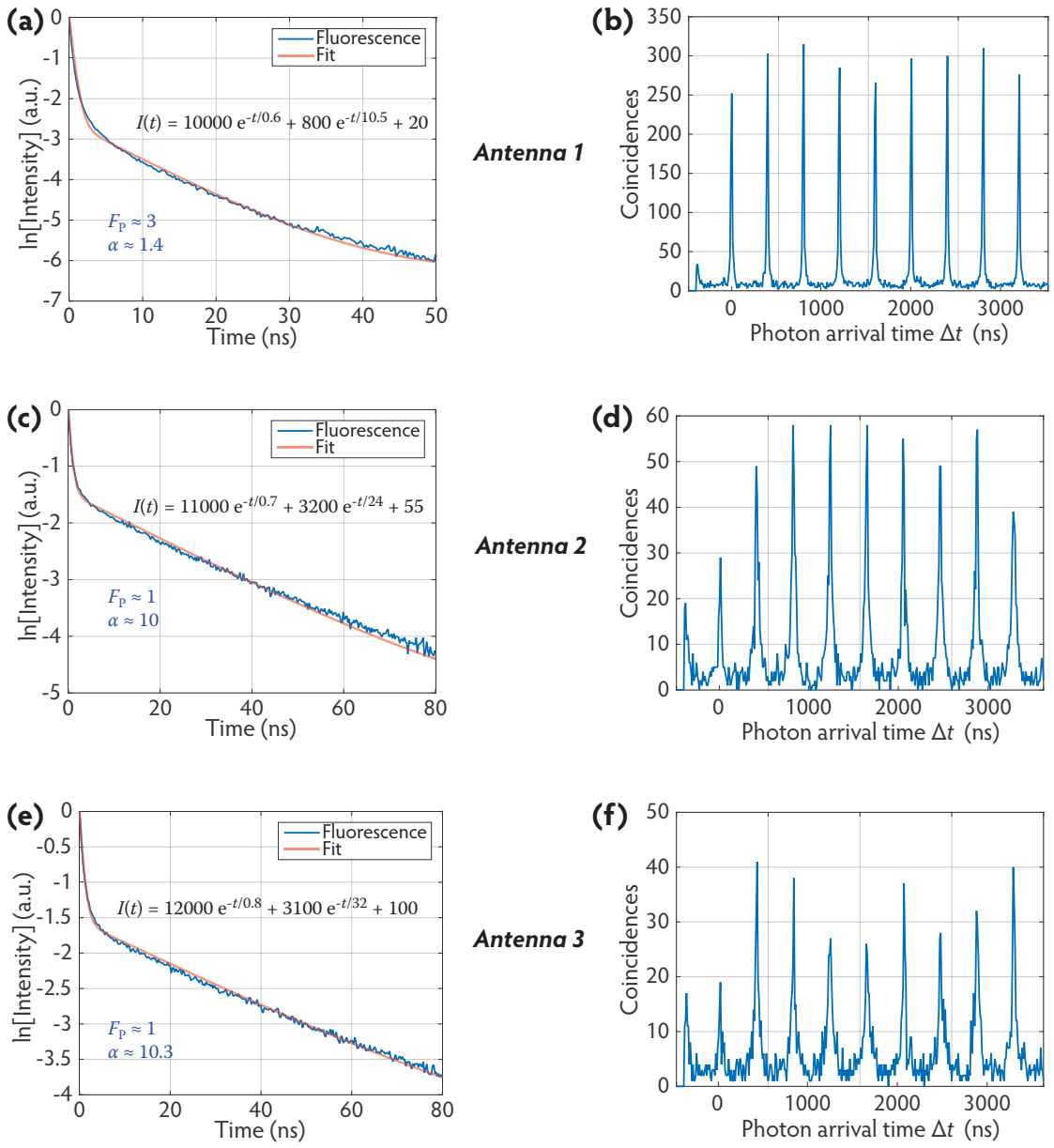

Figure 4.20 *Nanoantennas after three months*

These figure displays the results of measurements done on three antennas after three months of fabricating them using e-beam lithography. *Antenna 1* has $\alpha \approx 1.4$, and it shows no antibunching. *Antennas 1* and *2* are quite similar with a Purcell factor of about 1, $\alpha \approx 1$, and they show antibunching.

We have made several samples with single CdSe/CdS nanocrystal embedded in a layer of PMMA, and the samples were baked two times at 150°C for 2 minutes. It was observed that the single nanocrystals on these samples fluoresced even after 6 months from the date of sample creation. These samples had the following components:

Glass + PMMA (10–50 nm) + Nanocrystals + PMMA (15–50 nm)

The same was observed for samples that had undergone the Au deposition process with the appropriate parameters. These samples consisted of:

Si + Ti (10 nm) + Au (200 nm) + PMMA (10 nm) + Nanocrystals + PMMA (35 nm) + Au (20 nm)

We were interested in finding out if the nanocrystals in nanoantennas show similar fluorescence stability. Using the lithography protocol described in this chapter, we had made several nanoantennas on a sample. All these nanoantennas were active after their fabrication. We tested these antennas after 3 months and found that only half of them were active. Figure 4.20 shows the lifetime and photon antibunching curves measured on some of these nanoantennas, which were excited as usual, and the observations show typical behavior.

Following the discussion presented in this section, it seems that e-beam exposure on nanocrystals may result in damaging them, though the signs of fluorescence bleaching may not be visible immediately. This conclusion is based on the observations that nanocrystals fluorescence was bleached by excessive charge doses (section 4.3.4) and the penetration of electrons (section 4.3.7).

4.4.3.1 A proposed solution

We have used a 500 nm thick layer of LOR® 5A in our samples, which proved to be better than 300 nm thick LOR® 3A layer. Following the argument elaborated in section 4.3.7, we can use a thicker layer of LOR, for example, a 1 µm thick layer to further prevent the penetration of electrons during e-beam exposure. Under this layer, we should be able to observe the fluorescing nanocrystals. The thickness of the layer is limited by its luminescence. Generally, the thicker the layer of LOR®, the more luminescent it is. The thickness of this layer can be increased until we are able to observe the nanocrystals below it by fluorescence microscopy. Increasing the thickness of the layer op LOR® may require adjusting the parameters of its development, which can be found by experimentation.

4.5 Conclusion

The high resolution and precision of e-beam lithography permits the fabrication of advanced nanoscale structures. Combining e-beam writing capabilities with optical lithography allowed us to develop a new technique that uses fluorescence microscopy images to draw e-beam patterns and fabricate nanostructures of different sizes and shapes, while avoiding the destructive interaction of electrons with the fluorescing emitters. This method will find application in domains that require the precision of e-beam lithography but cannot observe some concerned components, such as fluorescing quantum dots, by cathodoluminescence because direct electron exposure can damage them. These components will be imaged harmlessly by fluorescence and the writing will be carried out by e-beam.

The accuracy of this method is mainly limited by the calibration of distances on the fluorescence microscopy images, which can be improved by using more suitable and advanced optical imaging systems. Analysis and improvement of details like e-beam resist thickness, development time, and electron exposure dose will increase the efficacy and applicability of the protocol. This technique can be used to fabricate nanostructures with complicated shapes, which is extremely difficult or impossible using only optical lithography.

The fabricated patch antennas showed acceleration of emission. Photon-antibunching could be observed in only those antennas which had a moderate Purcell factor and dominant exciton emission. Antennas with a high Purcell factor showed significant multiexciton emission, due to which photon-antibunching was lost. The same was observed in the patch

antennas fabricated by supercontinuum laser lithography. As compared to our relatively big quantum dots, smaller quantum dots show considerably less multiexciton emission. By using smaller quantum dots we can limit the photon emission due to multiexcitons and achieve high Purcell factors while preserving single photon emission. These plasmonic patch antennas can be improved by using well-oriented emitters and by reducing the spacer thickness. This will result in a better SPP coupling, a higher Purcell factor, and a lower excitation threshold. Moreover, using the capabilities of e-beam lithography, the antenna patch size and shape can be precisely controlled to obtain extremely high Purcell factors.

5 Lithography with Laguerre-Gaussian Modes

Searching for a solution to deterministically place a metal patch on a single emitter, we conceived and developed another technique that included generating Laguerre-Gaussian (LG) laser modes and performing in-situ optical lithography with them. Owing to the spatial distribution of light intensity in LG_{l0} ($l > 1$) modes, they can be used for doing specialized lithography and producing unconventional structures. At the beginning of chapter 3, we have discussed the problem of photobleaching of nanocrystals under the high intensity laser light that was required for optical lithography. Most lasers emit light as a Gaussian beam, usually in its fundamental (TEM_{00}) mode [194]. Figure 5.1 illustrates the light intensity distribution in a fundamental Gaussian mode and in a donut mode. Since the intensity of a Gaussian beam is maximum at the center, when such a beam is focused on a nanocrystal for optical lithography, the nanocrystal photobleaches as it is exposed to high intensity laser light. A donut mode, such as LG_{l0} modes, resolves this problem. The intensity of such a mode is minimum at its center and therefore by centering it on a nanocrystal, we can burn the resist locally around the nanocrystal without any photobleaching. Inspired by this idea, we acquired a spatial light modulator (SLM) to generate LG modes from Gaussian laser beams. The generated modes were focused though the microscope objective to carry out the lithography.

We used a phase-only liquid crystal on silicon (LCoS) SLM to generate LG modes. I am very grateful to Bruno Viaris de Lesegno and Laurence Provost of Laboratoire Aimé Cotton, Orsay for sharing their expertise on the generation of LG modes using SLMs, and for providing the phase masks for the SLM.

This chapter will begin with an introduction to LG modes, which will be followed by a description of their generation using spatial light modulation by means of specialized liquid crystal screens connected to a computer interface. After describing our optical setup, the subsequent sections will deal with in-situ optical lithography using LG modes on a resist bi-layer. Finally, we will show some results characterizing the optical performance of the nanoantennas fabricated with in-situ optical lithography using LG modes.

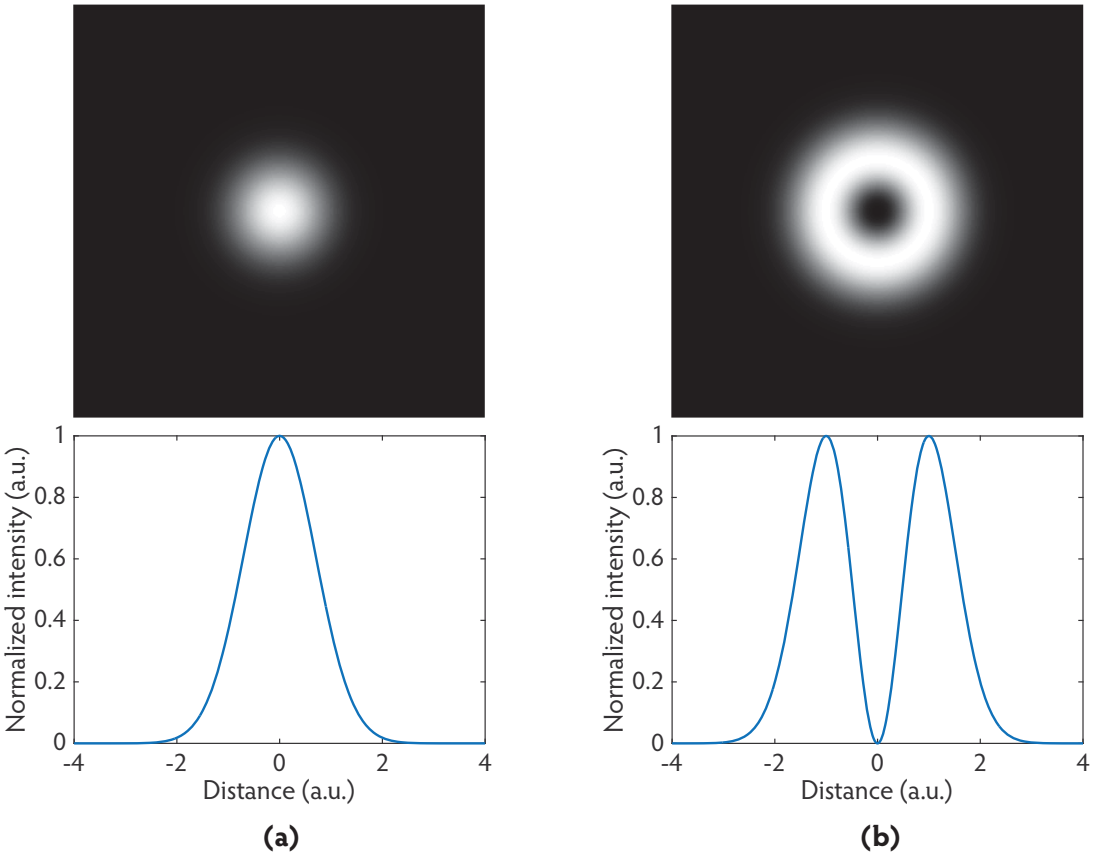

Figure 5.1 *A fundamental Gaussian mode and a donut mode*

The upper images in **(a)** and **(b)** show the respective light intensity distributions of a fundamental Gaussian beam and a donut beam. Corresponding to these images, the lower images show the intensity profile along a line passing through the center of the mode patterns shown above. Intensity at the center of an ideal donut mode is zero.

5.1 Laguerre-Gaussian modes

LG modes are a complete set of solutions to the paraxial wave equation in cylindrical coordinates [167, 66]. For an optical beam, e.g. a laser beam, propagating along the z axis with a propagation vector or wave vector $\mathbf{k}$, the paraxial approximation assumes [195]:

$$k^2 >> k_x^2 + k_y^2 \tag{5.1}$$

which leads to:

$$k_z = k\sqrt{1 - \frac{k_x^2 + k_y^2}{k^2}} \approx k - \left(\frac{k_x^2 + k_y^2}{2k}\right) \tag{5.2}$$

where $k = \|\mathbf{k}\|$, and k_x, k_y, and k_z are the respective components of $\mathbf{k}$ along the x, y, and z directions. In cylindrical coordinates[7] (ρ, φ, z), the complex amplitude $U_{l,p}(\rho, \varphi, z)$ of a scalar Laguerre-Gaussian mode is given as [66, 196]:

[7] **Complex amplitude**: For a real wavefunction $u(\mathbf{r},t)=a(\mathbf{r})\cos[\omega t+\phi(\mathbf{r})]$, the corresponding complex function is defined as $U(\mathbf{r},t)=a(\mathbf{r})\,e^{j\phi(\mathbf{r})}\,e^{j\omega t}$. The complex amplitude $U(\mathbf{r})$ of the complex function $U(\mathbf{r},t)$ is defined as $U(\mathbf{r})=a(\mathbf{r})\,e^{j\phi(\mathbf{r})}$. From this description it follows: $u(\mathbf{r},t)=\mathrm{Re}\{U(\mathbf{r},t)\}$. Here, $\mathbf{r}$ is the position vector, t is the time, ω is the frequency, and a and ϕ are the amplitude and phase of the wavefunction.

$$U_{l,p}(\rho,\varphi,z) = A_{l,p}\left[\frac{w_0}{w(z)}\right]\left(\frac{\rho}{w(z)}\right)^{|l|}\mathbb{L}_p^{|l|}\left(\frac{2\rho^2}{w^2(z)}\right)e^{-\frac{\rho^2}{w^2(z)}}\ e^{-\jmath\left(kz+k\frac{\rho^2}{2R(z)}+l\varphi-(2p+|l|+1)\zeta(z)\right)} \tag{5.3}$$

which contains the following terms:

$$w(z) = w_0\sqrt{1+\left(\frac{z}{z_R}\right)^2}, \tag{5.4}$$

$$R(z) = z\left[1+\left(\frac{z}{z_R}\right)^2\right], \tag{5.5}$$

$$\zeta(z) = \arctan\left(\frac{z}{z_R}\right), \tag{5.6}$$

$$w_0 = \sqrt{\frac{\lambda z_R}{\pi}}, \tag{5.7}$$

$$\mathbb{L}_p^{|l|}(x) = \frac{x^{-|l|}e^x}{p!}\frac{\mathrm{d}^p}{\mathrm{d}x^p}\left(x^{|l|+p}e^{-x}\right). \tag{5.8}$$

Here, $w(z)$ is the beam width, w_0 is the beam waist radius, $R(z)$ is the wavefront radius of curvature, z_R is the Rayleigh range, $A_{l,p}$ is a constant, and $\mathbb{L}_p^{|l|}(x)$ is the Laguerre polynomial function over x, where the integer l is the azimuthal index and the positive integer p is the radial index. The positive and negative values of l denote the left-handed and right-handed helicity, respectively. Eq. (5.3) contains information about the Gouy phase, which is [197]:

$$(2p+|l|+1)\zeta(z) = (2p+|l|+1)\arctan\left(\frac{z}{z_R}\right). \tag{5.9}$$

The LG mode of Eq. (5.3) has a topological charge of l, and $2p+|l|$ is the total order of the associated Laguerre polynomial [198].

From Eq. (5.8), we can write the following:

$$\mathbb{L}_0^1(x) = 1;\ \mathbb{L}_1^0(x) = 1-x;\ \mathbb{L}_2^0(x) = 1-2x+\frac{x^2}{2}. \tag{5.10}$$

5.1.1 Nomenclature

In this thesis, an LG_{lp} or LG_p^l mode corresponds to a field whose complex amplitude is described by Eq. (5.3), where l and p are the azimuthal and radial indices, respectively. We mention this explicitly to avoid confusion because some books, e.g. references [167] and [199], use the notation LG_{pl} by placing the radial index before the azimuthal index.

Figure 5.2 shows the intensity maps of a few LG modes. We note that the light intensity distribution in LG_{00} is the same as in TEM_{00}. For a given p, the size of the central zero intensity circular region increases with l. The number of rings in an LG_{lp} is $p+1$. The LG_{l0} modes, with $l>0$, are types of donut modes. Donut modes are called so because the distribution of intensity along their cross-section resembles a donut. They can be expressed in non-cylindrical coordinates as well.

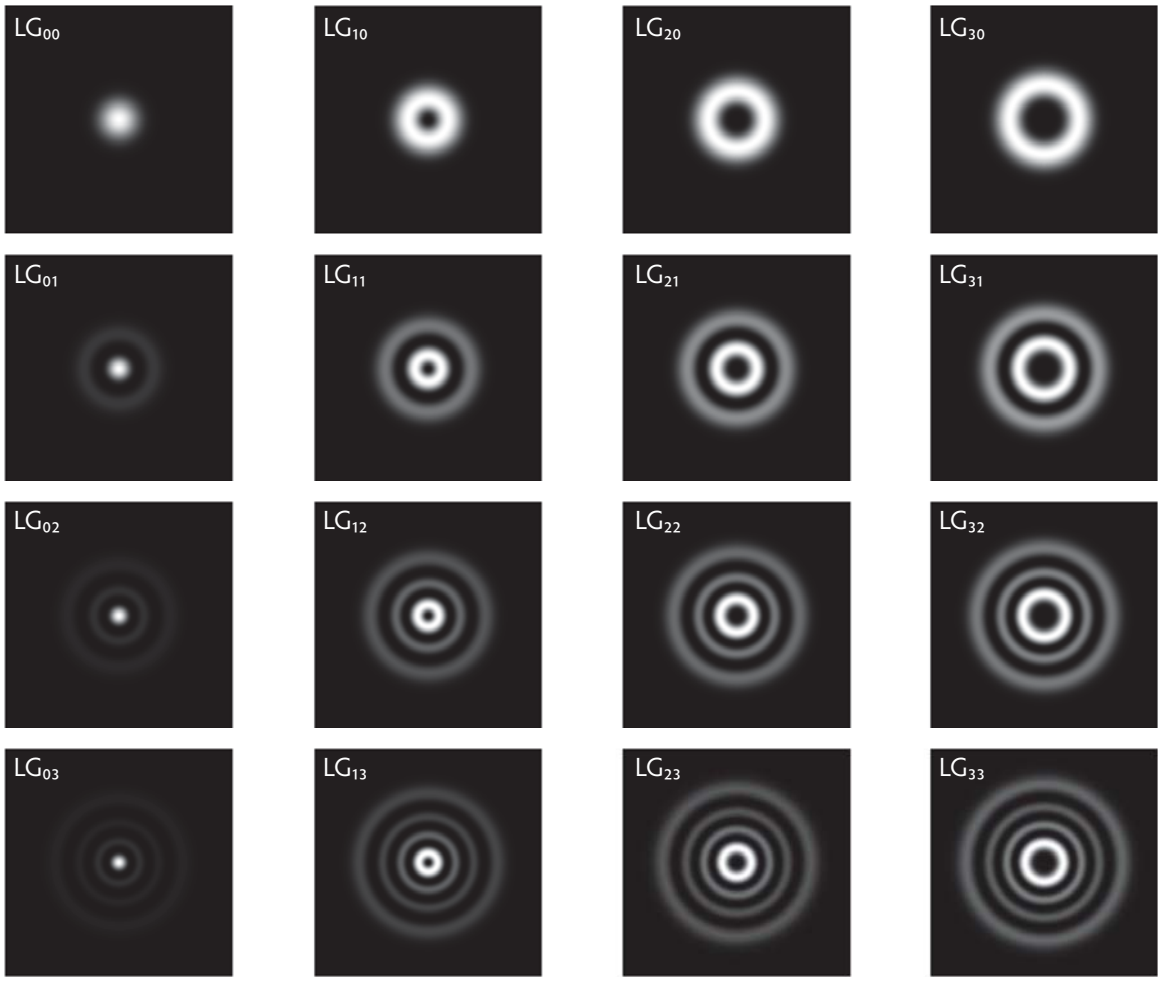

Figure 5.2 *LG modes*

The figure displays computer-generated intensity maps (in gray scale) of some LG_{lp} modes. White color corresponds to high energy intensity.

5.1.2 Angular momentum of light

The concept of the linear momentum of a photon p_{photon} is discussed in most introductory modern physics textbooks. It is stated as [200]:

$$p_{\text{photon}} = \frac{h}{\lambda} = \hbar k, \tag{5.11}$$

where $h = \hbar/2\pi$ is the Planck's constant, λ is the wavelength, and k is the wavenumber. In addition to linear momentum, light may have a spin angular momentum (SAM), which is connected to the polarization of the electric field. Its value per photon is [201]:

$$\text{SAM}_{\text{linear polarization}} = 0 \tag{5.12}$$

and

$$\text{SAM}_{\text{circular polarization}} = \pm\hbar. \tag{5.13}$$

The positive and negative signs correspond to right or left circular polarizations, respectively. A perfectly plane wave, even if circularly polarized, cannot carry any spin angular momentum

because it does not have any component of electric or magnetic field along the propagation direction. But real beams, such as laser beams, are not perfect plane waves—they may have a field component along the propagation direction, which results in non-zero spin angular momentum.

The concepts of spin angular momentum and orbital angular momentum (OAM) of light have been examined in scientific literature [202, 203], and the history of spin angular momentum of light dates back at least to 1909 in the work of Poynting [204, 205]. In 1992, Allen *et al.* [206] showed that all light beams with helical phase fronts carry orbital angular momentum, and such beams can be easily generated. Though the concepts of orbital and spin angular momenta of light were already known, Allen *et al.* were the first to report its relation to $\hbar$. LG laser modes are helical beams, and for an LG mode defined by Eq. (5.3), the orbital angular momentum per photon is [206]:

$$\text{OAM}_{\text{helical mode}} = l\hbar \tag{5.14}$$

where l is the azimuthal index. Since helical beams carry orbital angular momentum, they can exert torque on the illuminated system.

Because of their interesting properties and applications, LG modes have attracted much scientific interest in several fields, which include fundamental optics research [207, 208, 209, 210, 211], optical tweezers [212, 213, 214], precision interferometry [215, 216], and cold atom studies [197, 217, 218].

5.2 Spatial light modulators

We generate LG modes by phase only spatial light modulation of a TEM_{00} laser mode. The phase only spatial light modulation is obtained using a reflective liquid crystal on silicon (LCoS) HOLOEYE LETO SLM [219]. A spatial light modulator (SLM) is a device capable of modulating the amplitude, phase, polarization, or direction of light in space and time [220]. Depending on the method of addressing the modulator, SLMs can be categorized as *optically addressed* and *electrically addressed* [221, 222, 66]. All electrically addressed SLMs are pixelated and have diffraction issues but they have proven to be highly applicable in many fields. Therefore, they have been developed intensively and their drawbacks are minimizing with each new development stage. The HOLOEYE LETO SLM is electrically addressed. Moreover, it is a phase-only reflective LCoS SLM, which means that it uses a lattice of liquid crystals on silicon to modulate only the phase of the incident light, and utilizes an array of reflecting pixels.

LCoS devices benefit from the light modulating properties of liquid crystals (usually nematic) and state-of-the-art complementary metal oxide semiconductor transistors [223, 220]. Both of these domains have been blessed with remarkable progress in the recent years, as they are central to many modern electronic and optical applications. LCoS SLMs can be transmissive or reflective, and can offer amplitude or phase modulation. Phase-only LCoS SLMs offer real-time phase only modulation, which is highly functional and can be obtained effectively by using nematic liquid crystal displays [224]. Phase-only LCoS devices have found applications in various fields such as optical imaging and beam optics [225, 226, 227], holography [228, 229], wave-front and aberration correction [230, 231, 232], diffractive optics [233,

234], wavelength selective switching [235], telecommunication applications [236], compact optical correlators [237], and metrology [238]. For optics, specialized beams, such as Bessel and Mathieu beams, are of particular interest because under ideal conditions they propagate indefinitely while preserving their transverse shape [239, 240]. The phase modulation capability of SLMs along with other diffractive optical elements like axicons can be employed to generate such beams [214].

5.2.1 Principle of operation

An LCoS SLM uses layers of liquid crystals. A liquid crystal consists of many molecules which are oriented in a specific manner in a mesophase[8] state [241]. There are two types of liquid crystals: 1) thermotropic (their phase is just temperature-dependent), and 2) lyotropic (their phase depends on the temperature and the solution concentration). Following Freidel's characterization of liquid crystal mesophases, the alignment of the constituent molecules defines the three main liquid crystalline mesophases: nematic, smectic A, and smectic C [241, 242]. Figure 5.3 shows the temperature-dependent phases of liquid crystals. A liquid crystal molecule can be rod-like (calamitic) or disc-like (discotic). Most applications use rod-like molecules, which can be modeled as shown in Figure 5.4(b).

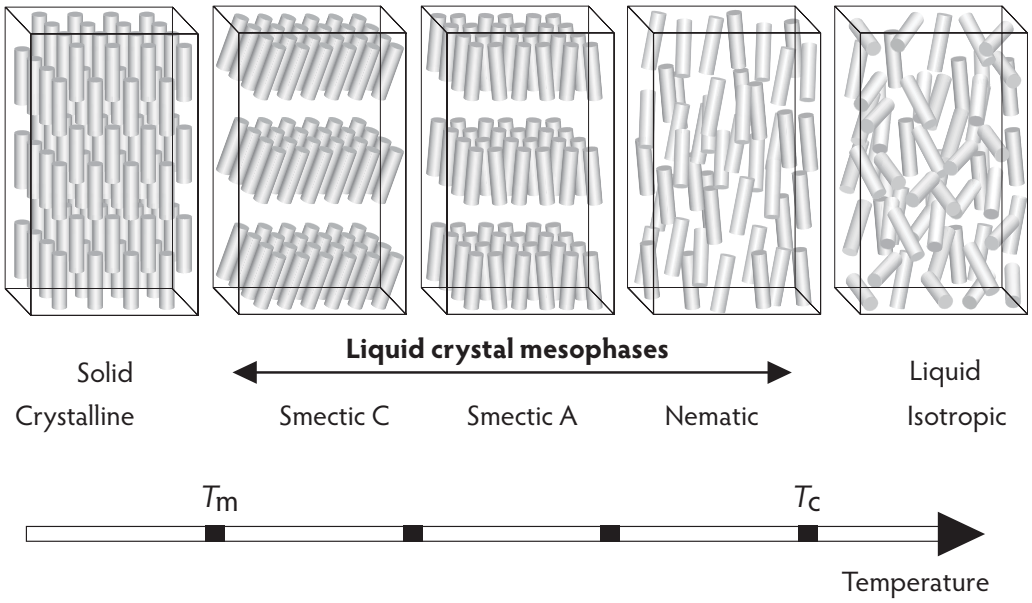

Figure 5.3 *Liquid crystal mesophases*

The rod-like shaped objects are molecules of the liquid crystal, which is in a solid crystalline form below the melting temperature T_m and in an isotropic liquid state above the clearing temperature T_c. At temperature T, when $T_m < T < T_c$, the liquid crystal is in a mesophase state and looks like a milky liquid.

[8] A mesophase is an intermediate phase between a solid and a liquid phase.

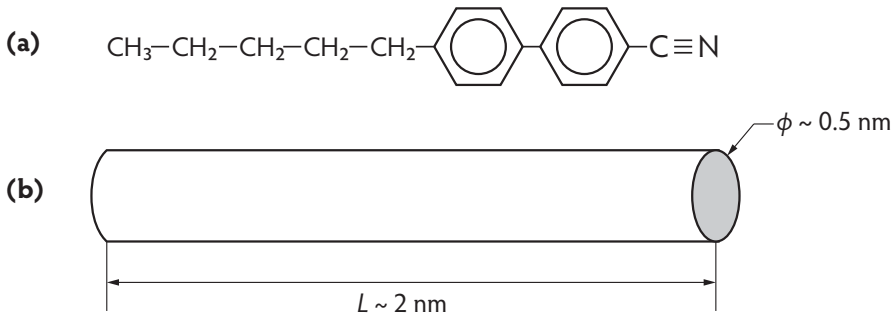

Figure 5.4 *A calamitic molecule and its physical model*

Figure **(a)** shows the chemical structure of 4′-Pentyl-4-biphenylcarbonitrile (5CB), which is a calamitic rod-like molecule and **(b)** depicts its physical model with approximate dimensions [243]. This liquid crystal undergoes a phase transition from crystalline solid to nematic at 18°C, and from nematic to isotropic liquid at 35°C [244].

The arrangement of the constituent atoms and molecules in some materials like liquid crystals and calcite ($CaCO_3$) makes them optically anisotropic, that is, their optical properties are not the same in all directions. The optic axis of a crystal is the direction in which the constituent atoms or molecules are arranged symmetrically [245] and light of any polarization propagates along this direction without any change in polarization [246]. A crystal is called uniaxial if it has only one optic axis. As a result of optical anisotropy, liquid crystals are birefringent; they exhibit two distinct indices of refraction depending on the polarization direction of the incident light. Birefringence Δn of a uniaxial crystal is defined as [245]:

$$\Delta n = n_e - n_o \tag{5.15}$$

where n_o is the ordinary refractive index that is experienced by the incident light whose polarization is perpendicular to the optic axis (director) of the crystal, and n_e is the principal extraordinary refractive index that is experienced by the incident light with polarization parallel to the optic axis (see Figure 5.5). Most liquid crystals are uniaxial and positively birefringent with Δn in the range of 0.05 to 0.45 [223].

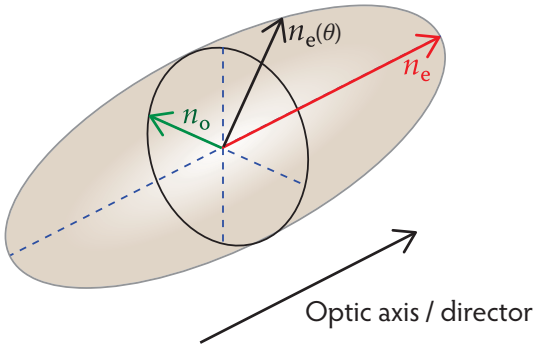

Figure 5.5 *Uniaxial refractive index ellipsoid*

The figure displays a schematic to model uniaxial birefringence. The value of the effective extraordinary refractive index n_{eff} depends on n_o, n_e, and θ.

Figure 5.6 illustrates the components of an SLM screen. The assembly is connected to a controller, which is connected to a computer interface, and the SLM screen is used as a

monitor screen. On the SLM screen, a phase map is displayed. A phase map is a greyscale image and the value of greyness of any pixel on this image decides the voltage applied across the corresponding pixel on the SLM screen, where the image is displayed. In this way by displaying specific images on the SLM screen, we control the voltage across each pixel of the SLM screen, and thus the orientation of liquid crystal molecules on each pixel. When a coherent monochromatic beam (e.g. a laser beam) with an appropriate polarization direction is incident on the SLM screen, the voltage-controlled orientation of the liquid crystal molecules induces a voltage-controlled birefringence, which introduces a specific retardation in the phase of the incident beam and the final resulting beam is modulated in phase. Figure 5.7 describes how a voltage-controlled liquid crystal cell modulates an incident light beam.

The phase retardation δ of the incident beam as it passes through a phase-only reflective LCoS device is given as [223, 247]:

$$\delta = \frac{2\pi 2d}{\lambda}\Big(n_{\mathrm{e}}(\theta) - n_{\mathrm{o}}\Big) \tag{5.16}$$

where λ is the wavelength of the incident light, and d is the thickness of the liquid crystal cell. n_{o} is the ordinary refractive index of the liquid crystal, and $n_{\mathrm{e}}(\theta)$ is the effective extraordinary refractive index of the liquid crystal, which depends on the on the liquid crystal tilt angle θ. By applying voltage across a pixel, the tilt angle θ is controlled, and thus $n_{\mathrm{e}}(\theta)$. To obtain a 2π phase retardation, the minimum required thickness of the liquid crystal cell of a phase-only reflective SLM is:

$$d = \frac{\lambda}{2\Big(n_{\mathrm{e}}(\theta) - n_{\mathrm{o}}\Big)} \tag{5.17}$$

which implies that thicker liquid crystal cells are required to implement a 2π phase retardation of larger wavelengths. For a liquid crystal cell of a given thickness, a transmissive SLM offers half the phase retardation of a reflective SLM.

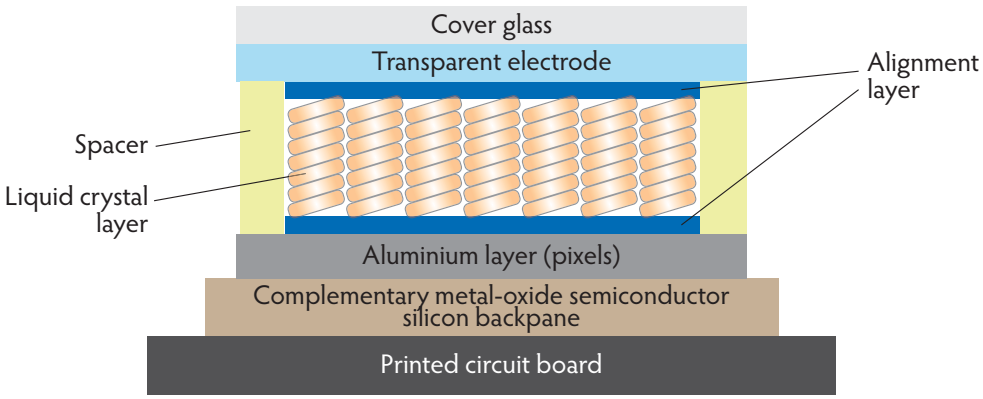

Figure 5.6 *Phase-only reflective LCoS SLM screen components*

The image shows the components of a phase-only reflective LCoS SLM screen. The transparent electrodes, typically made of indium tin oxide, with the help of the silicon back pane of transistors, apply the controlling voltage across the liquid crystal layer on each pixel and orient the liquid crystal molecules accordingly. The thickness of the spacer is related to the thickness of the liquid crystal layer, which is of operational importance. Most phase-only LCoS SLM configurations use parallel-aligned nematic liquid crystals, which act like a switchable waveplate [220].

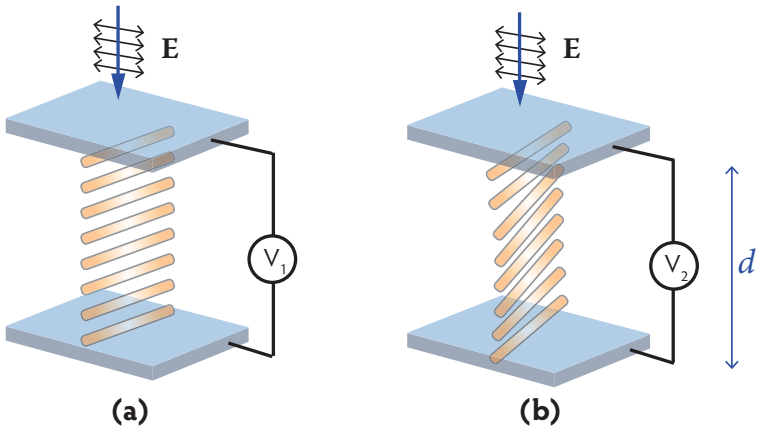

Figure 5.7 *Liquid crystal cell*

Figure **(a)** is a parallel-aligned liquid crystal cell. The incident beam propagates along the direction of the blue arrow, and polarization direction of the field is depicted with the black double arrows. As the polarization of the incident beam is perpendicular to the optic axis (Figure 5.5), it faces just the ordinary refractive index. **(b)** Changing the voltage across the liquid crystal layer can rotate its molecules and activate the extraordinary refractive index, which can modulate the phase of the incident beam. Depending on the SLM type, the modulated beam can be transmitted or reflected. The thickness of the liquid crystal layer is d.

5.2.2 LCoS SLM performance parameters

The key parameters that affect the capabilities and performance of an LCoS SLM are listed below. The method of measurement of these parameters may vary from manufacturer to manufacturer; therefore, the values stated as such are not absolute but they can give an estimate of device performance.

5.2.2.1 Fill factor

Due to fabrication constraints, there is a *dead space* (Figure 5.8) between the pixels on the SLM screen, which does not contribute to any light modulation. The fill factor of an SLM screen is defined as:

$$\text{Fill factor} = \frac{\text{Total pixel size}}{\text{Total pixel size + total dead space}}. \tag{5.18}$$

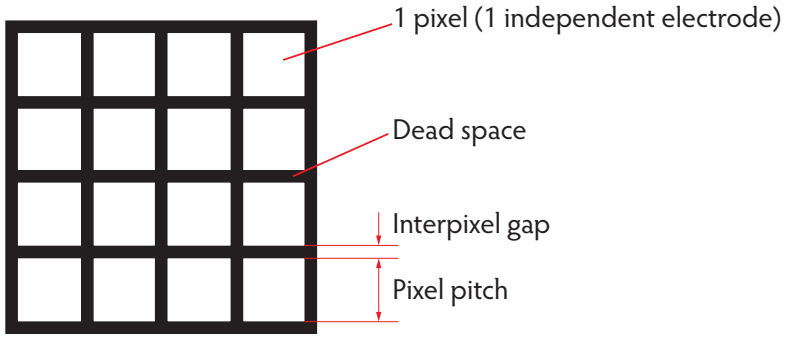

Figure 5.8 *SLM screen pixels and dead space*

The schematic shows the dead space between pixels, the interpixel gap, and pixel pitch.

The HOLOEYE LETO SLM has a fill factor of 93%, a pixel pitch of 6.4 µm, an interpixel gap of 0.2 µm, and a total number of pixels of 1920 × 1080 [248]. The higher the fill factor, the more the relative light intensity in the primary diffraction order (which is usually the first order) [224]. Increasing the fill factor is one of the goals of SLM manufacturers.

5.2.2.2 Diffraction efficiency

The light modulated by an LCoS SLM is diffracted light. The pixel lattice of the SLM behaves as a two-dimensional diffraction grating, thus light is diffracted into higher orders. The dead or inactive space between the pixels does not modulate light and contributes to the zeroth order of diffraction, also known as undiffracted light or the *dc* component/term [249, 250]. The diffraction efficiency is defined as the ratio of the intensity of light in the first diffraction order (I_1) to the intensity of light in the zeroth diffraction order (I_0) [251]:

$$\text{Diffraction efficiency} = \frac{I_1}{I_0}. \tag{5.19}$$

The diffraction efficiency of an SLM is wavelength dependent. For any particular wavelength, the SLM has to be calibrated to achieve the best diffraction efficiency. The goal of SLM calibration is to obtain the maximum light intensity in the first diffraction order. Usually, only the light of the first diffraction order (±1) is utilizable, e.g. we perform lithography with only the 1st order. The HOLOEYE LETO SLM claims diffraction efficiencies of more than 80% [248]. Figure 5.9 shows the light intensity in different diffraction orders after the SLM calibration.

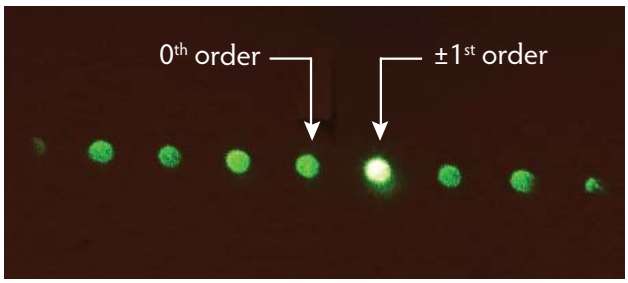

Figure 5.9 *Diffraction efficiency optimization*
A 532 nm laser light was projected onto the SLM screen, on which a binary 10-level blazed grating was displayed. The voltages corresponding to the minimum and maximum phase modulation were regulated for the incident wavelength till the power in the first diffraction order reached the maximum value. After measuring the laser power in the zeroth and first diffraction order spots, the diffraction efficiency was noted as 63%. Better calibration results in higher diffraction efficiency. Being very bright, the first order spot was saturating the camera, and therefore appears white in the image.

5.2.2.3 Light utilization efficiency

It is defined as the ratio of the intensity of the average reflected light (I_r) to the incident light (I_i) when the supply voltage is increased from 1 V to the maximum [251]:

$$\text{Light utilization efficiency} = \frac{I_r}{I_i} \tag{5.20}$$

The loss of light is due to the pixelated structure, scattering by liquid crystal molecules, absorption and losses due to other components. The HOLOEYE LETO SLM has a reflectivity of about 75% (the pixels are not 100% reflective) and a diffraction efficiency of 80%, which results in a total light utilization efficiency of 60% [248].

5.2.2.4 Angle of incidence

The angle between the incident beam and the normal to the SLM screen affects the diffraction efficiency [252], the polarization selectivity and modulation properties of the SLM [253]. Reference [252] reports that if the angle of incidence is below 30°, the change in diffraction efficiency is less than 15%. Lizana *et al.* [253] showed that an angle of incidence less than 10° does not significantly modify the modulation properties of a reflective LCoS SLM. For a more efficient operation, the angle of incidence should be kept as low as possible.

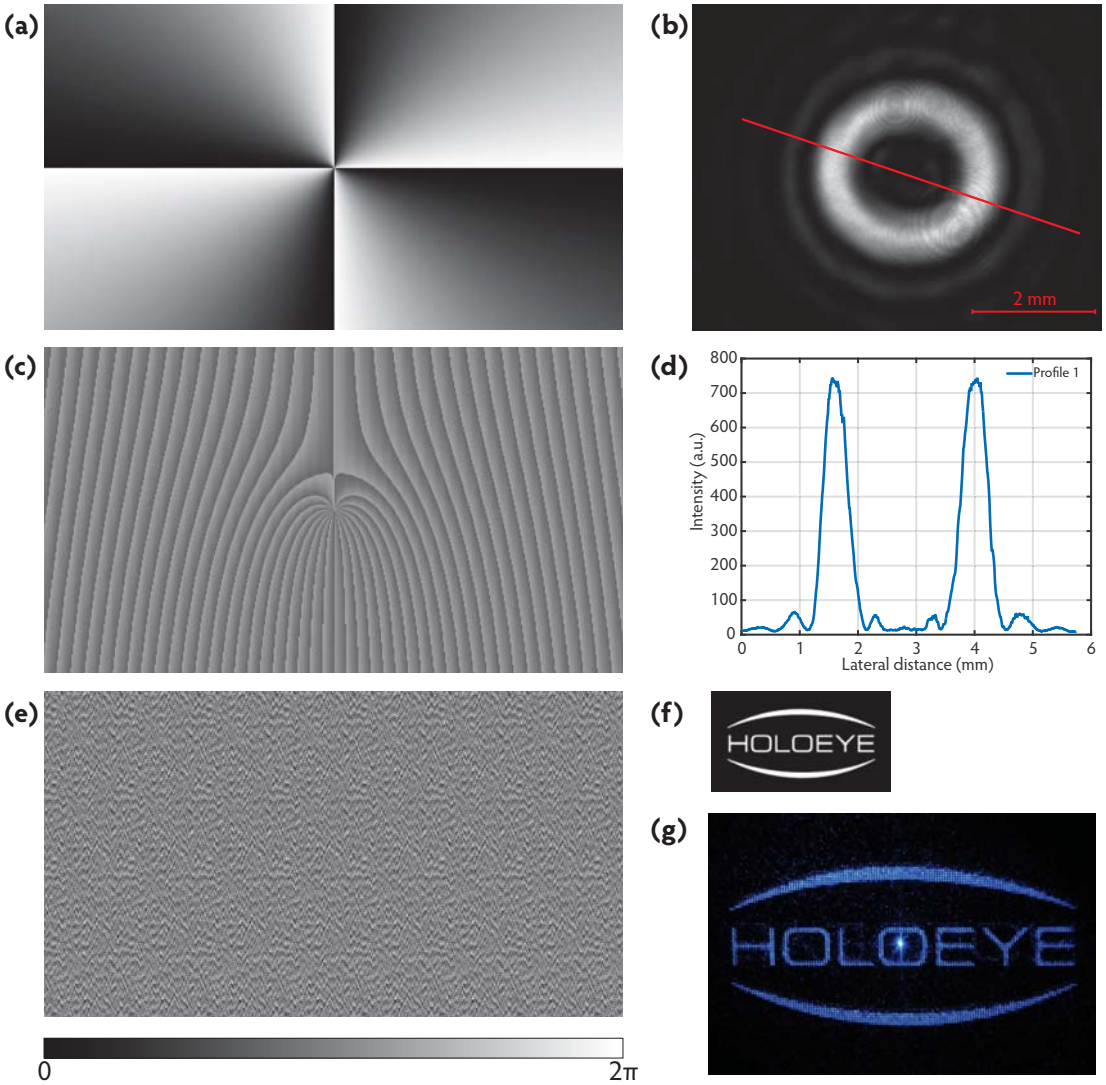

Figure 5.10 *Mode and image generation by SLM*

Figure **(a)** is an explicit binary phase mask of LG_{40} to which a 49-level binary blazed grating was added to shift the zero-order diffraction spot and to clean the mode—the obtained phase hologram is shown in **(c)**. Image **(c)** was displayed on the SLM screen and the incident TEM_{00} laser mode—after modulation—generated an LG_{40} mode. Figure **(b)** shows a CCD camera image of this mode, and **(d)** depicts the intensity profile along the red line in **(b)**. The SLM modulates the incident TEM_{00} mode as programmed by the phase mask displayed on its screen. The reflected light produces a Fourier transform of the phase mask in the far-field. Note the singularity at the center of **(a)** and **(c)**, which is responsible for the dark central region in the LG mode. Figure **(e)** is a computer-generated hologram of image **(f)**, which modulated fundamental mode laser light to form the photographed image of **(g)** in the far-field. Note the pixelation in **(g)** and the bright zero-order diffraction spot at its center. The phase scale of the holograms in **(a)**, **(c)** and **(e)** is shown at the bottom of the figure.

5.2.3 Binary phase masks and computer-generated holograms

A diffractive optical element is a component that can modify light wavefronts by interference and phase control [254]. An explicit binary phase mask, also known as an explicit binary phase hologram (Figure 5.10(a)), is a type of diffractive optical element in which the phase-controlling information encoded explicitly as a binary image. A computer-generated hologram (CGH) is a kind of diffractive optical element which contains a series of phase (or amplitude) masks which generates wavefronts of several orders with low diffraction efficiency [254, 195]. The 1920×1080-pixel image that we display on the SLM screen has information encoded in 256 grey levels (8 bits) that controls the phase of the light beam from 0 to 2π.

To generate a far-field image whose intensity distribution corresponds to a particular 2D image, the hologram of the 2D image should be displayed on the SLM screen. The quality of the generated image will depend on the quality of the hologram and the limitations of the SLM and the optical setup. Using the HOLOEYE *Application Software version 3.0*, the computer-generated hologram of Figure 5.10(e) was created, which modulated light as depicted in Figure 5.10(f). Low noise phase-only computer-generated holograms can be created using the Gerchberg-Saxton algorithm [255], which is based on iterative Fourier transform [195]. The Gerchberg-Saxton algorithm is known for its rapidity but other more accurate alternatives exist as well [256].

The synthesis of a computer-generated hologram, as described above, involves numerical approximations and simplifications. Thereby it can produce modulated light beams with some intensity distribution but these beams are not proper modes of propagation (Figure 5.11). In fact, even with explicit phase masks of proper modes of propagation, we cannot generate perfect proper modes of propagation due to the limitations of the apparatus. However, these are proper modes of propagation with some limitations and can be used as such. By using explicit phase masks of LG modes included with binary blazed gratings (Figure 5.10(a),(c)), we have generated real proper LG modes of propagation (Figure 5.10(b)) that could be focused by a microscope objective for scanning fluorescing quantum dots and doing in-situ optical lithography.

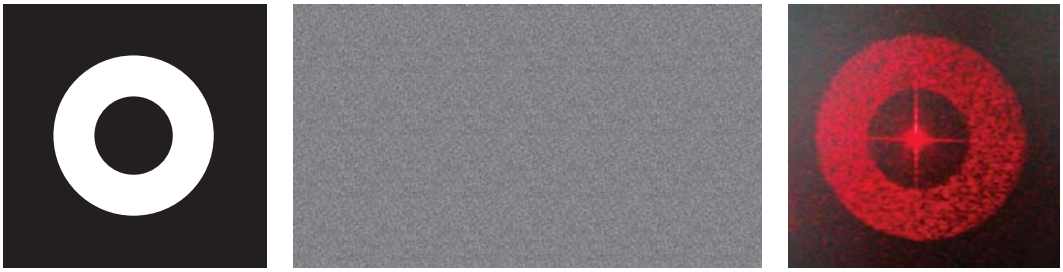

Figure 5.11 *A donut intensity distribution*

Figure **(a)** is a black background image created by overlaying the small black circle on the large white circle. This image was used to obtain the computer-generated hologram of **(b)**, which modulated the TEM_{00} mode to create a far-field image of **(c)**. Image **(c)** is a photograph of the intensity distribution of the modulated light beam projected onto a wall. This light beam was not a propagating mode and was very divergent. Due to divergence, alignment, and focusing issues, these beams cannot be used for in-situ optical lithography. Note the zero-order diffraction spot at the center of **(c)**—this can be removed by adding a binary blazed grating to **(b)**.

5.3 Generating Laguerre-Gaussian modes

Figure 5.12 illustrates the optical setup that we use to modulate the phase of an incident laser beam and generate other modes, such as LG and Bessel beams. A 170 mW CW diode laser is sent through a polarizing beam splitter (PBS) cube, which selects only the s-polarization part of the laser. A diode laser is generally polarized and by letting it pass through a PBS, we enhance the polarization purity of the transmitted laser light. The beam is spatially filtered by a diaphragm and transmitted through a half-wave plate (or retarder). This half-wave plate and the following PBS allow us to control the power of the laser beam incident on the SLM screen. After passing through another diaphragm, the beam passes through an assembly of two lenses, which acts as a beam expander. Using lenses of focal lengths f_1 and f_2, respectively, we attain a beam expansion of f_2/f_1. The goal of beam expansion is to cover the entire screen of the SLM—it eases the alignment of the centers of the phase mask and the incident laser beam (which results in better modulation) and reduces the incident laser beam intensity on the SLM screen (thus preventing damage to the liquid crystals). The expanded laser beam passes through a PBS, through which only the s-polarization is transmitted. The transmitted light beam is incident on a phase-only reflective SLM screen, which is connected to a computer and an LG_{lp} explicit phase mask (with an included binary blazed grating) is displayed on it. The direction of the optic axis of the SLM screen is almost parallel to the polarization of the incident beam. The resulting light consists of the phase-modulated diffracted light (which includes several orders of the diffraction) and the zero-order or undiffracted light. The blazed grating separates the zero-order spot from the center of the diffracted LG mode, and the diaphragm spatially filters only the first order of diffraction. The selected first diffraction order can be propagated and aligned as required.

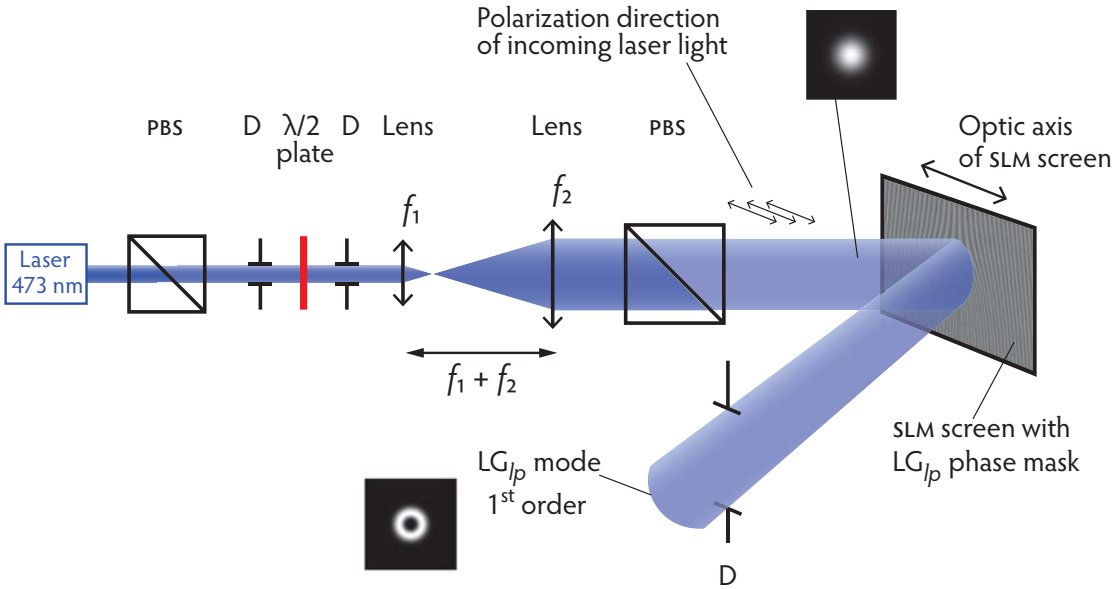

Figure 5.12 *Generating LG modes with SLM*

The schematic displays our optical setup that is used to generate LG modes by means of phase-only spatial light modulation. The term D denotes a diaphragm. We use a 5× Kepler beam expander. The two intensity maps show a fundamental laser mode incident on the SLM screen and a first diffraction order LG laser mode filtered by the diaphragm.

Figure 5.13 depicts two CCD camera images that show the light intensity distribution in LG_{20} and LG_{40} modes that were obtained after modulating a 473 nm fundamental laser mode by means of a reflective phase-only SLM. The modes were let directly into the CCD camera, which was placed in the far-field. As deduced from the computer-generated intensity maps of the modes (Figure 5.2), the first ring of the LG_{40} is larger than LG_{20}. Note that the phase masks used to generate the corresponding modes consisted of an explicit phase mask (LG_{20} or LG_{40}) and a 49-level blazed grating. The optical path of the mode does not change when the phase mask displayed on the SLM screen is altered between LG_{20} and LG_{40}, given that the same blazed grating is used in both the cases. This means that after selecting a suitable blazed grating (we used a 49-level blazed grating) and optically aligning the first diffraction order LG mode into the microscope, we can simply switch the phase masks on the SLM screen to obtain several modes such as LG_{10}, LG_{20}, LG_{30}, and LG_{40}, while still preserving the optical alignment.

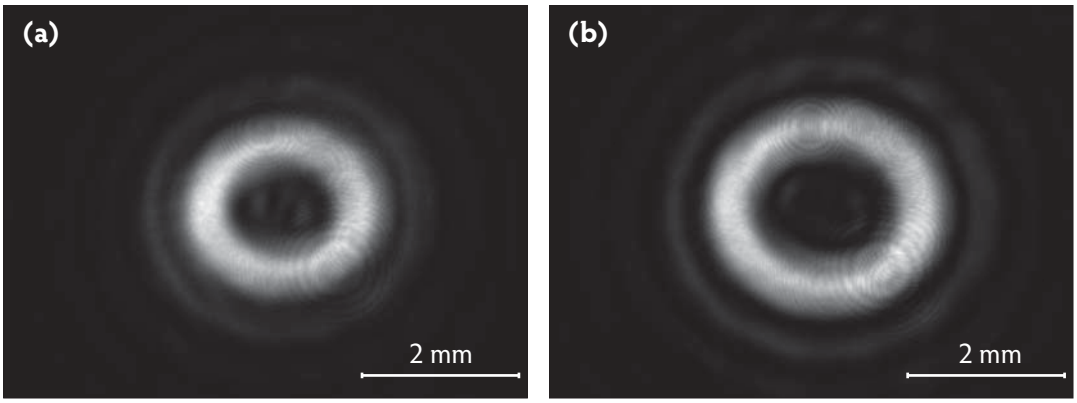

Figure 5.13 *LG20 and LG40 modes*

(a) shows an LG_{20} mode and **(b)** shows an LG_{40} mode. After filtering the zeroth diffraction order by using a binary blazed grating, the 1st diffraction orders of the two concerned modes were spatially filtered and imaged with a CCD camera placed about 3 m from the SLM screen without any added magnification. The cover glass protecting the camera sensor introduced some artifacts (circular rings) in the image.

5.3.1 Enhancing the quality of the generated modes

Before any optical measurement or lithography session, the generated LG modes (1st diffraction order) were imaged with a CCD camera and noted for uniformity in shape and light intensity distribution. If required, the optical setup was improved till a good mode pattern was observed on the CCD camera. The key optical alignment factors affecting the mode quality are:

1) **Collimation of the expanded laser beam**: The inappropriately set beam expander may generate a non-collimated laser beam. To check the quality of collimation, the divergence of the expanded laser beam is observed just after the beam expander and after a few meters from it—the lens separation in the beam expander assembly is adjusted to obtain a good collimation. The beam should pass through the centers of the two lenses.

2) **Aligning the centers of the incident collimated laser beam and the phase mask**: This is crucial for obtaining effective phase modulation. The collimated beam is approximately centered on the SLM screen, and then using the HOLOEYE SLM *Application Software*, the

phase mask is moved pixel-by-pixel to achieve the best results by simultaneously noting the LG mode on the CCD camera screen. Mounting the SLM screen on a micrometer lateral translation stage eases the alignment task.

3) **SLM calibration**: To efficiently modulate the phase of the laser beam of a given wavelength, the SLM should be calibrated to operate specifically for that wavelength. Firstly, the voltage values corresponding to the minimum and maximum phase are chosen such that the power in the first diffraction order is maximal (Figure 5.2.2.2). Secondly, the lookup table for the SLM is optimized by using wavelength specific files supplied by the manufacturer or by using the method of interference fringe shift calibration [257] and creating customized calibration files.

5.4 In-situ optical lithography with LG laser modes

This section will describe our protocol for performing optical in-situ lithography with LG laser modes to fabricate plasmonic patch nanoantennas that use a single quantum dot as an emitter. The protocol can be used to fabricate other nanophotonic structures as well. The process uses a 473 nm CW laser emitting at 170 mW and a HOLOEYE LETO reflective phase-only SLM.

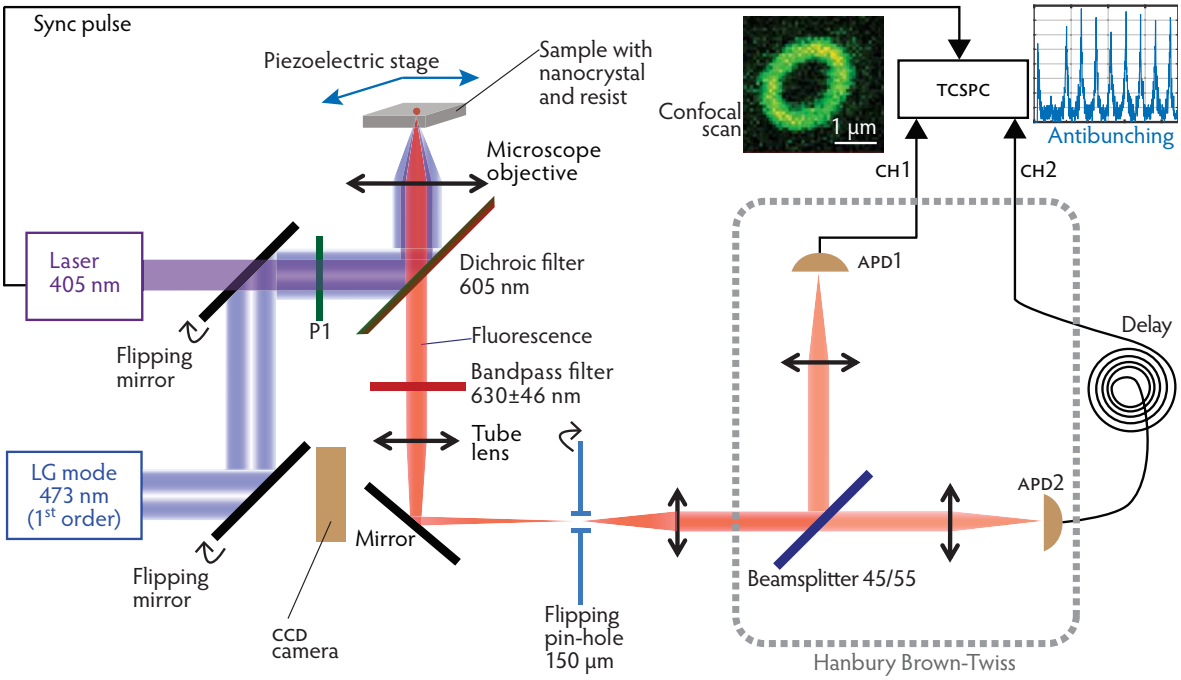

Figure 5.14 *LG mode in-situ lithography*

An emitter (CdSe/CdS core/shell quantum dot) is confocally scanned by the 405 nm laser and photon antibunching is noted to confirm if it is a single photon emitter. The piezoelectric stage position is fixed, the pin-hole is removed from the fluorescence path, and the first diffraction order of the LG mode (generated using an SLM) is used to scan the same nanocrystal—the inset shows a confocal scan of an LG_{40} mode. The nanocrystal is positioned at the center of the green-yellow ring of the mode. Before the LG mode is utilized for confocal scanning, it is let into the CCD camera by removing the flipping mirror and it is optimized as described in the previous section. At position P1, a power meter can be placed to measure the laser power or a mechanical blockage for blocking the laser beam can be positioned.

1) A sample is prepared as described in section 3.1, after which we are at the end of step **1** of Figure 5.15(a). For optical in-situ lithography with LG modes, we obtained the best results by using a resist bi-layer of LOR® 5A (500 nm) and PMMA (50 nm). The 50 nm thick top layer of PMMA (Figure 5.15(b)) was formed by spin-coating a 2% [m/m] solution of PMMA in toluene at 4000 rpm for 40 s.

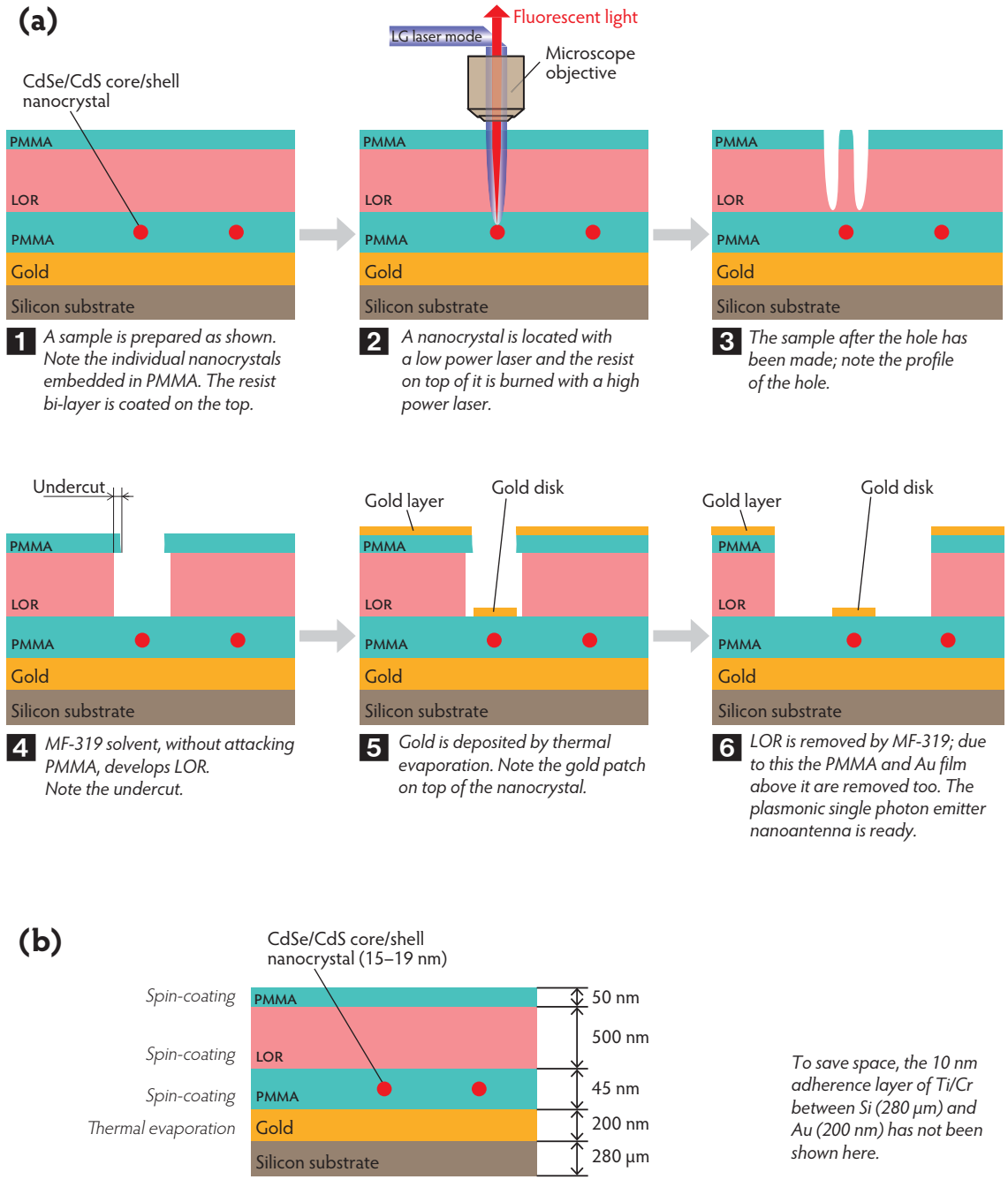

Figure 5.15 *LG mode optical in-situ lithography protocol*

Figure **(a)** displays the optical in-situ lithographic protocol with LG_{l0} laser modes. Figure **(b)** shows the thickness of the layers and their deposition method.

2) Using the 405 nm laser, the sample is confocally scanned and a single nanocrystal is selected for the lithography task. The pin-hole is lifted and the 473 nm LG laser mode is

let into the 100× microscope objective to scan the same emitter. In fact, the emitter scans the LG mode—the inset of Figure 5.14 shows the confocal scan of an LG_{40} mode. The LG laser mode is generated by a reflective phase-only SLM as explained in section 5.3. The power of the scanning mode is about 100–200 nW.

3) Using the piezoelectric stage, the selected nanocrystal is positioned at the center of the LG mode, and then the LG mode is blocked from entering into the microscope. The power of the laser mode at position P1 (Figure 5.14) is increased to 7 mW, the blockage is lifted, and the mode is passed into the 100× microscope objective to locally burn the resist around the nanocrystal for 90 s. After this time the laser mode is blocked from entering the microscope. The main parameters for optical in-situ lithography with LG_{40} or LG_{20} are recapitulated:

   Power of the LG mode at position P1 = 7 mW
   Exposure time to locally burn the resist around the nanocrystal = 90 s

   Now we are at the end of step **3** of Figure 5.15(a).

4) Steps 5–7 of the optical lithography protocol described in section 3.1 are followed and a plasmonic Au patch nanoantenna is realized. These steps include the development of LOR® 5A with MF®-319 for 5 s, the deposition of Au by thermal evaporation, and the lift-off using MF®-319 for 50–100 s.

5.5 LG mode holes and the development of LOR®

In this section, we would like to describe an interesting feature of resist bi-layer burning by LG_{l0} modes, especially when $l \geq 4$. Figure 5.16(a) shows a cylinder drilled into a resist bi-layer (LOR® 5A + PMMA) that was exposed to an LG_{40} mode for 90 s. The wavelength of the mode was 473 nm and its power was 7 mW. Note the height profile along path 1 in the figure below. Development of the sample with MF®-319 removed the central relief and the hole shown in Figure 5.16(c) was obtained. The height profile along path 1 in this image is shown in the figure below.

It has been confirmed in several cases, as depicted in Figure 5.16(a), that with LG mode optical lithography we can obtain cylindrical holes with sub-wavelength edge thickness. By reducing the development time in the following step, such that an undercut in the top 50 nm thick PMMA is created but the central relief is not completely removed, it should be possible to fabricate other interesting photonic structures.

When LG_{20} at 7 mW was used to burn the resist bi-layer for 90 s, it was observed that a complete hole was created and there was no remaining central part. However, when the exposure time was reduced to 30–45 s, the burn hole had a cylindrical profile as in Figure 5.16(a). Our understanding of the hole burning process suggests that a hole is burnt when the incident laser light is absorbed by LOR® and it heats up. The LOR® at high temperature heats the PMMA above it and finally both are evaporated. This explains why in 90 s, usually, a 7 mW 473 nm LG_{40} mode creates a cylindrical hole whereas an LG_{20} creates a complete hole. An LG_{40} mode is larger than an LG_{20} mode (Figure 5.13) and the same is true when they are focused by a 100× microscope objective. For the same average power, the light intensity is higher in LG_{20} than in LG_{40}, and the dark central region in LG_{20} is smaller than in LG_{40}.

Therefore in a given time, the region of LOR® that is heated by a focused LG_{20} is smaller (which means the heat energy density is more) and heat propagates quickly to the center from the edges and evaporates the resist bi-layer. But in the same exposure time, the heat absorbed from a relatively larger and low energy intensity LG_{40} mode does not have time to fully reach the central part, thus the holes are cylindrical.

Our work on the bi-layer burning process by LG modes enables us to conclude that by manipulating the LG mode order, its power, the exposure time, and the thicknesses of the resist bi-layers, other interesting features of this lithography technique can be explored and used.

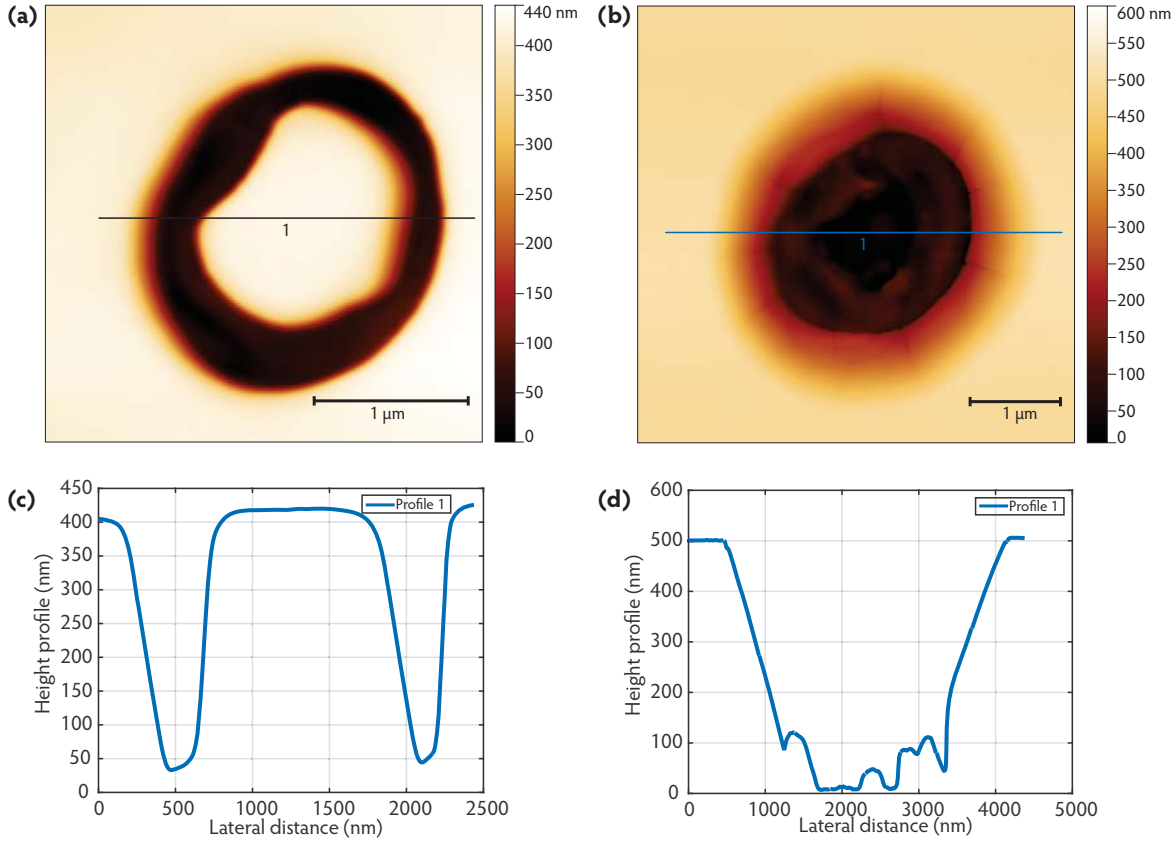

Figure 5.16 *LG40 hole before and after development*

Figure **(a)** is an AFM height image of a cylindrical hole burnt into a resist bi-layer of LOR® 5A + PMMA using an LG_{40} mode. The height profile along path 1 is plotted in **(c)**. The sample was developed with MF®-319 and the central relief inside the hole was removed as shown by **(b)**. The hole deepens to the bottom of the resist bi-layer **(d)**. The widening of the hole after development corresponds to the situation illustrated in Figure 3.11 and described in section 3.4. Usually, we generate smaller LG_{40} modes than the one used to burn the resist bi-layer of **(a)**. Therefore, the usual LG_{40} cylindrical hole is smaller than the one displayed in **(a)** and the developed hole is smaller than the one displayed in **(b)**.

5.6 LG mode patch antennas after lift-off

Following the lithography protocol described in section 5.4, after the vapor deposition of the Au patch, the lift-off is performed and plasmonic patch nanoantennas are obtained. To better understand the LG mode lithographic process, we will discuss some successful cases and an unsuccessful case.

On a sample (with a structure as shown in Figure 5.15(b)), in-situ optical lithography was performed using LG_{20} and LG_{40} laser modes. After the Au deposition, the lift-off was carried out by shaking the inverted sample in a bath of MF®-319 for 50 s. Figures 5.17, 5.18, 5.19, and 5.20 present an AFM analysis of some of these patch antennas.

The lift-off leaves some residual resist above and around the patch, which is not an issue as such (section 3.6). From the results obtained on this sample, a lift-off duration of about 100 s or larger seems more appropriate for the holes made with 473 nm CW LG modes at 7 mW. The presence of a Au patch in these structures is confirmed by the significant increase in the emission decay rate, and it is substantiated by the AFM image analysis. As expected, the patches obtained with LG_{20} laser modes were smaller than the ones realized with LG_{40} laser modes. The possibility of varying the cross-sectional size of the LG mode by means of optical components or by using a holographic lens on the SLM screen allows us to fabricate antenna patches of different sizes. Figure 5.20 describes an *incomplete* hole-burning process—this feature of LG mode optical lithography can be used to synthesize structures which are usually not possible to fabricate with TEM_{00} mode optical lithography.

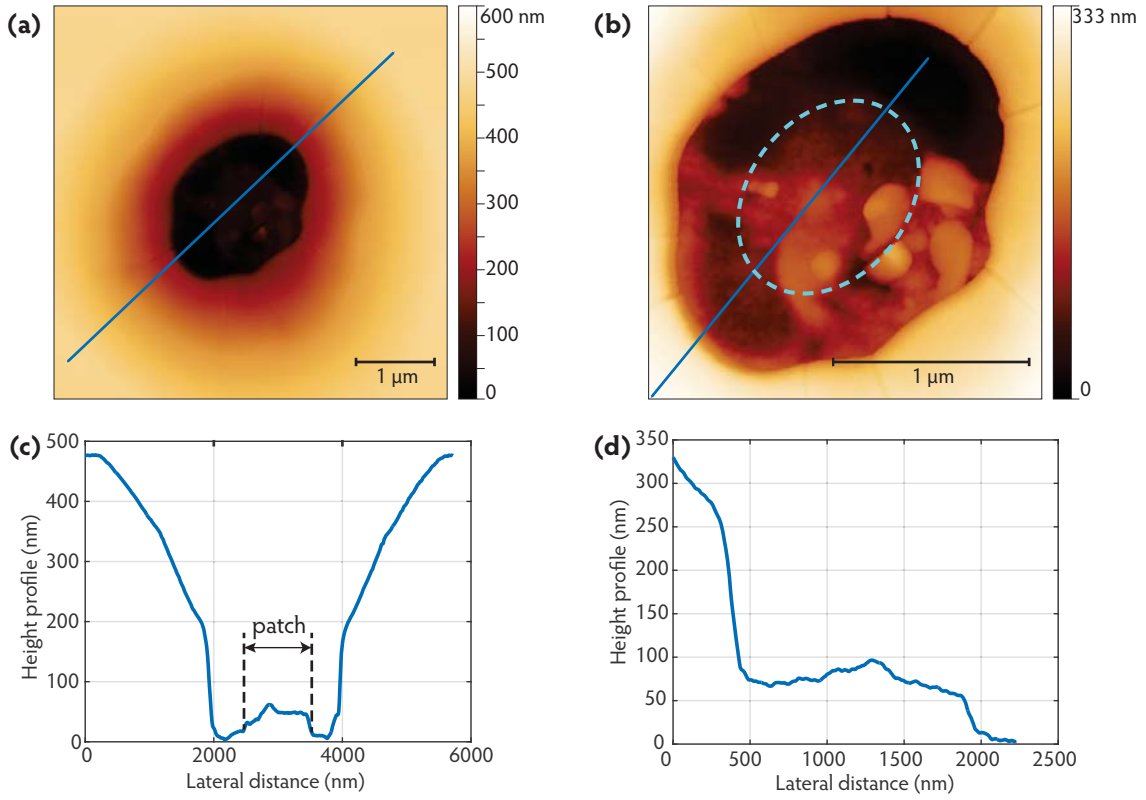

Figure 5.17 *Patch antenna made with LG20 mode lithography*

AFM height images **(a)** and **(b)** show the same Au patch antenna fabricated with LG_{20} mode lithography. Figures **(c)** and **(d)** plot the height profile along the straight lines marked in **(a)** and **(b)**, respectively. Along the edges of the lifted-off region in image **(a)**, the slope of change in height is very steep, and therefore the information provided by AFM may not be accurate. But this not an issue for imaging the patch because the topographic change around it is not so sudden. The resist residue remaining after the lift-off covers the patch and regions nearby. After measuring the height profiles along several directions, the estimated position of the Au patch is given by dashed cyan ellipse in **(b)**. The presence of a patch was confirmed by the reduction of nanocrystal emission lifetime in the antenna as compared to its lifetime in a homogeneous medium.

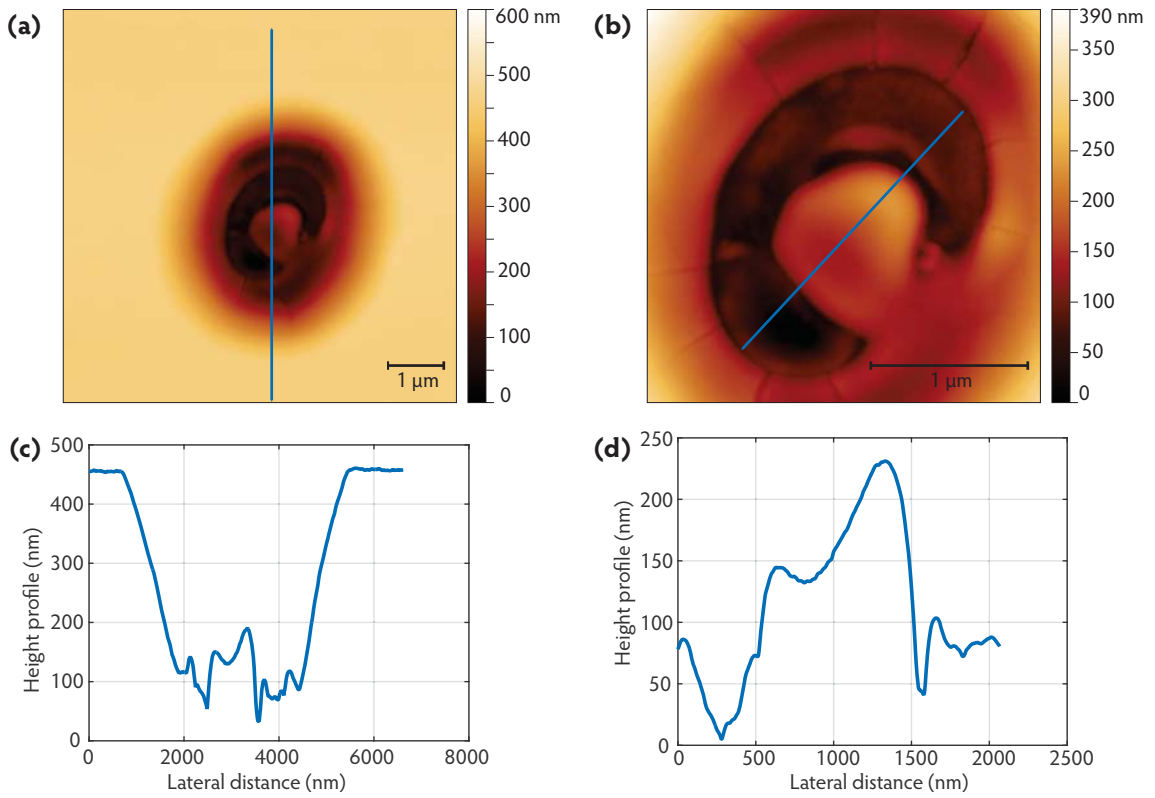

Figure 5.18 *LG20 patch antenna*

Figure **(a)** shows an AFM height image of a Au patch antenna made with LG_{20} mode lithography and **(b)** is a magnified view of the same antenna. Images **(c)** and **(d)** plot the height profiles along the paths marked in **(a)** and **(b)**, respectively. From **(b)**, the patch diameter seems to be about 1 µm, and a resist residue of 20–200 nm thickness can be seen above the patch. Some lift-off residue can be seen around the patch as well. One of the passages for the removal of the resist can be seen at the lower right corner in image **(b)**. The etched resist residue flowed from the sides of the treated region and settled on the patch—this resulted in depositing a non-uniformly distributed material of about 20 to 200 nm thickness on the patch. A structure like this can serve as a dielectric lens. This patch antenna was exceptionally bright that could be excited with very low laser intensity. Its emission characteristics are discussed in Figures 5.23(c) and (d).

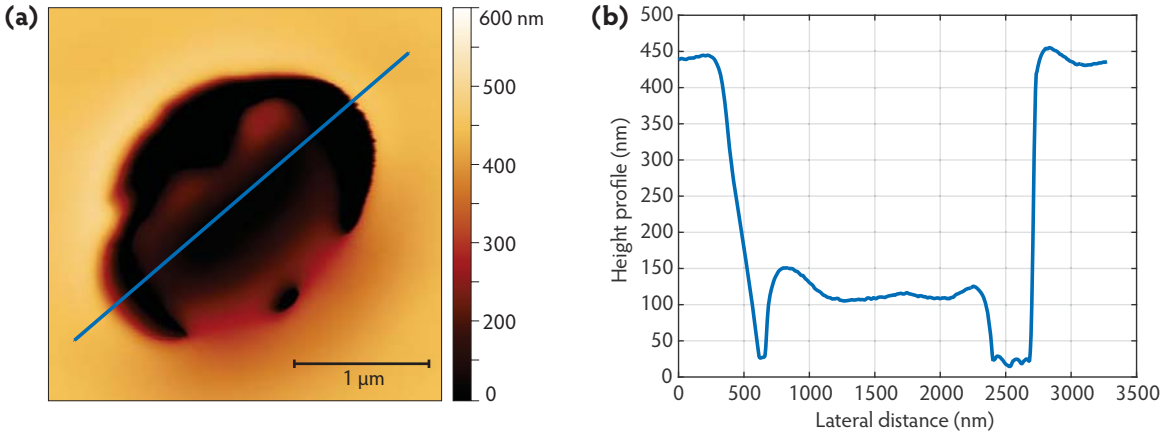

Figure 5.19 *Patch antenna made with LG40 mode lithography*

Figure **(a)** is an AFM height image of a patch antenna made with LG_{40} mode lithography, and **(b)** shows the height profile along the line marked in **(a)**. The antenna patch is covered with some resist residue.

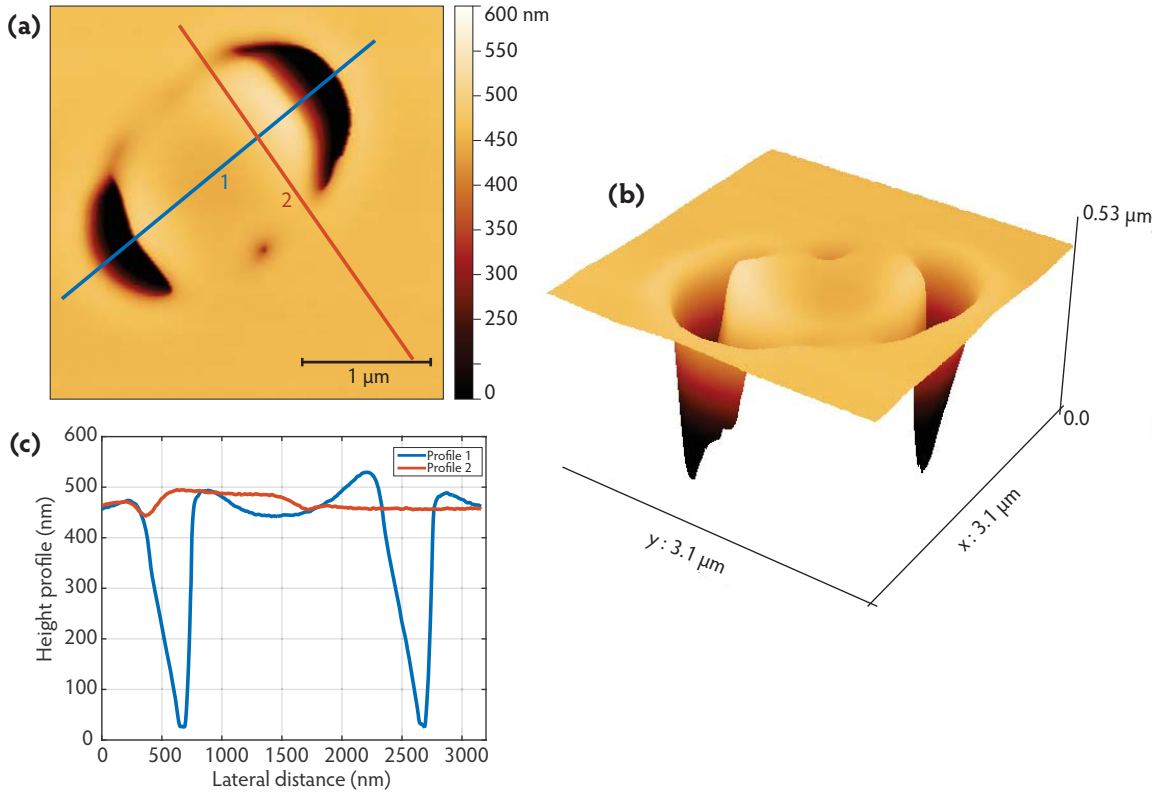

Figure 5.20 *Incomplete LG mode lithography*

Figure **(a)** displays an AFM height image of an LG_{40} incomplete hole-burning process recorded after the lift-off. Image **(b)** shows its 3D perspective view, and **(c)** depicts the height profile plots along the colored lines marked in **(a)**. The triangular shape of height profile 1 is an AFM artifact that occurs as the AFM tip (scanning from left to right) encounters a steep slope at the edge of the hole; this artifact can be made less pronounced by reducing the scan-rate. In **(a)**, we note that during the hole burning process, only two areas of the ring could be burned. This occurs when the intensity of the LG mode is not uniform around the entire ring or when the there is not sufficient time for burning the entire ring. Our observations of the hole burning process by an LG mode suggest that the creation of a cylindrical hole starts at a few points (mostly one or two) which correspond to the regions of maximum laser intensity. Then within a few seconds the entire ring is created. When the resist bi-layer starts evaporating, the edges thus created start diffracting light—we consider this as a sign of the state of the burning process. Incompletely burned rings cannot be usually developed to form a hollow hole but this feature can be exploited to fabricate specialized lithographic structures.

5.7 Nanoantenna Characterization

The structure of the plasmonic patch nanoantennas realized by deterministic LG mode laser lithography is illustrated in Figure 5.21. By using donut LG modes of different orders (e.g., LG_{20} and LG_{40}) and by varying the cross-sectional size of an LG mode with suitable components, the size of the hole burned into the resist bi-layer can be controlled, and thus the size of the deposited metal patch.

Figures 5.23, 5.24, and 5.25 show the emission-decay and photon-coincidence histogram plots of some plasmonic patch nanoantennas obtained with LG_{20} and LG_{40} mode lithography.

The measurement was carried out by exciting the antennas with a 405 nm pulsed laser (repetition rate: 2.5 MHz) that was focused through an air objective (0.80 $N.A.$, 100×). The optical measurement setup is illustrated in Figure 1.18.

As expected, these patch antennas show similar optical behavior as observed in the case of similar antennas that were made using the lithography techniques described in chapters 3 and 4. Using the discussion on patch antenna emission presented in section 3.7.2, we analyze the emission decay and $g^{(2)}$ histograms of these antennas. Table 5.1 recapitulates the results of Figures 5.23, 5.24, and 5.25.

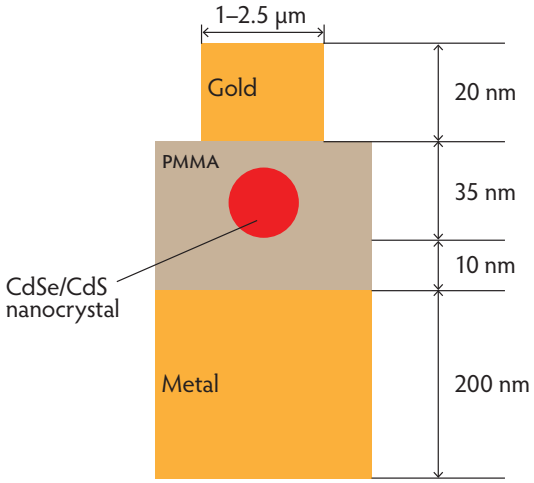

Figure 5.21 *Nanoantenna realized by LG mode lithography*

The figure shows the general schematic of the patch antennas obtained with LG_{20} and LG_{40} mode in-situ optical lithography. By varying the PMMA spacer thickness and the Au patch dimensions, these antennas can be optimized.

	Antenna #	F_P	α	Antibunching
LG_{20}	1	9	0.2	×
	2	1	147.4	✓
LG_{40}	3	1	4	✓
Figure 5.23	4	4	1.2	×
LG_{40}	1	6	5	✓
Figure 5.24	2	2	14.3	✓
	3	2	16.4	✓
	4	3.5	13.9	✓
LG_{40}		11	1.8	✓
Figure 5.25				

Table 5.1 *Purcell factor and α of patch antennas obtained with LG mode lithography*

LG_{20} antennas (Figure 5.23)

Antenna 1 shows the typical behavior of antennas that have a high Purcell factor and low α. It has $F_P \approx 9$ and $\alpha \approx 0.2$. Due to high multiexciton emission, it shows no antibunching.

Antenna 2 has $F_P \approx 1$ and a very high $\alpha \approx 147.4$. The emission decay is quite mono-exponential and a bi-exponential fit was required to account for the fluctuations. Its emission is mainly due to radiative exciton recombination, which manifests in very noticeable photon-antibunching. This antenna was exceptionally bright and it could be excited with a very low laser intensity. Nanocrystals placed on a glass slip cannot be excited with such low intensity. Fluorescence images show that the nanocrystal of this antenna was not bright before being placed inside the antenna. Figure 5.22 shows a fluorescence microscopy image of this antenna, and its AFM height image is given in Figure 5.18.

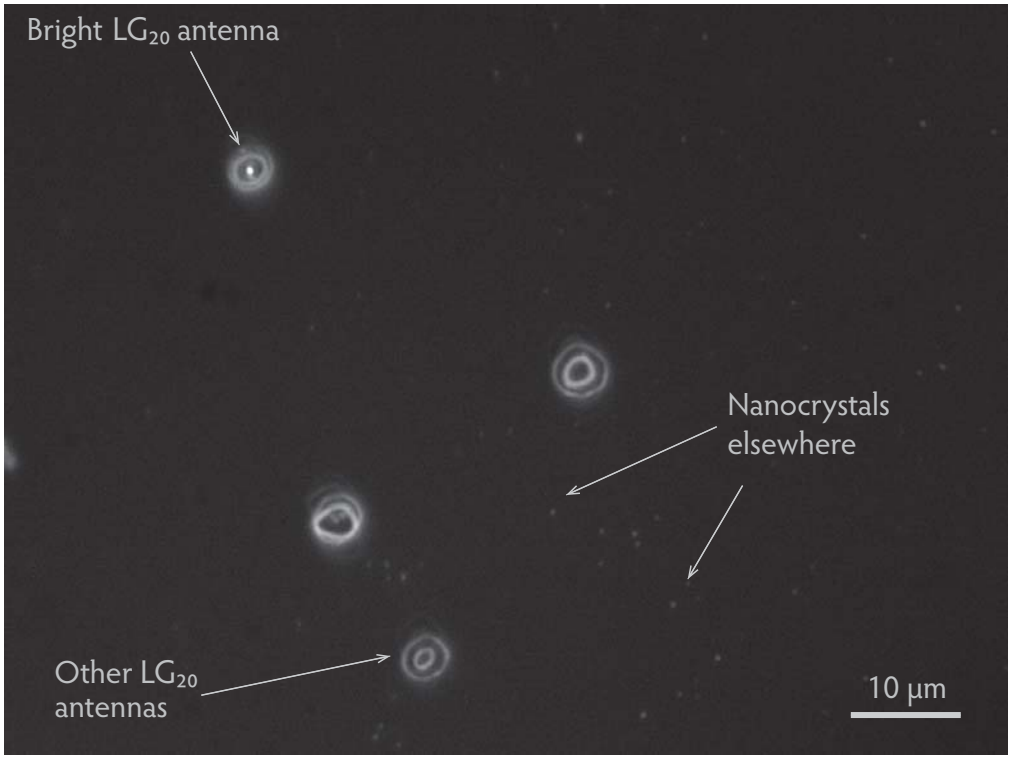

Figure 5.22 *An exceptionally bright LG20 antenna*

The figure is a fluorescence microscopy image (excitation source: 438±25 nm filtered from a mercury lamp), acquired by a CCD camera in 400 ms, after the lift-off procedure. There are four LG_{20} antennas and many nanocrystals elsewhere. The nanocrystals outside the antennas were fluorescing from beneath the following layers: LOR® (500 nm) + PMMA (50 nm) + Au (20 nm). Because of the usual patch antenna emission strength—which is low—the emission from the lower three antennas could not be recorded in 400 ms. The fluorescence from the individual nanocrystals outside the antennas is just noticeable—generally, these nanocrystals fluoresce more than the patch antennas. Contrary to the general trend, the antenna at the top was exceptionally bright—its high fluorescence saturated the CCD camera image. Figure 5.18 is an AFM height image of this antenna.

LG_{40} antennas (Figure 5.23)

Antenna 3 has $F_P \approx 1$, $\alpha \approx 4$, and shows partial antibunching.

Antenna 4 shows multiexciton (probably biexciton) emission with $F_P \approx 4$ and $\alpha \approx 1.2$. The measurement was carried out at very low excitation intensity.

LG_{40} antennas (Figure 5.24)

Antenna 1 displays good emission acceleration with $F_P \approx 6$ and shows antibunching with $\alpha \approx 5$.

Antenna 2 has a decay curve that is almost mono-exponential. The bi-exponential fit just accounts for lifetime fluctuations, thus its biexciton lifetime of 4.5 ns has no physical significance. The $g^{(2)}$ histogram shows clear antibunching.

Antenna 3 shows good antibunching like *antenna 2*. Its $F_P \approx 2$ and $\alpha \approx 16.4$.

Antenna 4 is interesting. It has a moderately high Purcell factor of about 3.5, and with $\alpha \approx 14.9$, it shows photon-antibunching ($g^{(2)}(0) \approx 0.4$).

LG_{40} antennas (Figure 5.25)

The antenna has a quasi mono-exponential emission decay, It has been fitted with a mono-exponential and a bi-exponential fit. Even with a small $\alpha \approx 1.8$, it shows antibunching. From the bi-exponential fit we deduce $F_P \approx 11$, and using the mono-exponential fit equation, we get $F_P \approx 13$.

Compared to other antennas, this antenna displays very different emission characteristics. One interpretation is that the non-radiative channels in the nanocrystal of this antenna were more efficient than in the typical case of other antennas. Consequently, even for a high acceleration of the radiative channels, the biexciton radiative recombination rate does not overcome the biexciton non-radiative recombination rate.

We note that most LG_{40} antennas are slower than LG_{20} antennas and the antennas fabricated using other techniques (supercontinuum and e-beam lithography). This seems to be due to the relatively large patch size of the LG_{40} antennas, which leads to a lower Purcell factor (Figure 1.2). However, it should be taken into account that the Purcell factor is very dependent on the orientation of the nanocrystal dipole. Therefore, from the analysis of a few results, it is difficult to discriminate between the effect of the dipole orientation from the effect of the patch size. It may have been the case that most LG_{40} antennas had a mainly horizontally aligned nanocrystal dipole, which worsened their emission acceleration. To make a sound conclusion, more cases have to be analyzed.

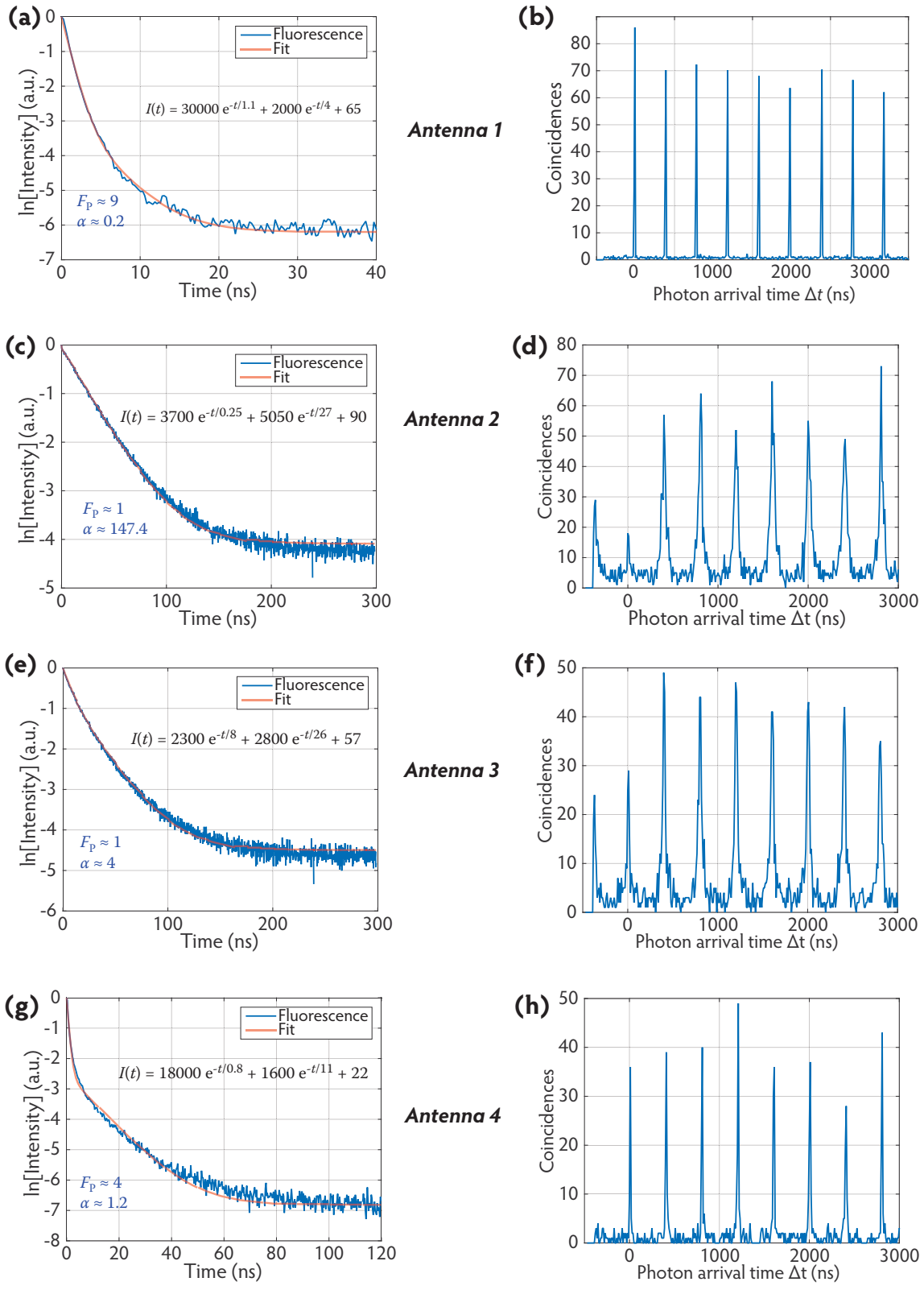

Figure 5.23 *Patch antennas obtained with LG20 and LG40 lithography*

The figure displays the results of optical measurements on the antennas fabricated by LG mode lithography: *Antennas 1 and 2* with LG_{20} and *Antennas 3 and 4* with LG_{40}. The histograms in the left and right columns show the lifetime and $g^{(2)}(\Delta t)$, respectively. The bi-exponential fit equation is mentioned for each decay curve. For most cases, the small and big values of τ correspond to the biexciton and exciton lifetimes, respectively. Compared to the typical lifetime of a nanocrystal in a homogeneous medium (~35 ns), the emission lifetime of some antennas is reduced. *Antenna 1* is quite fast but shows multiexciton emission. Antibunching is noted for antennas with slow decays and a low Purcell factor (*antennas 2 and 3*).

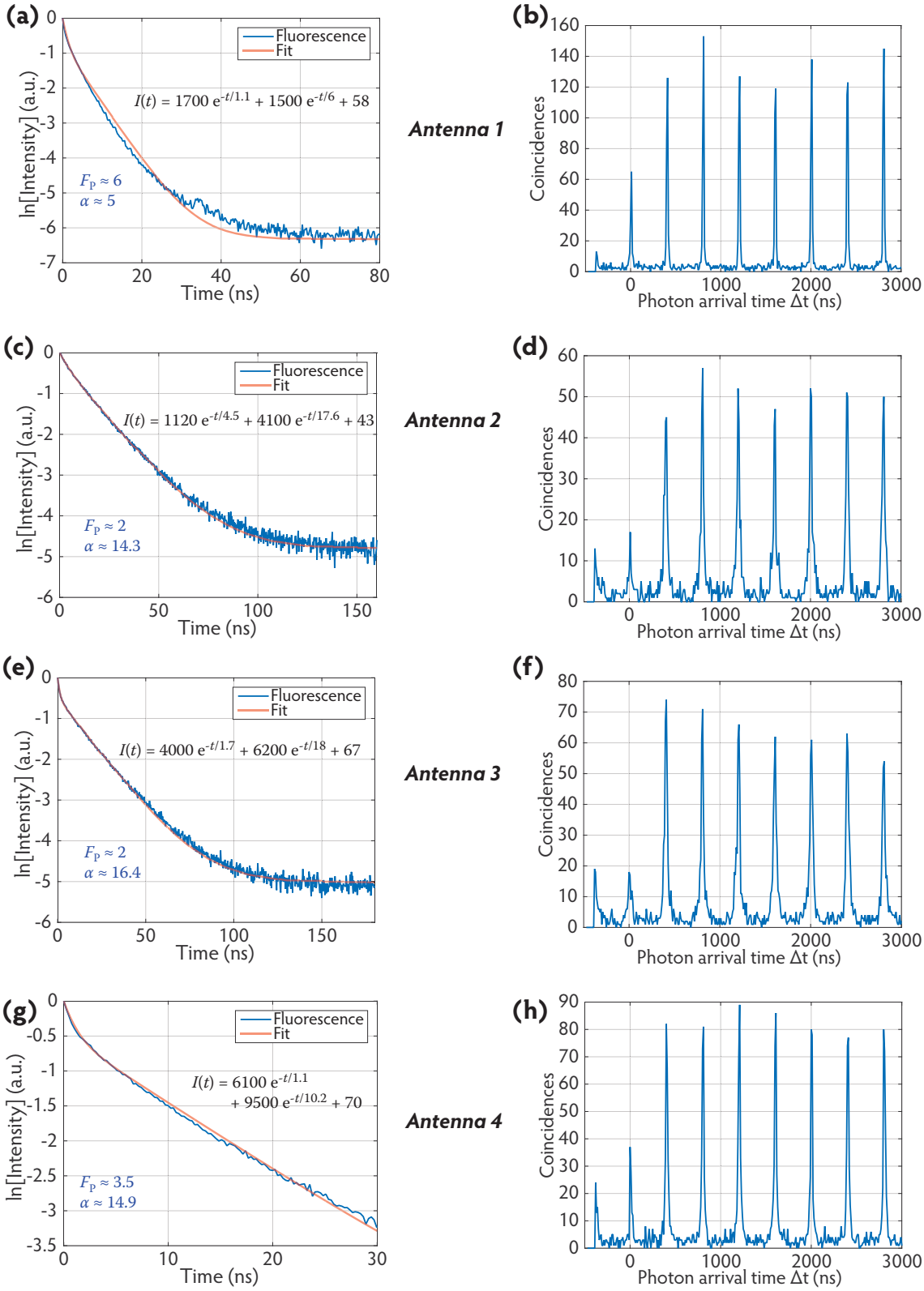

Figure 5.24 *LG40 patch nanoantennas*

All the four antennas were fabricated with LG_{40} laser mode lithography, and they show antibunching. The histograms in the left and right columns show the lifetime and $g^{(2)}(\Delta t)$, respectively.

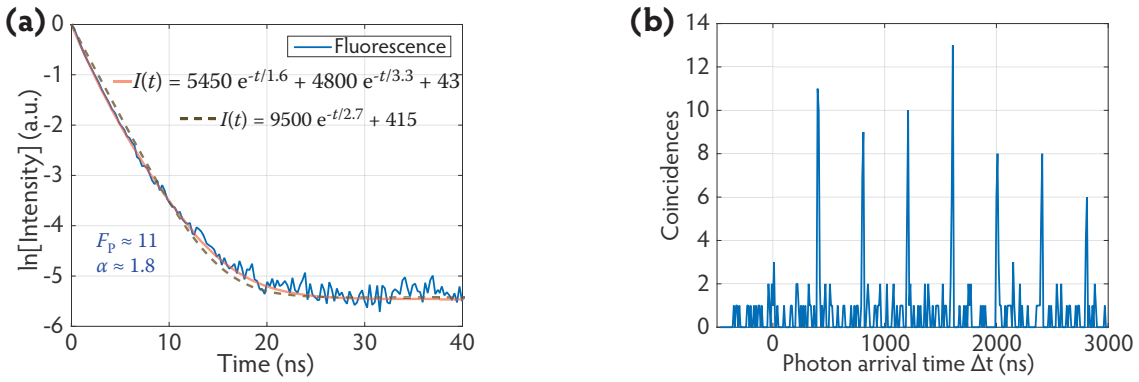

Figure 5.25 *An LG40 patch antenna*

The antenna was obtained with LG_{40} laser mode lithography. Its emission decay histogram **(a)** is almost mono-exponential, and in **(b)** we note antibunching. Based on the mono-exponential fit, its Purcell factor is deduced as 13 (higher than the bi-exponential fit value of 11).

5.8 Conclusion

Due to their special features, LG modes are of interest to many fields in optics and they have drawn significant scientific attention. Generation of *perfect* LG modes has been a challenge and new methods are being developed to achieve it. LCoS spatial light modulation, which benefits from the highly developing field of liquid crystals, offers a very practical solution to generate LG modes.

We have developed a technique in which the phase of a usual TEM_{00} laser mode is spatially modulated to generate LG modes of different orders. Using these LG laser modes, we perform deterministic in-situ optical lithography on single nanocrystals and fabricate single emitter plasmonic patch nanoantennas. To our knowledge, this is the first report on deterministic in-situ optical lithography with LG modes. This method avoids the photobleaching of the concerned emitter that occurs in optical lithography with TEM_{00} mode. Using SLMs, specialized optical beams can be generated to perform lithography and fabricate particular nanostructures. Moreover, these beams can be used to investigate other physical phenomena, which is usually not possible with conventional laser beams.

The patch antennas fabricated with LG_{20} and LG_{40} mode show acceleration of emission to a varying extent. Generally, the antennas with high Purcell factors show prominent multiexciton emission, as a result of which photon antibunching is lost. This is consistent with the observation of similar antennas fabricated using other protocols (supercontinuum and e-beam lithography). By controlling the nanocrystal dipole orientation and by reducing the patch diameter, we can optimize these antennas. The patch diameter can be reduced by using narrower LG_{20} and LG_{40} modes—this can be achieved by the SLM or through appropriate optics.

This page is intentionally left blank.

6 Conclusion and Perspectives

Single photon sources are of importance to fundamental science and are highly demanded in the field of quantum communications. Colloidal core/shell quantum dots are promising single photon sources. The field of plasmonics offers solutions for improving these single photon sources. One of these solutions is to use a plasmonic patch antenna to accelerate and direct the emission of single emitters. On the one hand, plasmonic patch antennas accelerate the emission of these single emitters, and on the other hand they provide a tool for understanding the light–matter interactions at a single emitter level. Many interesting phenomena, that are invisible due to averaging in ensemble studies, become evident in single emitter analysis.

Deterministic fabrication of single emitter plasmonic optical patch antennas demanded significant adaptation of the conventional lithography techniques. Techniques like photolithography and dielectric thin film deposition that could be used on a cluster of emitters to realize patch antennas were not suitable for the production of single emitter antennas. This was due to the low emission signal and photobleaching of a single emitter as compared to a cluster of emitters. To deterministically fabricate single emitter plasmonic patch antennas, we have developed three new lithography techniques. To our knowledge, this thesis is the first report on these methods and the single emitter patch antennas obtained implementing them. The first technique utilizes a supercontinuum laser to perform in-situ optical lithography on a resist bi-layer. The second method uses a combination of in-situ optical lithography and e-beam lithography on a resist bi-layer. The third process includes the generation of LG laser modes using spatial light modulation and performing in-situ optical lithography with them. All these techniques can be extended and adapted to fabricate a variety of nanostructures, especially single emitter photonic structures.

By comparing these protocols in their present form, it can be said that the in-situ optical lithography protocols using the supercontinuum laser and LG laser modes offers more accuracy than the combination of optical lithography and e-beam writing. The smallest antennas (which show a higher Purcell factor) were obtained with the supercontinuum laser lith-

ography protocol but as far as controlling the size and shape of the antenna patch is concerned, e-beam lithography is the best. Defocused supercontinuum laser lithography allows varying the patch size, and the emitter can be centered or off-centered with respect to the patch. LG mode lithography offers less possibility of controlling the patch size but due to the beam shape of LG modes, this technique can be used to fabricate specialized structures, which are usually not possible with TEM_{00} mode optical lithography. Improvement and optimization of these protocols will increase their accuracy, efficiency, and capability. Better calibration of distances on the fluorescence microscopy images will enhance the accuracy of the e-beam lithography protocol. The superior resolution of e-beam lithography can be exploited to fabricate such structures that are not possible with optical lithography.

The first studies on the plasmonic patch antennas obtained with the three techniques described in this thesis show similar optical characteristics. This was expected because all these antennas used the same kind of emitters (CdS/CdS quantum dots from the same production batch) and the same spacer thickness around the quantum dot. It was observed that most antennas with a high Purcell factor showed significantly high multiexciton emission, as a result of which photon-antibunching was lost. In these structures, the radiative multiexciton recombination rate becomes larger than the competing non-radiative Auger decay rate, and this leads to multiexciton emission. Many antennas with a low Purcell factor exhibit antibunching because the acceleration of multiexciton emission is not sufficient to overcome the more efficient and rapid non-radiative Auger processes. In a few cases, we observed a high Purcell factor and photon-antibunching—it seems that the emitters of these antennas had very efficient Auger recombination channels, which limited the radiative multiexciton decay rate, and this resulted in antenna emission which was mainly due to exciton recombination.

Our thick-shell and relatively big emitters easily show photon emission due to multiexciton recombination even when placed on a glass slip, and especially when excited with marginally higher laser fluence. We have noted that we could excite the single emitters inside the patch antennas with very low laser intensity. This laser intensity was lower than the intensity required to excite similar emitters placed outside the antenna or on a glass slip. This suggests that patch antennas are efficient in exciting the emitters. The interaction of the exciting laser light with the antenna patch probably creates strongly enhanced near-fields in the vicinity of the emitter, which is placed just below the patch. As the excitation intensity is enhanced by the patch, the emitters (which already have a tendency of showing multiexciton emission under high excitation) exhibit very pronounced multiexciton emission. Several studies show that the Auger effect is very efficient in small quantum dots (for example, CdSe/CdS and CdSe/ZnS of a total thickness of about 6 nm). Using such emitters in the antenna will limit the multiexciton emission, and photon-antibunching will be attained with a higher Purcell factor.

The thickness of the dielectric spacer, which holds the antenna emitter between the Au patch and the Au film, is a crucial parameter that affects the SPP coupling, and thereby the efficiency of the antenna. The first batches of antennas had a ~ 45 nm spacer, which is too thick to support an efficient coupling. By ultrathin spin-coated polymer films, we can regulate the spacer thickness. And by reducing the spacer thickness, we can enhance the Purcell factor.

Theoretical studies have shown that the orientation of the emitter dipole inside the antenna considerably influences the acceleration of emission. Through polarization analysis of the emission of a quantum dot, the three-dimensional orientation of its dipole can be estimated. By choosing well-oriented quantum emitters and then placing antenna patches on them, we

should be able to fabricate the spontaneous emission decay rate by more than 10–100 times. Optical characterization of antennas, whose emitter dipole orientation is known, will reveal interesting information about the optical interaction in these structures.

The efficiency of an antenna to direct emission is found in its radiation pattern. In addition to their directivity, the radiation pattern of patch antennas also reveals information about the patch size and its lateral position over the antenna emitter. These measurements could not be performed and presented during the writing of this thesis, but very soon we plan to measure the radiation pattern of the fabricated patch antennas.

The possibility of deterministically controlling the spacer thickness, the patch size, and the three-dimensional positioning of the patch over well-oriented emitter dipoles will lead to highly efficient plasmonic patch antennas which can serve as excellent single photon sources. The surface characteristics of the antenna patch and the metal film beneath the emitter can be influential to the propagation of SPPs. Theoretical and experimental work has shown that in these disordered films, electromagnetic energy can be confined in sub-wavelength structures called *hot spots*, which can cause strong enhancement of the intensity of the emitted light. This feature can be explored to make better patch antennas.

The protocols developed in my PhD work can be implemented to fabricate antennas or other photonic structures with a variety of single or multiple emitters, like quantum dots and nitrogen vacancy centers in nanodiamonds, using different types of dielectrics, and depositing different types of metals such as Au, Ag, and Al.

In our work, we have developed methods for obtaining clusters of quantum dots with controlled size distribution. Using these clusters as antenna emitters can give rise to special light–matter interactions. We may be able to observe and investigate (the clusters are size-controlled) effects like superradiance (radiation enhancement in systems with multiple quantum emitters). By including nanocrystals with a nonlinear optical response as antenna emitters, we can exploit the nonlinear interactions and create high intensity light sources. More generally, the possibility of creating highly confined and strong electromagnetic fields inside these antennas adds new dimensions to realizing and studying nanostructures which benefit from strong interaction of field with matter.

This page is intentionally left blank.

Appendix

A.1 Lasers

PicoQuant 405 nm laser

Manufacturer: PicoQuant
Type: LDH-D-C-405
Wavelength: 405±10 nm
Maximum repetition rate: 80 MHz
Maximum CW power: 50 mW
Maximum CW power after collimation: 7 mW
Pulse FWHM:
Low power < 50 ps
High power < 500 ps

SuperK EXTREME supercontinuum laser

Manufacturer: NKT Photonics
Type: SuperK EXTREME high power supercontinuum laser
Wavelength: 400–2400 nm
Master seed repetition rate: 80 (standard) or 40 MHz
Repetition rate reduction: 80–2 MHz (40 steps), 40–1 MHz (40 steps)
Pulse suppression ratio: > 1:10 000
Operation mode: Constant Pulse energy
Changing repetition rate: < 1 s (no need for electrical shutdown)
Timing trigger output jitter: < 20 ps
NIM trigger output (BNC): 0.1–1 V peak
Monitor trigger output (BNC): 0–1 V
Gate trigger output (BNC): 0–1 V
Delay shift between pulse picker ration: < ±250 ps

Adjustable trigger delay timing: up to 9.2 ns
Adjustable trigger delay resolution: 15 ps

SuperK VARIA (tunable wavelength filter for the supercontinuum laser)
Manufacturer: NKT Photonics
Type: SuperK VARIA tunable wavelength filter with variable bandwidth
Wavelength tuning range: 400–840 nm
Minimum bandwidth FWHM: < 10 nm
Maximum bandwidth FWHM: 100 nm
Transmission through module: (Average in 50 nm bandwidth) 70–90% (unpolarized)
Out of band suppression: > 50 dB
Output Polarization: Unpolarized or p-polarized (adding output polarizer)
Tuning speed: > 10 nm/s
Repeatability of wavelength position (with collimator inserted): < 0.2 nm
Absolute wavelength accuracy: ±5 nm
Wavelength temperature sensitivity: < 0.05 nm/deg
Transmission temperature sensitivity: < 0.2%/deg
Interlock: Collimator, lead
Output mode: Collimated free-space or SuperK CONNECT

A.2 Microscopy

Avalanche photodiode photon counting detector
Manufacturer: Micro Photon Devices (MPD)
Type: Solid-state based PDM series photon counting detector module

Specifications @ 25°C and 5 V overvoltage	Minimum	Typical	Maximum	Units
Photon Detection Efficiency @ 400 nm @ 550 nm @ 650 nm	 21 45 34	 24 49 37		%
Single Photon Timing Resolution TTL Counting Output NIM Timing Output(additional internal circuit board required)		 35	 250 50	ps (FWHM)
After -pulsing probability	0.1		3	%
Dead Time		77		ns
Supply Voltage	unregulated DC, any value 5V ~ 12V			
TTL Output Pulse rise and fall times Output pulse duration Gating input Supply input connector	 < 2 ns on 10 pF load 20 ns typical 5 V CMOS control (0 V, detector off) Standard 3.5 mm supply socket			

Intensified CCD camera

Manufacturer: Photonic Science
Type: Intensified CCD camera
CCD array size: 1392 × 1040 pixels
Input pixel size: 6.45 × 6.45 μm^2
13 fps at full resolution @ 25 MHz
32 fps in binning 2x2 @ 12.5 MHz
Readout noise: 8-9 electrons @ 12.5 MHz and 11–13 electrons @ 25 MHz
Dark current: 3 electrons/pixel/second
Synchronization/control: via TTL pulse

AFM cantilever specifications

Manufacturer: Bruker
Type: RTESPA MPP-11120-10
Shape: Rectangular
Resonant frequency: 300 kHz (minimum: 200 kHz, maximum: 400 kHz)
Spring constant: 40 N/m (minimum: 20 N/m, maximum: 80 N/m)
Length: 125 µm (minimum: 115 µm, maximum: 135 µm)
Width: 35 µm (minimum: 30 µm, maximum: 40 µm)
Thickness: 3.75 µm (minimum: 3 µm, maximum: 4.5 µm)
Material: 0.01–0.025 Ωcm Antimony (n) doped Si
Back Side Coating: Reflective Aluminum
Top Layer Back: 40 ± 10 nm of Al
Cantilever numbers: 1

AFM tip specifications

Manufacturer: Bruker
Type: RTESPA MPP-11120-10
Geometry: Rotated (Symmetric)
Tip height: 15–20 µm
Front angle: 15 ± 2°
Back angle: 25 ± 2°
Side angle: 17.5 ± 2°
Tip radius: 8 nm (maximum: 12 nm)
Tip setback: 15 µm (minimum: 5 µm, maximum: 25 µm)

A.3 Chemical products

PMMA powder

Product name: Poly(methyl methacrylate), secondary standard
Chemical formula: $[-CH_2C(CH_3)(CO_2CH_3)-]_n$
Producer: Aldrich Chemical Company, Inc.
Product number: 37003-7
CAS number: 9011-14-7

Lot number: 0159KU
Weight average molar mass, M_w = 101 000
Number average molar mass, M_n = 48 300

Toluene

Product name: Toluene AnalaR NORMAPUR®
Assay (on anhydrous substance): 99.8%
Chemical formula: C_7H_8
Producer: VWR International Ltd
Product number: 28676.297
CAS number: 108-88-3
Formula weight: 92.14 g/mol
Water ≤ 0.03%
Batch: 10J260505

Bibliography

[1] R. Esteban, T. V. Teperik, and J.-J. Greffet, "Optical patch antennas for single photon emission using surface plasmon resonances," *Phys. Rev. Lett.*, vol. 104, p. 026802, Jan 2010. [Online]. Available: http://link.aps.org/doi/10.1103/PhysRevLett.104.026802

[2] A. Dousse, L. Lanco, J. Suffczyński, E. Semenova, A. Miard, A. Lemaître, I. Sagnes, C. Roblin, J. Bloch, and P. Senellart, "Controlled light-matter coupling for a single quantum dot embedded in a pillar microcavity using far-field optical lithography," *Phys. Rev. Lett.*, vol. 101, p. 267404, Dec 2008. [Online]. Available: http://link.aps.org/doi/10.1103/PhysRevLett.101.267404

[3] C. Belacel, B. Habert, F. Bigourdan, F. Marquier, J.-P. Hugonin, S. M. de Vasconcellos, X. Lafosse, L. Coolen, C. Schwob, C. Javaux, B. Dubertret, J.-J. Greffet, P. Senellart, and A. Maitre, "Controlling spontaneous emission with plasmonic optical patch antennas," *PRL*, 2012.

[4] V. Klimov, *Nanocrystal Quantum Dots*, 2nd ed. CRC Press, 2010.

[5] R. Collin, *Antennas and radiowave propagation*, ser. McGraw-Hill series in electrical engineering. USA: McGraw-Hill, 1985.

[6] J.-J. Greffet, "Nanoantennas for light emission," *Science*, vol. 308, no. 5728, pp. 1561–1563, 2005. [Online]. Available: http://www.sciencemag.org/content/308/5728/1561.short

[7] L. Novotny and N. van Hulst, "Antennas for light," *Nature Photonics*, vol. 5, no. 2, pp. 83–90, 2011. [Online]. Available: http://www.nature.com/nphoton/journal/v5/n2/full/nphoton.2010.237.html

[8] C. Belacel, "Emission de nanocristaux semi-conducteurs dans une antenne patch plasmonique," Ph.D. dissertation, Université Pierre et Marie Curie, 2013.

[9] H. Aouani, S. Itzhakov, D. Gachet, E. Devaux, T. W. Ebbesen, H. Rigneault, D. Oron, and J. Wenger, "Colloidal quantum dots as probes of excitation field enhancement in photonic antennas," *ACS Nano*, vol. 4, no. 8, pp. 4571–4578, 2010, pMID: 20731440. [Online]. Available: http://dx.doi.org/10.1021/nn1009209

[10] M. S. Eggleston, K. Messer, L. Zhang, E. Yablonovitch, and M. C. Wu, "Optical antenna enhanced spontaneous emission," *Proceedings of the National Academy of Sciences*, vol. 112, no. 6, pp. 1704–1709, 2015. [Online]. Available: http://www.pnas.org/content/112/6/1704.abstract

[11] H. Aouani, O. Mahboub, E. Devaux, H. Rigneault, T. W. Ebbesen, and J. Wenger, "Plasmonic antennas for directional sorting of fluorescence emission," *Nano Letters*, vol. 11, no. 6, pp. 2400–2406, 2011, pMID: 21591739. [Online]. Available: http://dx.doi.org/10.1021/nl200772d

[12] J. Wolters, G. Kewes, A. W. Schell, N. Nüsse, M. Schoengen, B. Löchel, T. Hanke, R. Bratschitsch, A. Leitenstorfer, T. Aichele, and O. Benson, "Coupling of single

nitrogen-vacancy defect centers in diamond nanocrystals to optical antennas and photonic crystal cavities," *physica status solidi (b)*, vol. 249, no. 5, pp. 918–924, 2012. [Online]. Available: http://onlinelibrary.wiley.com/doi/10.1002/pssb.201100156/abstract

[13] S. Kawata, Y. Inouye, and P. Verma, "Plasmonics for near-field nano-imaging and superlensing," *Nature Photonics*, vol. 3, no. 7, pp. 388–394, 2009. [Online]. Available: http://www.nature.com/nphoton/journal/v3/n7/full/nphoton.2009.111.html

[14] A. Hartschuh, "Tip-enhanced optical spectroscopy," *Philosophical Transactions of the Royal Society of London A: Mathematical, Physical and Engineering Sciences*, vol. 362, no. 1817, pp. 807–819, 2004. [Online]. Available: http://www.optics.rochester.edu/workgroups/novotny/papers/hartschuh04a.pdf

[15] N. Hayazawa, Y. Inouye, Z. Sekkat, and S. Kawata, "Metallized tip amplification of near-field raman scattering," *Optics Communications*, vol. 183, no. 1, pp. 333–336, 2000. [Online]. Available: http://www.sciencedirect.com/science/article/pii/S0030401800008944

[16] D. Wang, W. Zhu, Y. Chu, and K. B. Crozier, "High directivity optical antenna substrates for surface enhanced raman scattering," *Advanced Materials*, vol. 24, no. 32, pp. 4376–4380, 2012. [Online]. Available: http://onlinelibrary.wiley.com/doi/10.1002/adma.201201625/abstract

[17] Y. Yu, V. E. Ferry, A. P. Alivisatos, and L. Cao, "Dielectric core–shell optical antennas for strong solar absorption enhancement," *Nano Letters*, vol. 12, no. 7, pp. 3674–3681, 2012, pMID: 22686287. [Online]. Available: http://dx.doi.org/10.1021/nl301435r

[18] C. Hägglund and B. Kasemo, "Nanoparticle plasmonics for 2d-photovoltaics: Mechanisms, optimization, and limits," *Opt. Express*, vol. 17, no. 14, pp. 11 944–11 957, Jul 2009. [Online]. Available: http://www.opticsexpress.org/abstract.cfm?URI=oe-17-14-11944

[19] S. Pillai, K. R. Catchpole, T. Trupke, and M. A. Green, "Surface plasmon enhanced silicon solar cells," *Journal of Applied Physics*, vol. 101, no. 9, 2007. [Online]. Available: http://scitation.aip.org/content/aip/journal/jap/101/9/10.1063/1.2734885

[20] H. A. Atwater and A. Polman, "Plasmonics for improved photovoltaic devices," *Nature materials*, vol. 9, no. 3, pp. 205–213, 2010. [Online]. Available: http://www.nature.com/nmat/journal/v9/n3/abs/nmat2629.html

[21] N. Yu, E. Cubukcu, L. Diehl, M. A. Belkin, K. B. Crozier, F. Capasso, D. Bour, S. Corzine, and G. Höfler, "Plasmonic quantum cascade laser antenna," *Applied Physics Letters*, vol. 91, no. 17, p. 173113, 2007. [Online]. Available: http://scitation.aip.org/content/aip/journal/apl/91/17/10.1063/1.2801551

[22] N. Yu, E. Cubukcu, L. Diehl, D. Bour, S. Corzine, J. Zhu, G. Höfler, K. B. Crozier, and F. Capasso, "Bowtie plasmonic quantum cascade laser antenna," *Opt. Express*, vol. 15, no. 20, pp. 13 272–13 281, Oct 2007. [Online]. Available: http://www.opticsexpress.org/abstract.cfm?URI=oe-15-20-13272

[23] C. A. Balanis, *Antenna theory: analysis and design*, 3rd ed. John Wiley & Sons, 2005.

[24] P. Bharadwaj, B. Deutsch, and L. Novotny, "Optical antennas," *Advances in Optics and Photonics*, vol. 1, no. 3, pp. 438–483, Nov 2009. [Online]. Available: http://aop.osa.org/abstract.cfm?URI=aop-1-3-438

[25] L. Novotny and B. Hecht, *Principles of Nano-Optics*, 2nd ed. Cambridge University Press, 2012.

[26] R. E. Collin, *Foundations for Microwave Engineering*, 2nd ed. New York: IEEE Press, 2001.

[27] J.-J. Greffet, M. Laroche, and F. Marquier, "Impedance of a nanoantenna and a single quantum emitter," *Phys. Rev. Lett.*, vol. 105, p. 117701, Sep 2010. [Online]. Available: http://link.aps.org/doi/10.1103/PhysRevLett.105.117701

[28] A. Alù and N. Engheta, "Input impedance, nanocircuit loading, and radiation tuning of optical nanoantennas," *Physical review letters*, vol. 101, no. 4, p. 043901, 2008. [Online]. Available: http://dx.doi.org/10.1103/PhysRevLett.101.043901

[29] J.-S. Huang, T. Feichtner, P. Biagioni, and B. Hecht, "Impedance matching and emission properties of nanoantennas in an optical nanocircuit," *Nano letters*, vol. 9, no. 5, pp. 1897–1902, 2009. [Online]. Available: http://dx.doi.org/10.1021/nl803902t

[30] B. C. Stipe, T. C. Strand, C. C. Poon, H. Balamane, T. D. Boone, J. A. Katine, J.-L. Li, V. Rawat, H. Nemoto, A. Hirotsune *et al.*, "Magnetic recording at 1.5 pb m- 2 using an integrated plasmonic antenna," *Nature Photonics*, vol. 4, no. 7, pp. 484–488, 2010. [Online]. Available: http://www.nature.com/nphoton/journal/v4/n7/abs/nphoton.2010.90.html

[31] L. Cao, P. Fan, A. P. Vasudev, J. S. White, Z. Yu, W. Cai, J. A. Schuller, S. Fan, and M. L. Brongersma, "Semiconductor nanowire optical antenna solar absorbers," *Nano Letters*, vol. 10, no. 2, pp. 439–445, 2010, pMID: 20078065. [Online]. Available: http://dx.doi.org/10.1021/nl9036627

[32] B. S. Luk'yanchuk, N. V. Voshchinnikov, R. Paniagua-Domínguez, and A. I. Kuznetsov, "Optimum forward light scattering by spherical and spheroidal dielectric nanoparticles with high refractive index," *ACS Photonics*, vol. 2, no. 7, pp. 993–999, 2015. [Online]. Available: http://dx.doi.org/10.1021/acsphotonics.5b00261

[33] C. Kittel, *Introduction to Solid State Physics*. Hoboken, NJ: Wiley, 2005.

[34] S. Maier, *Plasmonics: Fundamentals and Applications*. New York: Springer, 2007.

[35] J. Zhang and L. Zhang, "Nanostructures for surface plasmons," *Adv. Opt. Photon.*, vol. 4, no. 2, pp. 157–321, Jun 2012. [Online]. Available: http://aop.osa.org/abstract.cfm?URI=aop-4-2-157

[36] R. Gordon, "Surface plasmon nanophotonics: A tutorial," *Nanotechnology Magazine, IEEE*, vol. 2, no. 3, pp. 12 –18, september 2008. [Online]. Available: http://dx.doi.org/10.1109/MNANO.2008.931481

[37] E. M. Purcell, "Spontaneous emission probabilities at radio frequencies," vol. 69, 1946, pp. 681+. [Online]. Available: http://prola.aps.org/pdf/PR/v69/i11-12/p674_2

[38] K. J. Vahala, "Optical microcavities," *Nature*, vol. 424, no. 6950, pp. 839–846, Aug. 2003. [Online]. Available: http://dx.doi.org/10.1038/nature01939

[39] G. Grynberg, A. Aspect, and C. Fabre, *Introduction to Quantum Optics: From the Semi-classical Approach to Quantized Light*, ser. Introduction to Quantum Optics: From the Semi-classical Approach to Quantized Light. Cambridge University Press, 2010.

[40] B. Habert, "Contrôle de la fluorescence par des nanoantennes plasmoniques," Ph.D. dissertation, Institut d'optique Graduate School, 2014.

[41] A. Maître, "Polarimetric determination of the orientation of a single dipole," 2015.

[42] C. Belacel, "Emission polarisée de nanoémetteurs; excitation de plasmons sur une surface métallique," Ph.D. dissertation, Université Pierre et Marie Curie, 2014.

[43] C. Lethiec, J. Laverdant, H. Vallon, C. Javaux, B. Dubertret, J.-M. Frigerio, C. Schwob, L. Coolen, and A. Maître, "Measurement of three-dimensional dipole orientation of a single fluorescent nanoemitter by emission polarization analysis," *Phys. Rev. X*, vol. 4, p. 021037, May 2014. [Online]. Available: http://link.aps.org/doi/10.1103/PhysRevX.4.021037

[44] B. Bhushan, Ed., *Springer Handbook of Nanotechnology*, 2nd ed. Berlin: Springer, 2007.

[45] A. R. Dhawan, F. Feng, L. Coolen, and A. Maitre, "Breakthroughs in photonics 2014: Semiconductor luminescent colloidal core-shell nanorods and dot-in-rods," *Photonics Journal, IEEE*, vol. 7, no. 3, pp. 1–6, June 2015. [Online]. Available: http://ieeexplore.ieee.org/stamp/stamp.jsp?arnumber=7061434

[46] M. A. Reed, J. N. Randall, R. J. Aggarwal, R. J. Matyi, T. M. Moore, and A. E. Wetsel, "Observation of discrete electronic states in a zero-dimensional semiconductor nanostructure," *Phys. Rev. Lett.*, vol. 60, pp. 535–537, Feb 1988. [Online]. Available: http://link.aps.org/doi/10.1103/PhysRevLett.60.535

[47] A. M. Smith and S. Nie, "Semiconductor nanocrystals: Structure, properties, and band gap engineering," *Accounts of Chemical Research*, vol. 43, no. 2, pp. 190–200, 2010, pMID: 19827808. [Online]. Available: http://dx.doi.org/10.1021/ar9001069

[48] B. Mahler, P. Spinicelli, S. Buil, X. Quelin, J.-P. Hermier, and B. Dubertret, "Towards non-blinking colloidal quantum dots," *Nature Materials*, vol. 7, no. 8, pp. 659–664, Jun. 2008. [Online]. Available: http://dx.doi.org/10.1038/nmat2222

[49] A. Rogach, *Semiconductor Nanocrystal Quantum Dots: Synthesis, Assembly, Spectroscopy and Applications*, ser. Springer ebook collection / Chemistry and Materials Science 2005-2008. Springer Vienna, 2008.

[50] B. O. Dabbousi, J. Rodriguez-Viejo, F. V. Mikulec, J. R. Heine, H. Mattoussi, R. Ober, K. F. Jensen, and M. G. Bawendi, "(CdSe)ZnS core–shell quantum dots:

Synthesis and characterization of a size series of highly luminescent nanocrystallites," *J. Phys. Chem. B*, vol. 101, no. 46, pp. 9463–9475, Nov. 1997. [Online]. Available: http://dx.doi.org/10.1021/jp971091y

[51] P. Reiss, M. Protière, and L. Li, "Core/shell semiconductor nanocrystals," *Small*, vol. 5, no. 2, pp. 154–168, 2009. [Online]. Available: http://dx.doi.org/10.1002/smll.200800841

[52] S. Kim, B. Fisher, H.-J. Eisler, and M. Bawendi, "Type-II quantum dots: CdTe/CdSe(core/shell) and CdSe/ZnTe(core/shell) heterostructures," *Journal of the American Chemical Society*, vol. 125, no. 38, pp. 11 466–11 467, 2003, pMID: 13129327. [Online]. Available: http://dx.doi.org/10.1021/ja0361749

[53] S. Brovelli, R. Schaller, S. Crooker, F. García-Santamaría, Y. Chen, R. Viswanatha, J. Hollingsworth, H. Htoon, and V. Klimov, "Nano-engineered electron–hole exchange interaction controls exciton dynamics in core–shell semiconductor nanocrystals," *Nature Communications*, vol. 2, p. 280, apr 2011. [Online]. Available: http://dx.doi.org/10.1038/ncomms1281

[54] X. Peng, J. Wickham, and A. P. Alivisatos, "Kinetics of II-VI and III-V Colloidal Semiconductor Nanocrystal Growth: "Focusing" of Size Distributions," *Journal of the American Chemical Society*, vol. 120, no. 21, pp. 5343–5344, Jun. 1998. [Online]. Available: http://dx.doi.org/10.1021/ja9805425

[55] X. Peng, L. Manna, W. Yang, J. Wickham, E. Scher, A. Kadavanich, and A. P. Alivisatos, "Shape control of CdSe nanocrystals," *Nature*, vol. 404, no. 6773, pp. 59–61, Mar. 2000. [Online]. Available: http://dx.doi.org/10.1038/35003535

[56] M. Nasilowski, "Ligands around quantum dots," 2015, in a private conversation.

[57] H. Cang, Y. Liu, Y. Wang, X. Yin, and X. Zhang, "Giant suppression of photobleaching for single molecule detection via the purcell effect," *Nano Letters*, vol. 13, no. 12, pp. 5949–5953, 2013, pMID: 24245957. [Online]. Available: http://dx.doi.org/10.1021/nl403047m

[58] B. Herman, M. J. Parry-Hill, I. D. Johnson, and M. W. Davidson, "Photobleaching," Olympus—Microscopy resource center. [Online]. Available: http://www.olympusmicro.com/primer/java/fluorescence/photobleaching/. [Accessed: August 25, 2015].

[59] G. Kalyuzhny and R. W. Murray, "Ligand effects on optical properties of CdSe nanocrystals," *The Journal of Physical Chemistry B*, vol. 109, no. 15, pp. 7012–7021, 2005. [Online]. Available: http://dx.doi.org/10.1021/jp045352x

[60] A. Zhang, C. Dong, H. Liu, and J. Ren, "Blinking behavior of CdSe/CdS quantum dots controlled by alkylthiols as surface trap modifiers," *The Journal of Physical Chemistry C*, vol. 117, no. 46, pp. 24 592–24 600, 2013. [Online]. Available: http://dx.doi.org/10.1021/jp408544x

[61] P. Wang, J. Zhang, H. He, X. Xu, and Y. Jin, "The important role of surface ligand on CdSe/CdS core/shell nanocrystals in affecting the efficiency of H_2 photogeneration

from water," *Nanoscale*, vol. 7, pp. 5767–5775, 2015. [Online]. Available: http://dx.doi.org/10.1039/C4NR07343F

[62] L. Bergman and J. McHale, *Handbook of Luminescent Semiconductor Materials*. CRC Press, 2011.

[63] A. M. Munro, I. J.-L. Plante, M. S. Ng, and D. S. Ginger, "Quantitative study of the effects of surface ligand concentration on CdSe nanocrystal photoluminescence," *The Journal of Physical Chemistry C*, vol. 111, no. 17, pp. 6220–6227, 2007. [Online]. Available: http://dx.doi.org/10.1021/jp068733e

[64] Sigma Aldrich®, "Lumidot™ FAQ: Frequently asked questions about using QD nanocrystals," [Accessed: August 25, 2015]. [Online]. Available: https://www.sigmaaldrich.com/content/dam/sigma-aldrich/docs/Sigma-Aldrich/General_Information/lumidot_faqs.pdf

[65] M. Nasilowski, "Nanocrystals in highly concentrated colloidal dispersions," 2014, in a private conversation.

[66] B. Saleh and M. Teich, *Fundamentals of Photonics*, 2nd ed. New York: John Wiley & Sons, Inc., 2007.

[67] A. T. Dijksman, "Spectroscopy of colloidal quantum dots of controlled shape and size," Ph.D. dissertation, Université Pierre et Marie Curie, 2013.

[68] J. R. Lakowicz, *Principles of Fluorescence Spectroscopy*, 3rd ed. New York: Springer, 2006.

[69] O. Gywat, H. Krenner, and J. Berezovsky, *Spins in Optically Active Quantum Dots: Concepts and Methods*. John Wiley & Sons, 2010.

[70] C. Santori, D. Fattal, and Y. Yamamoto, *Single-photon Devices and Applications*, ser. Physics textbook. John Wiley & Sons, 2010.

[71] B. Lounis and M. Orrit, "Single-photon sources," *Reports on Progress in Physics*, vol. 68, no. 5, p. 1129, 2005. [Online]. Available: http://stacks.iop.org/0034-4885/68/i=5/a=R04

[72] M. D. Eisaman, J. Fan, A. Migdall, and S. V. Polyakov, "Invited review article: Single-photon sources and detectors," *Review of Scientific Instruments*, vol. 82, no. 7, 2011. [Online]. Available: http://scitation.aip.org/content/aip/journal/rsi/82/7/10.1063/1.3610677

[73] M. Nirmal, B. O. Dabbousi, M. G. Bawendi, J. J. Macklin, J. K. Trautman, T. D. Harris, and L. E. Brus, "Fluorescence intermittency in single cadmium selenide nanocrystals," *Nature*, vol. 383, no. 6603, pp. 802–804, Oct. 1996. [Online]. Available: http://dx.doi.org/10.1038/383802a0

[74] P. Frantsuzov, M. Kuno, B. Janko, and R. A. Marcus, "Universal emission intermittency in quantum dots, nanorods, and nanowires," *Nature Physics*, vol. 4, Oct. 2008.

[75] G. Margolin, V. Protasenko, M. Kuno, and E. Barkai, "Photon counting statistics for blinking CdSe–ZnS quantum dots: A Lévy walk process," *The Journal of Physical*

Chemistry B, vol. 110, no. 38, pp. 19 053–19 060, 2006, pMID: 16986903. [Online]. Available: http://pubs.acs.org/doi/abs/10.1021/jp061487m

[76] A. Demchenko, *Introduction to Fluorescence Sensing*, ser. Biomedical and Life Sciences. Springer Netherlands, 2008.

[77] A. P. Demchenko, "Optimization of fluorescence response in the design of molecular biosensors," *Analytical Biochemistry*, vol. 343, no. 1, pp. 1 – 22, 2005. [Online]. Available: http://www.sciencedirect.com/science/article/pii/S0003269704009455

[78] M. Abramowitz and M. W. Davidson, "Overview of fluorescence excitation and emission fundamentals," Olympus—Microscopy resource center. [Online]. Available: http://www.olympusmicro.com/primer/lightandcolor/fluoroexcitation.html. [Accessed: August 25, 2015].

[79] N. Ashcroft and N. Mermin, *Solid State Physics*, ser. HRW international editions. Holt, Rinehart and Winston, 1976.

[80] A. L. Efros, V. Kharchenko, and M. Rosen, "Breaking the phonon bottleneck in nanometer quantum dots: Role of auger-like processes," *Solid State Communications*, vol. 93, no. 4, pp. 281 – 284, 1995. [Online]. Available: http://www.sciencedirect.com/science/article/pii/0038109894007608

[81] W. Benenson and H. Stöcker, *Handbook of Physics*, ser. Prentice-Hall series in educational innovation. Prentice Hall, 2002.

[82] D. Chattarji, *The Theory of Auger Transitions*. Academic Press, 1976.

[83] J. Laverdant, W. D. de Marcillac, C. Barthou, V. D. Chinh, C. Schwob, L. Coolen, P. Benalloul, P. T. Nga, and A. Maître, "Experimental determination of the fluorescence quantum yield of semiconductor nanocrystals," *Materials*, vol. 4, no. 7, p. 1182, 2011. [Online]. Available: http://www.mdpi.com/1996-1944/4/7/1182

[84] B. Saleh and M. Teich, *Fundamentals of Photonics*. New York: John Wiley & Sons, Inc., 1991.

[85] C. Vion, "Couplage de nanocristaux colloïdaux à des structures photoniques," Ph.D. dissertation, Université Pierre et Marie Curie, 2009.

[86] S. Vezzoli, "Experimental study of nanocrystals as single photon sources," Ph.D. dissertation, Università degli Studi di Milano & Université Pierre et Marie Curie, 2013.

[87] M. Marceddu, M. Saba, F. Quochi, A. Lai, J. Huang, D. V. Talapin, A. Mura, and G. Bongiovanni, "Charged excitons, Auger recombination and optical gain in CdSe/CdS nanocrystals," *Nanotechnology*, vol. 23, no. 1, p. 015201, 2012. [Online]. Available: http://stacks.iop.org/0957-4484/23/i=1/a=015201

[88] R. D. Schaller and V. I. Klimov, "High efficiency carrier multiplication in PbSe nanocrystals: Implications for solar energy conversion," *Phys. Rev. Lett.*, vol. 92, p. 186601, May 2004. [Online]. Available: http://link.aps.org/doi/10.1103/PhysRevLett.92.186601

[89] A. Rogach, *Semiconductor Nanocrystal Quantum Dots: Synthesis, Assembly, Spectroscopy and Applications*, ser. Springer ebook collection / Chemistry and Materials Science 2005-2008. Springer Vienna, 2008.

[90] B. Fisher, J. M. Caruge, D. Zehnder, and M. Bawendi, "Room-temperature ordered photon emission from multiexciton states in single CdSe core-shell nanocrystals," *Phys. Rev. Lett.*, vol. 94, p. 087403, Mar 2005. [Online]. Available: http://link.aps.org/doi/10.1103/PhysRevLett.94.087403

[91] V. I. Klimov, A. A. Mikhailovsky, D. W. McBranch, C. A. Leatherdale, and M. G. Bawendi, "Quantization of multiparticle auger rates in semiconductor quantum dots," *Science*, vol. 287, no. 5455, pp. 1011–1013, 2000. [Online]. Available: http://www.sciencemag.org/content/287/5455/1011.full

[92] C. Santori, D. Fattal, J. Vučković, G. S. Solomon, and Y. Yamamoto, "Indistinguishable photons from a single-photon device," *Nature*, vol. 419, no. 6907, pp. 594–597, Oct. 2002. [Online]. Available: http://dx.doi.org/10.1038/nature01086

[93] "Experimental methods in the physical sciences," in *Single-Photon Generation and Detection Physics and Applications*, ser. Experimental Methods in the Physical Sciences, J. F. Alan Migdall, Sergey V. Polyakov and J. C. Bienfang, Eds. Academic Press, 2013, vol. 45. [Online]. Available: http://www.sciencedirect.com/science/article/pii/B9780123876959000159

[94] H. J. Kimble, M. Dagenais, and L. Mandel, "Photon antibunching in resonance fluorescence," *Phys. Rev. Lett.*, vol. 39, pp. 691–695, Sep 1977. [Online]. Available: http://link.aps.org/doi/10.1103/PhysRevLett.39.691

[95] R. Hanbury Brown and R. Q. Twiss, "Correlation between photons in two coherent beams of light," *Nature*, vol. 177, 1956. [Online]. Available: http://dx.doi.org/10.1038/177027a0

[96] P. Michler, A. Imamoglu, M. D. Mason, P. J. Carson, G. F. Strouse, and S. K. Buratto, "Quantum correlation among photons from a single quantum dot at room temperature," *Nature*, vol. 406, no. 6799, pp. 968–970, Aug. 2000. [Online]. Available: http://dx.doi.org/10.1038/35023100

[97] P. Michler, A. Kiraz, C. Becher, W. V. Schoenfeld, P. M. Petroff, L. Zhang, E. Hu, and A. Imamoglu, "A quantum dot single-photon turnstile device," *Science*, vol. 290, no. 5500, pp. 2282–2285, 2000. [Online]. Available: http://www.sciencemag.org/content/290/5500/2282.abstract

[98] R. Loudon, *The Quantum Theory of Light*. OUP Oxford, 2000.

[99] R. J. Glauber, "The quantum theory of optical coherence," *Phys. Rev.*, vol. 130, pp. 2529–2539, Jun 1963. [Online]. Available: http://link.aps.org/doi/10.1103/PhysRev.130.2529

[100] W. E. Moerner and L. Kador, "Optical detection and spectroscopy of single molecules in a solid," *Phys. Rev. Lett.*, vol. 62, pp. 2535–2538, May 1989. [Online]. Available: http://link.aps.org/doi/10.1103/PhysRevLett.62.2535

[101] M. Orrit and J. Bernard, "Single pentacene molecules detected by fluorescence excitation in a p-terphenyl crystal," *Phys. Rev. Lett.*, vol. 65, pp. 2716–2719, Nov 1990. [Online]. Available: http://link.aps.org/doi/10.1103/PhysRevLett.65.2716

[102] M. Wahl, "Time-correlated single photon counting," 2014. [Online]. Available: http://www.picoquant.com/images/uploads/page/files/7253/technote_tcspc.pdf

[103] M. Lippitz, F. Kulzer, and M. Orrit, "Statistical evaluation of single nano-object fluorescence," *ChemPhysChem*, vol. 6, no. 5, pp. 770–789, 2005. [Online]. Available: http://onlinelibrary.wiley.com/doi/10.1002/cphc.200400560/pdf

[104] M. N. O. Sadiku, *Elements of Electromagnetics*, 3rd ed. New York: Oxford University Press, Inc., 2001.

[105] K. Ray, M. H. Chowdhury, and J. R. Lakowicz, "Observation of surface plasmon-coupled emission using thin platinum films," *Chemical Physics Letters*, vol. 465, no. 1–3, pp. 92 – 95, 2008. [Online]. Available: http://www.sciencedirect.com/science/article/pii/S0009261408013237

[106] D. Gérard and S. K. Gray, "Aluminium plasmonics," *Journal of Physics D: Applied Physics*, vol. 48, no. 18, p. 184001, 2015. [Online]. Available: http://stacks.iop.org/0022-3727/48/i=18/a=184001

[107] J. Martin, M. Kociak, J. Proust, D. Gérard, and J. Plain, "High-order plasmonic modes on aluminum nanoantennas unveiled by electron energy loss spectroscopy," in *Condensed Matter in Paris 2014*, August 2014.

[108] J. Olson, A. Manjavacas, L. Liu, W.-S. Chang, B. Foerster, N. S. King, M. W. Knight, P. Nordlander, N. J. Halas, and S. Link, "Vivid, full-color aluminum plasmonic pixels," vol. 111, no. 40, pp. 14 348–14 353, 2014.

[109] H. Pulker, "Film deposition methods," in *Optical Interference Coatings*, ser. Springer Series in Optical Sciences, N. Kaiser and H. Pulker, Eds. Springer Berlin Heidelberg, 2003, vol. 88, pp. 131–153. [Online]. Available: http://dx.doi.org/10.1007/978-3-540-36386-6_6

[110] M. Friz and F. Waibel, "Coating materials," in *Optical Interference Coatings*, ser. Springer Series in Optical Sciences, N. Kaiser and H. Pulker, Eds. Springer Berlin Heidelberg, 2003, vol. 88, pp. 105–130. [Online]. Available: http://dx.doi.org/10.1007/978-3-540-36386-6_5

[111] P. Eaton, "Frequently asked questions about atomic force microscopy (AFM FAQ)." [Online]. Available: http://www.fc.up.pt/pessoas/peter.eaton/afm_faq.html#16

[112] R. E. Hopkins, "Applications of thin film coating," in *Military Standardization Handbook: Optical Design*. Washington DC: U. S. Defense Supply Agency, 1962.

[113] H. Nalwa, *Handbook of Thin Films, Five-Volume Set*, ser. Handbook of Thin Film Materials. Elsevier Science, 2001, ch. High-Permittivity (Ba, Sr)TiO_3 Thin Films.

[114] K. C. Kao, *Dielectric Phenomena in Solids: With Emphasis on Physical Concepts of Electronic Processes*. Amsterdam; Boston: Academic Press, 2004.

[115] M. Born, E. Wolf, and A. Bhatia, *Principles of Optics: Electromagnetic Theory of Propagation, Interference and Diffraction of Light*. Cambridge University Press, 1999.

[116] H. Lüth, *Solid Surfaces, Interfaces and Thin Films*, ser. Graduate Texts in Physics. Springer Berlin Heidelberg, 2010.

[117] W. G. J. H. M. van Sark, P. L. T. M. Frederix, D. J. V. den Heuvel, , H. C. Gerritsen, A. A. Bol, J. N. J. van Lingen, C. de Mello Donegá, , and A. Meijerink, "Photooxidation and photobleaching of single CdSe/ZnS quantum dots probed by room-temperature time-resolved spectroscopy," *The Journal of Physical Chemistry B*, vol. 105, no. 35, pp. 8281–8284, 2001. [Online]. Available: http://dx.doi.org/10.1021/jp012018h

[118] M. C. Barnes, I.-D. Jeon, D.-Y. Kim, and N. M. Hwang, "Generation of charged clusters during thermal evaporation of gold," *Journal of Crystal Growth*, vol. 242, no. 3–4, pp. 455 – 462, 2002. [Online]. Available: http://www.sciencedirect.com/science/article/pii/S0022024802014173

[119] B. S. Lee, M. C. Barnes, D.-Y. Kim, and N. M. Hwang, "Spontaneous generation of charged clusters of a few nanometers during thermal evaporation of copper," *Journal of Crystal Growth*, vol. 234, no. 2–3, pp. 599 – 602, 2002. [Online]. Available: http://www.sciencedirect.com/science/article/pii/S002202480101747X

[120] F. Feng, S. Portalupi, X. Lafosse, A. R. Dhawan, W. D. de Marcillac, J.-M. Frigerio, C. Schwob, B. Dubertret, A. Maître, P. Senellart, and L. Coolen, "Coupling colloidal nanocrystals to optical Tamm plasmons," *ICTON*, 2015.

[121] H. Nalwa, *Handbook of Thin Films, Five-Volume Set*, ser. Handbook of Thin Film Materials. Elsevier Science, 2001.

[122] MicroChem, "Spin coating of photoresists." [Online]. Available: http://www.microchemicals.com/technical_information/spin_coating_photoresist.pdf

[123] D. B. Hall, P. Underhill, and J. M. Torkelson, "Spin coating of thin and ultrathin polymer films," *Polymer Engineering & Science*, vol. 38, no. 12, pp. 2039–2045, 1998. [Online]. Available: http://dx.doi.org/10.1002/pen.10373

[124] K. Whitten, R. Davis, and M. Peck, *General Chemistry*. Saunders College Pub., 2000.

[125] MicroChem, "Baking steps in photoresist processing." [Online]. Available: http://www.microchemicals.eu/technical_information/photoresist_baking.pdf

[126] J. Golden, H. Miller, D. Nawrocki, and J. Ross, "Optimization of bi-layer lift-off resist process," 2009. [Online]. Available: http://www.microchem.com/pdf/LOR-Extended-Abstract-Final.pdf

[127] MicroChem, "PMGI and LOR resists: FAQs," 2015. [Online]. Available: http://www.microchem.com/pmgi-lor_faq.htm

[128] D. R. Lide, Ed., *CRC Handbook of Chemistry and Physics 90th Edition (Internet Version 2010)*, ser. CRC Handbook of Chemistry and Physics. Boca Raton, FL: CRC Press/Taylor and Francis, 2010.

[129] J. A. Woollam, B. D. Johs, C. M. Herzinger, J. N. Hilfiker, R. A. Synowicki, and C. L. Bungay, "Overview of variable-angle spectroscopic ellipsometry (vase), part i: Basic theory and typical applications," in *Optical Metrology*, G. A. Al-Jumaily, Ed., vol. CR72. SPIE, 1999, p. 26. [Online]. Available: http://spie.org/Publications/Proceedings/Paper/10.1117/12.351660

[130] R. M. A. Azzam, "Ellipsometry," in *Handbook of Optics: Fundamentals, Techniques, and Design*, 3rd ed., ser. Handbook of Optics, M. Bass, Ed. McGraw-Hill, 2010, no. v. 1.

[131] H. Fujiwara, *Spectroscopic Ellipsometry: Principles and Applications*. Wiley, 2007.

[132] A. Rothen, "The ellipsometer, an apparatus to measure thicknesses of thin surface films," *Rev. Sci. Instrum.*, vol. 16, pp. 26–30, 1945.

[133] O. Instruments, "Atomic layer deposition systems: ALD process solutions using FlexAL® and OpAL®." [Online]. Available: http://www.oxford-instruments.com/OxfordInstruments/media/plasma-technology/Documents/Brochures/ALD-Brochure_2011.pdf?width=0&height=0&ext=.pdf

[134] T. Tiwald, "Combining SE with QCM-D measurements," *J. A. Woollam Co. newsletter*, vol. 11, 2010. [Online]. Available: http://www.jawoollam.com/Newletters/Applications/se_for_qcmd.pdf

[135] R. Azzam and N. Bashara, *Ellipsometry and polarized light*, ser. North-Holland personal library. North-Holland Pub. Co., 1977.

[136] J. A. Woollam, B. D. Johs, C. M. Herzinger, J. N. Hilfiker, R. A. Synowicki, and C. L. Bungay, "Overview of variable-angle spectroscopic ellipsometry (vase), part ii: Advanced applications," in *Optical Metrology*, G. A. Al-Jumaily, Ed., vol. CR72. SPIE, 1999, p. 26.

[137] H. Tompkins and E. Irene, *Handbook of Ellipsometry*. Elsevier Science, 2005.

[138] I. J. A. Woollam Co., *Guide to using WVASE® Spectroscopic Ellipsometry Data Aquisition and Analysis Software*. J. A. Woollam Co., Inc., 2012.

[139] G. Binnig, C. F. Quate, and C. Gerber, "Atomic force microscope," *Phys. Rev. Lett.*, vol. 56, pp. 930–933, Mar 1986. [Online]. Available: http://link.aps.org/doi/10.1103/PhysRevLett.56.930

[140] N. Yao and Z. L. Wang, Eds., *Handbook of Microscopy for Nanotechnology*. New York, USA: Kluwer Academic Publishers, 2005.

[141] Bruker Corporation, "Dimension Icon User Guide," 2014.

[142] P. Eaton and P. West, *Atomic Force Microscopy*. OUP Oxford, 2010.

[143] V. I. Inc., *A Practical Guide to SPM: Scanning Probe Microscopy*. [Online]. Available: http://www.veeco.com/pdfs/library/SPM_Guide_0829_05_166.pdf

[144] R. D. Rodriguez, "Dynamic atomic force microscopy on hematite nanoparticles: beyond topographic measurements," Ph.D. dissertation, Université Pierre et Marie Curie, 2008.

[145] J. Tamayo and R. García, "Relationship between phase shift and energy dissipation in tapping-mode scanning force microscopy," *Applied Physics Letters*, vol. 73, no. 20, 1998.

[146] R. García, J. Tamayo, and A. S. Paulo, "Phase contrast and surface energy hysteresis in tapping mode scanning force microsopy," *Surface and Interface Analysis*, vol. 27, no. 5-6, pp. 312–316, 1999. [Online]. Available: http://dx.doi.org/10.1002/(SICI)1096-9918(199905/06)27:5/6⟨312::AID-SIA496⟩3.0.CO;2-Y

[147] R. Garcia, C. J. Gómez, N. F. Martinez, S. Patil, C. Dietz, and R. Magerle, "Identification of nanoscale dissipation processes by dynamic atomic force microscopy," *Phys. Rev. Lett.*, vol. 97, p. 016103, Jul 2006. [Online]. Available: http://link.aps.org/doi/10.1103/PhysRevLett.97.016103

[148] E. Forsén, P. Carlberg, L. Montelius, and A. Boisen, "Laser lithography on resist bi-layer for nanoelectromechanical systems prototyping," *Microelectron. Eng.*, vol. 73–74, no. 1, pp. 491–495, Jun. 2004. [Online]. Available: http://dx.doi.org/10.1016/j.mee.2004.03.023

[149] MicroChem Corp., "LOR® lift-off resists," PDF, 2001. [Online]. Available: https://www.nanofab.utah.edu/svn/public/documents/Non%20SOPs/Photoresist/LOR%20resist%20spec%20sheet2.pdf

[150] ——, "LOR® A: safety data sheet," 2008. [Online]. Available: http://signupmonkey.ece.ucsb.edu/wiki/images/0/0e/LOR_A_Photoresist_MSDS.pdf

[151] ——, "LOR® B: safety data sheet," 2008. [Online]. Available: https://crn2.3it.usherbrooke.ca/guide_sb/produits/litho/LORBSeriesResists.pdf

[152] Y. Chen, K. Peng, and Z. Cui, "A lift-off process for high resolution patterns using pmma/lor resist stack," *Microelectron. Eng.*, vol. 73-74, no. 1, pp. 278–281, Jun. 2004. [Online]. Available: http://dx.doi.org/10.1016/j.mee.2004.02.053

[153] MicroChem Corp., "LOR® and PMGI resists," PDF, 2001. [Online]. Available: http://microchem.com/pdf/PMGI-Resists-data-sheetV-rhcedit-102206.pdf

[154] Shipley Co., "Microposit® MF®-319 developer." [Online]. Available: http://cleanroom.ien.gatech.edu/media/resources/processing/sc319dev.pdf

[155] ——, "Microposit® MF®-319 developer safety data sheet." [Online]. Available: http://imdq.physique.usherbrooke.ca/resources/MSDS/MF319_MSDS.pdf

[156] PicoQuant GmbH, "LDH series: Picosecond laser diode heads for PDL 800-B/-D/808/828." [Online]. Available: http://www.picoquant.com/images/uploads/downloads/ldh_series.pdf

[157] Ophir Optronics Solutions Ltd, "Photodiode power sensors." [Online]. Available: http://www.ophiropt.com/laser--measurement/sites/default/files/PD300_PD300-1W_PD300-TP_1.pdf

[158] Varian Inc., "Varian Cary UV-Vis-NIR 4000, 5000, 6000i spectrometer: Preliminary performance data." [Online]. Available: http://science.unitn.it/~semicon/members/pavesi/Technical%20Spec_87-1942.pdf

[159] R. Alfano, *The Supercontinuum Laser Source: Fundamentals with Updated References*, 2nd ed. Springer, 2006.

[160] NKT Photonics, "Supercontinuum generation in photonics crystal fibers: Application note," 2009. [Online]. Available: http://www.nktphotonics.com/wp-content/uploads/2015/02/Application_note_-_Supercontinuum-General1.pdf

[161] ——, "Compact ultra-bright supercontinuum light source: Application note," 2009. [Online]. Available: http://www.nktphotonics.com/wp-content/uploads/2015/02/Application_note_-_Supercontinuum-SC-5.0-10401.pdf

[162] R. R. Alfano and S. L. Shapiro, "Emission in the region 4000 to 7000 Å via four-photon coupling in glass," *Phys. Rev. Lett.*, vol. 24, pp. 584–587, Mar 1970. [Online]. Available: http://link.aps.org/doi/10.1103/PhysRevLett.24.584

[163] ——, "Observation of self-phase modulation and small-scale filaments in crystals and glasses," *Phys. Rev. Lett.*, vol. 24, pp. 592–594, Mar 1970. [Online]. Available: http://link.aps.org/doi/10.1103/PhysRevLett.24.592

[164] NKT Photonics, "SuperK EXTREME high power supercontinuum fiber laser series." [Online]. Available: http://www.nktphotonics.com/wp-content/uploads/2015/05/SuperK_EXTREME.pdf

[165] ——, "SuperK VARIA tunable wavelength filter with variable bandwidth." [Online]. Available: http://www.nktphotonics.com/wp-content/uploads/2015/03/SuperK_VARIA.pdf

[166] Physik Instrumente (PI) GmbH & Co., "P-713 XY piezo scanner: Cost-effective oem system with low profile (datasheet)," 2009. [Online]. Available: http://www.pi-usa.us/products/PDF_Data/P713_Precision_Piezo_Nano-Positioning-Stage.pdf

[167] A. Siegman, *Lasers*. University Science Books, 1986.

[168] M. A. Hartney, D. W. Hess, and D. S. Soane, "Oxygen plasma etching for resist stripping and multilayer lithography," *Journal of Vacuum Science & Technology B*, vol. 7, no. 1, pp. 1–13, 1989. [Online]. Available: http://scitation.aip.org/content/avs/journal/jvstb/7/1/10.1116/1.584440

[169] J. R. Lakowicz, "Radiative decay engineering 5: metal-enhanced fluorescence and plasmon emission," *Analytical Biochemistry*, vol. 337, no. 2, pp. 171 – 194, 2005. [Online]. Available: http://www.sciencedirect.com/science/article/pii/S0003269704009303

[170] P. Anger, P. Bharadwaj, and L. Novotny, "Enhancement and quenching of single-molecule fluorescence," *Phys. Rev. Lett.*, vol. 96, p. 113002, Mar 2006. [Online]. Available: http://link.aps.org/doi/10.1103/PhysRevLett.96.113002

[171] G. Nair, J. Zhao, and M. G. Bawendi, "Biexciton quantum yield of single semiconductor nanocrystals from photon statistics," *Nano Letters*, vol. 11, no. 3, pp. 1136–1140, 2011, pMID: 21288042. [Online]. Available: http://dx.doi.org/10.1021/nl104054t

[172] L. Coolen, X. Brokmann, and J. Hermier, *Handbook of Self Assembled Semiconductor Nanostructures for Novel Devices in Photonics and Electronics*. Elsevier Science, 2008, ch. Quantum Optics with Single CdSe/ZnS Colloidal Nanocrystals.

[173] B. Ji, E. Giovanelli, B. Habert, P. Spinicelli, M. Nasilowski, X. Xu, N. Lequeux, J.-P. Hugonin, F. Marquier, J.-J. Greffet, and B. Dubertret, "Non-blinking quantum dot with a plasmonic nanoshell resonator," *Nat Nano*, vol. 10, no. 2, pp. 170–175, Feb 2015, article. [Online]. Available: http://dx.doi.org/10.1038/nnano.2014.298

[174] M. Nasilowski, "Golden quantum dots," 2015, in a private conversation.

[175] D. Canneson, I. Mallek-Zouari, S. Buil, X. Quélin, C. Javaux, B. Mahler, B. Dubertret, and J.-P. Hermier, "Strong purcell effect observed in single thick-shell cdse/cds nanocrystals coupled to localized surface plasmons," *Phys. Rev. B*, vol. 84, p. 245423, Dec 2011. [Online]. Available: http://link.aps.org/doi/10.1103/PhysRevB.84.245423

[176] P. Blais, M. Michaels, and J. N. Helbert, *Handbook of VLSI Microlithography: Principles, Technology, and Applications*, 2nd ed. Norwich, NY: Noyes Publications, 2001, ch. Issues and Trends Affecting Lithography Tool Selection Strategy.

[177] M. S. M. Saifullah, T. Ondarçuhu, D. K. Koltsov, C. Joachim, and M. E. Welland, "A reliable scheme for fabricating sub-5 nm co-planar junctions for single-molecule electronics," *Nanotechnology*, vol. 13, no. 5, p. 659, 2002. [Online]. Available: http://stacks.iop.org/0957-4484/13/i=5/a=323

[178] H. J. Zworykin, V.K. and R. Snyder, "A scanning electron microscope," *ASTM Bulletin*, vol. 117, 1942.

[179] J. Goldstein, D. Newbury, P. Echlin, D. Joy, C. Fiori, and E. Lifshin, *Scanning Electron Microscopy and X-Ray Microanalysis: A Text for Biologists, Materials Scientists, and Geologists*. New York: Plenum Press, 1984.

[180] T. H. P. Chang, "Combined micro-miniature processing and microscopy using a scanning electron probe system," Ph.D. dissertation, 1967.

[181] M. Hatzakis, "Electron resists for microcircuit and mask production," *Journal of The Electrochemical Society*, vol. 116, no. 7, pp. 1033–1037, 1969. [Online]. Available: http://jes.ecsdl.org/content/116/7/1033.abstract

[182] M. Altissimo, "E-beam lithography for micro-/nanofabrication," *Biomicrofluidics*, vol. 4, no. 2, pp. –, 2010. [Online]. Available: http://scitation.aip.org/content/aip/journal/bmf/4/2/10.1063/1.3437589

[183] D. M. Tennant and A. R. Bleier, *Handbook of Nanofabrication*. Elsevier Science, 2010, ch. Electron Beam Lithography of Nanostructures.

[184] Carl Zeiss NTS GmbH, "SUPRA® series: Ultra high resolution FE-SEM for versatile analytics." [Online]. Available: http://www.fis.unipr.it/dokuwiki/lib/exe/fetch.php?id=lmn%3Asem&cache=cache&media=lmn:brochure.pdf

[185] M. Gschrey, F. Gericke, A. Schüßler, R. Schmidt, J.-H. Schulze, T. Heindel, S. Rodt, A. Strittmatter, and S. Reitzenstein, "In situ electron-beam lithography of deterministic single-quantum-dot mesa-structures using low-temperature cathodoluminescence spectroscopy," *Applied Physics Letters*, vol. 102, no. 25, pp. –, 2013. [Online]. Available: http://scitation.aip.org/content/aip/journal/apl/102/25/10.1063/1.4812343

[186] A. Kaganskiy, M. Gschrey, A. Schlehahn, R. Schmidt, J.-H. Schulze, T. Heindel, A. Strittmatter, S. Rodt, and S. Reitzenstein, "Advanced in-situ electron-beam lithography for deterministic nanophotonic device processing," *Review of Scientific Instruments*, vol. 86, no. 7, pp. –, 2015. [Online]. Available: http://scitation.aip.org/content/aip/journal/rsi/86/7/10.1063/1.4926995

[187] M. Gschrey, A. Thoma, P. Schnauber, M. Seifried, R. Schmidt, B. Wohlfeil, L. Kruger, J.-H. Schulze, T. Heindel, S. Burger, F. Schmidt, A. Strittmatter, S. Rodt, and S. Reitzenstein, "Highly indistinguishable photons from deterministic quantum-dot microlenses utilizing three-dimensional in situ electron-beam lithography," *Nat Commun*, vol. 6, Jul 2015, article. [Online]. Available: http://dx.doi.org/10.1038/ncomms8662

[188] N. Yao, *Handbook of Microscopy for Nanotechnology*. New York, USA: Kluwer Academic Publishers, 2005, ch. Focused Ion Beam Systems—A Multifunctional Tool for Nanotechnology.

[189] G. Wiederrecht, Ed., *Handbook of Nanofabrication*. Elsevier Science, 2010.

[190] Raith GmbH, "Elphy quantum," 2015. [Online]. Available: https://www.raith.com/products/elphy-quantum.html

[191] M. Rosticher, "Accuracy of e-beam deflection," 2015, in a private conversation.

[192] MicroChem Corp., "NANO® PMMA and copolymer," PDF, 2001. [Online]. Available: http://www.microchem.com/pdf/PMMA_Data_Sheet.pdf

[193] W. W. Hu, K. Sarveswaran, M. Lieberman, and G. H. Bernstein, "Sub-10 nm electron beam lithography using cold development of poly(methylmethacrylate)," *Journal of Vacuum Science & Technology B*, vol. 22, no. 4, pp. 1711–1716, 2004. [Online]. Available: http://scitation.aip.org/content/avs/journal/jvstb/22/4/10.1116/1.1763897

[194] R. Paschotta, "Gaussian beams," 2015. [Online]. Available: https://www.rp-photonics.com/gaussian_beams.html

[195] T. Poon and J. Liu, *Introduction to Modern Digital Holography: With Matlab*, ser. Introduction to Modern Digital Holography: With MATLAB. Cambridge University Press, 2014.

[196] B. Viaris de Lesegno, "Propriétés des modes de laguerre-gauss: Applications en physique atomique." PAMO JSM 2014, 2014.

[197] N. C. C. Gutiérrez, "Modes de Laguerre-Gauss et canalisation d'atomes froids," Theses, Université Paris Sud - Paris XI, Nov. 2014. [Online]. Available: https://tel.archives-ouvertes.fr/tel-01216481

[198] F. S. Roux, *Laser Beam Propagation: Generation and Propagation of Customized Light*. Taylor & Francis, 2014, ch. Optical Waves.

[199] C. Maurer, A. Jesacher, S. Fürhapter, S. Bernet, and M. Ritsch-Marte, "Tailoring of arbitrary optical vector beams," *New Journal of Physics*, vol. 9, no. 3, p. 78, 2007. [Online]. Available: http://stacks.iop.org/1367-2630/9/i=3/a=078

[200] R. A. Serway and J. W. Jewett, *Physics for Scientists and Engineers*, 6th ed. Belmont, CA: Thomson-Brooks/Cole, 2004.

[201] A. M. Yao and M. J. Padgett, "Orbital angular momentum: origins, behavior and applications," *Adv. Opt. Photon.*, vol. 3, no. 2, pp. 161–204, Jun 2011. [Online]. Available: http://aop.osa.org/abstract.cfm?URI=aop-3-2-161

[202] J. Simmons and M. Guttmann, *States, waves, and photons: A modern introduction to light*, ser. Addison-Wesley series in physics. Addison-Wesley Pub. Co., 1970.

[203] J. D. Jackson, *Classical Electrodynamics*, 3rd ed. New York: Wiley, 1999.

[204] J. H. Poynting, "The wave motion of a revolving shaft, and a suggestion as to the angular momentum in a beam of circularly polarised light," 1909.

[205] ——, "The momentum of a beam of light," *Atti del IV Congresso internazionale die Matematici*, vol. 3, pp. 169–194, 1909.

[206] L. Allen, M. W. Beijersbergen, R. J. C. Spreeuw, and J. P. Woerdman, "Orbital angular momentum of light and the transformation of laguerre-gaussian laser modes," *Phys. Rev. A*, vol. 45, pp. 8185–8189, Jun 1992. [Online]. Available: http://link.aps.org/doi/10.1103/PhysRevA.45.8185

[207] L. Allen, S. Barnett, and M. Padgett, *Optical Angular Momentum*, ser. Optics & Optoelectronics. Taylor & Francis, 2003.

[208] N. B. Simpson, K. Dholakia, L. Allen, and M. J. Padgett, "Mechanical equivalence of spin and orbital angular momentum of light: an optical spanner," *Opt. Lett.*, vol. 22, no. 1, pp. 52–54, Jan 1997. [Online]. Available: http://ol.osa.org/abstract.cfm?URI=ol-22-1-52

[209] A. Forbes, Ed., *Laser Beam Propagation: Generation and Propagation of Customized Light*. Taylor & Francis, 2014.

[210] V. Klimov, D. Bloch, M. Ducloy, and J. R. R. Leite, "Detecting photons in the dark region of laguerre-gauss beams," *Opt. Express*, vol. 17, no. 12, pp. 9718–9723, Jun 2009. [Online]. Available: http://www.opticsexpress.org/abstract.cfm?URI=oe-17-12-9718

[211] M. Kasperczyk, S. Person, D. Ananias, L. D. Carlos, and L. Novotny, "Excitation of magnetic dipole transitions at optical frequencies," *Phys. Rev. Lett.*, vol. 114, p. 163903, Apr 2015. [Online]. Available: http://link.aps.org/doi/10.1103/PhysRevLett.114.163903

[212] M. Padgett, J. Molloy, and D. McGloin, *Optical Tweezers: Methods and Applications*, ser. Series in Optics and Optoelectronics. CRC Press, 2010.

[213] K. T. Gahagan and G. A. Swartzlander, "Optical vortex trapping of particles," *Opt. Lett.*, vol. 21, no. 11, pp. 827–829, Jun 1996. [Online]. Available: http://ol.osa.org/abstract.cfm?URI=ol-21-11-827

[214] M. Wördemann, *Structured Light Fields: Applications in Optical Trapping, Manipulation, and Organisation*, ser. Springer Theses. Springer Berlin Heidelberg, 2012.

[215] L. Carbone, P. Fulda, C. Bond, F. Brueckner, D. Brown, M. Wang, D. Lodhia, R. Palmer, and A. Freise, "The generation of higher-order Laguerre-Gauss optical beams for

high-precision interferometry," *J Vis Exp*, no. 78, p. 50564, Aug 2013, 50564[PII]. [Online]. Available: http://www.ncbi.nlm.nih.gov/pmc/articles/PMC3855912/

[216] P. Fulda, *Precision Interferometry in a New Shape: Higher-order Laguerre-Gauss Modes for Gravitational Wave Detection*, ser. Springer Theses. Springer International Publishing, 2013.

[217] M. Mestre, F. Diry, B. Viaris de Lesegno, and L. Pruvost, "Cold atom guidance by a holographically-generated Laguerre-Gaussian laser mode," *The European Physical Journal D*, vol. 57, no. 1, pp. 87–94, 2010. [Online]. Available: http://dx.doi.org/10.1140/epjd/e2010-00005-0

[218] V. Carrat, C. Cabrera-Gutiérrez, M. Jacquey, J. W. Tabosa, B. V. de Lesegno, and L. Pruvost, "Long-distance channeling of cold atoms exiting a 2D magneto-optical trap by a Laguerre-Gaussian laser beam," *Opt. Lett.*, vol. 39, no. 3, pp. 719–722, Feb 2014. [Online]. Available: http://ol.osa.org/abstract.cfm?URI=ol-39-3-719

[219] HOLOEYE Photonics AG, "LETO phase only spatial light modulator." [Online]. Available: http://holoeye.com/wp-content/uploads/LETO_Phase_Only_Modulator.pdf

[220] G. Lazarev, A. Hermerschmidt, S. Krüger, and S. Osten, *Optical Imaging and Metrology*. Wiley-VCH Verlag GmbH & Co. KGaA, 2012, ch. LCOS Spatial Light Modulators: Trends and Applications, pp. 1–29. [Online]. Available: http://dx.doi.org/10.1002/9783527648443.ch1

[221] B. Javidi and J. L. Horner, *The Optics Encyclopedia: Basic Foundations and Practical Applications, 5 Volumes Set*. Wiley, 2004, ch. Information Processing, Optical. [Online]. Available: https://books.google.fr/books?id=o6ZujgEACAAJ

[222] W. Hossack, "Spatial light modulators and modern optical systems (lecture slides)," 1998. [Online]. Available: http://www2.ph.ed.ac.uk/~wjh/teaching/mo/tutorials/slm-solutions.pdf

[223] Z. Zhang, Z. You, and D. Chu, "Fundamentals of phase-only liquid crystal on silicon (LCoS) devices," *Light Sci Appl*, vol. 3, p. e213, Oct 2014, review. [Online]. Available: http://dx.doi.org/10.1038/lsa.2014.94

[224] J. A. Davis and I. Moreno, *Laser Beam Propagation: Generation and Propagation of Customized Light*. Taylor & Francis, 2014, ch. Laser beams by digital holograms.

[225] A. Hussain, J. Martínez, and J. Campos, "Holographic superresolution using spatial light modulator," *Journal of the European Optical Society - Rapid publications*, vol. 8, no. 0, 2013. [Online]. Available: http://www.jeos.org/index.php/jeos_rp/article/view/13007

[226] A. Hussain, J. L. Martínez, A. Lizana, and J. Campos, "Super resolution imaging achieved by using on-axis interferometry based on a spatial light modulator," *Opt. Express*, vol. 21, no. 8, pp. 9615–9623, Apr 2013. [Online]. Available: http://www.opticsexpress.org/abstract.cfm?URI=oe-21-8-9615

[227] C.-S. Guo, Z.-Y. Rong, and S.-Z. Wang, "Double-channel vector spatial light modulator for generation of arbitrary complex vector beams," *Opt. Lett.*, vol. 39, no. 2, pp. 386–389, Jan 2014. [Online]. Available: http://ol.osa.org/abstract.cfm?URI=ol-39-2-386

[228] S. Reichelt, R. Häussler, G. Fütterer, N. Leister, H. Kato, N. Usukura, and Y. Kanbayashi, "Full-range, complex spatial light modulator for real-time holography," *Opt. Lett.*, vol. 37, no. 11, pp. 1955–1957, Jun 2012. [Online]. Available: http://ol.osa.org/abstract.cfm?URI=ol-37-11-1955

[229] P. A. Cheremkhin, N. N. Evtikhiev, V. V. Krasnov, L. A. Porshneva, R. S. Starikov, and S. N. Starikov, "Optical reconstruction of digital off-axis fresnel holograms using phase-only LCOS SLM "HoloEye PLUTO VIS"," *Journal of Physics: Conference Series*, vol. 536, no. 1, p. 012008, 2014. [Online]. Available: http://stacks.iop.org/1742-6596/536/i=1/a=012008

[230] L. Hu, L. Xuan, Y. Liu, Z. Cao, D. Li, and Q. Mu, "Phase-only liquid crystal spatial light modulator for wavefront correction with high precision," *Opt. Express*, vol. 12, no. 26, pp. 6403–6409, Dec 2004. [Online]. Available: http://www.opticsexpress.org/abstract.cfm?URI=oe-12-26-6403

[231] V. Korkiakoski, C. U. Keller, N. Doelman, J. Codona, and M. Kenworthy, "High-order wavefront correction with a spatial light modulator: Calibrations with dOTF method," in *Imaging and Applied Optics*. Optical Society of America, 2013, p. OM3A.4. [Online]. Available: http://www.osapublishing.org/abstract.cfm?URI=AOPT-2013-OM3A.4

[232] E. J. Fernández, P. M. Prieto, and P. Artal, "Wave-aberration control with a liquid crystal on silicon (LCOS) spatial phase modulator," *Opt. Express*, vol. 17, no. 13, pp. 11 013–11 025, Jun 2009. [Online]. Available: http://www.opticsexpress.org/abstract.cfm?URI=oe-17-13-11013

[233] A. Lizana, I. Moreno, A. Márquez, C. Iemmi, E. Fernández, J. Campos, and M. J. Yzuel, "Time fluctuations of the phase modulation in a liquid crystal on silicon display: characterization and effects in diffractive optics," *Opt. Express*, vol. 16, no. 21, pp. 16 711–16 722, Oct 2008. [Online]. Available: http://www.opticsexpress.org/abstract.cfm?URI=oe-16-21-16711

[234] M. Zheng, Y. Ogura, and J. Tanida, "Three-dimensional dynamic optical manipulation by combining a diffractive optical element and a spatial light modulator," *Optical Review*, vol. 15, no. 2, pp. 105–109, 2008. [Online]. Available: http://dx.doi.org/10.1007/s10043-008-0015-y

[235] H.-H. Chou, F. Zhang, T. D. Wilkinson, N. Collings, and W. A. Crossland, "Implementation of a 6 × 6 free-space optical fiber ribbon switch for storage area networks," *J. Lightwave Technol.*, vol. 30, no. 11, pp. 1719–1725, Jun 2012. [Online]. Available: http://jlt.osa.org/abstract.cfm?URI=jlt-30-11-1719

[236] B. Robertson, Z. Zhang, M. M. Redmond, N. Collings, J. Liu, R. S. Lin, A. M. Jeziorska-Chapman, J. R. Moore, W. A. Crossland, and D. P. Chu, "Use of wavefront encoding in optical interconnects and fiber switches for cross talk mitigation," *Appl. Opt.*, vol. 51, no. 5, pp. 659–668, Feb 2012. [Online]. Available: http://ao.osa.org/abstract.cfm?URI=ao-51-5-659

[237] X. Zeng, J. Bai, C. Hou, and G. Yang, "Compact optical correlator based on one phase-only spatial light modulator," *Opt. Lett.*, vol. 36, no. 8, pp. 1383–1385, Apr 2011. [Online]. Available: http://ol.osa.org/abstract.cfm?URI=ol-36-8-1383

[238] K. Malgorzata, P.-A. Rosario, and Z. Weronika, "LCoS spatial light modulators as active phase elements of full-field measurement systems and sensors," *Metrol. Meas. Syst.*, vol. XIX, no. 3, pp. 445–458, 2012.

[239] Z. Bouchal, "Nondiffracting optical beams: Physical properties, experiments, and applications," *Czechoslovak Journal of Physics*, vol. 53, no. 7, pp. 537–578, 2003. [Online]. Available: http://dx.doi.org/10.1023/A%3A1024802801048

[240] J. C. Gutiérrez-Vega, *Laser Beam Propagation: Generation and Propagation of Customized Light*. Taylor & Francis, 2014, ch. Helmholtz–Gauss Beams.

[241] E. Priestley, P. Wojtowicz, and P. Sheng, Eds., *Introduction to Liquid Crystals*. Princeton, New Jersey: Plenum Press, 1975.

[242] E. Lueder, *Liquid Crystal Displays*. John Wiley & Sons, Ltd, 2010. [Online]. Available: http://dx.doi.org/10.1002/9780470688342.ch1

[243] D.-K. Yang and S.-T. Wu, *Fundamentals of Liquid Crystal Devices*, 2nd ed. John Wiley & Sons, Ltd, 2014. [Online]. Available: http://dx.doi.org/10.1002/9781118751992.ch1

[244] Sigma-Aldrich Co. LLC., "4'-pentyl-4-biphenylcarbonitrile." [Online]. Available: http://www.sigmaaldrich.com/catalog/product/aldrich/328510?lang=en&region=US

[245] E. Hecht, *Optics*, 4th ed. San Francisco: Addison Wesley, Aug. 2002.

[246] D. Dunmur and K. Toriyama, *Handbook of liquid crystals: Four volume set*, 1998, vol. 1, ch. Optical Properties.

[247] D. Yang and S. Wu, *Fundamentals of Liquid Crystal Devices*, ser. Wiley Series in Display Technology. Wiley, 2014.

[248] HOLOEYE Photonics AG, "LETO phase only spatial light modulator (reflective)." [Online]. Available: http://holoeye.com/spatial-light-modulators/leto-phase-only-spatial-light-modulator/

[249] B. Guenther, *Modern Optics*. John Wiley & Sons, 1990.

[250] U. Schnars and W. Jüptner, *Digital Holography: Digital Hologram Recording, Numerical Reconstruction, and Related Techniques*. Springer, 2005.

[251] HAMAMATSU Photonics K.K., *Opto-semiconductor Handbook*, ch. Phase spatial light modulator LCOS-SLM.

[252] Y. Igasaki, F. Li, N. Yoshida, H. Toyoda, T. Inoue, N. Mukohzaka, Y. Kobayashi, and T. Hara, "High efficiency electrically-addressable phase-only spatial light modulator," *Optical Review*, vol. 6, no. 4, pp. 339–344, 1999. [Online]. Available: http://dx.doi.org/10.1007/s10043-999-0339-2

[253] A. Lizana, N. Martin, M. Estapé, E. Fernández, I. Moreno, A. Márquez, C. Iemmi, J. Campos, and M. J. Yzuel, "Influence of the incident angle in the performance of liquid crystal on silicon displays," *Opt. Express*, vol. 17, no. 10, pp. 8491–8505, May 2009. [Online]. Available: http://www.opticsexpress.org/abstract.cfm?URI=oe-17-10-8491

[254] D. C. O'Shea, T. J. Suleski, A. D. Kathman, and D. W. Prather, *Diffractive Optics: Design, Fabrication, and Test*, ser. SPIE Press Monograph. Society of Photo Optical, 2004.

[255] R. W. Gerchberg and W. O. Saxton, "A practical algorithm for the determination of the phase from image and diffraction plane pictures," *Optik (Jena)*, vol. 35, pp. 237–246, 1972. [Online]. Available: http://www.u.arizona.edu/~ppoon/GerchbergandSaxton1972.pdf

[256] M. Pasienski and B. DeMarco, "A high-accuracy algorithm for designing arbitrary holographic atom traps," *Opt. Express*, vol. 16, no. 3, pp. 2176–2190, Feb 2008. [Online]. Available: http://www.opticsexpress.org/abstract.cfm?URI=oe-16-3-2176

[257] S. Popoff, "How to characterize and calibrate a phase only SLM [tutorial]," May 2013. [Online]. Available: http://wavefrontshaping.net/index.php/events/57-community/tutorials/spatial-lights-modulators-slms/60-how-to-characterize-and-calibrate-a-phase-only-slm

Index